Comas, M.C., Zahn, R., Klaus, A., et al., 1996
Proceedings of the Ocean Drilling Program, Initial Reports, Vol. 161

6. SITE 976[1]

Shipboard Scientific Party[2]

HOLE 976A

Date occupied: 0100, 21 May 1995

Date departed: 0900, 21 May 1995

Time on hole: 8 hr

Position: 36°12.318′N, 4°18.800′W

Drill pipe measurement from rig floor to seafloor (m): 1118.6

Distance between rig floor and sea level (m): 11.05

Water depth (drill pipe measurement from sea level, m): 1107.5

Total depth (from rig floor, m): 1124.5

Penetration (m): 5.9

Number of cores (including cores having no recovery): 1

Total length of cored section (m): 5.9

Total core recovered (m): 5.92

Core recovery (%): 100.0

Oldest sediment cored:
Depth (mbsf): 5.9
Nature: Clay
Age: Pleistocene

Comments: Mudline core; jet-in test conducted.

HOLE 976B

Date occupied: 0100, 21 May 1995

Date departed: 1245, 1 June 1995

Time on hole: 11 days, 3 hr, 45 min

Position: 36°12.313′N, 4°18.763′W

Drill pipe measurement from rig floor to seafloor (m): 1119.1

Distance between rig floor and sea level (m): 11.05

Water depth (drill pipe measurement from sea level, m): 1108.0

Total depth (from rig floor, m): 2047.8

Penetration (m): 928.7

Number of cores (including cores having no recovery): 106

Total length of cored section (m): 928.7

Total core recovered (m): 535.54

Core recovery (%): 57.7

Oldest sediment cored:
Depth (mbsf): 669.7
Nature: Sandstone and gravel
Age: Miocene

Basement:
Depth (mbsf): 669.7-928.7
Nature: Metamorphic rocks

HOLE 976C

Date occupied: 1245, 1 June 1995

Date departed: 1145, 3 June 1995

Time on hole: 1 day, 23 hr

Position: 36°12.313′N, 4°18.735′W

Drill pipe measurement from rig floor to seafloor (m): 1119.5

Distance between rig floor and sea level (m): 11.35

Water depth (drill pipe measurement from sea level, m): 1108.2

Total depth (from rig floor, m): 1499.2

Penetration (m): 379.7

Number of cores (including cores having no recovery): 40

Total length of cored section (m): 379.7

Total core recovered (m): 340.16

Core recovery (%): 89.6

Oldest sediment cored:
Depth (mbsf): 379.7
Nature: Clay
Age: Pleistocene

HOLE 976D

Date occupied: 1145, 3 June 1995

Date departed: 1645, 3 June 1995

Time on hole: 5 hr

Position: 36°12.330′N, 4°18.744′W

Drill pipe measurement from rig floor to seafloor (m): 1119.0

Distance between rig floor and sea level (m): 11.38

Water depth (drill pipe measurement from sea level, m): 1107.6

Total depth (from rig floor, m): 1149.0

Penetration (m): 30.0

Number of cores (including cores having no recovery): 4

Total length of cored section (m): 30

Total core recovered (m): 30.79

Core recovery (%): 102.6

Oldest sediment cored:
Depth (mbsf): 30.0
Nature: Clay
Age: Pleistocene

[1]Comas, M.C., Zahn, R., Klaus, A., et al., 1996. *Proc. ODP, Init. Repts.,* 161: College Station, TX (Ocean Drilling Program).
[2]Shipboard Scientific Party is given in the list preceding the Table of Contents.

HOLE 976E

Date occupied: 1645, 3 June 1995

Date departed: 0830, 8 June 1995

Time on hole: 4 days, 15 hr, 45 min

Position: 36°12.323′N, 4°18.744′W

Drill pipe measurement from rig floor to seafloor (m): 1119.0

Distance between rig floor and sea level (m): 11.38

Water depth (drill pipe measurement from sea level, m): 1107.6

Total depth (from rig floor, m): 1855.30

Penetration (m): 736.3

Number of cores (including cores having no recovery): 28

Total length of cored section (m): 192.5

Total core recovered (m): 64.85

Core recovery (%): 33.7

Oldest sediment cored:
Depth (mbsf): 652.3
Nature: Claystone
Age: middle Miocene

Basement:
Depth (mbsf): 652.3-736.3
Nature: Metamorphic rocks

Comments: Drilled without coring from 0.0 to 543.8 mbsf.

Principal results: Site 976 (proposed Site Alb-2) is situated in the western Alboran Sea, 60 km off the southern Spanish coast and about 110 km east of the Strait of Gibraltar, on the lower part of a gentle slope that dips to the south from the Spanish Margin toward the Western Alboran Basin. It is located in a water depth of 1108 m, 8 km northeast of DSDP Site 121.

Site 976 was the first of three Leg 161 sites planned to address tectonic objectives in the western Mediterranean Sea and the westernmost site of the trans-Mediterranean drilling transect designed to refine paleoceanographic models of sapropel formation. The main tectonic question in the Alboran Sea basin concerns the long-standing problem in understanding convergent plate boundaries: how extensional basins develop in a collisional setting. Paleoceanographic objectives of Site 976 focus on monitoring the Atlantic–Mediterranean water exchange during the late Cenozoic with special emphasis on periods of sapropel deposition.

Five holes were drilled at Site 976. Except for Hole 976A, which was used to determine the mudline, they were dedicated to distinct scientific objectives: at Hole 976B the entire 650-m-thick sedimentary sequence was cored continuously, penetrating 267 m into metamorphic basement, and thus meeting our highest priority tectonic objective. Hole 976C was designated to meet our paleoceanographic objectives and cored down to the Pleistocene/Pliocene boundary at 375 mbsf; Hole 976D was dedicated to high-resolution interstitial water geochemistry and cored to a depth of 30 mbsf. Hole 976E was designed to fill gaps in recovery around major unconformities within the sedimentary sequence, and to sample and log the sediment–basement transition and the top of the basement.

The stratigraphic interval cored and sampled at Site 976 ranges from uppermost middle Miocene (Zone NN7, *N. continuosa/G. siakensis* Zone) to uppermost Pleistocene/Holocene (Subzone NN21B, *G. truncatulinoides excelsa* Zone). The Pliocene/Pleistocene boundary is between 357.92 and 361.01 mbsf, and three major hiatuses were recorded: between late and early Pliocene (Zanclean and Piacenzian), early Pliocene and latest Miocene (Zanclean and Messinian), and within the late Miocene (Tortonian). Sedimentation rates are 208 m/m.y for the Pleistocene-Holocene; 340 m/m.y. for the upper Pliocene; 453 m/m.y. for the lower Pliocene, and 15 m/m.y. for the upper Miocene.

Sediments at Site 976 are subdivided into four lithostratigraphic units:

Unit I: Hole 976A, 0–5.9 mbsf; Hole 976B, 0.0–362.1 mbsf; Hole 976C, 0.0–362.8 mbsf; Hole 976D, 0.0–30.0 mbsf. Unit I contains a Holocene–Pleistocene open marine hemipelagic facies of nannofossil-rich clay, nannofossil clay, and nannofossil silty clay. Continuous and discontinuous clayey silt laminae occur irregularly throughout. Unit I carbonate content averages 28%. The carbonate fraction consists of nannofossils, foraminifers, bioclasts, micrite, inorganic calcite, and dolomite. Laminated beds of diatomaceous ooze up to 5 cm thick can be correlated between holes. Downhole variations in detrital siliciclastic grains suggest that Unit I contains three major cycles of upward-increasing terrigenous input.

Twenty-eight organic-rich layers (ORLs) occur in five discrete intervals within Unit I. They consist mainly of nannofossil clay to nannofossil-rich clay and generally contain 0.9% to 1.3% TOC (background is 0.5% TOC). These ORLs are identified by low magnetic susceptibilities and very subtle color changes. ORLs range from less than 20 cm to more than 2 m in thickness. Examination of smear slides reveals an amorphous organic component as well as terrigenous plant fragments and spores.

Unit II: Hole 976B, 362.1–518.3 mbsf; Hole 976C, 362.8–379.7 mbsf. Unit II consists of Pliocene sand, silt, calcareous silty clay, and nannofossil clay. Core recovery was low (12%), probably because poorly consolidated sand intervals were washed during drilling. Average carbonate content is 33%. Where recovered, the sand consists mainly of quartz and shell fragments with minor components of rock fragments (including schist and serpentinite), feldspar, micas, heavy minerals, plant fragments, and traces of glauconite.

Unit III: Hole 976B, 518.3–660.2 mbsf; Hole 976E, 543.8–652.0 mbsf. Unit III is Miocene–Pliocene in age, and consists of grayish olive nannofossil and nannofossil-rich clay and claystone. Hiatuses and unconformities occur between early and late Pliocene, at the Miocene/Pliocene boundary, and within the Tortonian. Average carbonate content is 37%. The unit is bioturbated extensively and *Chondrites* and *Zoophycos* ichnofacies are found throughout. Laminations are present in a few intervals, in places delineated by aligned organic matter. At Hole 976E, immediately above Unit IV, the clays of Unit III exhibit a well-defined fissility (shale).

Unit IV: Hole 976B, 660.2–669.73 mbsf; Hole 976E, 651.95–652.08 mbsf. Unit IV immediately overlies basement in both holes. In Hole 976B it consists of coarse-grained, poorly sorted, coarse pebbly sand. The pebbly sand is of marine facies, Serravallian in age, and is composed of quartz, biotite, feldspar, and rock and shell fragments. Rounded, gravel-sized metamorphic clasts are present as minor components throughout the sandy interval. In Hole 976E, Unit IV is formed by a 15-cm-thick interval of glauconite-rich, sandy-silty claystone, also Serravallian in age.

Beneath the sedimentary sequence, we cored 259 m (669.7–928.7 mbsf) and 50.53 m (652.08–702.5 mbsf) of high-grade metamorphic rocks in Holes 976B and 976E, respectively. The contact between the basement and the middle Miocene sediments is sharp and has an irregular topography, possibly produced by faulting. Basement faulting is indicated by tectonic breccia intervals throughout the basement in Holes 976B and 976E. In the upper 40 m of basement, some fault breccias are formed by highly angular metamorphic clasts in a matrix of Miocene sedimentary rock.

The metamorphic basement of the Alboran Basin at Site 986 yields the following lithotypes:

1. High-grade schist: dark-grey graphitic schist with biotite, sillimanite aggregates, and andalusite and garnet porphyroblasts.
2. Gneiss: medium gray felsic gneiss, commonly with biotite, feldspar, plagioclase, sillimanite, andalusite porphyroblasts up to 1 cm, inky blue or blue-green cordierite porphyroblasts up to 1 cm, and locally some muscovite. Locally the gneiss grades with increasing biotite content into high-grade schist, and with increasing felsic component into migmatitic gneiss.
3. Migmatitic gneiss: medium grey felsic biotite-cordierite-sillimanite-andalusite-gneiss with irregular veins and patches of light gray, weakly foliated or unfoliated granite with biotite and tourmaline. The granitic material forms veins parallel to, or cutting across, the foliation, and associated coarse-grained quartz veins with tourmaline are abundant. In places the granitic material contains cordierite.
4. Marble: very pale green, gray or white crystalline dolomite marble and calcite marble, with minor amounts of phlogopite and chlorite. The calcite marble near the top of the basement in Hole 976E is interlay-

ered on a small scale with calc-silicate rock and biotite-sillimanite schist.

5. Calc-silicate rock: banded rocks with thin layers of calcite or dolomite, garnet, plagioclase, green calc-silicate minerals including diopside and calcic amphibole, and serpentine? after forsterite?. These commonly occur as reaction zones between marble and schist.
6. Granite: discrete pieces of light gray to white, fine-grained hypidiomorphic granular leucogranite occur throughout the sequence, probably in the form of dikes. The granite has small amounts of biotite and tourmaline.

With the exception of the leucogranite dikes and the granitic leucosomes, all basement rock types show a well-developed foliation. They show evidence of penetrative ductile deformation that produced a suite of minor structures and fabrics. At least three sets of ductile fabrics and structures can be distinguished. The metamorphic sequence is also cut by numerous zones of fault-breccia and fault-gouge that mark zones of brittle faulting. Marble occurs as layers dispersed throughout the sequence, and the dolomitic marble in particular is commonly associated with zones of brecciation and faulting. At the bottom of Hole 976B, samples include a larger amount of well-cemented fault breccia. Some left-lateral oblique slip along discrete faults is suggested by striae on subvertical fault-planes crosscutting the metamorphic rocks.

First estimates of pressure and temperature conditions of metamorphism suggest that the high-grade schist underwent a significant decrease in pressure accompanied by constant or increasing temperature. Migmatite gneiss and gneiss also indicate a superimposed high-temperature metamorphism under low-pressure conditions with granite formation. The metamorphic history of basement rocks at Site 976 likely reflects the tectonic exhumation of middle crustal rocks.

The basement rocks recovered from Holes 976B and 976E closely resemble high-grade metamorphic rocks belonging to the Alpujarride Complex of the western Betic Cordillera (Spain), which have early Miocene radiometric ages, particularly those neighboring the Ronda peridotite massif.

Site 976 sediments average 0.5% TOC, with maximum values up to 1.6%. C/N ratios of samples containing a minimum of 1% TOC average 15.5 and indicate that the organic-carbon–rich sediments contain a mixture of partially degraded algal material and continental organic matter. Maximum temperature values are relatively low, showing that organic matter is thermally immature with respect to petroleum generation. Concentrations of headspace methane are high at Site 976 and are probably derived from in situ microbial fermentation of the marine organic matter. Gas levels never became hazardous at Site 976.

Interstitial water concentrations of salinity, Cl, Na, and Br increase downcore to approximately 2–3 times seawater concentrations. Ca, Mg, Sr, and Li also increase linearly with depth. These profiles suggest the presence of a deep-seated brine, which is preliminarily interpreted to be either a Messinian-age paleo-fluid or a brine originating from dissolution of salts in a deeper part of the basin. The circulation of this brine may be driven by compaction or by hydrothermal influx along the basement-sediment contact.

High-resolution (1.5-m interval) interstitial water sampling of the upper 30 m at Hole 976D revealed a classical sequence of diagenetic redox reactions driving organic carbon degradation. The Mn- and Fe-reduction zones are located within the upper 1.5 m of the core. Sulfate decreases linearly and is depleted at 19.95 mbsf, indicating that organic matter degradation above this depth is primarily sustained by sulfate reduction. Below 20 m, headspace methane concentration increases rapidly, marking the onset of bacterially mediated methanogenesis, which is responsible for organic matter degradation in the absence of interstitial water sulfate.

Downhole temperature measurements with the ADARA and WSTP temperature tools indicate a heat flow of 102 mW/m^2 at this site which is in excellent agreement with other values measured nearby. Remanent magnetization of the sediments at Site 976 is weak and exhibits a stepwise decrease by about one order of magnitude down to 50–60 mbsf. Declinations are scattered and inclinations dominantly positive, with only a few negative inclinations above 360 mbsf for Holes 976B and 976C. Between 675 and 710 mbsf, at Hole 976B, negative inclinations suggest a reversed interval. A strong magnetic overprinting makes magnetostratigraphy difficult. Reliable MST velocity and GRAPE measurements could not be made at Site 976 because of high gas concentrations in the sediments. Velocities in basement samples range from 3.3 to 6.5 km/s and have 20%–30% anisotropy.

One of the most exciting results of Site 976 is the discovery that basement beneath the Alboran Basin is formed by rocks of continental origin that have undergone high-temperature metamorphism, exhumation, and isothermal decompression. We cored a >250-m-thick section of high-grade metamorphic basement and obtained a spectacular suite of basement logs (quad combo, FMS, BHTV, and geochemical). Tectonic models that propose an early-to-middle Miocene continental extensional origin for the Alboran Basin postulated the existence of such metamorphic rocks at depth. Drilling results from Site 976 will significantly contribute to our understanding of the tectonic evolution of the Alboran Sea, as well as other backarc basins in the Mediterranean Sea. Integration of tectonic and paleoceanographic results from Site 976 will help to establish links between the paleogeographic history of the Atlantic–Mediterranean gateway and the evolution of the Atlantic–Mediterranean water exchange since the Miocene.

BACKGROUND AND OBJECTIVES

Site 976 (proposed Site Alb-2) was drilled to investigate the origin and tectonic evolution of the Alboran Sea basin, a well-defined example of "Mediterranean type" backarc basin (see "Introduction" chapter, this volume). The highest priority at Site 976 was to penetrate at least 200 m into the predicted metamorphic basement. Information thus obtained could constrain geodynamic models for the origin of these basins and the tectonic evolution of the westernmost circum-Mediterranean thrust-belt that surrounds the Alboran Sea: the Betic and Rif Chains, which are linked through the Gibraltar Arc.

Paleoceanographic objectives of Site 976 focus on monitoring the Atlantic-Mediterranean exchange of water masses during the late Cenozoic. Site 976 is the westernmost site of the trans-Mediterranean drilling transect, which was designed to establish paleoceanographic patterns across the Mediterranean with special emphasis on periods of sapropel deposition.

Site 976 is located in the westernmost Mediterranean (Alboran Sea) on the lower part of a gently sloping seafloor that dips from the Spanish Margin south toward the Western Alboran Basin (Fig. 1). It is about 60 km south of Málaga, 110 km east of the Strait of Gibraltar, and 8 km northeast of DSDP Site 121, which was drilled during Leg 13 in 1970 (Ryan, Hsü, et al., 1973). The position of the site was selected by coordinates from the preexisting site-survey data (Fig. 2). The site was drilled at shotpoint 1295 of multichannel seismic line ALB-39 (Fig. 3), and 600 m southeast of the intersection of seismic lines 75-230 and 75-334 (Fig. 4). To verify the site location, the *JOIDES Resolution* conducted a geophysical survey, and the site was positioned at the intersection of line ALB-39 and the two *JOIDES Resolution* single-channel seismic profiles (see "Underway Geophysics" chapter, this volume).

Site 976 was drilled on a basement high in order to penetrate predicted metamorphic basement more easily, and it was positioned away from areas where the acoustic basement was suspected to be composed of volcanic rocks. Pre-cruise geological and geophysical survey data suggested that the same high that was drilled by DSDP Site 121 was the most appropriate location to address the Leg 161 basement objectives. This prominent basement structure in the Alboran Sea basin is believed to be a continental crustal horst that formed during early- to mid-Miocene rifting. At Site 976, the horst is ~50 km long and 17 km wide and is bounded by a set of north-south- to northeast-southwest–trending normal faults (Fig. 5). Toward the south, the horst changes to a northwest-southeast orientation and extends for another 50 km. A major graben depocenter bounds the horst to the

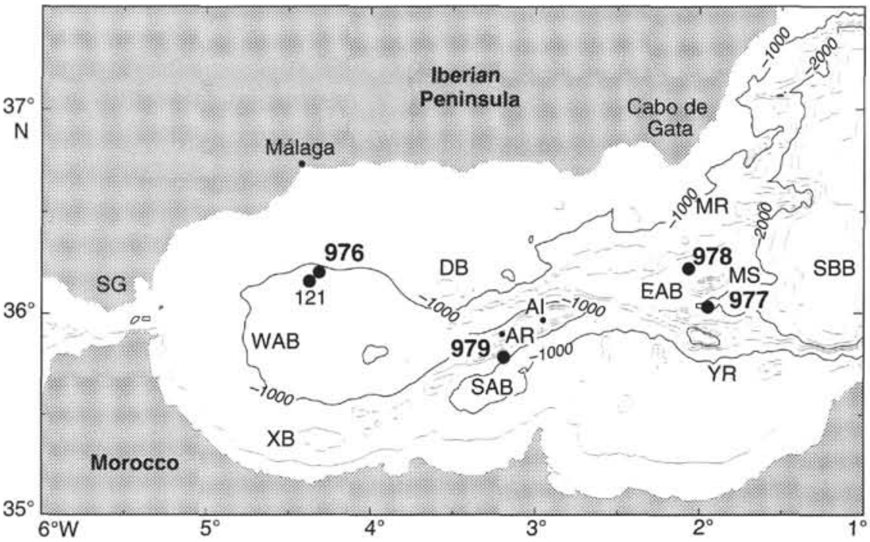

Figure 1. Location of Leg 161 Sites 976, 977, 978, and 979 and DSDP Site 121 in the Alboran Sea. Contours in meters, contour interval is 200 m. AI = Alborán Island, AR = Alboran Ridge, DB = Djibuti Bank, EAB = Eastern Alboran Basin, MR = Maimonides Ridge, MS = Al-Mansour Seamount, SAB = South Alboran Basin, SBB = South Balearic Basin, SG = Strait of Gibraltar, WAB = West Alboran Basin, XB = Xauen Bank, YR = Yusuf Ridge.

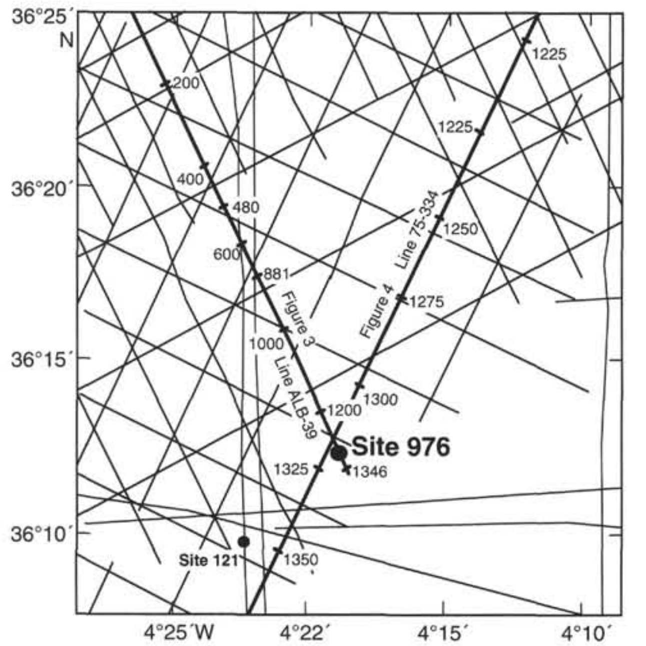

Figure 2. Shotpoint map of multichannel seismic reflection lines around the Site 976 structural high. Location of seismic profiles in Figures 3 and 4 is shown.

west (Fig. 6). Seismic reflection profiles show that this graben is filled by at least 6 km of lower Miocene to Pleistocene sediments (Comas et al., 1992, 1993; Watts et al., 1993).

Seismic-reflection profiles across the Site 976 structural high show that the top of acoustic basement lies at depths ranging from 2 to 2.4 s (two-way traveltime, TWT) and that Messinian sediments have been eroded from the top of the high (Fig. 7). Multichannel seismic stacking velocities indicated we would encounter the acoustic basement at about 650 mbsf (0.67 s TWT). As at DSDP Site 121, we expected to sample a Pliocene–Quaternary sedimentary sequence and some upper Miocene deposits. Drilling at DSDP Site 121 cored, with a very low recovery, a 864-m-thick sedimentary sequence in which the oldest sediments recovered were late Miocene in age (Tortonian after Ryan, Hsü, et al., 1973a; or Messinian after Montenant et al., 1975). Below this sequence, DSDP scientists recovered some pieces of metamorphic rocks believed to be clasts from a marine conglomerate on top of the acoustic basement (Ryan, Hsü, et al., 1973a).

Data from commercial wells on the Spanish continental shelf (Comas et al., 1992; Jurado and Comas, 1992; Watts et al., 1993) and from DSDP Site 121 results (Kornprobst, 1973; Steiger and Frick, 1973) suggested that the basement beneath the Alboran Sea is formed of metamorphic rocks, closely related to metamorphic sequences exposed in the Internal Zones of the surrounding Betic and Rif Chains (Alboran Crustal Domain, Fig. 5). This crustal domain consists of a thrust stack with three nappe-complexes: the Nevado-Filabride, the Alpujarride, and the Malaguide complexes. The Nevado-Filabride complex, the lower tectonic unit of the thrust stack, and the overlying Alpujarride complex contain sequences of Alpine medium- to high-grade metamorphic rocks, probably of Paleozoic and Triassic age. The Malaguide complex (Paleozoic to Miocene in age), the uppermost unit of the stack, has undergone only low-grade metamorphism. These metamorphic complexes belong to a late Cretaceous–Paleogene orogen generated by collisional stacking that experienced a complex history of repeated extensional and compressional tectonic phases (see "Introduction" chapter, this volume).

In the Alboran Crustal Domain, large-scale extensional detachments of Miocene age, which developed in both ductile and brittle conditions, are superimposed upon the continental collision structures (Balanyá and García-Dueñas, 1987; Galindo et al., 1989; Platt and Vissers, 1989; García-Dueñas et al., 1992). The remains of this orogen underwent Miocene extension and are believed to underlie much of the Alboran Sea. It was this basement beneath the basin that was the principal tectonic objective on Leg 161. More specifically, tectonic objectives at Site 976 were to determine:

1. The tectonic history prior to the origin of the Alboran Sea basin, and the basement affinity to a particular crustal domain, or tectonic unit, within those known in the surrounding Betic and Rif Cordilleras. In particular, to establish the extent that preexisting collisional orogeny controlled the origin and evolution of the Alboran Basin.
2. The age, rate, and thermal history of the extension beneath the Alboran Sea and the timing and role of igneous activity during extension. The pressure-temperature histories and absolute ages of basement rocks at this site will constrain the initial thermal structure and the uplift history and processes that have modified the crust since rifting began.
3. The geometry of the mid-Miocene rifting. Drilling results at Site 976 combined with on-land structural data will help to discriminate between prevailing models for rifting and crustal

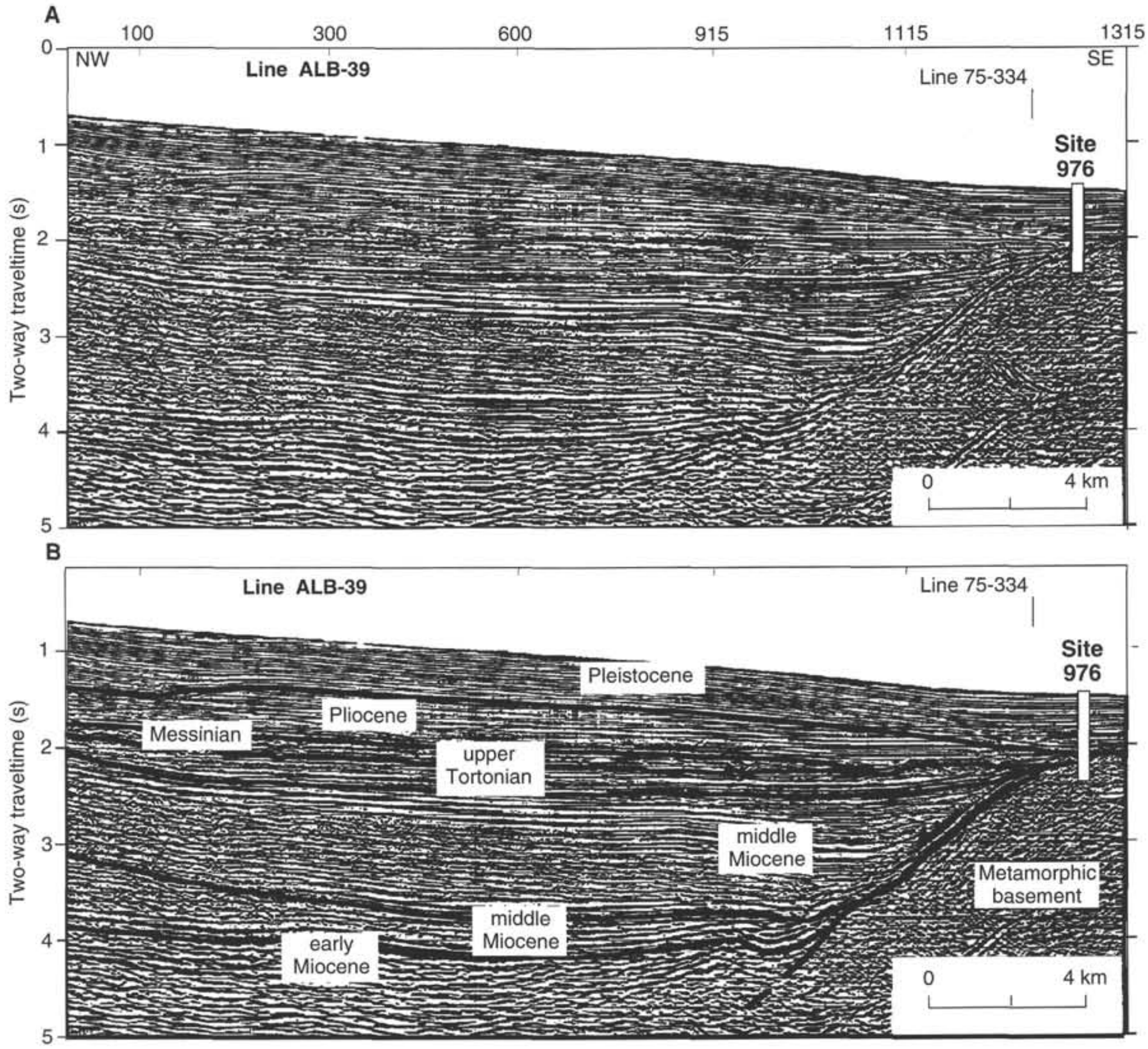

Figure 3. Location of Site 976 on migrated MCS profile ALB-39 (dip-line). The profile shows the northwest-facing fault that bounds the Site 976 high and the sedimentary infill of a mid-Miocene graben. **A.** Original seismic reflection profile. **B.** Interpreted profile based on seismic sequence analysis and stratigraphic subdivision proposed by Comas et al. (1992). Intersection with Line 75-334 (Fig. 4) is shown. Location of line shown is in Figure 2.

thinning. If the continental floor of the basin has been greatly extended, as suggested from refraction data, metamorphic rocks may have been exhumed from considerable depth within the crust along normal faults. The nature of the basement rocks will help constrain the rifting geometry and models for crustal thinning in the region.

4. Total tectonic subsidence and uplift of the basement horst. Comparison with back-stripped subsidence curves computed for the commercial wells on the Spanish and Moroccan Margins will allow the magnitude and timing of the extension in the Alboran Basin to be quantified.

Structural and petrological studies, analysis of metamorphic fabrics and pressure-temperature-time (PTt) paths, and radiometric dating of the metamorphic and igneous rocks sampled at Site 976 will provide the basis to accomplish these objectives. In addition, FMS and BHTV images of the borehole walls in the basement will permit detailed analysis of structural patterns of the basement metamorphic rocks.

Paleoceanographic work at Site 976 concentrated on retrieving a complete Pliocene–Pleistocene sedimentary sequence and sampling Miocene deposits in the westernmost Mediterranean, near the Strait of Gibraltar gateway. Paleoceanographic records at this site will help to decipher whether today's anti-estuarine current pattern (surface inflow, deep outflow) had changed to an estuarine circulation (surface outflow, deep inflow) during the past. Such current reversals have been proposed in conceptual models that explain the deposition of sapropels by enhanced nutrient levels in the Mediterranean (Sarmiento et al., 1988). As the Mediterranean's heat budget is controlled by the water exchange through the Strait of Gibraltar (Bryden and Kinder, 1991; Macdonald et al., 1994), reversed inflow-outflow patterns between the Atlantic and the Mediterranean are also likely to alter the fluxes of heat across the Mediterranean, thereby affecting regional climates in the Mediterranean climatic belt.

Isolation and desiccation of the Mediterranean during the Messinian was a significant paleoenvironmental event, important not only for the immediate Mediterranean region (Cita and McKenzie, 1986; McKenzie et al., 1990), but potentially for the world ocean's thermohaline circulation (see discussion in Thunell et al., 1987). Recovery of Tortonian sequences at Site 976 that immediately precede the onset of evaporitic conditions in the Mediterranean, as well as penetrating the Messinian erosional unconformity (laterally equivalent to the seismic "M"-reflector), are essential to document both the transition from open-marine to restricted conditions and the terminal Messinian flooding, as open-marine conditions were re-established in the Mediterranean. Integrating tectonic and paleoceanographic results from

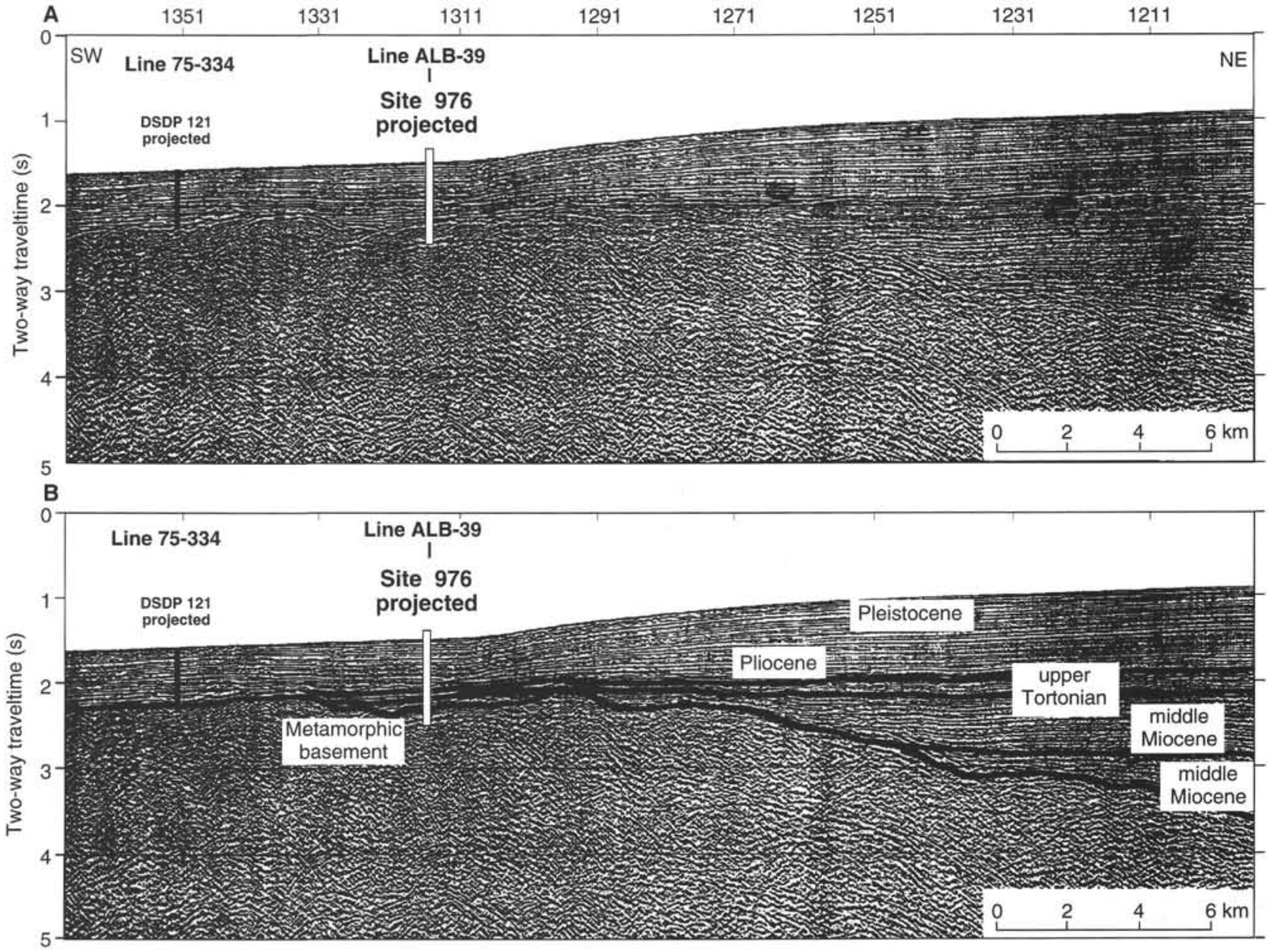

Figure 4. Location of Sites 976 and DSDP 121 on stacked MCS profile 75-334 (strike line) and cross point with seismic profile ALB-39 (Fig. 3). **A.** Original seismic reflection profile. **B.** Interpreted profile based on seismic sequence analysis and stratigraphic subdivision proposed by Comas et al. (1992). Lithoseismic units discussed in "Introduction" chapter, this volume. Location of line shown is in Figure 2.

Site 976 will help to establish links between the paleogeographic history of the Atlantic-Mediterranean gateway and the evolution of water circulation in the westernmost Mediterranean and Atlantic-Mediterranean water exchange since the Miocene.

OPERATIONS

Transit Site 975 to Site 976 (Alb-2)

After a 439-nmi transit from Site 975 (36 hr at 12 nmi/hr), we conducted a seismic survey at Site 976 (52 nmi; 9.75 hr). We then positioned over the site and deployed two beacons, at 0100 hr and 0330 hr, 21 May). Because of heavy seas and strong currents, both beacons were left on. The strong surface current from the Atlantic flowed between 2.0 and 2.5 nm/hr and varied from 250° to 280°. Site 976 was in the general shipping lane for all traffic entering and exiting the Mediterranean Sea. At times, more than 10 ships could be seen on the radar within a 12-nmi radius. This level of ship traffic continued throughout the time the *JOIDES Resolution* spent at Site 976. The elevation of the DES above sea level was 11.05 m for Holes 976A and 976B, 11.35 m for Hole 976C, and 11.38 m for Holes 976D and 976E.

Hole 976A

A re-entry cone installation was planned at Site 976, so the first hole was used to establish the mudline and conduct a jet-in test. We spudded Hole 976A at 0615 hr on 21 May. Core 976A-1H was taken with the bit at 1115 mbrf and recovered 5.92 m (Table 1; see also detailed coring summary on the CD-ROM, back pocket, this volume); therefore, the seafloor was defined to be at 1107.5 mbsl. We continued lowering the bit into the seafloor by circulating water only, to determine the amount of 16-in conductor casing that could be safely washed into the seafloor with the re-entry cone. An XCB core barrel with a center bit was used during the jet-in test. The jet-in test took 1.5 hr and penetrated to 65 mbsf using up to 45 strokes per minute (spm).

Hole 976B

We offset the ship 15 m to the southeast (i.e., up-current to the deep Mediterranean outflow) and spudded Hole 976B at 1000 hr, 21 May. The hole was vertically offset 2 m from Hole 976A. Core 976B-1H was taken with the bit at 1113 mbrf and recovered 3.45 m of sediment. The seafloor was defined to be at 1108 mbsl. Sea conditions at the time the mudline core was taken may have contributed to the difference in the mudline core recovery between Holes 976A and 976B. APC Cores 976B-1H through 14H were taken to 127 mbsf and recovered 128.04 m (101%; Table 1). Cores 3H through 14H were oriented with the Tensor tool. Temperature measurements were attempted during Cores 3H and 6H, but good data were not recovered due to tool movement caused by the sea conditions and the short, rigid drill string. The failure of one of the flappers in the core-catcher resulted in part of Core 3H being extruded onto the drill floor. The recovered

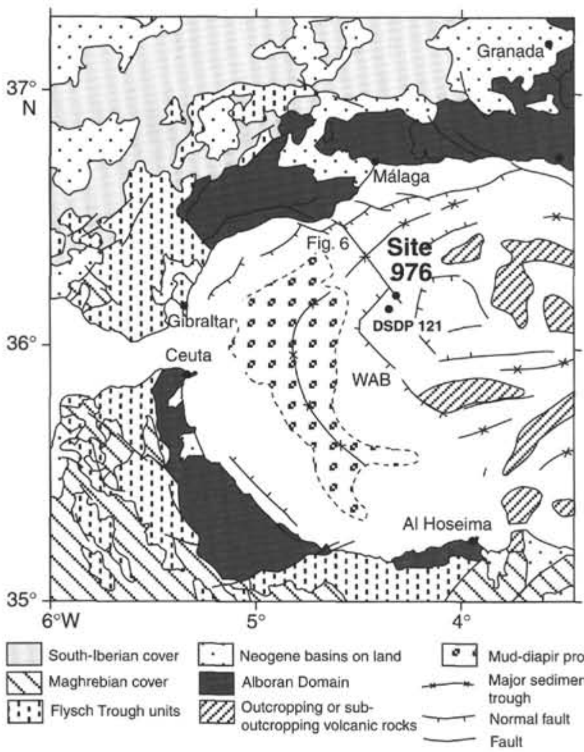

Figure 5. Tectonic sketch of the Western Alboran Basin around the Site 976 structural high. Normal faults define the grabens, which are the major lower to middle Miocene depocenters of the Alboran Basin (from Comas et al., 1993).

cores experienced significant gas-induced expansion, causing parts of the cores to extrude from the liner. To reduce core disturbance and expansion, holes were drilled in the core liners to allow the gas to escape prior to cutting the cores into sections. In the APC cores, a C_1 maximum of 66,555 ppm was measured in a headspace sample from Core 12H; however, no trends that might affect safety were observed.

XCB Cores 976B-15X to 74X were taken from 127.0 to 677.3 mbsf and recovered 486.39 m (65%). Three WSTP measurements were attempted prior to Cores 18X, 20X, and 26X (1284.4, 1303.7, 1351.7 mbrf). Gas was present in the XCB cores, and the maximum C_1 recorded was 14,662 ppm from headspace analyses. No significant trends were seen in either C_1 or C_1/C_2 ratios.

Fine sands encountered from 367 to about 518 mbsf resulted in very low core recovery. Less than 10 min was required to cut some of the cores in this interval. Before recovering the core barrel each time, the borehole was completely circulated from the bottom up to the seafloor while coring through the sands. Despite the loose nature of the formation, no fill or significant hole problems were encountered while coring this interval. Firmer clays were encountered below 518.3 mbsf (1637 mbrf). Additional sandy intervals were seen from 621.6 mbsf down to about 670 mbsf, where basement was reached. Overall recovery for both the APC and XCB portion of the Hole was 71.8%.

The hole was conditioned for logging with a wiper trip. Overpull of about 30,000 lb was observed in two zones while pulling the pipe up the hole. We had to use the top drive and rotate the drill pipe to get it to pass through numerous indurated layers throughout the sand interval (357.7 to 518.3 mbsf). After passing the drill pipe down through the sand we found 36 m of fill in the bottom of the hole. The bottom of the hole was reamed and swept with 30 barrels of high-viscosity mud, and the bit was positioned to log at 72 mbsf (1191 mbrf). Since the first tool was unable to exit the bit, we dropped and retrieved an XCB core barrel. This cleared the lockable float valve and allowed the tool to pass through the bit on the second attempt. The tool, however, only made it to 350 mbsf before encountering a bridge, and the hole was logged from 350 to 36 mbsf. The quad combo caliper data indicated that most of the hole had washed out to larger than the calipers' limit of 18.5 in. Therefore, we decided to terminate logging at 0930 hr on 26 May.

We then deployed a free-fall funnel (FFF) so that we could continue Hole 976B using RCB-coring. The BHA for the RCB was assembled with the following hardware: (1) one 9-⅞-in RBI C-4 bit, (2) mechanical bit release (MBR), (3) a head sub, (4) an outer core barrel (OCB), (5) a top sub, (6) a head sub, (8) eight 8-¼-in drill collars (DC), (9) jars, (10) two 8-¼-in drill collars (DC), (11) a crossover sub (XO), (12) a 7-¼-in. DC, (13) an XO sub, (14) 5 joints of 5-½-in drill pipe (DP), and (15) an XO sub.

We reentered the FFF at 2330 hr, 26 May. The drill string was run into the hole and approximately 37 m of fill was found at the bottom. The hole was washed and reamed to the bottom. RCB coring began at 0830 hr, 27 May. RCB Cores 976B-75R to 106R were taken from 677.2–928.7 mbsf (1796.3 to 2047.7 mbrf; Table 1) and recovered 49.12 m (19.5%). RCB drilling parameters were 15,000–23,000 lb WOB, 50–70 spm, and 40–70 rpm. Pump pressures with the core barrel ranged from 350 to 700 psi.

Core jamming was noted in the first two cores. Short cores were attempted as a means to increase core recovery, but this strategy did not appear to make much of a difference. The material being cored appeared to be a mixture of hard rocks and soft, unconsolidated, fine-grained fault gouge (only minimally recovered) resulting in quick penetration (5 m/hr) but poor recovery. We believe that the fault gouge was being washed away and only the rocks were recovered. We also attempted to take cores both with and without a core line, because coring without a core liner might reduce the chances that a piece of core might jam and prevent more core from entering the core barrel.

Before completing the hole, we made two wiper trips when the bit had penetrated to 1869.6 and 1961.1 mbrf (750 and 842 mbsf), in order to relieve an increase in pressure and as a preventative measure to help keep the hole open. During each wiper trip, the bit was pulled up to 659 mbsf (1778 mbrf). We terminated coring in Hole 976B after a final penetration to 928.7 mbsf.

To prepare for logging, a final wiper trip to 535.9 mbsf (1655 mbrf) was made to condition the hole. We had some difficulty using the releasing tool to trigger the MBR to release the bit, but after numerous attempts over a two-hour period to jar off the overshot, the MBR sleeve shifted and released the bit. The releasing tool was rerun back down the pipe to confirm that the bit was released and to shift the sleeve into the logging position.

We used a conservative two-step approach to log. First, good log data was obtained in the basement sections. For the first log, the BHA was placed just deeper than the top of basement at 698 mbsf, because it not certain whether the BHA could repenetrate the basement after being pulled above it. We ran the logging tools in the following order: quad combo, FMS, BHTV, and geochemical. The logs were run to 916.7, 914.7, 914.7, and 908.7 mbsf, respectively (2035, 2033, 2033 and 2027 mbrf). According to the drill-pipe weight indicator, during the first run material might have been tightening around the drill pipe. Between runs, the top drive was used to circulate and make sure the pipe remained free. Logging was allowed to continue since the weight increase did not appear to be a serious threat to the drill string or BHA.

The logs indicated a >5° hole angle. This deviation is not surprising based on the range of structural dips observed in the core and the variability in hardness of the formation. The hole diameter was relatively constant from 781 to 928 mbsf (1900 to 2047 mbrf). Hole diameters were considerably more variable above 1900 mbrf. However, the log data were still considered to be very good. The basement logs were finished at 0600 hr, June 1.

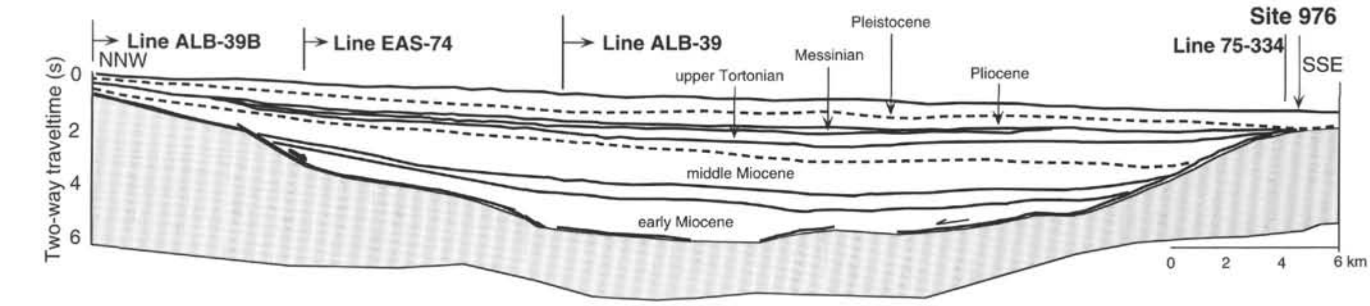

Figure 6. True-scale cross section from the Site 976 structural high to the Spanish Margin, showing the graben between the tectonic high and the margin. Note the inferred low-angle normal faults that bound the basin. Location of profiles is shown in Figure 5.

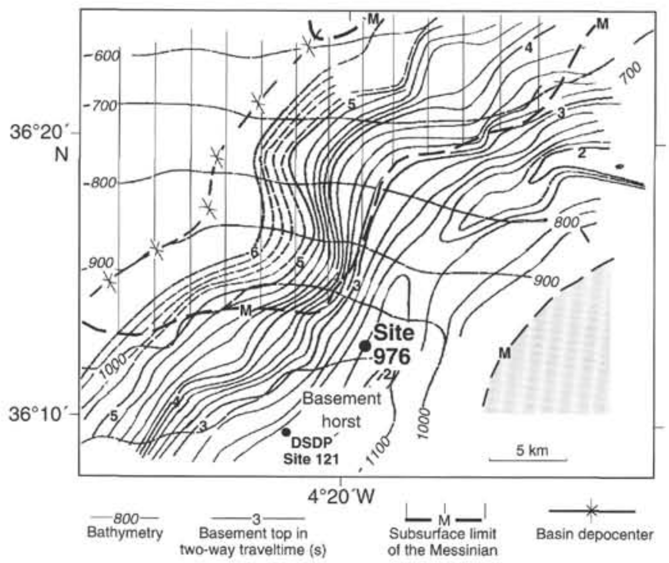

Figure 7. Contour map of depth of basement around the Site 976 basement high. Note that Site 976 is located in a Messinian window. Bathymetric contours in meters. Basement depth contours in seconds TWT. Limits of Messinian "M"-reflector tick marks face toward Messinian deposits. Axis of maximum lower to middle Miocene deposit thickness (basin depocenter) of the middle Miocene graben can be seen in Figure 6. Multichannel seismic data used for this map are shown in Figure 2.

The BHA was pulled up to 536 mbsf (1655 mbrf) to attempt a second series of logs from 536 mbsf to the top of basement. Results from the quad combo caliper data during the first run revealed that this portion of the hole was seriously washed out. We decided to terminate logging and try to log this interval in one of the next holes to be drilled at this site. Logging operations were completed at 1100 hr June 1. The hole was displaced with 80 bbl of 10.5 lb/gal barite mud before pulling out. The bottom of the drill pipe cleared the seafloor at 1245 hr, June 1.

Hole 976C

The ship was offset 50 m east (upstream to the deep Mediterranean outflow) of Hole 976B and Hole 976C was spudded at 2000 hr on 01 June. Core 976C-1H was taken with the bit at 1116.0 mbrf and recovered 5.98 m; therefore, the seafloor was defined to be at 1108.2 mbsl. APC Cores 976C-1H to 14H were taken to 129.5 mbsf (Table 1) and recovered 135.88 m (105%). Cores were oriented beginning with 3H. ADARA temperature measurements were taken during Cores 3H, 6H, 9H and 12H. The maximum C_1 gas measured in a head space sample from Core 8H was 32,543 ppm.

XCB Cores 976C-15X to 40X were taken (Table 1) from 129.5 to 379.7 mbsf (1249.0 to 1499.2 mbrf) and recovered 204.28 m (81.65%). Several cores with very low recovery occurred in similar depth intervals as in Hole 976B. Sediment residue was observed inside of the liner. Two low-recovery cores (20X and 25X) had holes through the middle of the material that remained inside the cutting shoe. A possible explanation for this is that the sediment in the core barrel may have been forced out by gas expansion as the cores were being withdrawn from the seafloor. Penetration rates of about 8–12 m/hr were achieved with circulation rates of 30–40 spm, 10,000 lb WOB, and 50–60 rpm. Overall APC/XCB recovery for Hole 976C was 89.58%. Before pulling out the bit, 100 barrels of 10.5 lb/gal heavy-weight mud was displaced into the hole. The bit cleared the seafloor at 1145 hr, 03 June.

Hole 976D

Hole 976D was cored primarily to be able to take high-resolution interstitial water samples in the upper 30 mbsf. The ship was offset 25 m northwest of Hole 976C (we could not move farther to the east because of our distance from the beacon) and we spudded Hole 976D at 1230 hr, 3 June. Core 976D-1H was taken with the bit at 1111.0 mbrf and recovered 1.54 m of sediment. The seafloor, therefore, was defined at 1107.6 mbsl. APC Cores 1H to 4H were taken (Table 1) from 0–30 mbsf (1119 to 1149 mbrf) and recovered 30.76 m (102.5%). After taking Core 4H, the APC/XCB BHA was pulled out of the hole, clearing the seafloor at 1445 hr and the rig floor at 1645 hr, 3 June.

Hole 976E

Hole 976E was drilled and cored so that additional samples could be taken across the sediment-basement contact and so that this same interval could be logged. Therefore, an MBR was added to the RCB BHA. Hole 976E was spudded at 2130 hr, 3 June. We washed and drilled with a center bit to 543.81 mbsf (1662.81 mbrf), where we began RCB coring. RCB Cores 976E-1R to 28R were taken (Table 1) from 543.8 to 736.3 mbsf, coring 192.5 m and recovering 64.85 m (33.69%). To reduce the possibility of core pieces jamming, we advanced only 5.0 or 4.6 m in 16 of these 28 cores, hoping to enhance our chances of good core recovery by taking short cores. The other 12 cores advanced the standard 9.5 m.

Recovery in Hole 976E was better than in Hole 976B across what was initially believed to be the same transition zone of breccia, fault gouge, and metamorphic basement. The basement, however, was encountered approximately 10 m higher than in Hole 976B. A significant portion of the metamorphic basement exhibited a vertical foliation that may have caused less core jamming and enhanced the core recovery.

We used a combination of an 8-finger and a 4-petal core catcher for the first four cores in the hard clay. The core catchers were then

Table 1. Site 976 coring summary.

Core	Date (1995)	Time (UTC)	Depth (mbsf)	Length cored (m)	Length recovered (m)	Recovery (%)
161-976A-						
1H	21 May	0430	0.0–5.9	5.9	5.92	100.0
Coring totals:				5.9	5.92	100.0
161-976B-						
1H	21 May	0820	0.0–3.5	3.5	3.45	98.6
2H	21 May	0845	3.5–13.0	9.5	9.65	101.0
3H	21 May	0940	13.0–22.5	9.5	3.35	35.2
4H	21 May	1030	22.5–32.0	9.5	10.09	106.2
5H	21 May	1110	32.0–41.5	9.5	9.86	104.0
6H	21 May	1205	41.5–51.0	9.5	10.09	106.2
7H	21 May	1240	51.0–60.5	9.5	10.02	105.5
8H	21 May	1320	60.5–70.0	9.5	10.04	105.7
9H	21 May	1400	70.0–79.5	9.5	10.07	106.0
10H	21 May	1430	79.5–89.0	9.5	10.20	107.3
11H	21 May	1510	89.0–98.5	9.5	10.51	110.6
12H	21 May	1555	98.5–108.0	9.5	10.34	108.8
13H	21 May	1655	108.0–117.5	9.5	10.05	105.8
14H	21 May	1745	117.5–127.0	9.5	10.37	109.1
15X	21 May	1840	127.0–136.5	9.5	9.55	100.0
16X	21 May	1920	136.5–146.2	9.7	7.38	76.1
17X	21 May	2010	146.2–155.8	9.6	9.89	103.0
18X	21 May	2100	155.8–165.4	9.6	9.26	96.4
19X	21 May	2310	165.4–175.1	9.7	9.72	100.0
20X	22 May	0000	175.1–184.7	9.6	9.78	102.0
21X	22 May	0200	184.7–194.4	9.7	2.92	30.1
22X	22 May	0230	194.4–203.9	9.5	9.57	101.0
23X	22 May	0305	203.9–213.5	9.6	6.39	66.5
24X	22 May	0350	213.5–223.1	9.6	9.92	104.0
25X	22 May	0445	223.1–232.7	9.6	10.21	106.3
26X	22 May	0550	232.7–242.4	9.7	9.45	97.4
27X	22 May	0820	242.4–252.1	9.7	0.00	0.0
28X	22 May	0930	252.1–261.8	9.7	10.25	105.7
29X	22 May	1110	261.8–271.3	9.5	10.49	110.4
30X	22 May	1240	271.3–280.9	9.6	10.09	105.1
31X	22 May	1400	280.9–290.6	9.7	0.00	0.0
32X	22 May	1545	290.6–300.1	9.5	9.76	103.0
33X	22 May	1715	300.1–309.7	9.6	10.13	105.5
34X	22 May	1825	309.7–319.3	9.6	10.11	105.3
35X	22 May	2000	319.3–328.9	9.6	10.14	105.6
36X	22 May	2135	328.9–338.5	9.6	9.77	102.0
37X	22 May	2320	338.5–348.1	9.6	9.71	101.0
38X	23 May	0025	348.1–357.7	9.6	9.82	102.0
39X	23 May	0145	357.7–367.4	9.7	7.29	75.1
40X	23 May	0215	367.4–377.0	9.6	0.90	9.4
41X	23 May	0245	377.0–386.6	9.6	0.27	2.8
42X	23 May	0335	386.6–396.3	9.7	0.33	3.4
43X	23 May	0445	396.3–405.9	9.6	0.00	0.0
44X	23 May	0600	405.9–415.5	9.6	2.29	23.8
45X	23 May	0635	415.5–425.1	9.6	0.00	0.0
46X	23 May	0730	425.1–434.8	9.7	0.05	0.5
47X	23 May	0835	434.8–444.5	9.7	5.52	56.9
48X	23 May	0915	444.5–454.0	9.5	2.44	25.7
49X	23 May	1030	454.0–463.7	9.7	0.02	0.2
50X	23 May	1150	463.7–473.3	9.6	0.16	1.7
51X	23 May	1250	473.3–482.8	9.5	1.50	15.8
52X	23 May	1400	482.8–492.4	9.6	0.85	8.9
53X	23 May	1500	492.4–502.0	9.6	2.06	21.4
54X	23 May	1630	502.0–511.7	9.7	0.70	7.2
55X	23 May	1745	511.7–518.3	6.6	0.01	0.2
56X	23 May	2000	518.3–525.3	7.0	10.07	143.8
57X	23 May	2215	525.3–534.9	9.6	9.88	103.0
58X	24 May	0015	534.9–544.6	9.7	10.18	104.9
59X	24 May	0210	544.6–554.2	9.6	10.15	105.7
60X	24 May	0350	554.2–563.9	9.7	10.33	106.5
61X	24 May	0535	563.9–573.5	9.6	10.23	106.5
62X	24 May	0705	573.5–583.1	9.6	0.35	3.6
63X	24 May	0840	583.1–592.8	9.7	9.89	102.0
64X	24 May	1100	592.8–602.4	9.6	9.95	103.0
65X	24 May	1300	602.4–612.0	9.6	6.53	68.0
66X	24 May	1520	612.0–621.6	9.6	10.05	104.7
67X	24 May	1830	621.6–631.2	9.6	4.42	46.0
68X	24 May	2100	631.2–633.9	2.7	0.01	0.4
69X	24 May	2300	633.9–640.9	7.0	2.39	34.1
70X	25 May	0130	640.9–650.5	9.6	9.67	101.0
71X	25 May	0315	650.5–660.2	9.7	10.08	103.9
72X	25 May	0450	660.2–669.7	9.5	4.17	43.9
73X	25 May	0645	669.7–674.8	5.1	0.21	4.1
74X	25 May	0915	674.8–677.3	2.5	1.08	43.2
75R	27 May	0910	677.3–680.7	3.4	1.67	49.1
76R	27 May	1205	680.7–684.4	3.7	2.50	67.5
77R	27 May	1505	684.4–688.4	4.0	3.35	83.7
78R	27 May	1830	688.4–698.0	9.6	1.75	18.2
79R	27 May	2020	698.0–702.6	4.6	1.15	25.0
80R	27 May	2220	702.6–707.6	5.0	1.72	34.4
81R	28 May	0100	707.6–717.2	9.6	2.52	26.2
82R	28 May	0330	717.2–726.8	9.6	2.50	26.0
83R	28 May	0530	726.8–736.4	9.6	1.58	16.4
84R	28 May	0745	736.4–746.0	9.6	1.20	12.5
85R	28 May	0845	746.0–750.6	4.6	0.45	9.8
86R	28 May	1110	750.6–755.6	5.0	1.86	37.2
87R	28 May	1550	755.6–760.1	4.5	1.01	22.4
88R	28 May	1740	760.1–765.1	5.0	0.83	16.6
89R	28 May	1930	765.1–769.8	4.7	0.55	11.7
90R	28 May	2100	769.8–774.8	5.0	0.48	9.6
91R	28 May	2300	774.8–784.4	9.6	0.61	6.4
92R	29 May	0030	784.4–794.0	9.6	0.77	8.0
93R	29 May	0230	794.0–803.6	9.6	0.65	6.8
94R	29 May	0430	803.6–813.2	9.6	0.91	9.5
95R	29 May	0700	813.2–822.8	9.6	3.10	32.3
96R	29 May	0900	822.8–832.5	9.7	1.32	13.6
97R	29 May	1225	832.5–842.1	9.6	2.67	27.8
98R	29 May	1545	842.1–851.7	9.6	1.82	18.9
99R	29 May	2200	851.7–861.3	9.6	0.37	3.9
100R	30 May	0045	861.3–871.0	9.7	0.34	3.5
101R	30 May	0340	871.0–880.6	9.6	2.72	28.3
102R	30 May	0640	880.6–890.2	9.6	1.79	18.6
103R	30 May	0910	890.2–899.9	9.7	0.52	5.4
104R	30 May	1150	899.9–909.5	9.6	1.97	20.5
105R	30 May	1430	909.5–919.1	9.6	2.64	27.5
106R	30 May	1800	919.1–928.7	9.6	1.79	18.6
Coring totals:				928.7	535.54	57.7
161-976C-						
1H	1 June	1815	0.0-6.0	6.0	5.98	99.6
2H	1 June	1900	6.0-15.5	9.5	9.91	104.0
3H	1 June	2000	15.5–25.0	9.5	10.02	105.5
4H	1 June	2030	25.0–34.5	9.5	9.97	105.0
5H	1 June	2115	34.5–44.0	9.5	9.95	105.0
6H	1 June	2215	44.0–53.5	9.5	9.98	105.0
7H	1 June	2245	53.5–63.0	9.5	9.91	104.0
8H	1 June	2315	63.0–72.5	9.5	9.88	104.0
9H	2 June	0000	72.5–82.0	9.5	10.09	106.2
10H	2 June	0030	82.0–91.5	9.5	10.02	105.5
11H	2 June	0100	91.5–101.0	9.5	9.79	103.0
12H	2 June	0145	101.0–110.5	9.5	10.39	109.3
13H	2 June	0215	110.5–120.0	9.5	9.87	104.0
14H	2 June	0300	120.0–129.5	9.5	10.12	106.5
15X	2 June	0405	129.5–139.2	9.7	9.52	98.1
16X	2 June	0445	139.2–148.8	9.6	9.46	98.5
17X	2 June	0520	148.8–158.5	9.7	4.02	41.4
18X	2 June	0555	158.5–168.1	9.6	9.40	97.9
19X	2 June	0630	168.1–177.8	9.7	9.37	96.6
20X	2 June	0715	177.8–187.4	9.6	5.10	53.1
21X	2 June	0800	187.4–197.1	9.7	0.00	0.0
22X	2 June	0830	197.1–206.6	9.5	9.66	101.0
23X	2 June	0915	206.6–216.2	9.6	10.19	106.1
24X	2 June	1030	216.2–225.8	9.6	10.15	105.7
25X	2 June	1150	225.8–235.4	9.6	3.07	32.0
26X	2 June	1315	235.4–245.1	9.7	9.82	101.0
27X	2 June	1450	245.1–254.8	9.7	9.84	101.0
28X	2 June	1710	254.8–264.4	9.6	9.49	98.8
29X	2 June	1845	264.4–274.0	9.6	10.09	105.1
30X	2 June	2000	274.0–283.6	9.6	0.01	0.1
31X	2 June	2135	283.6–293.2	9.6	9.91	103.0
32X	2 June	2250	293.2–302.7	9.5	10.09	106.2
33X	3 June	0000	302.7–312.3	9.6	9.84	102.0
34X	3 June	0130	312.3–321.9	9.6	10.02	104.4
35X	3 June	0245	321.9–331.6	9.7	9.66	99.6
36X	3 June	0400	331.6–341.1	9.5	10.14	106.7
37X	3 June	0515	341.1–350.8	9.7	10.41	107.3
38X	3 June	0635	350.8–360.4	9.6	8.83	92.0
39X	3 June	0730	360.4–370.1	9.7	5.54	57.1
40X	3 June	0800	370.1–379.7	9.6	0.65	6.8
Coring totals:				379.7	340.16	89.6
161-976D-						
1H	3 June	1040	0.0–1.5	1.5	1.54	102.0
2H	3 June	1105	1.5–11.0	9.5	9.62	101.0
3H	3 June	1130	11.0–20.5	9.5	9.82	103.0
4H	3 June	1205	20.5–30.0	9.5	9.81	103.0
Coring totals:				30.0	30.79	102.6
161-976E-						
Drilled from 0.0 to 543.8 mbsf						
1R	3 June	0405	543.8–553.4	9.6	7.06	73.5
2R	5 June	0620	553.4–563.1	9.7	0.00	0.0
3R	5 June	0845	563.1–572.7	9.6	0.12	1.3
4R	5 June	1010	572.7–577.3	4.6	0.00	0.0
5R	5 June	1210	577.3–582.3	5.0	0.00	0.0
6R	5 June	1520	582.3–592.0	9.7	7.57	78.0
7R	5 June	1730	592.0–601.7	9.7	2.20	22.7
8R	5 June	2030	601.7–611.3	9.6	0.15	1.6
9R	5 June	2315	611.3–620.9	9.6	0.00	0.0
10R	6 June	0245	620.9–630.6	9.7	6.13	63.2
11R	6 June	0530	630.6–640.2	9.6	5.41	56.3

Table 1 (continued).

Core	Date (1995)	Time (UTC)	Depth (mbsf)	Length cored (m)	Length recovered (m)	Recovery (%)
12R	6 June	0810	640.2–649.8	9.6	9.45	98.4
13R	6 June	1035	649.8–659.4	9.6	3.52	36.6
14R	6 June	1325	659.4–664.0	4.6	2.69	58.5
15R	6 June	1630	664.0–669.0	5.0	2.96	59.2
16R	6 June	1830	669.0–673.7	4.7	1.87	39.8
17R	6 June	2030	673.7–678.7	5.0	1.92	38.4
18R	6 June	2145	678.7–683.3	4.6	0.50	10.8
19R	6 June	2330	683.3–688.3	5.0	1.19	23.8
20R	7 June	0100	688.3–692.9	4.6	1.73	37.6
21R	7 June	0245	692.9–697.9	5.0	3.01	60.2
22R	7 June	0430	697.9–702.5	4.6	2.01	43.7
23R	7 June	0620	702.5–707.5	5.0	1.87	37.4
24R	7 June	0810	707.5–712.1	4.6	0.73	15.8
25R	7 June	1005	712.1–717.1	5.0	1.68	33.6
26R	7 June	1115	717.1–721.7	4.6	0.00	0.0
27R	7 June	1230	721.7–726.7	5.0	0.13	2.6
28R	7 June	1430	726.7–736.3	9.6	0.95	9.9
Coring totals:				192.5	64.85	33.7
Drilled:				543.8		
Total:				736.3		

Note: See also detailed coring summary on the CD-ROM, back pocket, this volume.

switched to a 10-finger placed in front of the 4-petal core catcher for the remainder of the sediment coring. Once basement was reached we switched to two, rotatable 8-finger core catchers.

Drilling parameters while coring with the RCB were: 35–45 spm, 15–25,000 lb WOB, and 50–70 rpm. The annular velocity was kept low to reduce the hole erosion (to enhance chances for good logging conditions), which resulted in slow penetration. The pump strokes were increased slightly to 45 spm on the sixth core which helped the rate of penetration and decreased the pressure, better cleaning the hole of cuttings.

A short wiper trip was made to 570 mbsf (1689 mbrf). When we moved the bit back to the bottom, approximately 20 m of fill were encountered. We reamed the fill out of the hole, released the bit, and shifted the MBR sleeve back into the logging position. The pipe was raised to 570 mbsf (1689 mbrf) and logging began. The standard quad combo log was run first. Some difficulty was encountered getting the tool through the sediment-basement transition. Once logging was started, however, approximately 9000 lb of tension occurred while pulling the tool through the basement section. This tension, combined with the severely washed-out borehole above 631 mbsf, caused us to terminate logging. The quad combo was able to obtain logs from 713 to 570 mbsf.

Erratic signals from the two seafloor dynamic positioning beacons occurred almost daily. Signals from both beacons were temporarily lost around 1500 hr, 7 June. We deployed a backup beacon, but it too failed to respond. After we deployed a second backup, the signals from the first two beacons returned.

The bottom of the drill pipe cleared the seafloor at 0545 hr and the rig floor at 0800 hr, 8 June. Three of the four beacons deployed were recovered at the conclusion of operations at Hole 976E. We began the transit to Site 977 at 0830 hr, 8 June.

LITHOSTRATIGRAPHY

Unit Descriptions

Five holes were drilled at Site 976 (Table 1): Hole 976A was a missed mudline, Hole 976B was cored continuously from the seafloor into the top of metamorphic basement, Hole 976C penetrated the upper part of the sedimentary sequence, Hole 976D was cored to a depth of 20 mbsf, and Hole 976E penetrated the lower part of the sedimentary sequence and the uppermost basement. Comparison of descriptions, ages, and core photographs from Site 976 and DSDP Site 121 (8 km southeast of Site 976) indicates that the same sedimentary sequence was penetrated at both sites. Thus, the three main lithostratigraphic subdivisions established by Site 121 shipboard scientists (Ryan et al., 1973b) can be extrapolated to the sequence recovered at Site 976. More complete core recovery of sediments at Site 976 has allowed us, however, to provide a more detailed description of the sedimentary sequence, and to sample new lithostratigraphic intervals, immediately overlying the metamorphic basement. Sediments at Site 976 are subdivided into four lithostratigraphic units (Table 2), based primarily on downhole changes in grain size. Unit I was recovered from Holes 976A, 976B, 976C, and 976D; Unit II is present in Holes 976B and 976C; Units III and IV are only present in Holes 976B and 976E. Unit boundaries were readily correlated between Holes 976B and 976C, and between Holes 976B and 976E where they overlap. The stratigraphic column for Hole 976B best represents the sequence present at Site 976 (Fig. 8).

Unit I

Hole 976A, 0.0–5.9 mbsf, Section 976A-1H-1, 0 cm, to 1H-CC, 21 cm;

Hole 976B, 0.0–362.1 mbsf, Sections 976B-1H-1, 0 cm, to 39X-3, 144 cm;

Hole 976C, 0.0–362.8 mbsf, Sections 976C-1H-1, 0 cm, to 39X-2, 89 cm;

Hole 976D, 0.0–30.0 mbsf, Sections 976D-1H-1, 0 cm to 4H-CC, 26 cm.

Unit I comprises 362 m of open-marine hemipelagic facies in which the dominant sediment types are nannofossil-rich clay, nannofossil clay, and nannofossil silty clay. It is Pleistocene to late Pliocene in age. Clay content ranges between 50% and 97% (average 81%), with silt and sand composing 3%–45% (average 17%) and 0%–10% (average 2%), respectively (Fig. 8).

The unit is typified by gradational alternations of structureless, mottled (Fig. 9), and burrowed clay, giving an overall uniform appearance to the sediment. Faint color bands are present in a few places. The sediments are mainly dark greenish gray (5GY 4/1) in color, although they vary to olive gray (5Y 4/1) or grayish olive (10Y 4/2) (Fig. 10). In contrast to Sites 974 and 975, at Site 976 there is no relationship between carbonate content and color. Carbonate content of Unit I, as determined by chemical analysis (Fig. 8; see also "Organic Geochemistry" section, this chapter), ranges between 19% and 42% (average 28%). The carbonate fraction is dominated by nannofossils, which range from 7% to 40% (visual estimation from smear slides), but includes foraminifers (0%–5%), bioclasts (0%–5%), micrite (0%–35%), inorganic calcite (0%–2%), and dolomite (0%–2%). The average bulk mineralogical composition of Unit I sediments, as determined by X-ray diffraction (XRD) analysis, is 66% total clay minerals, 18% calcite, 15% quartz, 1% feldspar, and a minor amount of dolomite.

Downhole variation in the detrital siliciclastic component (quartz + feldspar + mica) of the dominant lithologies in Hole 976B (estimated from smear slides; Fig. 8) suggests a periodic waxing and waning of terrigenous input during the deposition of Unit I.

The major lithologies of Unit I are typified by the abundant presence of small (<1–2 mm) silt-rich blebs, which we interpret to be burrow fills. Most are composed of nannofossil silty clay enriched in framboidal pyrite (up to 50%) compared with the adjacent sediment (0%–5%). Pyrite imparts a dark gray color to these patches, many of which are smeared along the core during splitting (Fig. 11). Other, less common, patches are enriched in quartz and feldspar, or in shell fragments (Fig. 12).

Minor lithologies in Unit I include diatom-bearing sediments, organic-rich layers (ORLs), and clayey silt laminae. The first include rare, thin (up to 5 cm) laminated beds of diatomaceous ooze (Figs. 13–16) and diatom clayey silt that are light brownish gray (5YR 6/1) to olive gray (5Y 4/1) in color. These diatom-bearing intervals can be

Table 2. Lithostratigraphic units for Site 976.

Unit	Age	Lithology	Sedimentary structures	Occurrence	Interval (mbsf)
I	Pleistocene to late Pliocene	Major: Nannofossil-rich clay, nannofossil clay, and nannofossil silty clay	Structureless, burrows, rare color banding, mottling; shell fragments and disseminated pyrite framboids throughout	Core 976A-1H, 0 cm, to Core 976A-1H-CC, 21 cm	0.0–5.9
				Core 976B-1H-1, 0 cm, to Core 976B-39X-3, 144 cm	0.0–362.1
		Minor: Opaque-rich nannofossil-rich clay (burrow fill); calcareous clayey sandy silt; silty clay; micrite-rich nannofossil clay; organic matter-enriched layers	Burrows, rare laminations, color banding	Core 976C-1H-1, 0 cm, to Core 976C-40X-CC, 25 cm	0.0–362.8
				Core 976D-1H-1, 0 cm, to Core 976D-4H-CC, 25 cm	0.0–30.0
II	late Pliocene	Major: Sand and nannofossil clay	Poor recovery (12%) and considerable drilling deformation; normal grading, laminations in sand (probable drilling effect)	Core 976B-39X-3, 144 cm, to Core 976B-56X-1, 0 cm	362.1–518.3
		Minor: Clayey micritic silt, silt with micritic cement		Core 976C-39X-2, 86 cm, to Core 976C-40X-CC, 25 cm	362.8–379.7
III	early late Pliocene to middle Miocene	Major: Nannofossil and nannofossil-rich clay and claystone	Horizontal burrows including common *Chondrites* and rare *Zoophycos*; rare laminations	Core 976B-56X-1, 0 cm, to Core 976B-72X-1, 0 cm	518.3–660.2
		Minor: Nannofossil ooze, nannofossil sandy claystone, nannofossil-foraminifer claystone, calcareous claystone, calcareous silty claystone		Core 976E-1H-1, 0 cm, to Core 976E-13R-2, 65 cm	543.8–652.0
IV	middle Miocene	Major: Glauconite, calcitic and zeolitic sand, and pebbly sand	None	Core 976B-72X-1, 0 cm, to 976B-73X-1, 3 cm	660.20–669.73
		Minor: Extraformational gravel		Core 976E-13R-2, 65 cm, to Core 976E-13R-2, 78 cm	651.95–652.08

correlated between Holes 976B and 976C: the interval 976B-15X-3, 0–55 cm (130.0–130.55 mbsf), correlates with the interval 976C-15X-1, 50–70 cm (130.0–130.2 mbsf), and the interval 976B-26X-5, 60 cm, to 26X-6, 24 cm (237.7–238.9 mbsf), correlates with the interval 976C-26X-1, 90 cm to 26X-2, 112 cm (236.3–237.2 mbsf) (Fig. 8). One diatomaceous unit found in Section 976B-30X-5, 38–61 cm (276.7–276.9 mbsf), was not recovered in Hole 976C. In addition, diatoms are present in smear slides from Section 976C-32X-3, 48 cm, to 32X-5, 62 cm. In the former they are mixed with the nannofossil clay and are not discernible as discrete beds; in the latter they are part of a burrow fill. The detailed lithostratigraphy of the diatom-bearing interval from Core 976-26X is shown in Figure 13.

Twenty-eight ORLs are present in Unit I (Table 3) and the majority can be correlated between Holes 976B and 976C (Fig. 17). The lithology of ORLs is mainly nannofossil clay to nannofossil-rich clay. They are characterized by between 0.9% and 1.3% TOC, up to a maximum of 1.85%, compared with a background TOC level of ≤0.5% (Fig. 18; see "Organic Geochemistry" section, this chapter). These layers are most readily identified by their relatively low magnetic susceptibilities compared with nannofossil clay with background TOC values (see "Physical Properties" section, this chapter), but in most cases this low susceptibility is associated with a subtle color change (e.g., from more "grayish" dark greenish gray [5GY 4/1] to a more "greenish" dark greenish gray [5GY 4/1]). ORLs range from less than 20 cm to more than 2 m in thickness. Examination of smear slides from ORLs and from other sediment in Unit I reveals that the organic material includes an amorphous component, as well as terrigenous plant fragments and spores. ORLs occur in five discrete intervals within Unit I. Their distribution is shown in Figure 8.

Very rare, continuous-to-discontinuous clayey silt laminae occur irregularly throughout Unit I. These layers are typified by enrichment in pyrite grains and shell fragments relative to the dominant nannofossil lithologies. Because of the presence of both dark pyrite and pale shell fragments, many of these layers have a speckled appearance.

The base of Unit I is placed at the top of the highest stratigraphic occurrence of sand beds and separates the younger clay-dominated unit from the underlying unit which contains discrete sand layers (Fig. 8). The contact is located across a gradational boundary at a depth of 362.1 mbsf in Hole 976B (Section 976B-39X-3, 144 cm) and 362.8 mbsf in Hole 976C (Section 976C-39X-2, 86 cm; Fig. 19).

Unit II

Hole 976B, 362.1–518.3 mbsf, Section 976B-39X-3, 144 cm to 56X-1, 0 cm;
Hole 976C, 362.8–379.7 mbsf, Section 976C-39X-2, 86 cm to 40X-CC, 25 cm).

Unit II consists of 142 m of late Pliocene sand, silt, calcareous silty clay, and nannofossil clay (Table 2). The unit cannot be described in detail because core recovery was low (17 m from 141.9 m drilled; about 12%) and recovered intervals were intensely disturbed during drilling. The conformable contact between Units I and II has been described above. In Hole 976C, the contact has been deformed by biscuiting during drilling. Recovery rates in Unit II decreased significantly below Core 976B-39X, and the 90 cm of recovered material in Core 976B-40X includes some sandy material, suggesting that the unrecovered interval was, at least in part, composed of poorly consolidated sand. The unit is thought to comprise interstratified graded/laminated sand and silt and nannofossil clay. Based on the ratio of sand + silt to total recovery in core, these two fractions make up about 22% of the recovered sequence, but probably represent a larger proportion of the unrecovered material.

The range of textural components in Unit II is indicated by the estimates of sand, silt, and clay from smear-slide analysis (Fig. 8). Sand proportion ranges from 0% to 70% overall, with an average of 23%. Silt ranges between 5% and 40% (average 24%). Clay is the dominant component ranging from 0%–90% with an average of 53%. Carbonate content ranges between 26% and 45% with an average of 33%

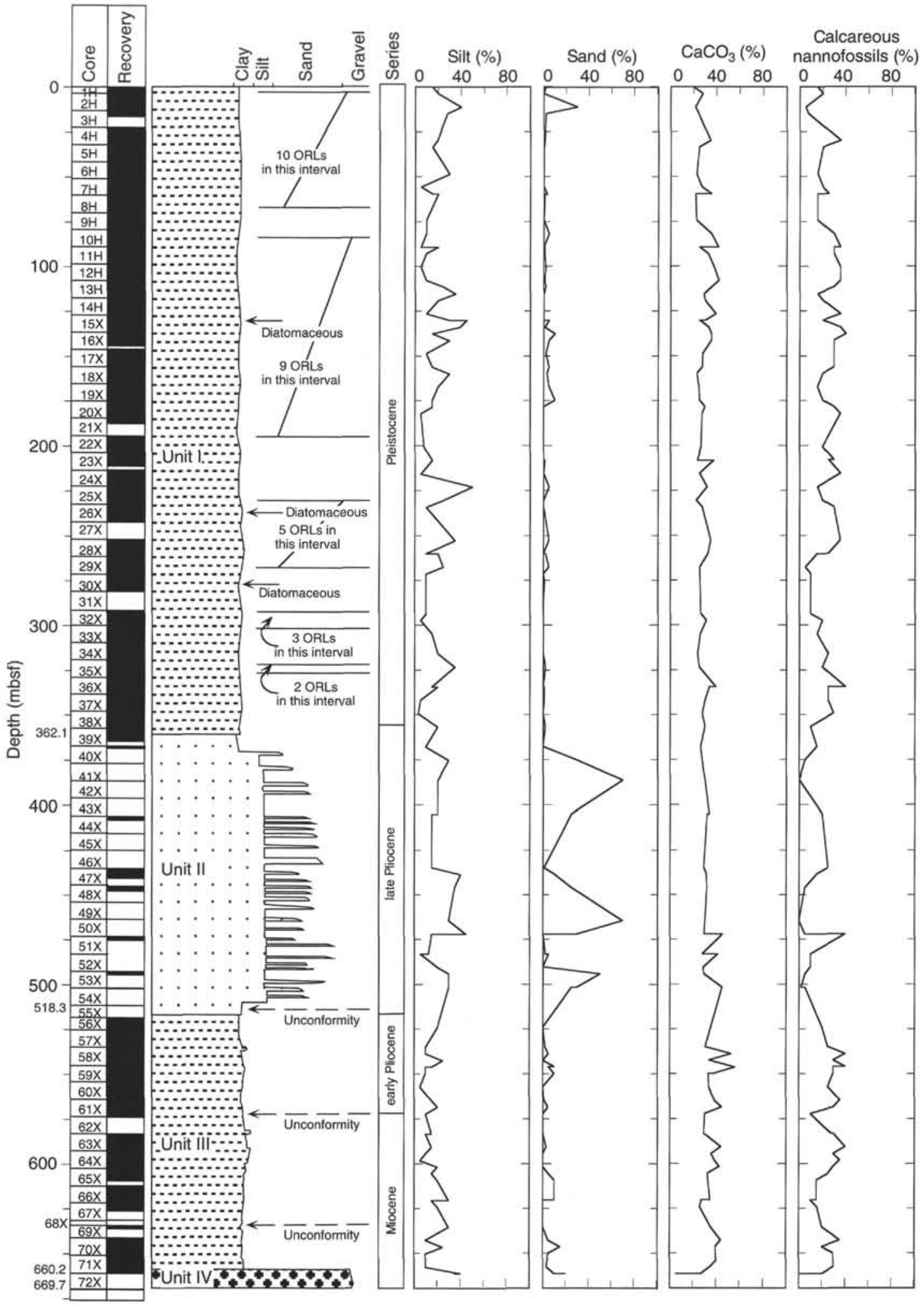

Figure 8. Neogene lithostratigraphy and variation in selected lithologic components for Hole 976B. The stratigraphy shown is representative of all holes drilled at Site 976. Bedding shown in lithostratigraphic Unit II is diagrammatic because of poor recovery across this interval. No trends should be inferred across Unit II. The symbols are explained in Figure 1 of the "Explanatory Notes" chapter, this volume.

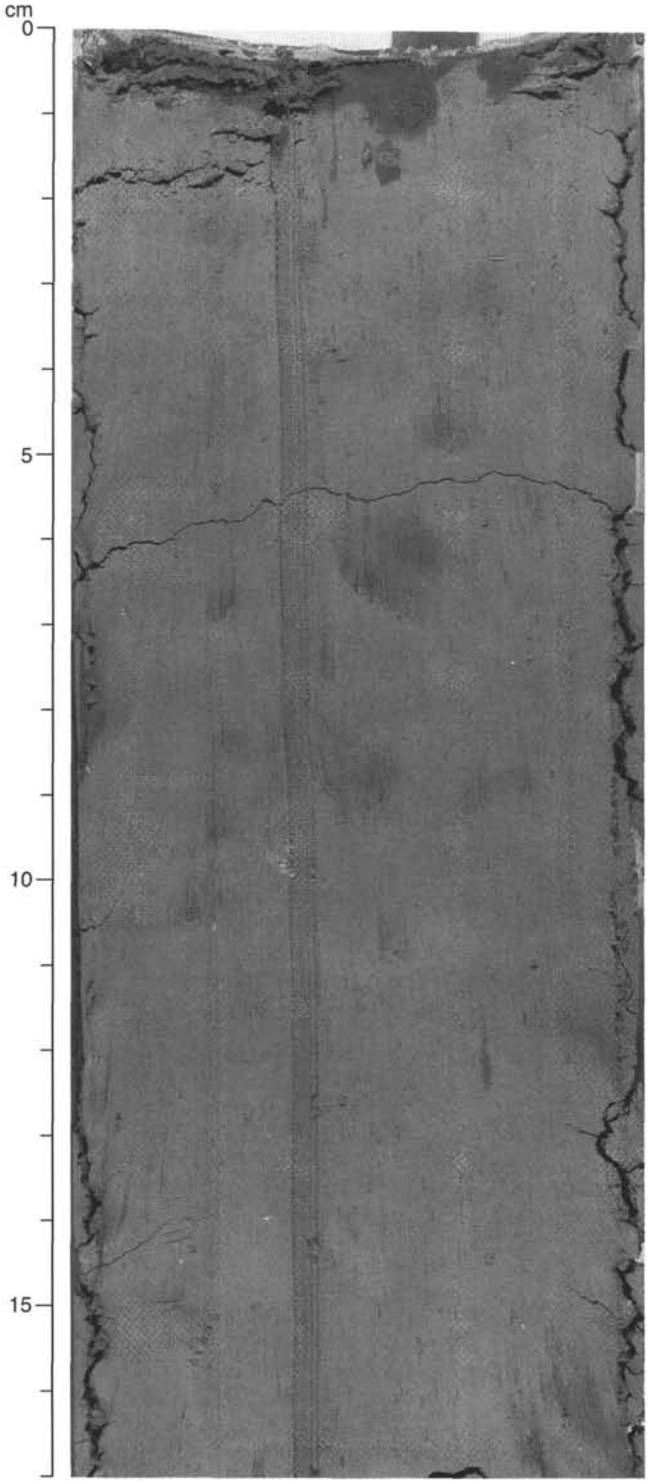

Figure 9. Grayish olive (10Y 4/2) nannofossil-rich clay from Section 976C-13H-2 (112.0 mbsf) showing medium dark gray color mottling, probably a result of burrowing.

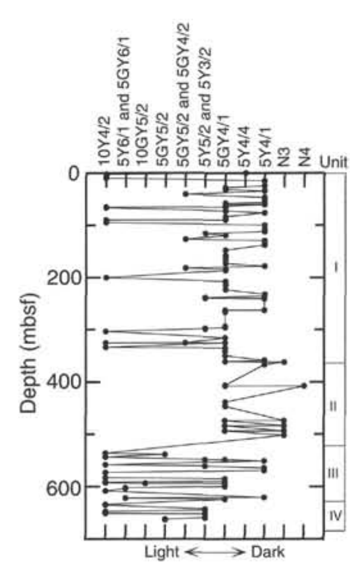

Figure 10. Downhole variation in Munsell color for Hole 976B.

(Fig. 8; see also "Organic Geochemistry" section, this chapter). Bulk mineralogy from XRD analyses of Unit II sediments indicates that they contain an average of 40% total clay minerals (range 21%–75%), 40% quartz (range 15%–59%), 18% calcite (range 5%–26%), 2% feldspar (1%–6%), and minor amounts of dolomite.

Smear slides of unconsolidated sand beds contain up to 20% silt and 15% clay, although this matrix may have been intermixed during drilling. The main components of the coarser-grained fraction are quartz and shell fragments. Subordinate rock fragments (including schist and serpentinite), feldspar, muscovite, chlorite, biotite, garnet, tourmaline, apatite, zircon, epidote, chrome spinel, organic matter (mainly plant fragments), and traces of glauconite make up the remainder of the sand fraction. Thin sections of locally indurated sand (carbonate-cemented sandstone) (976B-47X-4, 52–54 cm, 47X-4, 77–80 cm, 50X-CC, 0–4 cm, 50X-CC, 4–5 cm, 54X-1, 8–10 cm) show that they are lithic arenites. The sediments are moderately well-sorted, matrix-poor sandstones with up to 35% microcrystalline carbonate cement. Grains are well rounded to very angular with point to straight contacts. Their average normalized QFL (quartz-feldspar-noncarbonate lithic fragment) composition is approximately 43:8:49 (ranges: Q [30–54], F [5–14], L [41–65]).

In semi-coherent, intact parts of the cores, where discrete beds are encased in finer grained lithologies (e.g., Cores 976B-39X, 44X, and 47X), sand beds are locally laminated. However, these structures, which are clearly visible on the core photographs, are thought likely to be the product of deformation during drilling. Normal grading seen in short sections (e.g., Section 976B-42X-CC) may also have been artificially produced by settling of sediment suspended in the mostly water-filled core liner. Structures in Unit II cores were also masked by the slurry formed when the locally cemented sand was cut with a saw. Where the fabric has not been destroyed by drilling, coarse-grained layers have sharp lower contacts, gradational upper contacts, and are normally graded. Finer grained, interbedded lithologies are best preserved in longer sections of core (Core 976B-47X) where the sand beds are more widely spaced. Interstratified finer grained material includes nannofossil-rich clay and nannofossil clay, as well as clayey micritic silt and silt with micritic cement.

The base of Unit II is placed at the top of the first consolidated clay bed beneath the sandy, low-recovery zone, at the top of Core 976B-56X. The small amount of recovered material (<1 cm) from Core 976B-55X is sandy and contains a microfaunal assemblage resembling that found in the core catchers from the overlying sandy interval. The faunal assemblage in Core 976B-56X indicates a significant time gap across the Unit II/Unit III boundary (see "Biostratigraphy" section, this chapter).

Unit III

Hole 976B, 518.3–660.2 mbsf, Section 976B-56X-1, 0 cm, to 72X-1, 0 cm;

Hole 976E, 543.8–652.0 mbsf, Section 976E-1R-1, 0 cm, to 13R-2, 65 cm)

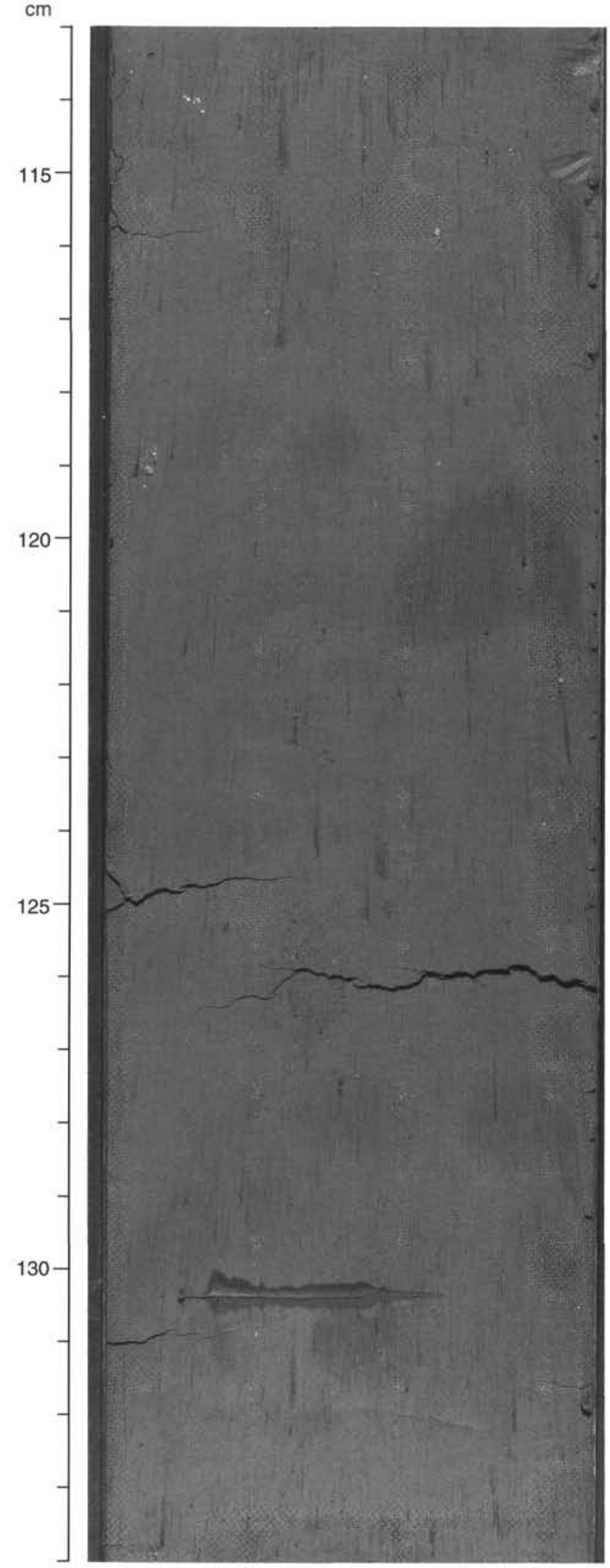

Figure 11. Grayish olive (10Y 4/2) nannofossil clay from Section 976B-11H-3 (91.75 mbsf; lithostratigraphic Unit I) showing disseminated shell fragments (white fragments at 114 cm and 119 cm) and pyrite flecks. The latter have been smeared along the core during splitting. Note also the light diagenetic halo surrounding the pyrite fleck within the darker burrow fill at 120.5 cm.

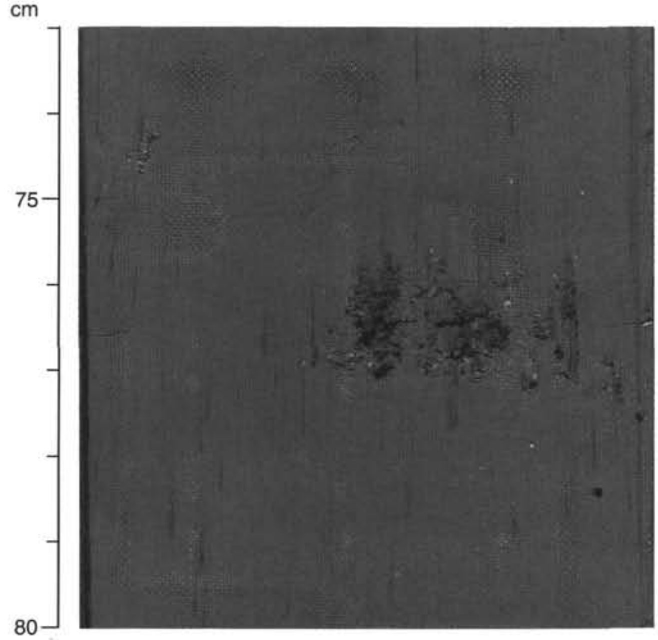

Figure 12. Isolated pyritized shell fragment and sand grain pocket in dark greenish gray (5GY 4/1) nannofossil-rich clay from Section 976C-4H-4 (30.23 mbsf; lithostratigraphic Unit I).

Unit III unconformably underlies Unit II and is about 142 m thick. It is Miocene to early Pliocene in age and contains two depositional hiatuses or unconformities (see "Biostratigraphy" section, this chapter). It is composed mainly of nannofossil and nannofossil-rich clay, silty clay, and claystone. The unit consists mostly of homogeneous clay with traces of dark flecking visible in some biscuits. The main color is grayish olive (10Y 4/2), but there is wide variation (Fig. 10) with no clear relationship between carbonate content and color. Clay is the dominant grain size fraction of the unit ranging from 60% to 95% (smear slide visual estimate) and averages 81%. Silt ranges from 5%–30% (average 15%) and sand makes up 0%–15% (average 3%; Fig. 8). Carbonate content ranges from 26% to 68% with an average of 37% (Fig. 8; see also "Organic Geochemistry" section, this chapter). The main carbonate components are nannofossils, but micrite, bioclasts, foraminifers, intraclasts, and inorganic carbonate are also present. Shell fragments are rare, but foraminifers become increasingly common below 563.9 mbsf (Core 976B-60X). Unit III is compositionally similar to Unit I; bulk mineralogy from XRD analysis comprises 64% total clay minerals (range 47%–74%), 21% calcite (12%–42%), 14% quartz (9%–19%), and 1% feldspar. Minor amounts of ankerite are present in all Unit III samples analyzed. Unit III is more compacted, especially below the intra-Tortonian unconformity, which is located between 631.2 and 635.4 mbsf (interval 976B-67X-CC, 42 cm to 69X-1, 147 cm). In Cores 976B-67X and 976B-68X, biscuits are irregularly fractured, and slickensides are visible at the biscuit/drilling slurry interface.

Minor lithologies include nannofossil ooze, nannofossil sandy claystone, nannofossil-foraminifer claystone, calcareous claystone, and calcareous silty claystone. In addition, there are rare beds and laminae of very fine-grained sand to sandy foraminifer-rich silt that are more common below Core 976B-60X. Sand and sandy silt layers are structureless, laminated, or variably homogenized by burrowing, although laminations may be an artifact of drilling disturbance.

Several types of identifiable burrows are present. The most common can be assigned to the ichnogenus *Chondrites* (Fig. 20), but representatives of *Zoophycos,* rind and halo burrows, and *Planolites. Cylindrichnus*? are also present. Rare cylindrical burrows filled with pyrite-cemented silty clay are present throughout. Intervals with intense horizontal bioturbation have a laminated appearance (Fig. 21). Elsewhere (e.g., Sections 976B-58X-1 and 58X-2; Section 976B-

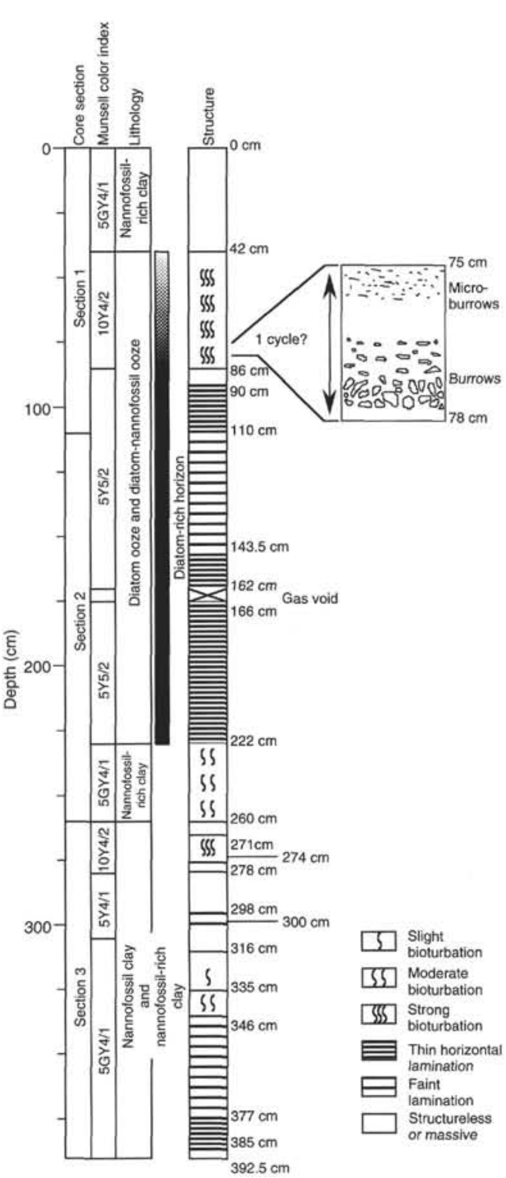

Figure 13. Detailed lithology and stratigraphic relationships of the diatomaceous interval in Sections 976C-26X-1, 2, and 3. The lowermost diatom-rich layers are laminated, whereas the upper part of the sequence is burrowed.

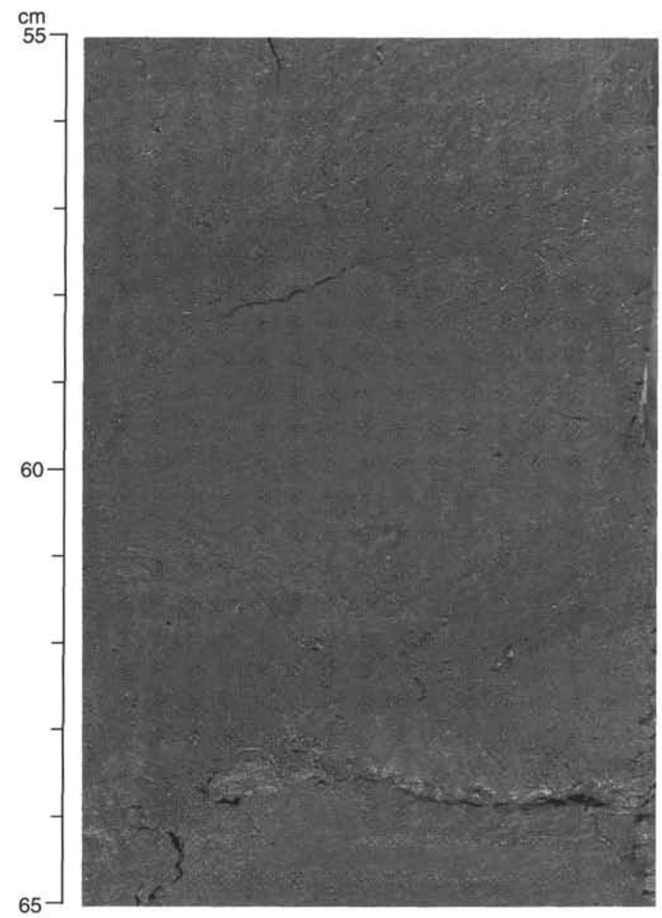

Figure 14. Bioturbated interval in diatomaceous ooze from Section 976C-26X-1 (235.98 mbsf), exhibiting cycles similar to that shown at 75–78 cm in Figure 13.

63X-6), it was not possible to determine if thin laminations were of biological or depositional origin (Fig. 22). Depositional laminations are present in a few places, particularly where silt or sand content is higher: for instance, in Section 976B-60X-6, 48–83 cm. In places laminations are well formed, planar, and horizontal to inclined. Elsewhere, they are faint, wispy, and discontinuous (e.g., Section 976B-61X-8). Some laminations are delineated by aligned organic matter (e.g., interval 976B-64X-1, 115–120 cm).

The base of Unit III is located at the top of the first medium-grained sand beneath the nannofossil clay-dominated section. In Hole 976B, the boundary is located between Cores 976B-71X and 72X; the nature of this contact is indeterminate because of drilling disturbance in Core 976B-72X. In Hole 976E the contact is gradational from poorly sorted clayey sand into overlying nannofossil silty clay.

Unit IV

Hole 976B, 660.20–669.73 mbsf, Sections 976B-72X-1, 0 cm to 73X-1, 3 cm;

Hole 976E, 651.95–652.08 mbsf, Sections 976E-13R-2, 65 cm, to 13R-2, 78 cm)

Unit IV immediately overlies basement and is a thin, coarse-grained unit dominated by biotite- and glauconite-bearing, calcitic and zeolitic silty sand, and pebbly sand (Fig. 23). Subordinate extraformational gravel and calcareous sandstone are also present. Clasts are up to 2 cm in diameter and consist of biotite gneiss and schist, quartzite and marble. An equivalent lithostratigraphic unit was not recognized at Site 121.

The bulk mineralogy of Unit IV sediments at Hole 976B changes gradually downsection, from a composition similar to overlying Unit III sediments to one that reflects a major contribution of components from the underlying metamorphic basement. The mineralogy of Sample 976B-72X-1, 42–43 cm (660.62 mbsf) is dominated by clay minerals (45%), calcite (35%), quartz (19%), and dolomite (not quantified, but present). Trace amounts of feldspar and annite are also present. Dolomite is the primary constituent of Sample 976B-72X-2, 62–64 cm (662.32 mbsf). Minor components include quartz, feldspar, calcite, siderite, and annite. In Section 976B-72X-3, the three samples analyzed are dominated by quartz, phillipsite, and annite, with relative proportions of phillipsite and annite increasing downsection. Variable amounts of clay minerals (kaolinite and smectite?) and minor dolomite are also present. One sample was analyzed from Unit IV at Hole 976E (Section 976E-13R-2, 70–71 cm; 652.00 mbsf). Its bulk mineralogy is similar to that of overlying Unit III sediments (63% total clay minerals, 18% quartz, 18% calcite, 1% feldspar, and a trace amount of ankerite), but it also contains siderite. The metamorphic constituents characteristic of Unit IV sediments at Hole

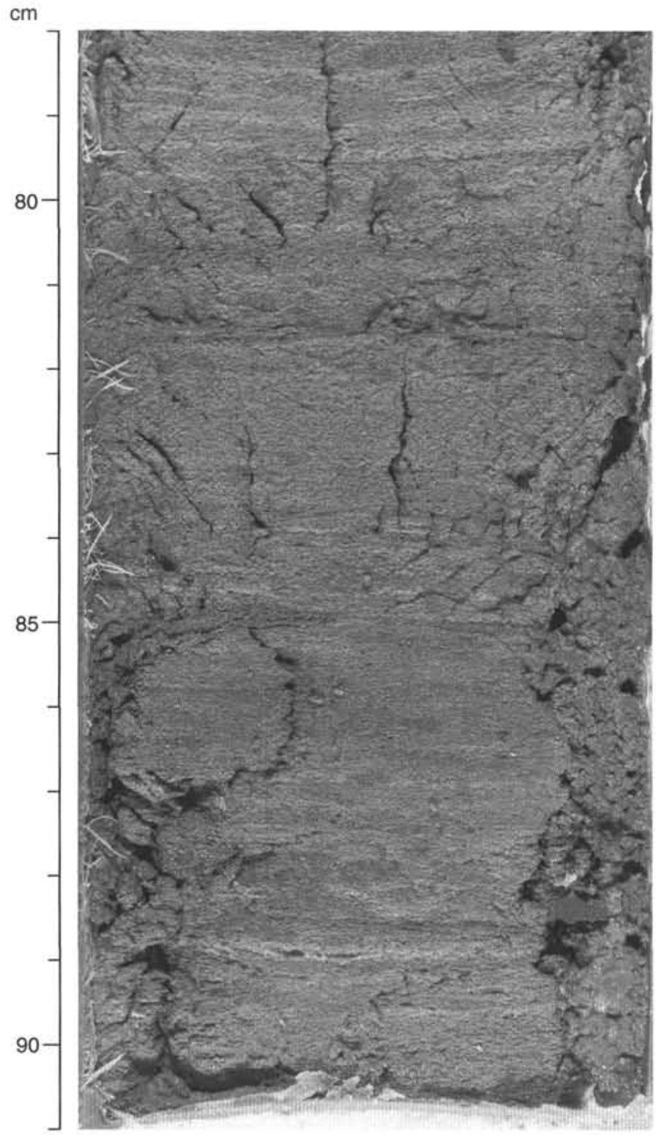

Figure 15. Laminated interval in diatomaceous ooze from Section 976B-26X-5 (238.51 mbsf), similar to lithology at 200 cm in Figure 13.

Figure 16. Photomicrograph of diatomaceous ooze from Section 976B-26X-5, 89 cm (238.63 mbsf).

976B (annite and abundant feldspar) are not present in Unit IV at Hole 976E.

In Hole 976B, Unit IV is 4.2 m thick and consists of poorly-sorted sand and pebbly sand. The framework contains quartz, biotite, feldspar, and rock and shell fragments in subequal proportions. Most of the grains are medium to coarse in size, with only few very coarse-sized grains, and a significant fine-grained sand and silt fraction (Fig. 24). The finer grained matrix material is mainly calcareous silty clay containing nannofossils, inorganic calcite, mica, quartz, and feldspar as accessory components. Unit IV is mostly dusky yellow green (5GY 5/2) in color, but the presence of biotite gives it a black-flecked appearance in places. In Hole 976E, Unit IV is 13 cm thick and consists of poorly-sorted clayey silty sand containing abundant foraminifers and a dark phyllosilicate mineral (10Å type). In Hole 976B, the lowermost 5 mm comprises a very coarse sand with angular fragments of calc-silicate hornfels cemented by micrite.

There are no sedimentary structures visible within Unit IV, apart from poorly defined layering in a gravel bed (interval 976B-72X-2, 87–95 cm). The overall poor sorting and mixing of sediment may be attributed to drilling disturbance, as most of the sandy material is not consolidated and contains free water in the pore spaces.

Unit IV contains a mixed shallow- and deep-water benthic-pelagic foraminifer assemblage, which is dominated by bathyal forms suggesting deposition in a deep marine environment (see "Biostratigraphy" section, this chapter) with periodic sediment input from proximal shallow environments.

The top of the metamorphic basement is placed at a depth of 669.73 mbsf in Hole 976B and 652.08 mbsf in Hole 976E; however, the exact location of the contact remains equivocal. In Hole 976B, the boundary is placed between two cores and has not been recovered. Immediately below the specified contact in Hole 976E there are four rounded metamorphic clasts of uncertain origin. The lower three are of similar diameter to the core barrel (Fig. 24) and are lithologically similar to the immediately underlying basement (see "Basement Structural Geology and Petrology" section, this chapter). These may be "rollers" of basement produced by drilling. However, the uppermost clast has indentations containing foraminifer-bearing calcite cement, indicating that at least this clast was part of a sedimentary conglomerate.

Discussion

Site 976 is located on the Iberian slope some 60 km south of the coast of Spain. In this area the continental shelf is relatively narrow, and the adjacent hinterland (Betic Chain) is elevated up to 3000 m, and may have undergone as much as 1500 m of uplift in the last 10 Ma (J. Platt, pers. comm., 1995). Site 976 was drilled on a long, nar-

Table 3. Location of organic-rich layers (ORLs) in Hole 976B.

Type	Key bed number	Core, section, interval (cm)	Top	Bottom	TOC (%)	Lithological description	Magnetic susceptibility
		161-976B-					
II	A1	1H-3, 16, to 2H-1, 97	3.160	4.470	1.13		*
II	A2	3H-2, 28–29	14.350	14.360	1.09		
II	A3	No recovery					
II	A4	4H-3, 40 or 121, to 4H-4, 124	25.900 or 28.210	28.240	0.82	*	*
II	A5	4H-CC, 27.5–31	32.425	32.460	1.19	*	*
II	A6	5H-6, 89, to 5H-7, 25	40.390	41.250	1.42	*	*
II	A6	5H-7, 30–45	41.300	41.450	1.16	*	*
II	A7	6H-6, 136, to 6H-7, 40	50.360	50.900	1.18		*
II	A8	7H-4, 65–90	56.150	56.400	1.04	*	*
III	A9	7H-CC, 0–43	60.590	61.020	0.95	*	(*)
II	A10	8H-4, 45–110 or 8H-4, 45, to 8H-5, 7	65.450	66.100 or 66.570	0.89, 1.28	*	*
II	A11	10H-6, 13, to 11H-2, 94	87.180	90.060	1.01, 1.18		*
II	A12	13H-1, 118, to 13H-4, 7	109.180	112.570	1.16		*
II	A12	13H-4, 76, to 13H-5, 13	113.260	114.130			*
II	A13	15X-3, 91, to 15X-4, 40	130.910	131.900	1.61		*
III	A14	16X-2, 82, to 16X-3, 136	138.820	140.860			*
II	A15	18X-3, 0–150	158.800	160.300	1.11, 1.25	*	*
V	A16	20X-2, 84–100	177.440	177.600		*	*
III	A17	20X-4, 0, to 20X-5, 15	179.600	181.250		*	*
III	A18	20X-7, 0, 21X-1, 40	184.100	185.100	0.75, 0.85	*	*
III	A19	21X-2, 85, to 21X-CC, 32	187.050	187.620	0.95 above	No recovery at base	*
II	?	24X-3, 41–42	216.910	216.920	1.58		*
II	A20	26X-6, 55–60	239.200	239.250	0.89	*	*
III	A21	26X-6, 112, to 26X-7, 55	239.770	240.600	0.79, 0.85		*
II	A23	29X-2, 7.5–11	262.175	262.210	1.34	*	*
III	A24	?29X-5, 55–56	267.020	267.030	0.97		
II	A25	32X-5, 126.5, to 32X-6, 80	296.755	297.640	1.37	*	*
II	A26	32X-6, 134, to 32X-7, 56	298.100	298.900	1.07, 0.90	*	*
III	A28	35X-5, 2–44	324.890	325.310	0.77, 0.74	*	*
		161-976C-					
II	A1	1H-3, 64, to 1H-4, 45	3.640	4.950	0.80, 0.95	*	*
II	A2	2H-6, 29–75 or 110	13.790	14.250 or 14.600	1.10	*	*
II	A3	3H-2, 143, to 3H-4, 132	18.430	21.320		*	*
II	A3	3H-5, 19–36	21.690	21.860		*	*
II	A3	3H-5, 57–137	22.070	22.870		*	*
II	A4	4H-1, 97, to 4H-3, 60 or 80	25.970	28.600 or 28.800	1.10, 0.76	*	*
II	A5	4H-6, 1–15	32.510	32.650		*?	*
II	A6	5H-5, 0–120	40.500	41.700	1.85	*	*
II	A7	6H-4, 80–130	49.300	49.800	0.58?	*	*
II	A8	7H-2, 123, to 7H-2, 132 or 140	56.230	56.320 or 56.400	0.94	*	*
III	A9	7H-5, 80–110	60.300	60.600	0.68	*	*
III	A9	7H-5, 125–150	60.750	61.000		*	*
II	A10	8H-2, 87, to 8H-3, 55	65.370	66.550	1.10, 0.97	*	*
II	A11	10H-5, 142, to 10H-6, 56	89.420	90.060	0.75	*	*
II	A11	10H-6, 84, to 11H-1, 58	90.340	92.080	0.94, 0.71	*	*
II	A12	12H-7, 10 or 38, to 13H-2, 94	110.100 or 110.380	112.940	0.72, 0.67, 0.75	*	*
II	A12	13H-2, 111, to 13H-3, 49	113.110	113.990	0.73	*	*
II	A13	15X-1, 48–100	129.800	130.500	0.98, 0.93	*	*
III	A14	16X-1, 0, to 16X-2, 50	139.200	141.200	0.78, 0.96	*	*
II	A15	18X-1, 0, to 18X-2, 18	158.500	160.180	0.83, 1.25	No recovery above *	*
V	A16	No recovery					
III	A17	20X-1, 131, to 20X-3, 55	179.110	181.350	0.67, 0.84	*	*
III	A18	No recovery					
III	A19	No recovery					
II	A20	26X-2, 149, to 26X-3, 15.5	237.990	238.155	1.07, 1.02	*	*
III	A21	26X-3, 58.5, to 26X-4, 13	238.585	239.440	0.87	*	*
III	A22	27X-7, 10, to 27X-CC, 47	254.100	254.94*	0.91	*	*
III	A24	28X-7, 104, to 28X-CC, 56.5	263.420	264.290	0.88	*	*
II	A25	31X-7, 19, to 31X-7, 41, or 31X-8, 36	291.890	292.110 or 293.010	0.91	*	*
II	A26	32X-1, 0, to 32X-2,49, or 32X-2, 50	293.200	294.170 or 295.680	0.54, 0.48, ?	*	*
III	A27	32X-6, 88–108	300.520	300.720	0.71	*	*
III	A28	35X-1, 112.5, to 35X-2, 15	323.025	323.550	0.73	*	*
		161-976D-					
II	A1	2H-2, 60, to 2H-3, 50	3.600	5.000	0.93	*	*
II	A2	3H-2, 36–75	12.860	13.250		*	*
II	A2	3H-2, 131, to 3H-3, 47 or 80	13.810	14.470 or 14.800	0.97		*
II	A3	3H-6, 51, to 4H-3, 10	19.010	23.600	1.08, 0.75, 0.56	*	*
II	A4	4H-4, 101, to 4H-6, 51 or 69	26.010	28.510 or 28.690	0.92, 1.01		*
		161-976A-					
II	A1	1H-3, 58, to 1H-4, 49	3.580	4.990			*

Notes: Asterisks in columns headed "lithological description" and "magnetic susceptibility" indicate whether these properties were used for original identification of the ORL. Type: I: >2% TOC, II: 2%–1% TOC, III: 1%–0.8% TOC, V: TOC unknown. Note that classification scheme of ORL types varies among sites, and that ORLs with same key bed number at different holes are correlative. This table is also on the CD-ROM, back pocket, this volume.

row basement horst that is draped by post-Miocene sediments and no longer has bathymetric expression (see Fig. 140).

Sedimentation at Site 976 (Western Alboran Basin) began with the deposition of structureless coarse-grained sand and gravel (Unit IV) on top of metamorphic basement. Clast lithologies are similar to the rocks found in the underlying metamorphic basement sequence. This, along with the coarse grain size, suggests a local derivation and accumulation as an unconformity-related conglomerate with minimal lateral transport. However, the local provenance of constituent rock fragments does not preclude long-distance transport, because similar metamorphic rocks are also present in surrounding uplifted highlands to the north and south of the site. The presence of a mixed deep- and shallow-water fauna in Unit IV may represent a shallow- to deep-water transgressive sequence associated with basement subsidence, or, alternatively, the fauna may indicate downslope redeposition of sediment initially deposited in a shallow marine environment.

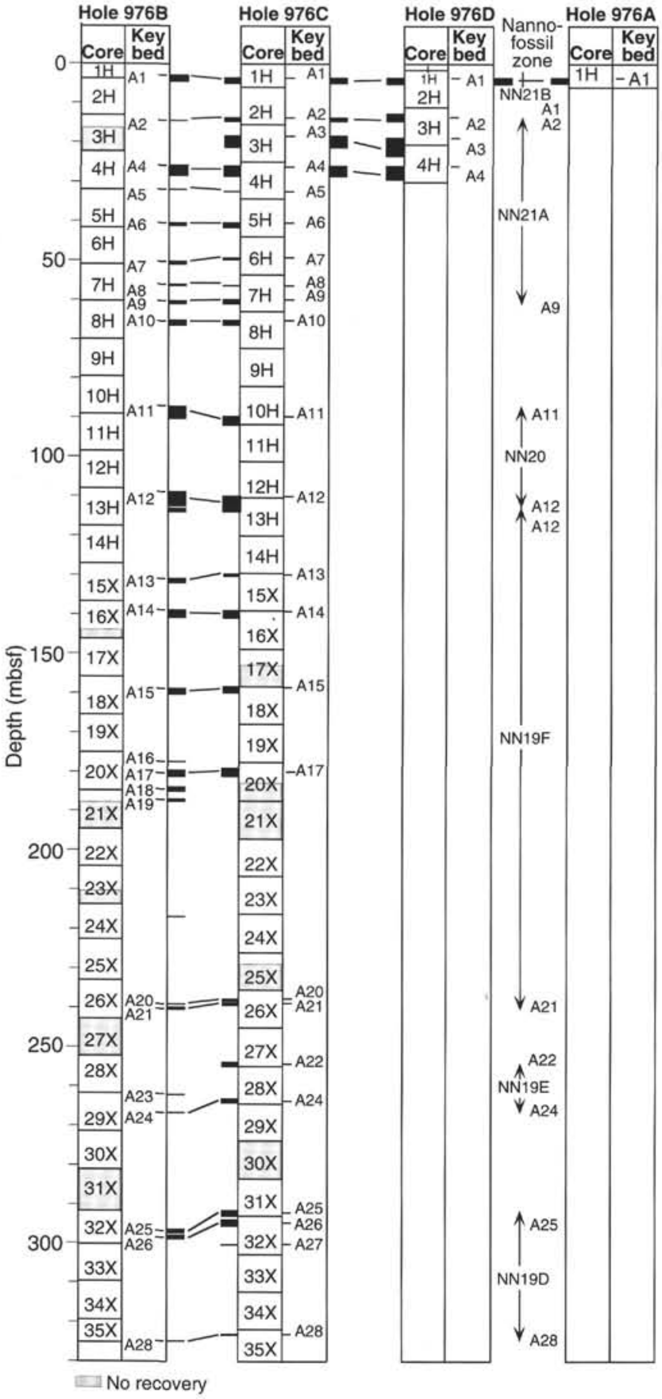

Figure 17. Correlation of organic-rich layers at Site 976.

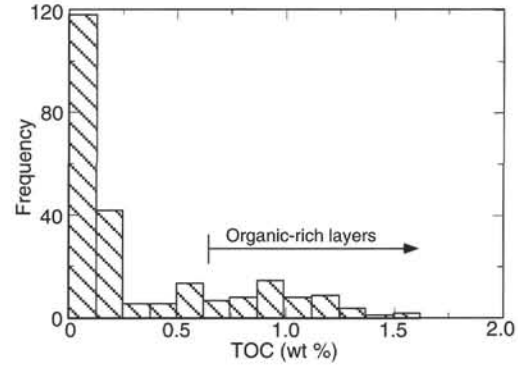

Figure 18. Frequency distribution of total organic carbon (TOC) in lithostratigraphic Unit I from Hole 976B. Sediment with ≥0.8% TOC are ORLs, whereas those with <0.8% TOC are considered "backgound."

The sediments of Units III and I are lithologically similar, and the dominantly nannofossil and nannofossil-rich clays present in both fall between Facies Class E ("silty clays and clays") and Group G2 ("biogenic muds") of Pickering et al. (1989, p. 66), indicating continental margin deep marine hemipelagic sedimentation. A deep-water hemipelagic interpretation is further supported by the trace fossil assemblage present in Units I and III. Where classifiable burrows are present, they indicate a bathyal (slope) to abyssal (basin plain) environment (Chamberlain, 1978).

The nannofossil and pelagic foraminifer components of Units I and III were derived by settling from the overlying water column. Determination of a transport and depositional mechanism for the subordinate siliciclastic silt- and sand-sized fraction within the hemipelagic facies is problematic, mainly because of the virtual absence of depositional sedimentary structures and because of the poor sediment sorting. Two explanations are possible to explain the current sediment composition and distribution: (1) unsorted sediment was delivered to the basin by debris flow that mixed all muddy and sandy lithologies together, or (2) the sand and silt fraction was transported via seafloor gravity flows and interstratified with the autochthonous hemipelagic facies. Intermixing of the two sediment fractions took place after deposition by the action of burrowing organisms. There is evidence to suggest that sand and silt were delivered to the basin by bottom-flowing currents, independently of the clay and biogenic fraction. Rare, thin, graded, sharp-based foraminifer-, quartz-, and feldspar-bearing sands suggest that transport and deposition of this material took place by laterally flowing bottom currents. Site 121 shipboard scientists also speculated that these units, together with thin layers of organic-rich material, displaced shallow-water faunas, and the occurrence of older reworked nannoplankton were all evidence for in situ sediment reworking and size sorting by bottom currents (Ryan et al., 1973b), but they did not attempt to identify the mechanism of original emplacement of sediment.

Four cycles of upward-increasing terrigenous sedimentation, each between 100 m and 150 m thick, have been identified in Units I and II (Fig. 25). These cycles correlate, with variable degrees of certainty, with (1) the location of diatomaceous intervals, which occur just below the termination of the lower two cycles in Unit I, (2) the distribution of ORLs, which are found across the middle and lower part of the three Unit I cycles, during the phase of upward-increasing terrigenous input, and (3) cycles of upward-increasing rates of sedimentation, except for the middle cycle of Unit I.

The almost ubiquitous presence of burrows or bioturbation, the strong association between silt and sand pockets and burrows, the presence of discontinuous foraminifer and other thin, coarse-grained layers, the presence of disseminated sand and silt throughout the mainly clayey sequence, and the recognition of possible cyclic distribution of terrigenous components (Fig. 25) all support a model of periodic input of coarse-grained terrigenous clastic and organic material.

The conceptual model we envision involves erosion of material from the Betic Cordillera and stream transport to the Alboran Sea. The sediment comprising Unit I was probably delivered to the basin by turbidity, or other sediment gravity flow, and deposited as discrete silt or sand layers amongst a continuous settling of hemipelagic components. Sedimentation rate appears to have been a critical parameter in the final form of the sediment. If the average rate was less than 250–300 m/m.y. (see "Biostratigraphy" section, this chapter), these layers were likely reworked almost entirely by the benthic fauna. Unit II is interpreted as a turbiditic sequence, during which the sedimentation rate was too high to allow destructive reworking by the fauna. Unit III probably accumulated under similar conditions, but

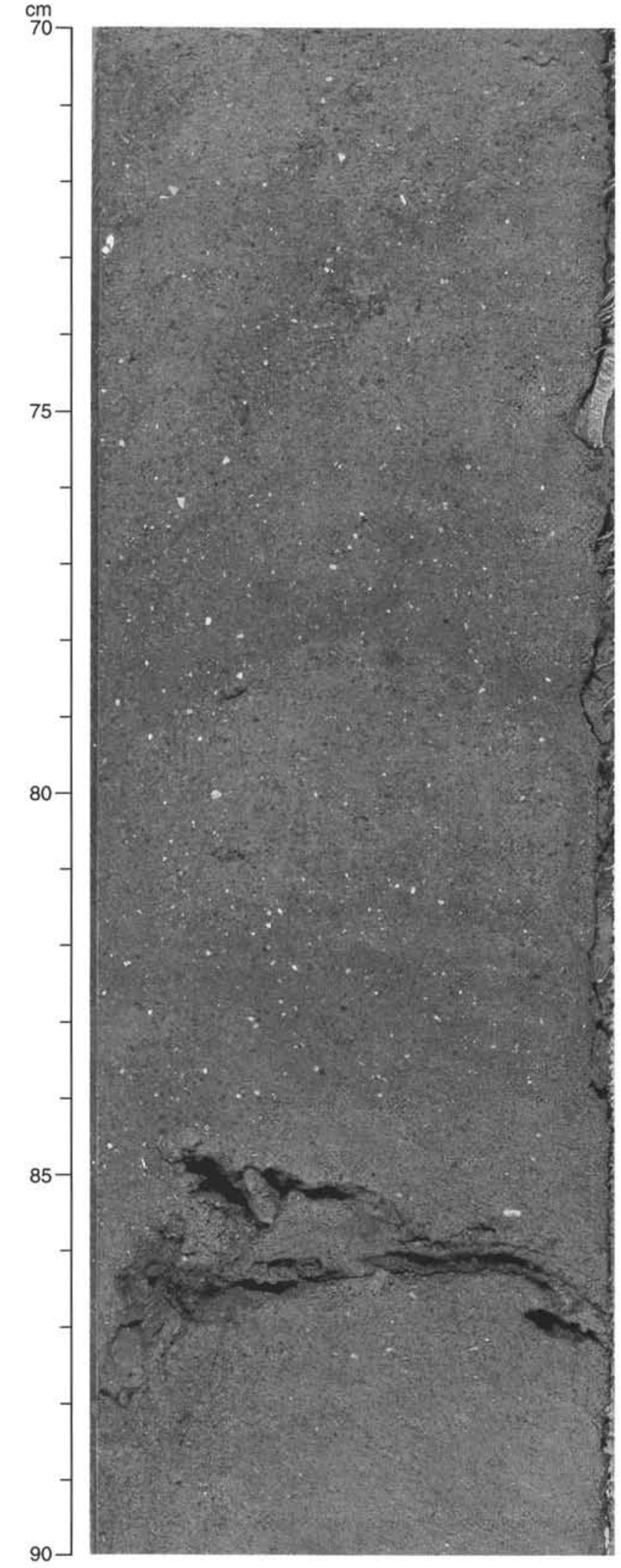

Figure 19. Sand at the top of lithostratigraphic Unit II in Hole 976C, Section 976C-39X-3 (364.26 mbsf). The boundary between lithostratigraphic Units I/II is at 86 cm. Sand between 70 and 85 cm is a veneer produced during splitting and washing of the core.

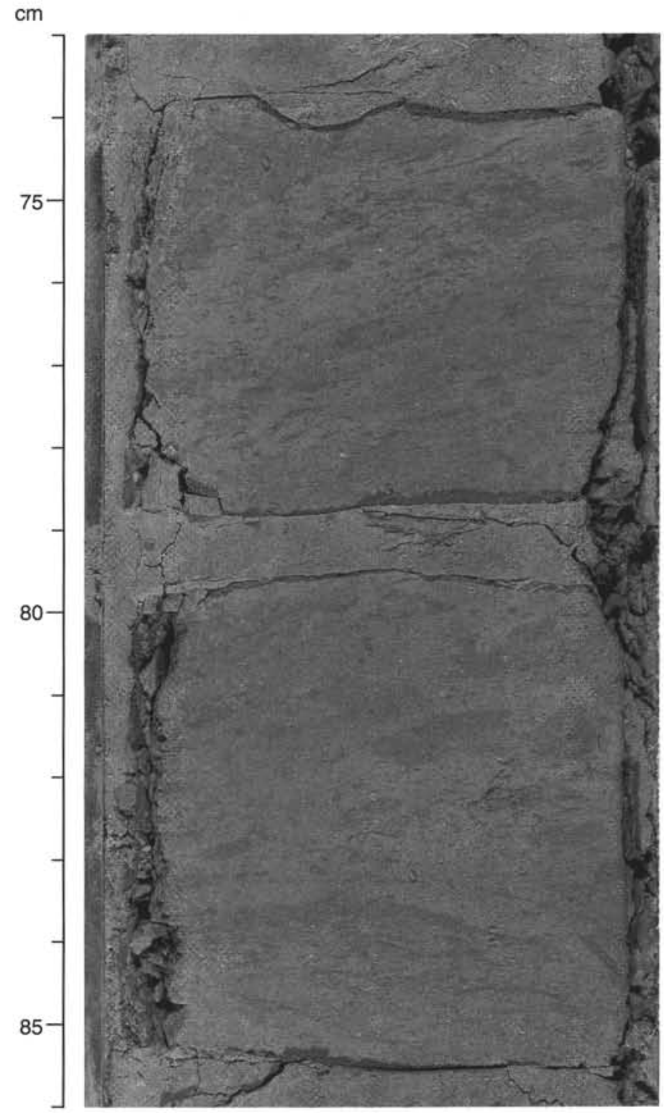

Figure 20. Pervasive small-scale *Chondrites* burrows in nannofossil-rich claystone, mainly around 75–77 cm, from lithostratigraphic Unit III (Section 976B-63X-2, 585.35 mbsf). Subordinate trace fossils include *Planolites*? (horizontal trace at 83.5 cm). Note drilling slurry surrounding "biscuits" of undeformed core.

the presence of at least two lacunae makes this unit more difficult to interpret. Discontinuous silt or sand pockets and foraminifer laminae may be the depositional remnants of these original turbidite deposits.

The relative importance of tectonic uplift vs. eustatic sea-level changes in controlling clastic input is not clear. Third-order global sea-level low stands (Haq et al., 1987) may coincide in time with maxima in clastic input (Fig. 25). The 100–150-m thickness of the cycles identified at Site 976 are of an appropriate magnitude for eustatic-driven control. However, the subsidence history of this tectonically active setting will need to be fully established before any sea-level control can be identified.

BIOSTRATIGRAPHY

Calcareous Nannofossils: Abundance and Preservation

Cores recovered at Site 976 contain common to abundant nannofossils except for intervals from 976B-39X-CC to 42X-CC and

Figure 21. Apparent layering in nannofossil-rich silty clay produced by horizontal to inclined, structureless burrows (interval 976B-35X-5, 12–37 cm, 324.87 mbsf).

976B-47X-CC to 48X-CC, and Samples 976B-72X-CC, 73X-CC, 75R-CC in Hole 976B, and 976C-40X-CC in Hole 976C. Nannofossils are rare to few in these intervals, and one sample (976B-42X-CC) is barren. Preservation is good or moderate to good except in samples taken from Cores 976B-72X, 73X, 74X, and 75R, and in 976C-40X, in which preservation is poor or poor to moderate.

Biostratigraphy

Hole 976A

Only one core was recovered from Hole 976A. Sample 976A-1H-CC (5.71 mbsf) contains common to abundant *Emiliania huxleyi* and is assigned to Subzone NN21B.

Hole 976B (Fig. 26)

The stratigraphic interval in this hole ranges from uppermost middle Miocene (Zone NN7) to uppermost Pleistocene–Holocene (Subzone NN21B). All zones and subzones from NN18 to NN21B are present. The Pliocene/Pleistocene boundary is between Samples 976B-38X-CC and 39X-3, 31–33 cm (357.92–361.01 mbsf).

Sample 976B-55X-CC (511.71 mbsf) is assigned to Zone NN18, whereas Sample 976B-56X-1, 18–19 cm (518.48 mbsf) is in Zone NN12, indicating the presence of a hiatus. The lower/upper Pliocene boundary could not be determined because it lies within the missing interval.

Sample 976B-61X-7, 71–73 cm (572.35 mbsf) is in Zone NN12 and 976B-61X-CC (574.08 mbsf) is in Zone NN11. Although Zones NN11 and NN12 are contiguous, a hiatus probably exists between these two samples, based on the occurrence of *Reticulofenestra rotaria* in Sample 976B-61X-CC. This species normally becomes extinct below the top of Zone NN11, but is found in Sample 976B-61X-CC (574.08 mbsf) immediately below Sample 976B-61X-7, 71–73 cm, (572.35 mbsf) assigned to Zone NN12. The Miocene/Pliocene

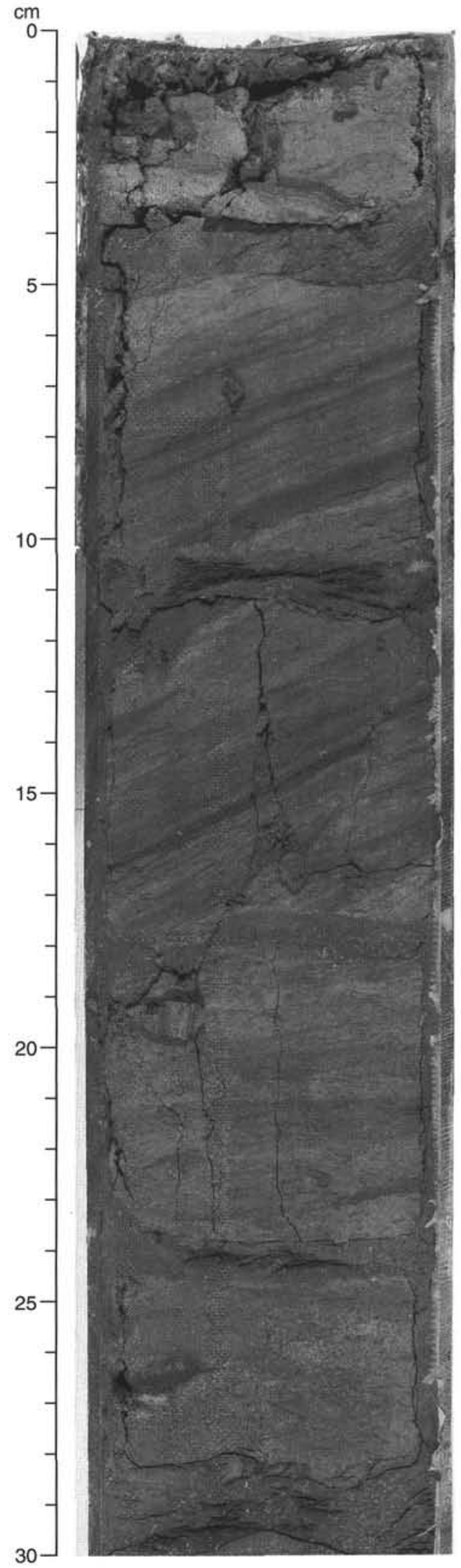

Figure 22. Inclined laminations of indeterminate, but probable biological, origin from lithostratigraphic Unit III (between 5–17 cm) in interval 976B-63X-6, 0–30 cm (590.60 mbsf). The presence of discontinuous layers, both within and below this level, suggest that the structures may have been produced by burrowing.

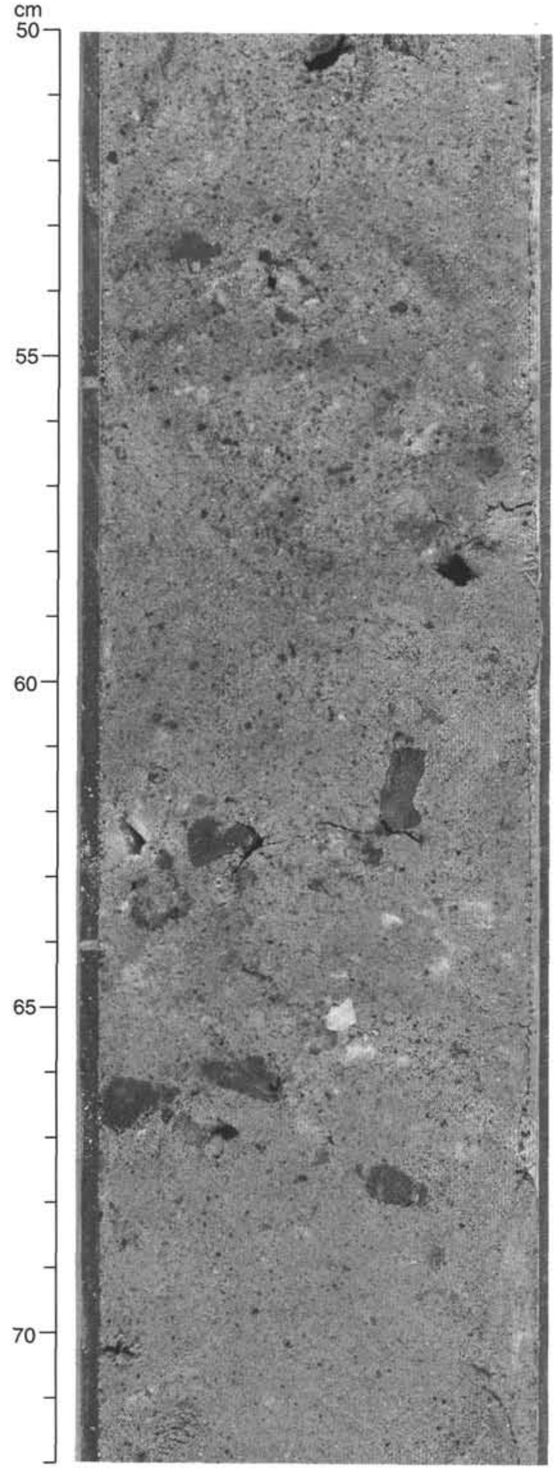

Figure 23. Poorly sorted sand and pebbly sand from lithostratigraphic Unit IV in Hole 976B (Section 976B-72X-2, 662.20 mbsf). The poor sorting of this unit may have been caused by drilling disturbance. Dark sand-sized specks are detrital biotite and rock fragments.

boundary is approximated by the last occurrence of *R. rotaria* in Sample 976B-61X-CC (574.08 mbsf).

Sample 976B-68X-CC (631.2 mbsf) is in Zone NN11 and 976B-69X-1, 21–22 cm (639.11 mbsf) is in Zone NN8, suggesting another hiatus is present at this level. The middle/upper Miocene boundary (within Zone NN8) is between Sections 976B-70X-CC and 976B-71X-CC (650.56–660.58 mbsf).

The interval from Sample 976B-71X-4, 21–22 cm, to Sample 976B-75R-2, 67–69 cm (654.64–679.08 mbsf) is assigned to the upper Serravallian (Zone NN7), based on the presence of *Helicosphaera walbersdorfensis, Discoaster kugleri,* and *Calcidiscus macintyrei.* Sample 976B-75R-1, 1–5 cm (677.83 mbsf) is in Zone NN12, suggesting that the sediments at the top of Core 976B-75R contain downhole contamination. Samples 976B-75R-1, 16 cm (Piece 2, 677.46 mbsf), 75R-2, 22–24 cm (678.63 mbsf), 75R-2, 41–43 cm (678.83 mbsf), and 75R-2, 67–69 cm (679.08 mbsf) are found within the sedimentary matrix of breccias and contain rare to common nannofossils. Preservation is generally moderate in all samples, but with usually well-preserved *Reticulofenestra* spp. and poorly preserved *Coccolithus* spp. This variation in preservation is thought to reflect environmental conditions that indicate that the sediment was deposited in shallow water on the inner part of the shelf.

Scrapings from Samples 976B-80X-1, 22 cm (702.82 mbsf), and 80X-1, 124 cm (703.84 mbsf) contain very rare nannofossils, which could only be assigned a Miocene age. Samples 976B-80X-1, 33 cm (702.93 mbsf), 976B-80X-2, 61–62 cm (704.56 mbsf) are barren of nannofossils.

Hole 976C (Fig. 27)

The stratigraphic interval in this hole ranges from uppermost Pliocene (Subzone NN19A) to uppermost Pleistocene–Holocene (Subzone NN21B). All nannofossil subzones within this interval were identified (Fig. 27). The Pliocene/Pleistocene boundary is located between Samples 976C-38X-CC and 39X-CC (359.58–365.94 mbsf).

Hole 976D

Four cores were taken in this hole; all are assigned to the upper Pleistocene. Sample 976D-1H-CC (1.49 mbsf) is assigned to Subzone NN21B, as indicated by the dominance of *E. huxleyi* over *Gephyrocapsa* spp. (small). Samples 976D-2H-CC (9.62 mbsf), 3H-CC (11.12 mbsf), and 4H-CC (20.77 mbsf) are all assigned to Subzone NN21A, based on the dominance of *Gephyrocapsa* spp. (small) over *E. huxleyi.*

Hole 976E (Fig. 28)

RCB cores were only taken below 534.8 mbsf in this hole, and range from middle Miocene to lower Pliocene.

The interval from Sample 976E-1R-1, 2–4 cm to Sample 976E-3R-CC (543.82–563.17 mbsf) is assigned to lower Pliocene Zone NN12 on the basis of the presence of *Amaurolithus delicatus, Pontosphaera japonica,* and *Helicosphaera intermedia* and the absence of *Pseudoemiliania lacunosa.* The interval from Sample 976E-6R-1, 1–3 cm to 976E-6R-5, 114–116 cm (582.32–589.45 mbsf) is assigned to the lower part of the Messinian (Rotaria and Leptoporus Subzones). The presence of *Discoaster quinqueramus, R. rotaria, Helicosphaera stalis,* and *H. orientalis* indicates the upper Miocene Zone NN11b. The Tortonian/Messinian boundary is between Samples 976E-6R-CC and 7R-CC (589.87-594.20 mbsf) based on the presence *A. delicatus* in Sample 976E-7R-CC to 8R CC (589.87 mbsf). The interval from Sample 976E-7R-CC to 8R–CC (594.20-601.85 mbsf) is assigned to the upper Tortonian based on the presence of *Discoaster pentaradiatus* and on the absence of *R. rotaria* and *A. delicatus.* The interval below Sample 976E-8R-CC down to 976E-12R-1, 10–12 cm (640.31 mbsf) is assigned to the late Miocene Zone NN8 (Tortonian). A hiatus spanning part of the upper Tortonian occurs between Samples 976E-7R-CC and 8R-CC (594.20–601.85 mbsf). Nannofossil zonal markers of Zones NN9 and NN10 are not found, which may indicate a possible hiatus. The interval from Samples 976E-12R-2, 82–84 cm to 13X-2, 77–78 cm (642.53–652.07 mbsf) is assigned to middle Miocene Zone NN7 (Serravallian), based on the presence of *D. kugleri* and *C. macintyrei* (>11.0 mm).

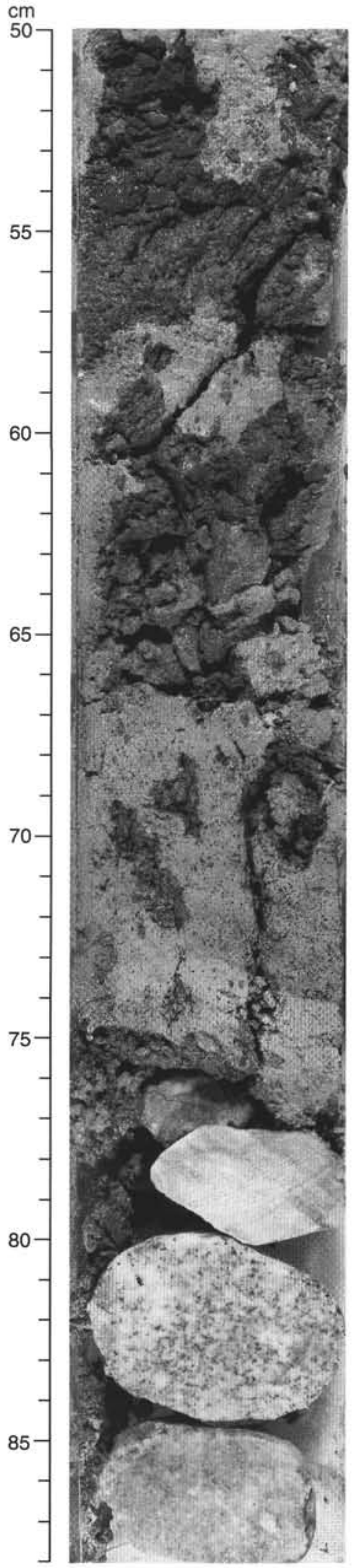

Figure 24. Unit IV (interval 976E-13R-2, 50–88 cm) lithologies include the pebbly base(?) and the sandy upper part of the unit; the latter grades upward into nannofossil-rich silty clay at 65 cm (651.95 mbsf).

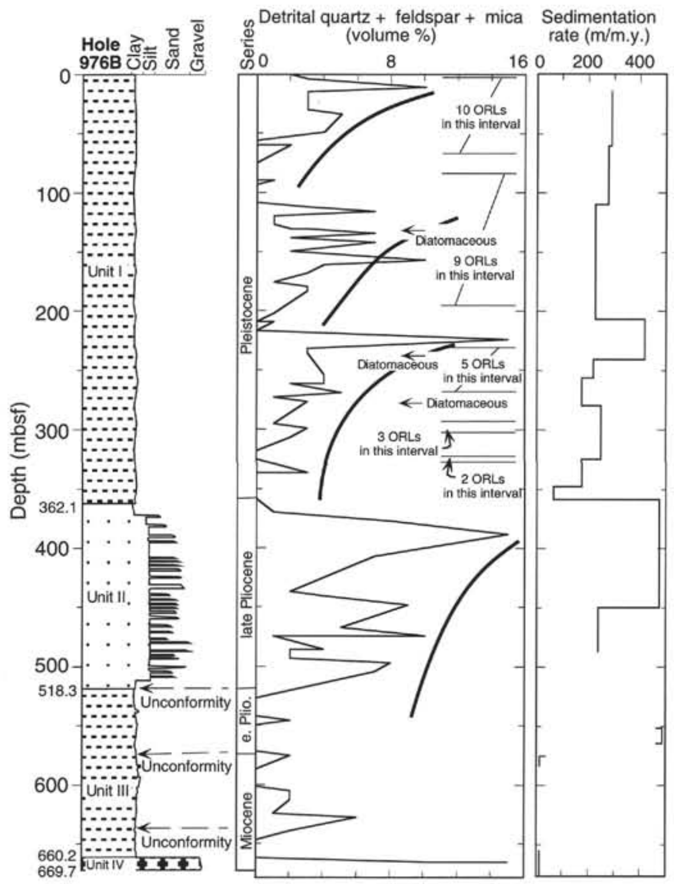

Figure 25. Stratigraphic variation of detrital components quartz + feldspar + mica (QFM) in Hole 976B. Stratigraphic positions of diatomaceous and organic-rich intervals are also indicated. The QFM index was calculated from smear-slide data and is used as an indicator of terrigenous clastic sediment influx.

Samples taken from within the sedimentary breccia in the basement contain very rare to rare nannofossils. Preservation is good to moderate. Sample 976E-17R-1, 124 cm (Piece 7B, 674.94 mbsf) contains *Geminilithella rotula,* which indicates an age younger than the uppermost Aquitanian (22 Ma). The first occurrence of *G. rotula* is in middle Zone NN2. Sample 976E-20R-2, 48 cm (689.99 mbsf) contains very rare *Reticulofenestra minutula.* Samples 976E-21R-1, 93 cm (693.83 mbsf) and 28R–1, 34 cm (722.04 mbsf) are barren of calcareous nannofossils.

Planktonic Foraminifers: Abundance and Preservation

Planktonic foraminifers are abundant and well preserved through the Pleistocene stratigraphic intervals, in Holes 976A, 976B, 976C, and 976D. Through the late Pliocene (MPL6) intervals, from Sample 976B-39X-CC (364.99 mbsf) down to Sample 976B-54X-CC (502.70 mbsf), they are mostly absent, or rare and poorly preserved, except for Samples 976B-49X-CC, 52X-CC, and 53X-CC, in which they are common. Cores 976B-52X, 53X, and 54X contain reworked Eocene to early Pliocene species. In the lower Pliocene interval (MPL2), planktonic foraminifers are abundant and well preserved. In the Miocene interval, foraminifers are abundant, although preservation in some of the samples is very poor.

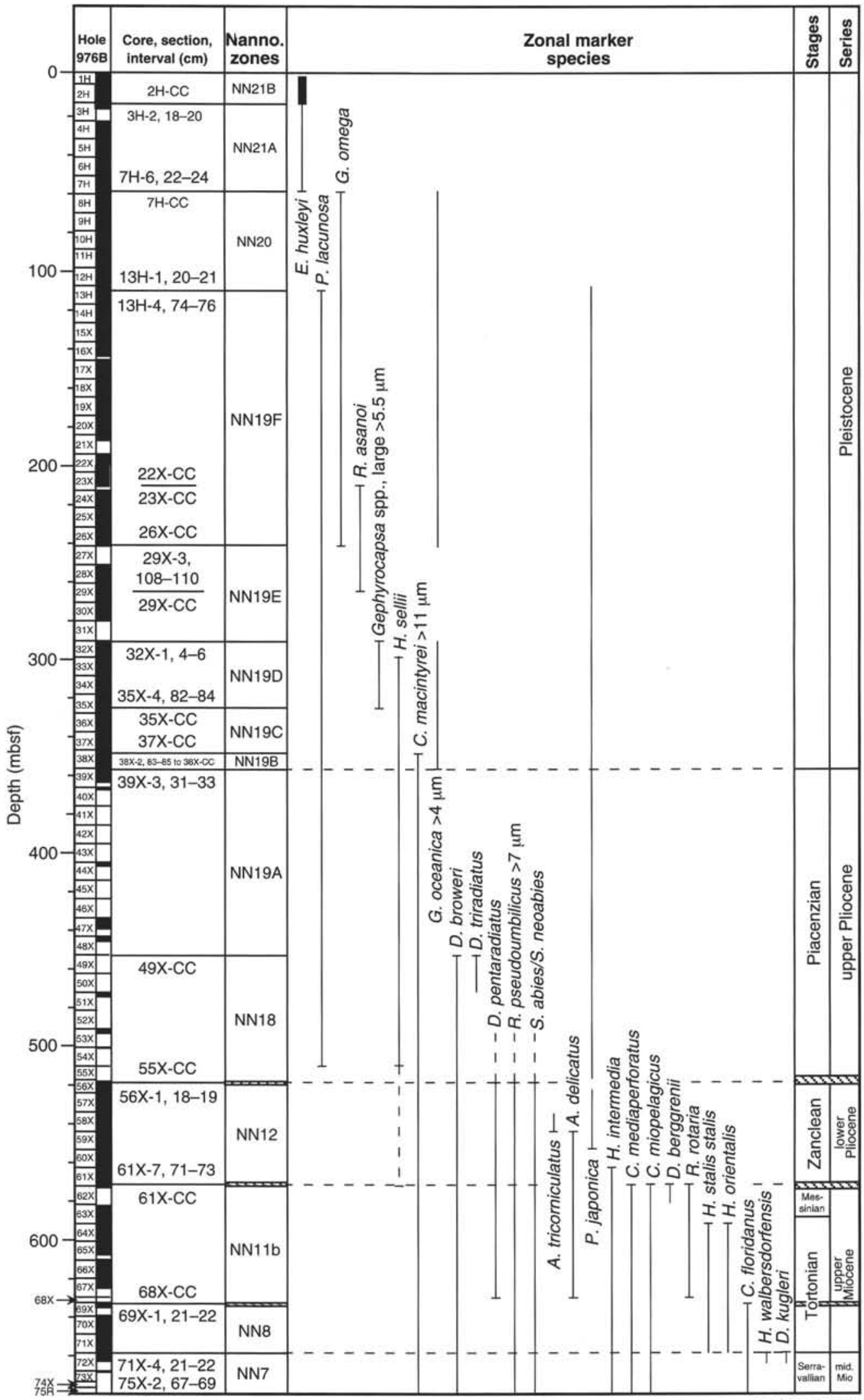

Figure 26. Calcareous nannofossil zonation of Hole 976B. Bold line represents acme interval. Lack of a short horizontal line at the end of a species' vertical range line indicates that the range of that species is incomplete. Dashed vertical lines below the Mediterranean bases of *H. sellii* indicate its irregular global occurrence. Dashed vertical lines above the LO indicate possible reworking.

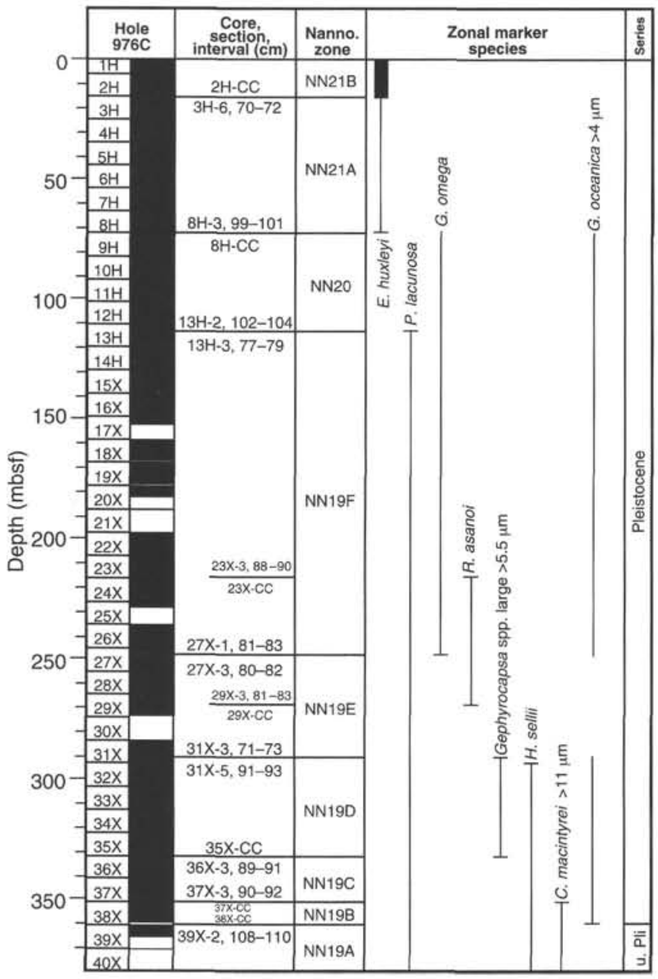

Figure 27. Calcareous nannofossil zonation of Hole 976C. Bold line represents acme interval.

A consistent terrigenous input is attested to by detrital quartz, feldspars, and mica, which are common or abundant in the Pliocene–Pleistocene interval throughout all the holes.

Biostratigraphy

Biozones, the distribution of marker species, and sampling intervals are shown in Figures 29–31.

Hole 976A

Only one core was recovered from this hole and the planktonic foraminiferal assemblage is characterized by abundant *Globigerina bulloides, G. quinqueloba,* and *Neogloboquadrina pachyderma* (sinistral and dextral coiling).

Hole 976B (Figs. 29, 32)

An uppermost middle Miocene (Serravallian)–Pleistocene sedimentary sequence (670 m thick) was recovered above the basement. Three major unconformities were recognized: between upper and lower Pliocene (Zanclean and Piacenzian), lower Pliocene and uppermost Miocene (Zanclean and Messinian), and within the upper Miocene (Tortonian).

The Pleistocene is well represented by both *Globorotalia truncatulinoides excelsa* and *Globigerina cariacoensis* Zones. The marker

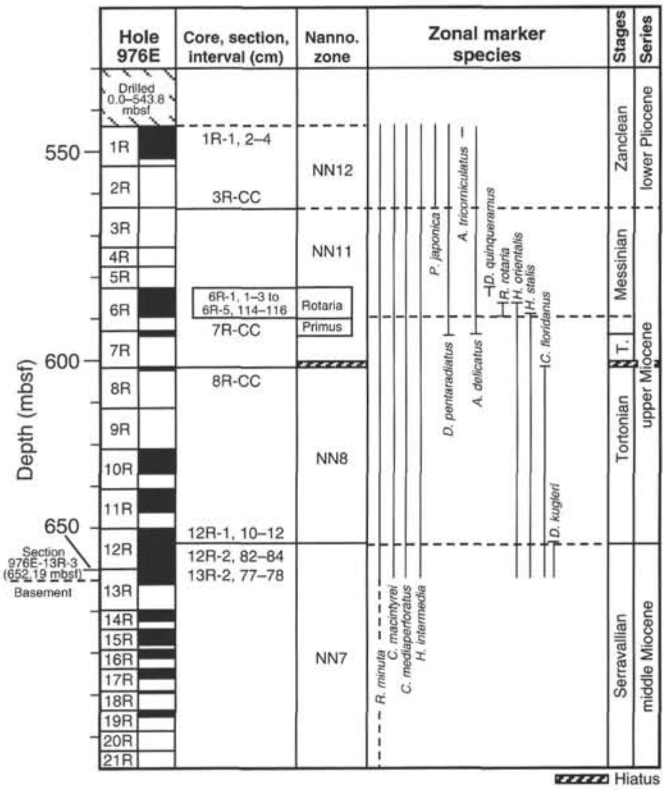

Figure 28. Calcareous nannofossil zonation of Hole 976E.

species are common only in some samples. The other taxa commonly recorded in this interval are *Globorotalia inflata, Neogloboquadrina dutertrei, N. pachyderma* (dextral coiling), and *Globigerinoides ruber*. The *Globorotalia crassaformis* group occurs irregularly.

The Pliocene is represented only by Zones MPL6, MPL5b, and MPL2. Zones MPL5a, MPL4b, MPL4a, and MPL3 are missing or partially present in the poorly recovered sandy interval (see "Lithostratigraphy" section, this chapter). The occurrence of reworked *Globorotalia puncticulata* and *Globorotalia margaritae* in Cores 976B-52X, 53X, and 54X indicates that sediments belonging to Zones MPL3 and MPL4a have been eroded. The elevated thickness of MPL6 (about 122.65 m) attests to a high sedimentation rate for this interval. Zone MPL5b is recorded from Sample 976B-53X-1, 111–113 cm (492.51 mbsf) to 976-B-55X-CC (511.71 mbsf) and Zone MPL2 from Sample 976B-56X-2, 65–67 cm (519.75) down to 976B-61X-7, 71–73 cm (572.35 mbsf). Between the two zones there is an unconformity spanning 1.0–1.5 m.y. Also between Zone MPL2 and the underlying *Globoratalia conomiozea* Zone is a hiatus encompassing the Miocene/Pliocene boundary, which occurs between Sample 976B-61X-7, 71–73 cm (572.37 mbsf) and 976B-61X-CC (574.13 mbsf). From Sample 976B-61X-CC (574.13 mbsf) to 976B-63X-3, 90–92 cm (587.02 mbsf) the *G. conomiozea* Zone was recognized. In addition to the marker species *Globorotalia mediterranea, Globorotalia saphoae, Globorotalia miotumida, Globorotalia conoidea* are present in Sample 976B-63X-3, 90–92 cm (587.02 mbsf). Sample 976B-63X-6, 56–58 cm (589.68 mbsf) yields *Globorotalia suterae,* which indicates the upper part of the Tortonian. The absence of *Globigerinoides extremus* in the interval from Sample 976B-69-1, 147–149 cm (635.39 mbsf) to 976B-70X-CC suggests that the *G. extremus* Zone is missing, and only the lower part of the Tortonian is present (*Neogloboquadrina acostaensis* Zone). From Sample 976B-71X-1, 79–81cm to 976B-72X-CC, *Globorotalia siakensis, Neogloboquadrina continuosa,* and *N. acostaensis* co-occur. This interval, following Foresi et al. (in press), has been assigned to the Serravallian. The

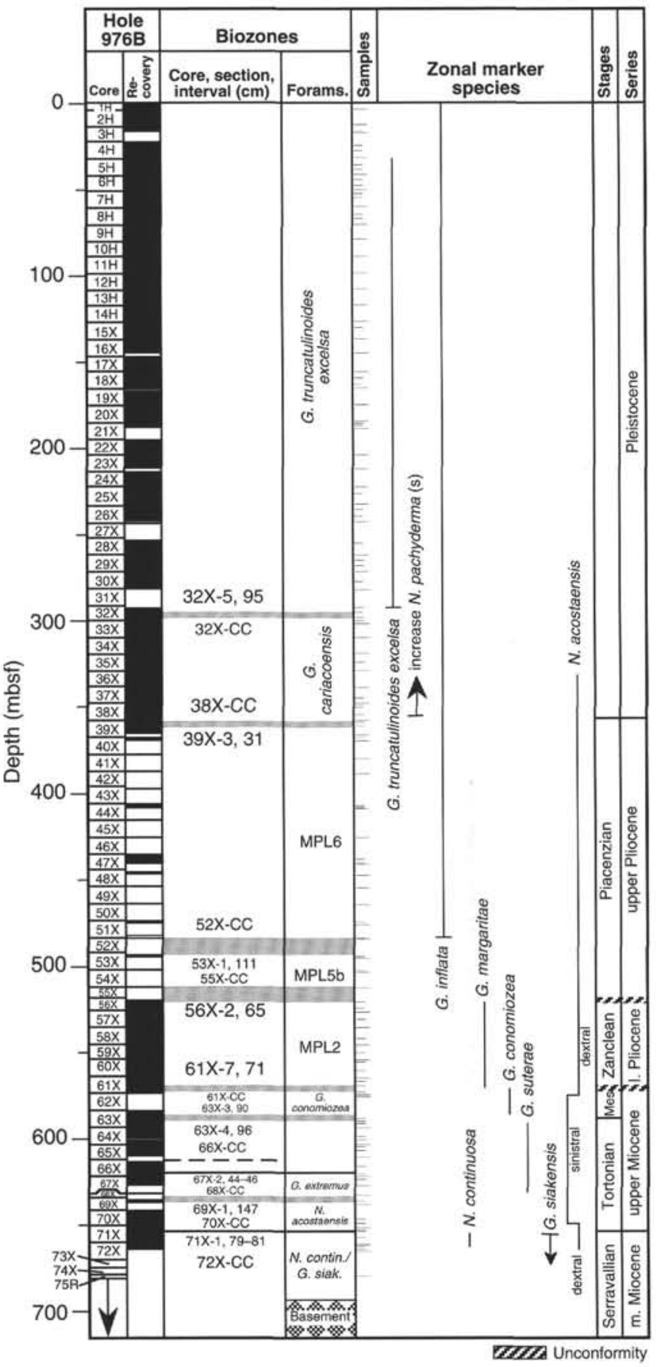

Figure 29. Planktonic foraminiferal zonation of Hole 976B. Shaded areas represent intervals not sampled.

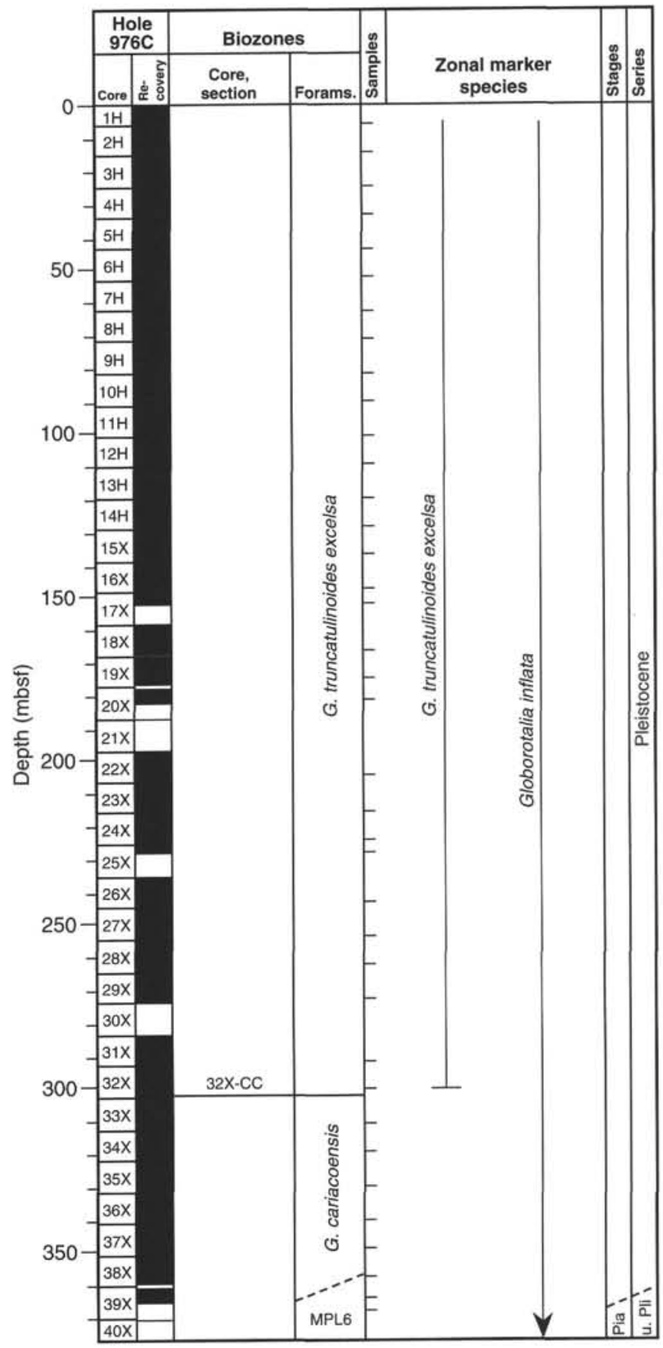

Figure 30. Planktonic foraminiferal zonation of Hole 976C.

Serravallian/Tortonian boundary has been placed at the FCO of *N. acostaensis,* which virtually coincides with the LO of *G. siakensis.*

Hole 976C (Fig. 30)

The Pleistocene sedimentary sequence recovered from this hole correlates well with that of Hole 976B with respect to the *G. truncatulinoides excelsa* Zone. The base of this zone occurs in Sample 976C-32X-CC (303.29 mbsf). The lower boundary of *G. cariacoensis* Zone is not recognizable because the increase of *N. pachyderma* (sinistral coiling) was not detected. Therefore, in this hole, no determination of the Pliocene/Pleistocene boundary was made using planktonic foraminifers.

Hole 976D

The sedimentary sequence (30.05 m-thick) is entirely within the Pleistocene *G. truncatulinoides excelsa* Zone.

Hole 976E (Fig. 31)

This sedimentary sequence spans from the uppermost middle Miocene (Serravallian) to the early Pliocene (Zanclean). Zone MPL2 was recognized in the topmost cores 976E-1R to 3R. As in Hole 976B, an upper Miocene to lower Pliocene unconformity appears to be present between Samples 976E-3R-CC (563.22 mbsf) and 976E-6R-1, 1–3 cm (582.33 mbsf). However, since Cores 976E-4R and 5R had no recovery, the exact extent of the missing interval cannot be de-

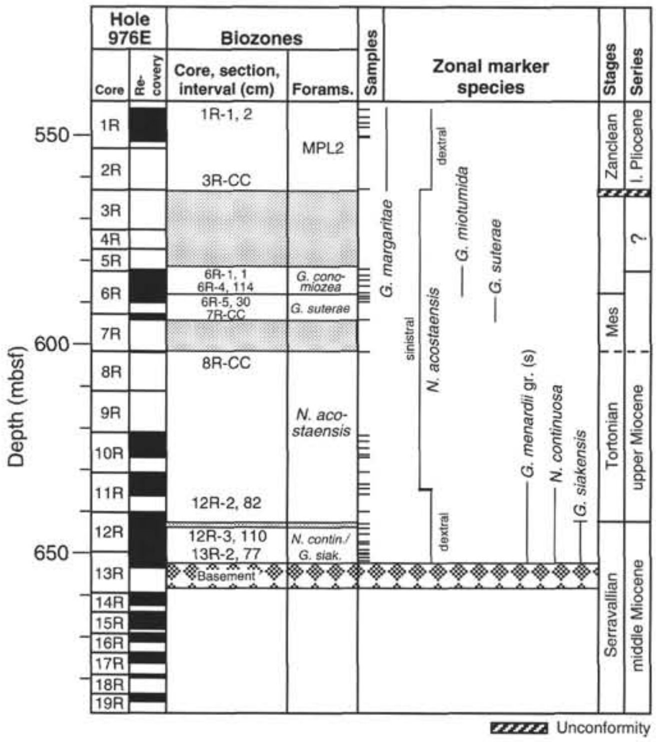

Figure 31. Planktonic foraminiferal zonation of Hole 976E. Shaded areas represent intervals not sampled.

termined. Unlike Hole 976B, *G. conomiozea, G. mediterranea,* and the sinistral to dextral coiling change of *N. acostaensis* were not observed. However, the Messinian was recognized through the presence of *G. miotumida* (belonging to the *G. conomiozea* group, according to Krijgsman et al. [in press]) from Sample 976E-6R-2, 81–83 cm (584.63 mbsf) to 976E-6R-4, 114–116 cm. *G. suterae,* the marker species of the *G. suterae* Zone, is present from Sample 976E-6R-5, 30–32 cm (588.62 mbsf) to 976E-7R-CC (594.20 mbsf). The *N. acostaensis* Zone was recognized from Sample 976E-8R-CC (601.85 mbsf) to 976E-12R-2, 82–84 cm, implying an intra-Tortonian unconformity (as was observed in Hole 976B) involving the *G. extremus* Zone. However, the elevated thickness of this zone suggests that the boundary with *G. extremus* has not been detected but could be present in this interval. The *Globorotalia menardii* group is absent in the upper part of this zone and is consistently present from Sample 976E-11R-3, 60–62 cm (634.22 mbsf) to the bottom of the sedimentary sequence. From Sample 976E-12R-3, 110–112 cm to 976E-13R-2, 77–79 cm (652.08 mbsf) the *N. continuosa–G. siakensis* Zone was recognized, indicating a Serravallian age.

Benthic Foraminifers

Benthic foraminifers at Site 976 are larger in size, more abundant, and more diverse than at Sites 974 or 975. This may be linked to the fact that Site 976 is shallower (present-day water depth is 1108 m), and has a distinctly higher background TOC than at Sites 974 or 975. This observation is consistent with those previously made in the Mediterranean Sea (Wright, 1978).

Benthic foraminifers from hemipelagic lithostratigraphic Units I and III (0–362.8 and 518.3–660.2 mbsf) in Hole 976B are diagnostic of lower epibathyal (500–1300 m) to upper mesobathyal (1000–1800 m) depths as defined by Wright (1978). They generally comprise <1%–2% of the total foraminiferal assemblage, except where there is a variable influx of terrigenous material and shallow-water forms, mostly *Elphidium, Ammonia, Asterigerina,* and *Valvulineria* genera.

The few benthic foraminifers in lithostratigraphic Unit II (362.8–518.3 mbsf) are forms diagnostic of inner to outer neritic environments and dominate over the few bathyal forms present, and, at times, even the few planktonic foraminifers. The samples are primarily composed of either coarse detrital quartz, feldspars, and micas, or calcite-cemented grains. In Sample 976B-40X-CC, 35–40 cm (368.25 mbsf), >90% of the total foraminiferal assemblage is composed of benthic foraminifers (mostly *Elphidium* and *Ammonia* species). In Sample 976B-41X-CC, 22–27 cm (377.22 mbsf), >60% of the assemblage is composed of poorly preserved bathyal and neritic benthic foraminifers. These shallow-water benthic species have been transported to bathyal depths several hundred meters deeper than their original habitat.

Nine samples were examined from Core 976B-72X from lithostratigraphic Unit IV (660.2–669.7 mbsf). Preservation is poor, and many foraminifers are encrusted. Glauconite, clear quartz, and euhedral crystals of biotite are present in varying quantities. Samples are either barren, are dominated by larger-sized benthic foraminifers characteristic of neritic environments, or are composed of shallow-water benthic foraminifers as well as bathyal benthic foraminiferal forms and planktonic foraminifers. The deepest sample, Sample 976B-72X-CC, 25–30 cm (664.32 mbsf), immediately overlies basement and contains a benthic assemblage that consists of predominately bathyal forms (*Cibicidoides kullenbergi, Globocassidulina subglobosa, Gyroidinoides* spp., *Oridorsalis umbonatus, Siphonina reticulata,* and others). Lithostratigraphic Unit IV appears to have been deposited in bathyal depths with significant and variable contamination of shallow-water forms brought in by downslope sediment transportation.

Biozonal Correlation

Correlation of the calcareous nannofossil and planktonic foraminiferal zonations for Hole 976B is shown in Figure 32. The placement of the Pliocene/Pleistocene boundary is based on the calcareous nannofossils and planktonic foraminifers. The estimated missing intervals in the lower to upper Pliocene, and the upper Miocene–lower Pliocene are based on calcareous nannofossils and planktonic foraminifers. The upper Miocene (intra-Tortonian) unconformity is based on both groups of microfossils; the basal chronostratigraphic assignment (Serravallian/Tortonian) is not well established because of the absence of a well-calibrated *N. acostaensis* FO, which is used to recognize this boundary at the stratotype of the Tortonian.

Sedimentation Rates

Figure 33 shows the sedimentation rates for Hole 976B. Age data used (Table 4) for construction of the age-depth plot in Figure 33 are based on first and last appearance events of selected nannofossils and planktonic foraminifers (see Table 2 in "Explanatory Notes" chapter, this volume). Table 5 gives biostratigraphic ages for Hole 976C. Average sedimentation rates in Hole 976B were 208 m/m.y for the Pleistocene/Holocene, 340 m/m.y. for the late Pliocene, 453 m/m.y. for the early Pliocene, and 15 m/m.y. for the late Miocene. The very high sedimentation rate obtained for the early Pliocene is possibly due to the lack of biostratigraphic control close to the hiatus between early and late Pliocene.

PALEOMAGNETISM

The cryogenic magnetometer was used to measure 102 archive APC and XCB halves. Blanket AF demagnetization was applied at 15 or 25 mT, depending on the NRM intensity. Archive sections and/or discrete samples were progressively demagnetized and measured by using both the cryogenic and spinner magnetometer. Discrete samples were selected to augment the results from the archives and were also used for various rock-magnetic experiments.

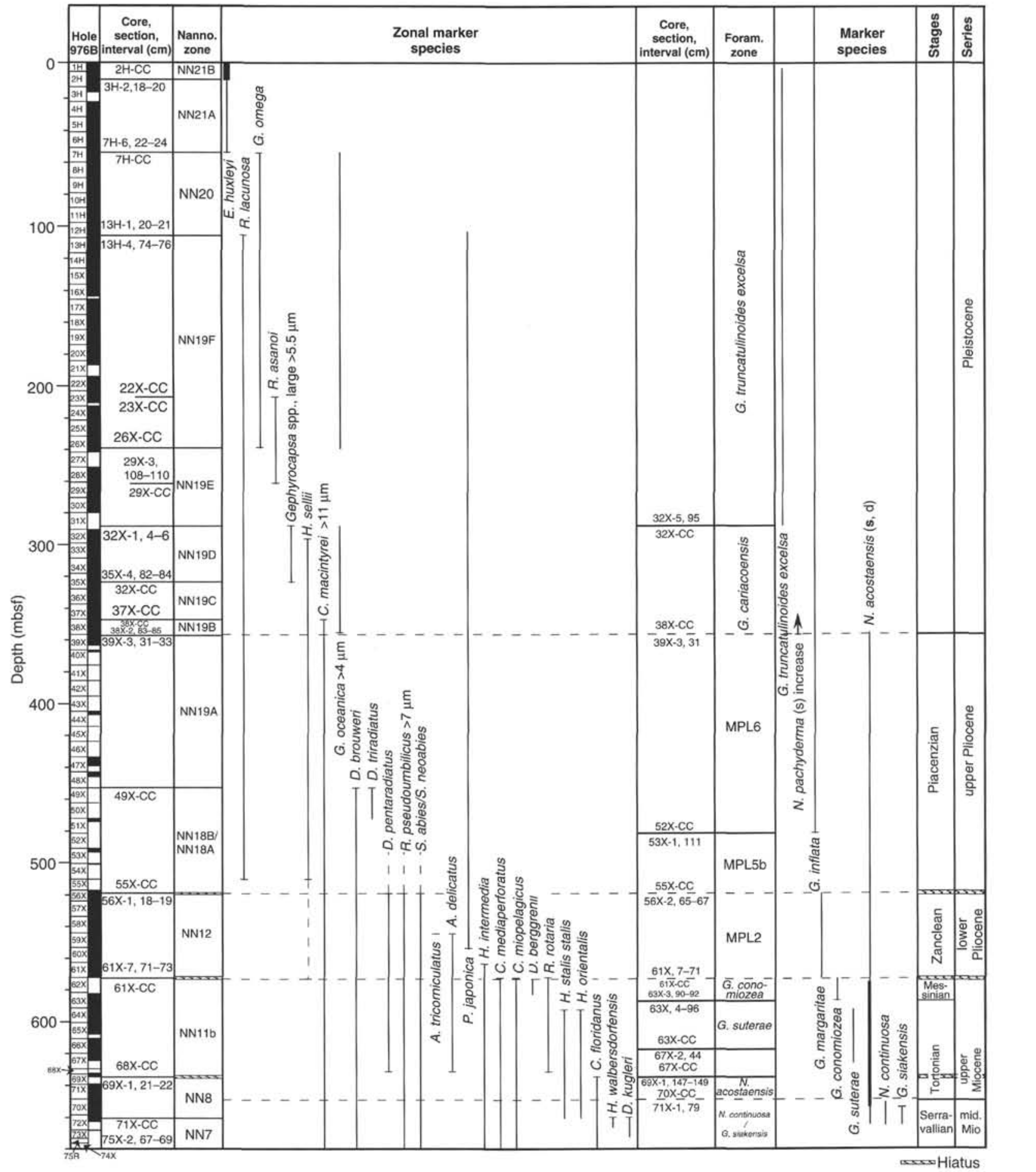

Figure 32. Summary of nannofossil and foraminiferal zonations of Hole 976B. See Figure 26 caption for explanation of symbols.

At Hole 976B, 19 mini-core samples were collected from hard-rock cores to measure remanent magnetization, anisotropy of magnetic susceptibility (AMS), and rock-magnetic properties.

APC cores from Holes 976B and 976C were oriented with the Tensor tool (Table 6).

Remanent Magnetization

Sediment remanent magnetizations at this site are relatively weak, and show scattered declinations and dominantly positive inclinations as compared to Sites 974 and 975 (Figs. 34–37). Remanent intensity decreases by about one order of magnitude at 50–60 mbsf. Below this level the intensity is mostly less than 1 mA/m after AF demagnetization, but still above the noise level of the cryogenic magnetometer. Significant changes in declinations correspond to intensity decreases. Above 50–60 mbsf, declinations cluster core by core. After reorienting with Tensor tool data (Table 6), the declinations somewhat converge to north (Fig. 38), suggesting possible recording of the past geomagnetic field. Below 50–60 mbsf declination is smeared, but clusters mostly around 0° (Figs. 35, 36) possibly indicating a perva-

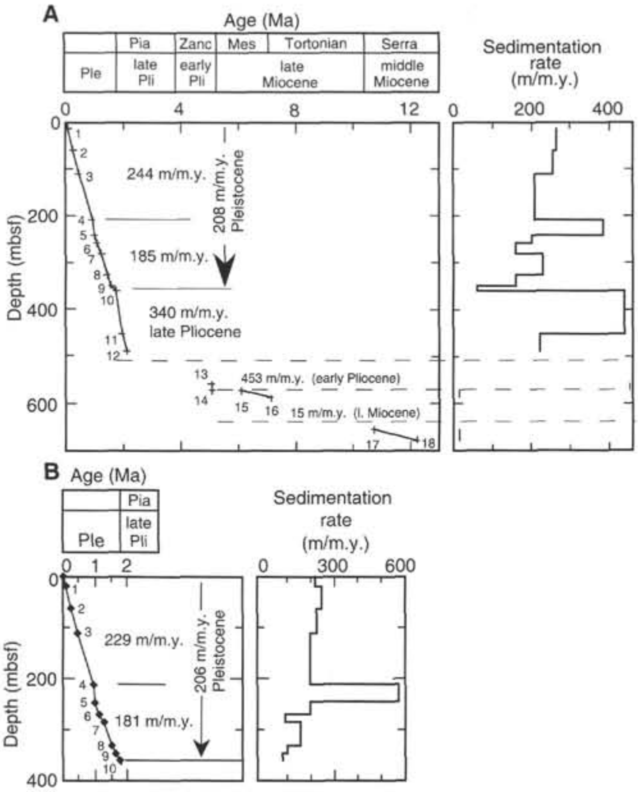

Figure 33. Sedimentation rates at (**A**) Hole 976B and (**B**) Hole 976C.

sive radial remagnetization (PRR; Shipboard Scientific Party, 1995). The PRR is not as prominent at Site 976 as at Sites 974 and 975.

Above 360 mbsf in Holes 976B and 976C, inclinations are mostly positive with only a few negative inclinations (Figs. 35, 36). From 550 mbsf to 660 mbsf in Hole 976B, the numbers of negative inclination data increase to almost half of the total data points (Fig. 35). It will be possible to show reversed polarity intervals at this depth by shore-based demagnetization experiment.

Progressive AF cleaning on discrete samples was performed using the cryogenic magnetometer and its degausser (CryoCube mode) at Hole 976B. However, most samples acquired spurious anhysteretic remanent magnetization (ARM) at 20 mT or below. This must be caused mainly by the relatively weak intensity of these samples and partly because of a very small imbalance among the degaussing coils, which makes demagnetization of small discrete samples difficult. To avoid this complication, we decided on a stepwise AF demagnetization up to 30 mT for the selected sections of archive halves from Holes 976C and 976D. Some discrete samples were collected from the corresponding working sections and measured with the spinner magnetometer.

Typical progressive AF demagnetizations of archive halves from Hole 976C are displayed in Figure 39. A steep, positive large-intensity overprinting (drilling-induced remanence) was found in most cores, although this overprinting was apparently removed by demagnetization at 5 to 10 mT. After removing this steep component, a few samples seem to converge to the origin, but a demagnetizing field of 30 mT is not enough to fully reduce the stable component (Fig. 39C, K). Most samples do not converge to the origin after applying the maximum field demagnetization (30 mT; Fig. 39A, E, G) or seem to have acquired spurious ARM due to the AF demagnetization (Fig. 39H, I, L). Stepwise demagnetized directions plotted on an equal-area projection change sequentially along great circles (Fig. 40). All vectors start with steep positive directions and end with shallow ones. The fan pattern of great circles in the APC section (Fig. 40A) suggests possible twisting of the core section. In addition, similar behavior of great circle trajectories in strongly biscuited XCB sections may indicate the presence of a secondary high coercive overprint in XCB samples (Fig. 40B, C).

We made detailed investigations on short reversals that occurred in the upper part of all holes (Fig. 34–37). At Holes 976C and 976D, we observed short but sequential changes in inclination from positive to negative values in Cores 976C-5H and 976D-3H. Archive half demagnetization shows a gradual change in inclination from positive to negative values (Fig. 41A). Several discrete samples were collected from the corresponding working-half section (976C-5H-3). These samples were measured with the spinner magnetometer for higher AF demagnetization (up to 70 mT by using the single axis AF demagnetizer). These discrete samples did not reveal negative inclinations, however (Fig. 41B, C). In these archive halves and discrete samples, soft components of steep positive inclination were removed by applying 10 mT. After removing this common drill string overprinting, the remanent vectors of archive and discrete samples decreased smoothly to the origin but along different trends. About one-third of stable remanence remained after applying 30 mT, indicating similar demagnetization efficiency for the two different instruments. Conflicting results between archive halves and discrete samples were also obtained in Core 976D-3H.

As this kind of apparent reversal is only found in the pass-through measurement data of split cores, we believe it could be an artifact related to the geometry of magnetization of a core sample as well as PRR.

We are not able to suggest magnetostratigraphic zones at this site, as shown in Figs. 35–37. In contrast to the previous sites, Site 976 is not strongly affected by PRR, but we still could not determine remanence directions from the cores. Weak NRM intensities and insufficient demagnetization are plausible reasons for the inconclusive results.

Rock-Magnetic Properties

Discrete samples collected from Hole 976B sediments were used for rock-magnetic studies to try to understand why magnetostratigraphy was difficult. We measured low-field susceptibility (K) and its frequency dependence (F_d), susceptibility of anhysteretic remanent magnetization (K_{arm}), and saturated isothermal remanence (SIRM) and its ratio to back-field magnetization at 0.3 T ($S_{-0.3T}$; Table 7). Implications and limitations for each parameter are described in the "Explanatory Notes" chapter, this volume. A high value of $S_{-0.3T}$ (>0.9) suggests a dominance of low coercive ferrimagnetic minerals, such as magnetite, throughout the core. The other parameters reflect major lithologic changes such as those between lithostratigraphic Units I, II, and III. Rapidly decreasing values for K, K_{arm}, and SIRM in the upper part of the site, from 0 to 50 mbsf (Fig. 42), were observed. These parameters are controlled either by the abundance of magnetic minerals and/or by grain size. It seems reasonable to assume that this reflects rapid dissolution of fine-grained magnetic minerals at increasing burial depths (Karlin, 1990; Torii et al., 1992). The selective dissolution of fine-grained minerals causes the magnetic mean grain size to increase to coarse, while size-sensitive parameters drastically decrease. It also causes K_{arm}/SIRM and K_{arm}/K_f to decrease (Fig. 42), which are all interpreted to show coarsening of the mean magnetic grain size. Although frequency dependence of susceptibility (F_d) measurement was not very stable, it also indicated rapid coarsening of magnetic minerals in the uppermost part of the hole.

We suggest that the dissolution of fine grains and resultant coarsening of the magnetic mineral fraction by sub-bottom diagenesis is an important factor that controls overprinted magnetization below 50 mbsf at this site. The high-coercivity magnetic fraction, which has

Table 4. Age of calcareous nannofossil and planktonic foraminiferal biostratigraphic events and depth of their occurrence in Hole 976B.

		Biostratigraphic event	Age (Ma)	Depth (mbsf) Top	Bottom	Mean
1	Base	*E. huxleyi* acme	0.085	13.15	14.25	13.7
2	FO	*E. huxleyi*	0.26	58.73	61.02	59.875
3	LO	*P. lacunosa*	0.46	108.21	113.26	110.735
4	LO	*R. asanoi*	0.93	203.97	211.79	207.88
5	FO	*G. omega* >4.0 μm	1.02	242.15	242.9	242.525
6	FO	*R. asanoi*	1.10	252.65	264.68	258.66
7	LO	*Gephyrocapsa* spp. >5.5 μm	1.24	281	281	281
8	FO	*Gephyrocapsa* spp. >5.5 μm	1.44	324.39	329.44	326.915
9	LO	*C. macintyrei* >11 μm	1.58	348.21	350.43	349.32
10	FO	*G. oceanica* >4.0 μm	1.75	357.92	361.01	359.465
		Pliocene/Pleistocene boundary	1.83			
11	LO	*D. brouweri*	1.96	447.94	454.02	450.98
12	FO	*G. inflata*	2.13	483.65	493.51	488.58
		Early Pliocene/Late Pliocene boundary		511.71	518.48	515.10
13	LcO	*H. intermedia*	5.07	554.75	564.53	559.64
14	FCO	*G. margaritae*	5.1	572.35	574.13	573.24
		Miocene/Pliocene boundary				573.24
15	LO	*R. rotaria*	6.12	572.35	574.13	573.24
16	FRO	*G. conomiozea* gr.	7.11	587.02	588.56	587.79
		Tortonian/Messinian boundary				587.79
		Serravallian/Tortonian boundary	10.5	650.57	651.29	650.93
17	LO	*H. walbersdorfensis*	10.72	651.93	660.58	656.255
18	FO	*C. macintyrei*	12.20	677.46	680.7	679.08

Notes: FO = first occurrence, LO = last occurrence, LCO = last common occurrence, LcO = last consistent occurrence, FCO = first common occurrence, FRO = first regular occurrence; also indicated are the main chronostratigraphic boundaries. This table is also on the CD-ROM, back pocket, this volume.

Table 5. Age (Ma) of calcareous nannofossil biostratigraphic events and depth of their occurrence (mbsf) in Hole 976C.

		Biostratigraphic event	Age (Ma)	Depth (mbsf) Top	Bottom	Mean
1	Base	*E. huxleyi* acme	0.085	15.91	23.7	19.805
2	FO	*E. huxleyi*	0.26	63.36	67	65.18
3	LO	*P. lacunosa*	0.46	113.02	114.27	113.645
4	LO	*R. asanoi*	0.93	209.46	216.79	213.125
5	FO	*G. omega* >4.0 μm	1.02	245.91	248.9	247.405
6	FO	*R. asanoi*	1.10	267.37	274.49	270.93
7	LO	*Gephyrocapsa* spp. >5.5 μm	1.24	286.49	289.69	288.09
8	FO	*Gephyrocapsa* spp. >5.5 μm	1.44	330.61	334.76	332.685
9	LO	*C. macintyrei* >11 μm	1.58	344.16	351.51	347.835
10	FO	*G. oceanica* >4.0 μm	1.75	359.63	362.98	361.305
		Pliocene/Pleistocene boundary	1.83			361.305

Note: FO = first occurrence, LO = last occurrence. This table is also on the CD-ROM, back pocket, this volume.

been carrying the primary detrital magnetization, was dissolved during the sub-bottom diagenesis and remained unstable. Larger grains may have acquired secondary overprinting magnetization. Most magnetic parameters display a sharp peak at about 40 mbsf, which is superimposed on the decreasing trend. We have no obvious explanation at this moment and further magnetic mineralogical experiments will be carried out after the cruise.

MST and discrete measurement of low-field magnetic susceptibility (Fig. 43), after applying a factor of 0.63×10^{-5} to MST data (see "Explanatory Notes" chapter, this volume), show close agreement.

Hard Rock Samples

We collected 19 mini-core samples in the metamorphic basement from 670 to 890 mbsf. These gneissic rocks exhibit strong regular foliation. NRM was also measured on the mini-cores (Table 8) and 9 samples were demagnetized with stepwise AF up to 20 mT. Most of these samples show apparent reversed magnetizations, but no clear component of magnetization can be seen. In particular, we found no evidence of viscous magnetization that can be used for core reorientation.

We also measured mean low-field magnetic susceptibility (K_m), K_{arm}, and IRM in these samples (Table 8). In addition, we carried out thermal demagnetization of composite IRMs of 6 samples (Fig. 44)

Table 6. Azimuthal orientation of APC cores from Holes 976B and 976C using Tensor tool data.

Core	Magnetic toolface MTF (°)
161-976B-	
3H	30
4H	98
5H	38
6H	240
7H	222
8H	127
9H	304
10H	82
11H	119
12H	228
13H	236
161-976C-	
3H	130
4H	267
5H	288
6H	189
7H	347
8H	227
9H	263
10H	152
11H	289
12H	351
13H	56
14H	277

Note: The orientation parameter (MFT) is an angle between true north and X-axis of the core-coordinate.

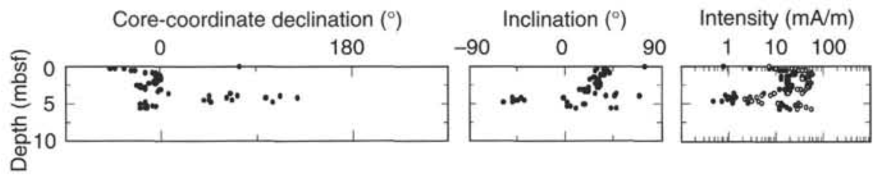

Figure 34. Declination, inclination, and intensity after 25 mT AF demagnetization for Hole 976A. Intensity of NRM is indicated by open circles and demagnetized intensity by solid circles.

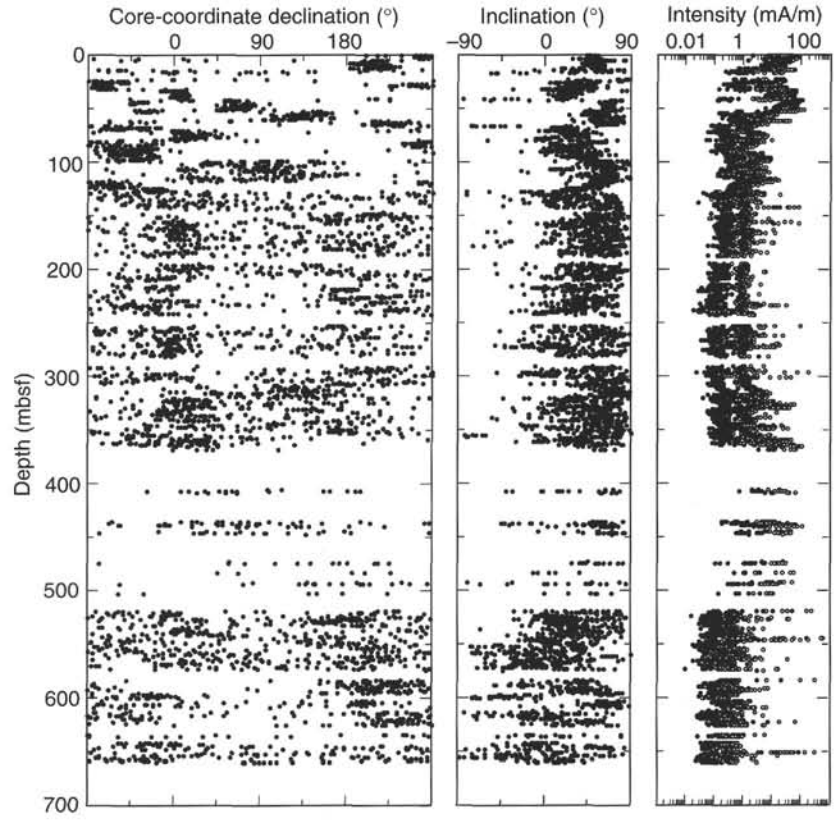

Figure 35. Declination, inclination, and intensity for Hole 976B. Cores 976B-1H through 10H were demagnetized at 25 mT and the rest at 15 mT. Symbols as in Figure 34.

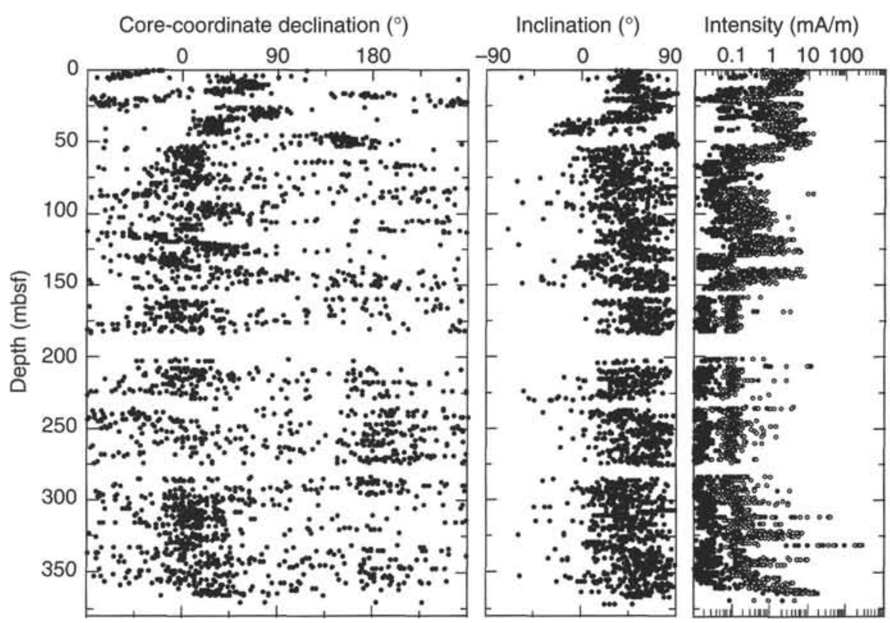

Figure 36. Declination, inclination, and intensity after 25 mT AF demagnetization for Hole 976C. Symbols as in Figure 34.

following the Lowrie method (see "Explanatory Notes" chapter, this volume). Along X, Y, and Z axis of each samples, we imparted respectively hard (1 T), medium (0.3 T) and soft IRM (0.1 T).

K_m ranges from 2×10^{-4} up to 2×10^{-2} SI units at about 830 mbsf (Fig. 45A; Table 8). The high K_m values, ~1%, indicate abundant magnetic material, whereas the low K_m values are only ~0.01%. Samples 976B-76R-1, 12–14 cm and 976B-77R-2, 78–80 cm show the same thermal demagnetization curves with a sharp decrease of the hard component at 350°C (Fig. 45). High values of K_m and a strong degree of magnetic anisotropy ($P = K_1/K_3$) suggest the occurrence of an iron sulfide like pyrrhotite (Rochette, 1987). Higher grade metamorphic Samples 976B-96R-2, 8–10 cm, and 976B-101R-2, 35–37

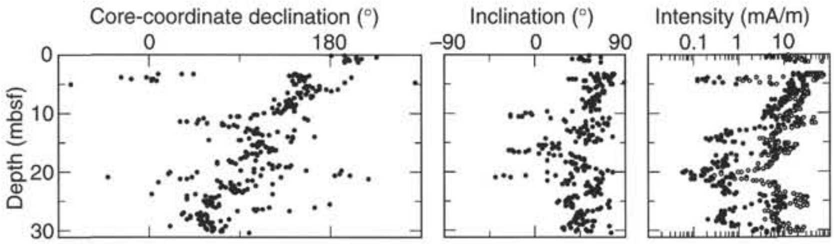

Figure 37. Declination, inclination, and intensity after 15 mT AF demagnetization for Hole 976D. Symbols as in Figure 34.

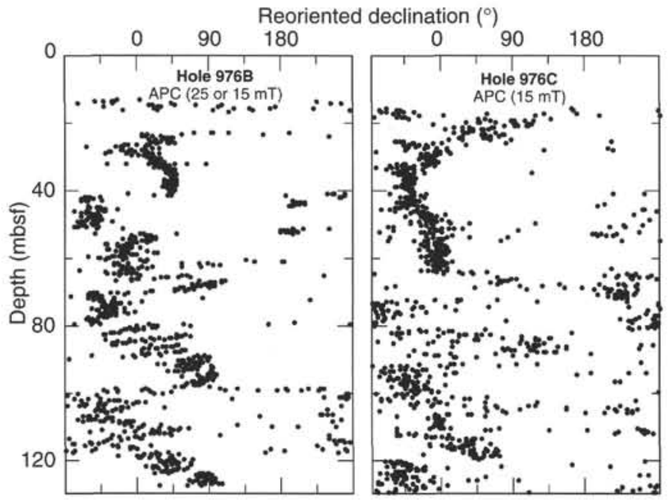

Figure 38. Reoriented declination by using Tensor tool for APC cores from Holes 976B and 976C. Orientation data is listed in Table 6.

cm, show a sharp decrease of the hard IRM component at ~400°–500°C, whereas medium and soft components end at ~700°C. The occurrence of magnetite as the main magnetic mineral is likely as it has been recognized in thin sections (see "Structural Geology and Petrology of the Basement" section, this chapter). Hematite is also present in minor amounts. We have no interpretation yet for the hard magnetite and soft hematite. For Samples 976B-74X-1, 42–44 cm and 976B-80R-1, 27–29 cm, we have no definitive conclusions. The succession of pyrrhotite and magnetite in metamorphic complexes suggests a higher grade in the metamorphism (Rochette and Lamarche, 1986), as described in the "Structural Geology and Petrology of the Basement" section (this chapter).

We measured the anisotropy of low-field magnetic susceptibility (AMS) in gneiss samples to document the preferred orientation of the magnetic carrier assemblages. AMS results are compiled in Table 8. The anisotropy is well determined with a confidence angle for each susceptibility axis lower than 5°. The magnetic fabric in all samples is oblate ($L = 1.046 \pm 0.047 < F = 1.202 \pm 0.111$). The degree of anisotropy P varies from 1.1 to 1.5 (Fig. 45B), which is clearly related to K_m (Fig. 45A, D). A good correlation also exists between the anisotropy of seismic velocities (see "Physical Properties" section, this chapter) and P (Fig. 45D, E). This suggests that P is controlled by changes in magnetic mineralogy (K_m) and by preferred grain orientation. High P and seismic velocity anisotropy values may therefore suggest an increase of the deformation.

Correlation between dip of structural foliation and magnetic foliation (Fig. 45F) is good (see also "Structural Geology and Petrology of the Basement" sections, this chapter). In addition to magnetic foliation, AMS displays well-defined magnetic lineations that likely mark the preferred linear orientation within the foliation plane. If core sections can be oriented using FMS data, magnetic lineation will be helpful for understanding the tectonic history of the basement high.

COMPOSITE DEPTHS

High-resolution (2–10-cm-scale) data were collected on the multisensor track (MST) and with a hand-held spectrophotometer on cores recovered from all holes of Site 976. Four principal variables (GRAPE density, magnetic susceptibility, natural gamma radiation, and 550-nm-wavelength color reflectance) were used to construct a composite depth section from Holes 976B, 976C, and 976D to 352 mbsf. Distinctive features were correlated between cores from each hole and depth-shifted to a common depth scale (meters composite depth = mcd) so that overlapping cores from different holes would produce a single composite section. The offsets for each core used for alignment are listed in Table 9, which gives standard ODP meters below seafloor depths (mbsf), offset in meters, and meters composite depth (mcd) for each core. Shifted and aligned core data are shown in Figures 46–49.

The composite (or "spliced") section seeks to provide a complete stratigraphic record utilizing overlapping intervals of cores from the different holes. The composite section is described in Table 10. Splices from Table 10 are indicated by arrows in Figure 46. Correlation between cores was consistent between the seafloor and approximately 151 mbsf (to Cores 976B-17X and 976C-17X). Below this depth a continuous record could not be constructed with confidence because of gaps in core recovery or intervals of poor depth overlap of recovered sediments. However, large sections of the cored interval below 151 mbsf, although somewhat disturbed by exsolved gas, exhibited sufficient coherent signal to merit depth-shifting and splicing (Fig. 48). Organic-rich layers listed in Table 3 in the "Lithostratigraphy" section, this chapter, generally plot within 1 m of each other in mcd in Holes 976B and 976C throughout the section drilled, as does a diatomite layer seen in Cores 976B-26X and 976C-26X.

Gamma-ray and GRAPE density records for cores immediately above basement in Holes 976B and 976E are illustrated in Figure 50. No depth-shifts or correlations were made, although "best guess" matches between cores are indicated in the figure with double-ended arrows. These layers are likely offset because of deposition on top of pre-existing irregular basement topography.

STRUCTURAL GEOLOGY AND PETROLOGY OF THE BASEMENT

Introduction

Hole 976B reached the base of the Miocene–Pleistocene sedimentary column at 669.73 mbsf (Section 976B-73R-1, Piece 3) and penetrated basement. The hole terminated at 928.7 mbsf. The total thickness of basement rocks cored was 258.97 m, and the total recovery was 50.4 m (19%), mostly in the form of separate pieces from 1–20 cm in length. Hole 976E reached hard rock at 652.08 mbsf (Core 976E-13R-3, Piece 1) and terminated at 736.3 mbsf. The total thickness cored was 84.22 m, and the total recovery was 24.74 m (29%), including pieces up to 1 m long. In both holes the recovered basement rock consists largely of high-grade metamorphic rocks with sedimentary protoliths, including high-grade pelitic schist, pelitic paragneiss, marble, and calc-silicate rock, with minor granite intrusions and migmatitic segregations (Figs. 51, 52). The cores also include numerous

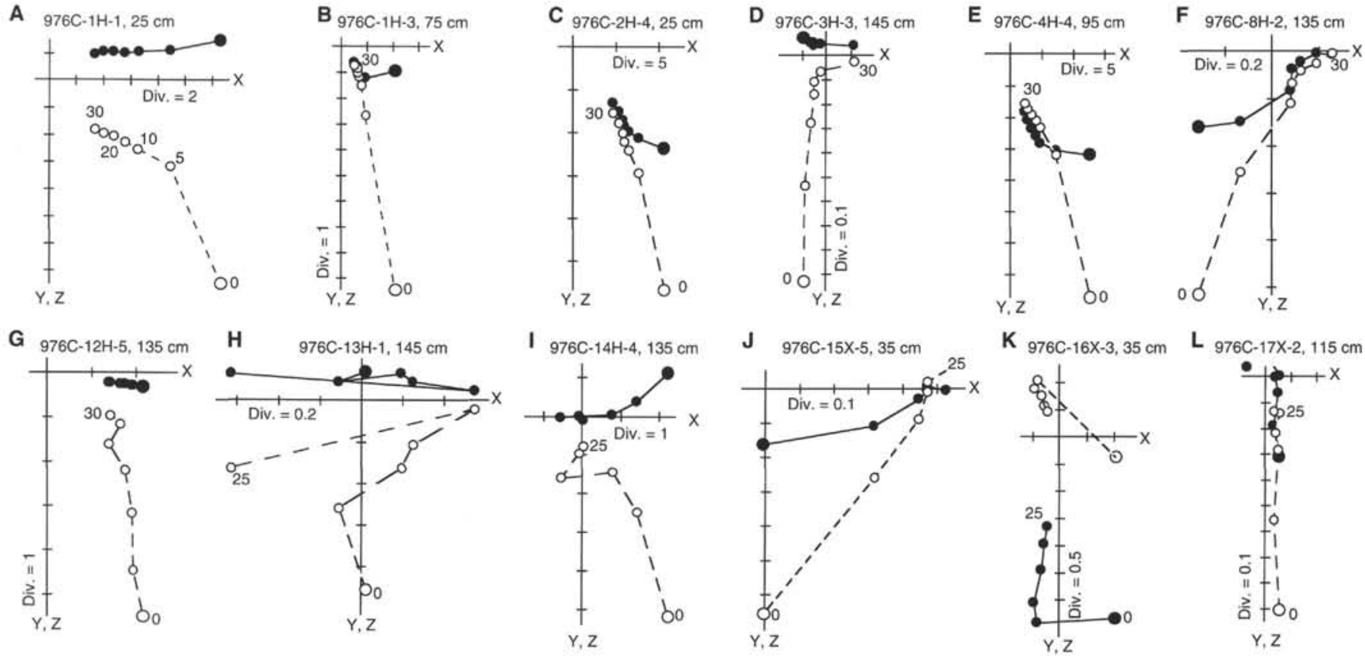

Figure 39. Examples for progressive AF demagnetization of some archive halves from Hole 976C. Open circles give projection of vector end-point on vertical plane, solid circles are on the horizontal plane. Unit for division (Div.) is mA/m. **A–L** are described in text.

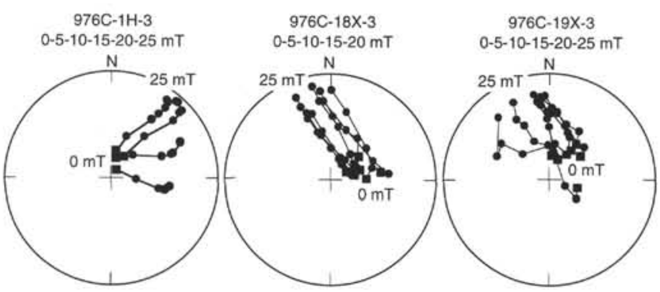

Figure 40. Progressive AF demagnetization results for various depths within three archive sections. Vector trajectories are along great circles on an equal-area projection. These originate from a downward vertical direction (solid squares) and then diverge.

intervals of breccia and clay-rich gouge that mark zones of brittle faulting. The recovered basement rocks were on the whole remarkably fresh and free of alteration, except in intervals of few centimeters associated with faulting and within about 1 m of the sediment/basement contact, where minerals such as plagioclase are partly altered to clay.

Like most high-grade metamorphic rocks, the basement rocks encountered at Site 976 have a prolonged and complicated history of deformation and metamorphism and are extremely rich in information. In order to present the information as clearly as possible, we have written this section using the following structure. The nature of the basement/sediment contact is discussed first. We then briefly summarize the sequence of rock types encountered in the two holes from the top down. This is followed by a more detailed description of the rock types, concentrating on those aspects that distinguish them from one another. The fabrics and textures in the rocks are then presented within the framework of the deformational history. The rock fabrics and textures provide the essential basis for analyzing the metamorphic evolution, presented in the next section. We conclude with a brief discussion of the significance of the basement rocks, and, in particular, their remarkable metamorphic history, in the context of the Alboran Sea and the surrounding mountain ranges.

The Basement-Sediment Contact

The contact between the basement and the overlying Miocene sediments apparently is sharp in both holes. In Hole 976B a possible pebble of granite lay above the schist (Core 976B-73R-1, Piece 2), overlain in turn by a poorly sorted coarse-grained immature pebble-sandstone interval with abundant detritus derived from basement lithotypes (Section 976B-73R-1, Piece 1). This sandy interval is the base of Unit IV of the Miocene–Pleistocene sequence, dated as Serravallian (see "Biostratigraphy" section, this chapter). In Hole 976E, three fragments (two of marble and one of granite) were recovered from the contact zone (Section 976E-13R-2, Pieces 1 to 3). The uppermost of these three fragments is certainly a pebble, and it has indentations filled with foraminiferal limestone and clay. This is overlain by Serravallian silty sandstone (attributed to Unit IV), which contains several small pebbles at the base. The other two fragments may be pebbles, or they may be "rollers" induced by drilling. Undoubted basement starts in Section 976E-13R-3, Piece 1.

The lowest 20 m of the Miocene sedimentary sequence in Hole 976E (Cores 976E-11R, 12R, and 13R, 630 to 652 mbsf) exhibit a diffuse disjunctive cleavage with variable orientation (Fig. 53). This core interval also contains a number of minor faults dipping 40°–70° with a left-lateral strike-slip or transtensional shear sense, based on steps in the striations. Some of these faults (for example in Section 976E-13R-2) with undeformed striations cut and deflect the cleavage, indicating that it is not a drilling-induced artifact. The cleavage locally cuts bedding obliquely, suggesting that it is a tectonic fabric rather than one induced by compaction. This disjunctive cleavage does not occur in the recovered Miocene sediments in Hole 976B. The remainder of the late Miocene–Pleistocene sequence shows little evidence of deformation. Dips are close to horizontal, apart from moderate inclinations (5°–30°) in Cores 976B-32X, 33X, 58X, and 63X.

Within the limits of the evidence available, it appears that the basement-sediment contacts at the two holes represent deposition of

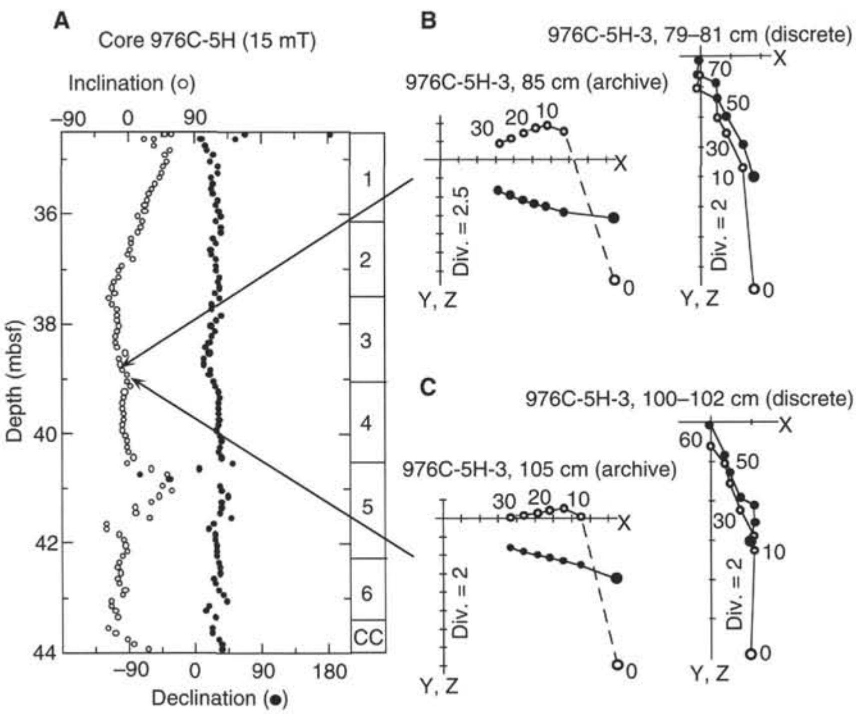

Figure 41. Apparent reversal in Core 976C-5H. **A.** Inclination (open circles) and declination (solid circles) after AF demagnetization at 15 mT. Shallow inclination interval is revealed below Section 976C-5H-2. **B, C.** Progressive demagnetization of archive halves and corresponding discrete samples for two depth intervals within the apparent reversal.

a marine clastic sequence directly on basement rock. The nature of the contact is complicated, however, by the presence of breccias with a calcareous or dolomitic matrix containing microfossils of Miocene age (see "Biostratigraphy" section, this chapter) down to 40 m below the contact (705 mbsf in Hole 976B and 695 mbsf in Hole 976E). These breccias are described in more detail later in this section. A possible explanation for this phenomenon is that the basement was fissured along active faults to a depth of several tens of meters, and sediment deposited on the contact settled down into the fissures to mix with the fault breccia.

There is a significant difference in depth to the basement-sediment contact between Holes 976B and 976E, which were approximately 20 m apart. The difference in depth is uncertain, because the true depth in each hole could be up to 5–6 m greater than the depths given above, given the low recovery. The difference is at least 11 m, however, and indicates that the top of the basement shows considerable relief (Fig. 54). This is also clearly visible in seismic profiles across the site (see "Underway Geophysics" chapter). The basement relief at the sites may well have been created by the faulting that produced the breccia-filled fissures. The lack of significant deformation in all but the Serravallian section of the overlying Miocene–Pleistocene sediment column, however, suggests that faulting at Site 976 itself is likely to have ceased by late Miocene time, although it may have continued on the margins of the basement high (see "Underway Geophysics" chapter).

Summary of the Cored Basement Section

The vertical distribution of rock-types in the two holes is summarized in Figures 51 and 52, and the distribution of dips of layering and the main foliation are summarized in Figures 55 and 56. A more detailed description of the various rock types is given below, and descriptions and drawings of the individual pieces of core are printed in the visual-core description section of this volume.

Down to 794 mbsf (Section 976B-93R-1, Piece 2), Hole 976B consists largely of dark-gray quartz-biotite-sillimanite-plagioclase schist with visible porphyroblasts of garnet and andalusite (Fig. 51). We refer to this rock type as high-grade schist. Within this schist interval, there are interlayers of calcite and dolomite marble and associated calc-silicate rock, particularly in Cores 976B-81R and 83R through 85R.

Below 794 mbsf to the bottom of Hole 976B, the predominant rock type is still a high-grade metasedimentary rock with quartz, biotite, and sillimanite, but it has a medium-gray color and a more massive appearance than the schist higher up in the hole. This is in part a result of a higher proportion of plagioclase and K-feldspar and the presence of abundant large porphyroblasts of andalusite and cordierite. We refer to this rock type as "gneiss," and, as discussed later in this section, it also differs from the high-grade schist to some extent in its deformational and metamorphic history. The gneiss is locally migmatitic, with irregular veins and segregations of granitic material, throughout this cored interval. No marble occurs within the gneiss.

Small discrete bodies of leucogranite with quartz, feldspar, plagioclase, and cordierite, which we interpret as dikes, occur throughout the hole, but they are more abundant in the gneiss than in the schist. There are significant occurrences in Cores 976B-81R and 82R in the schist, and in Cores 976B-93R and 97R through 107R in the gneiss.

Zones of breccia and fault gouge, characterized by very low recovery and hence uncertain thickness, occur in most cores throughout Hole 976B. There are particularly thick breccia and fault gouge intervals in Cores 976B-75R, 80R, 86R through 88R, and 105R.

Hole 976E followed a zone of interlayered biotite schist, marble, and calc-silicate rocks almost directly down the dip in Cores 976E-14R through 17R (see Figs. 52, 56). The hole passed into more homogeneous high-grade schist with more moderate dips at 680 mbsf (Section 976E-18R-1), with interlayers of marble in Sections 976E-20R-1 and 22R-1. The only granite bodies encountered in this hole are in Sections 976-13R-2, Piece 2, and 976-13R-2, Pieces 3–5. The gneiss and migmatitic gneiss were not found. Significant zones of breccia occur throughout the hole, particularly in Cores 976E-17R through 20R, and 28R.

There is a significant difference in the proportions and distribution of recovered rock types between Holes 976B and 976E, even though they are only 20 m apart. These differences are largely fortuitous. One difference arises from the fact that Hole 976E terminated at 736.3 mbsf, and hence did not reach the gneiss that was cored below 794 mbsf in Hole 976B. The other difference is that Hole 976E

Table 7. Rock-magnetic parameters for Hole 976B sediments.

Core, section, interval (cm)	Depth	K(SI)	F_d (%)	K_{arm} (SI)	SIRM (mA/m)	$S_{-0.3T}$	K_{arm}/SIRM	K_{arm}/K_f
161-976B-								
1H-1, 29	0.29	2.80E–04	9.67	4.321E–03	2.636E+00	0.96	1.639E–03	0.056
1H-2, 29	5.29	2.83E–04	11.18	6.634E–03	3.355E+00	0.96	1.977E–03	0.037
2H-3, 33	6.83	1.77E–04	4.77	3.899E–03	2.260E+00	0.96	1.725E–03	0.035
2H-5, 33	9.83	1.60E–04	8.42	4.277E–03	2.168E+00	0.95	1.972E–03	0.028
3H-2, 34	14.41	1.14E–04	0.84	2.131E–04	5.757E–01	0.90	3.701E–04	0.349
4H-3, 34	25.84	9.43E–05	3.44	1.401E–04	3.796E–01	0.95	3.690E–04	0.388
4H-5, 35	28.85	1.09E–04	6.12	2.711E–04	5.357E–01	0.94	5.061E–04	0.253
5H-3, 115	36.15	2.72E–04	3.26	6.713E–04	3.542E+00	0.99	1.895E–04	0.345
5H-6, 35	39.85	1.89E–04	3.98	6.901E–03	2.863E+00	0.97	2.410E–03	0.022
6H-3, 115	45.65	2.00E–04	3.33	3.421E–04	2.220E+00	0.93	1.541E–04	0.468
6H-4, 33	46.33	2.11E–04	5.88	3.840E–03	2.442E+00	1.00	1.573E–03	0.045
7H-3, 115	55.15	8.00E–05	5.15	7.203E–05	3.771E–01	0.96	1.910E–04	0.556
7H-6, 130	59.80	8.29E–05	5.60	6.493E–05	3.042E–01	0.97	2.134E–04	0.660
8H-3, 115	64.65	6.00E–05	0.00	6.103E–05	4.575E–01	0.99	1.334E–04	0.328
8H-5, 10	66.60	6.86E–05	7.63	5.420E–05	7.664E–02	0.95	7.072E–04	0.528
9H-3, 115	74.15	1.09E–04	4.34	6.403E–05	1.068E–01	0.92	5.996E–04	1.071
9H-6, 60	78.15	4.86E–05	0.73	5.922E–05	7.001E–02	0.92	8.459E–04	0.145
10H-3, 115	83.65	6.86E–05	7.68	4.202E–05	8.063E–02	0.94	5.211E–04	0.680
10H-5, 130	86.85	8.57E–05	2.99	6.025E–05	7.283E–02	0.95	8.274E–04	0.759
11H3, 115	91.77	7.72E–05	8.24	6.303E–05	1.342E–01	0.94	4.696E–04	0.590
12H-3, 115	102.65	7.14E–05	3.21	1.053E–04	2.632E–01	0.98	4.002E–04	0.299
13H-3, 115	112.15	5.14E–05	3.21	6.367E–05	3.741E–02	1.00	1.702E–03	0.180
14H-3, 115	120.39	8.86E–05	11.64	1.038E–04	1.244E–01	0.94	8.347E–04	0.468
15H-3, 121	131.21	7.14E–05	8.07	7.405E–05	4.640E–02	0.95	1.596E–03	0.425
16X-3, 120	140.70	4.29E–05	16.89	4.002E–05	5.421E–02	0.93	7.382E–04	0.072
17X-3, 120	149.81	6.29E–05	4.08	2.101E–05	6.438E–02	0.94	3.263E–04	1.089
18X-2, 121	158.51	7.14E–05	6.11	3.201E–05	3.696E–02	0.99	8.662E–04	0.982
19X-2, 120	167.82	1.09E–04	15.00	7.303E–05	8.581E–02	0.98	8.511E–04	0.939
20X-2, 120	177.80	6.00E–05	18.00	4.902E–05	5.930E–02	0.94	8.267E–04	0.408
21X-1, 146	186.16	4.57E–05	6.62	5.202E–05	5.412E–02	0.98	9.613E–04	0.110
22X-2, 120	197.10	8.00E–05	1.17	4.502E–05	5.557E–02	0.94	8.101E–04	0.889
23X-2, 119	206.59	9.43E–05	4.98	6.603E–05	1.102E–01	0.94	5.990E–04	0.823
24X-2, 121	216.20	7.72E–05	3.29	3.602E–05	4.204E–02	0.96	8.566E–04	1.032
25X-2, 120	224.61	9.72E–05	6.62	7.803E–05	1.168E–01	0.96	6.682E–04	0.733
26X-2, 122	234.44	1.03E–04	1.27	7.103E–05	9.598E–02	0.96	7.401E–04	0.885
28X-2, 120	253.70	8.29E–05	6.62	5.302E–05	7.846E–02	0.96	6.758E–04	0.809
29X-2, 120	263.30	7.72E–05	6.90	5.502E–05	7.909E–02	0.96	6.957E–04	0.675
30X-2, 120	273.36	1.17E–04	6.80	6.003E–05	1.001E–01	0.93	5.999E–04	1.286
32X-2, 120	292.19	1.26E–04	2.40	6.403E–05	1.098E–01	0.94	5.832E–04	1.339
33X-2, 124	301.77	9.43E–05	3.18	5.602E–05	8.626E–02	0.93	6.494E–04	0.969
34X-2, 123	312.17	8.00E–05	4.04	6.803E–05	1.282E–01	0.96	5.306E–04	0.588
35X-2, 120	321.68	1.06E–04	8.26	5.202E–05	8.536E–02	0.94	6.095E–04	1.264
36X-2, 120	330.48	9.72E–05	0.96	5.803E–05	1.158E–01	0.93	5.012E–04	0.985
37X-2, 123	340.59	9.72E–05	0.00	4.902E–05	1.081E–01	0.93	4.533E–04	1.166
38X-2, 123	350.83	8.29E–05	0.00	4.902E–05	9.680E–02	0.92	5.064E–04	0.875
39X-2, 119	360.39	1.49E–04	6.33	1.791E–04	3.297E–01	0.97	5.431E–04	0.607
47X-2, 120	437.50	1.69E–04	0.41	6.161E–04	8.523E–01	0.96	7.229E–04	0.209
56X-2, 120	520.28	6.86E–05	9.86	5.831E–05	3.087E–02	0.93	1.889E–03	0.490
56X-2, 132	520.40	1.09E–04	7.15	1.438E–04	6.602E–02	0.96	2.178E–03	0.477
56X-2, 137	520.45	9.15E–05	6.91	1.198E–04	4.232E–02	0.97	2.832E–03	0.429
56X-2, 141	520.49	9.72E–05	16.03	1.221E–04	5.330E–02	0.97	2.291E–03	0.468
56X-2, 145	520.53	9.43E–05	8.96	1.070E–04	4.413E–02	0.96	2.426E–03	0.507
57X-2, 125	528.05	1.00E–04	1.73	4.402E–05	3.051E–02	0.94	1.443E–03	1.364
58X-3, 142	538.38	8.29E–05	0.32	4.002E–05	3.986E–02	0.94	1.004E–03	1.072
59X-3, 143	549.03	8.57E–05	5.28	4.102E–05	2.597E–02	0.97	1.579E–03	1.115
60X-3, 127	557.34	6.86E–05	3.88	2.201E–05	1.889E–02	0.94	1.165E–03	1.299
61X-3, 129	567.06	6.57E–05	15.65	2.701E–05	2.098E–02	0.95	1.288E–03	0.953
65X-3, 126	606.66	1.09E–04	0.00	5.192E–05	3.741E–02	0.96	1.388E–03	1.321

Notes: K = low-field susceptibility (SI); F_d = frequency dependence of low-field susceptibility; K_{arm} = susceptibility of anhysteretic remanent magnetization; SIRM = saturated remanence magnetization; $S_{-0.3T}$ = back-field ratio to SIRM; K_f = ferrimagnetic susceptibility.

contains a higher proportion of carbonate rocks (Fig. 52), which arises at least in part because the hole followed a layer of marble down the dip of the layering.

The vertical sequences outlined above and shown in Figures 51 and 52 are the result of a protracted history of intense ductile and brittle deformation. Neither sequence is likely to bear any relationship to the original stratigraphic sequences in the sedimentary protoliths, and, because of the lack of fossils or sedimentary criteria for younging direction, the intense and complicated deformation, and the high grade of metamorphism, it is not possible to reconstruct the original stratigraphy. The lithologic repetitions may be a result of primary repetitions in the sequence, folding, or faulting. Nevertheless, there appears to be a distinct increase of metamorphic grade from the high-grade schist to the gneiss, evidenced most clearly by the occurrence of partial melting in the gneiss.

Lithological Descriptions

For convenience we have divided the core into a number of lithotypes, which are described below and illustrated in the lithologic columns (Figs. 51, 52). We have termed the two most abundant lithotypes "high-grade schist" and "gneiss," both of which are derived by metamorphism from aluminous sediments, and the distinction between the two is not always clear. Some of the high-grade schist is strongly banded, contains abundant plagioclase and some K-feldspar, and it may be massive or gneissic in appearance; some of the gneiss is micaceous and schistose. There appears to be a gradation from one rock type to the other. This, and combined with the fact that the rocks are characteristically heterogeneous on a small scale, caused us some difficulty in assigning individual pieces of core to these two lithotypes in the interval from Core 976B-92R through

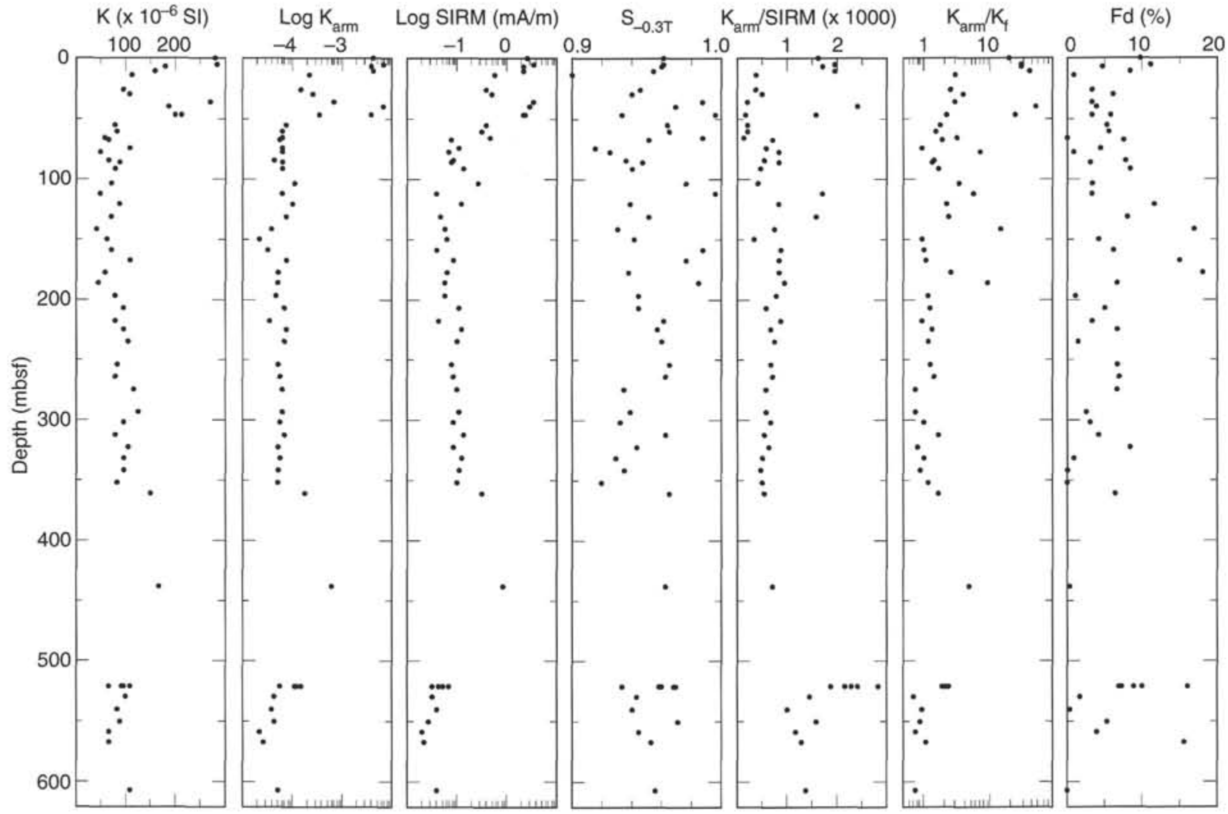

Figure 42. Downhole plot of rock-magnetic parameters. K = low-field magnetic susceptibility, F_d = percent frequency dependence of low-field susceptibility, K_{arm} = anhysteretic remanence susceptibility, SIRM = saturated isothermal remanent magnetization, $S_{-0.3T}$, and K_{arm}/K_f. Ferrimagnetic susceptibility (K_f) is computed assuming a constant clay mineral paramagnetic susceptibility (about 4×10^{-5} SI). For a detailed description of the procedure see "Explanatory Notes" chapter, this volume.

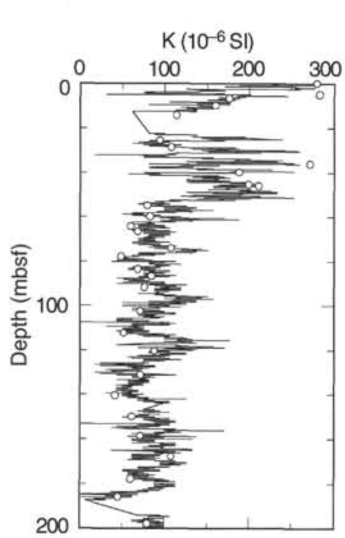

Figure 43. Comparison of MST and discrete sample (open circles) low-field susceptibility.

97R. We have somewhat arbitrarily defined the first occurrence of gneiss (below) at the top of Section 976B-93R-1 Piece 5, and this boundary corresponds approximately to a number of related changes in the deformational and metamorphic history of the rocks and to their physical and chemical properties as recorded by logging data (see "Downhole Logging" section, this chapter).

Lithotype 1: High-Grade Schist

Lithotype 1 forms most of the upper half of Hole 976B, above 794 mbsf, and most of Hole 976E. It consists of dark-gray graphitic schist with visible biotite (0.1–0.5 mm), white sillimanite aggregates (1–2 mm), andalusite porphyroblasts (up to 15 mm) that may be pink but are more commonly dark colored by inclusions of graphite and biotite (Fig. 57), and variable amounts of quartz and plagioclase. Garnet porphyroblasts 1–2 mm across, corroded in appearance, occur in places. Much of the rock has a visible compositional layering defined by laminae rich in quartz, and by varying proportions of the constituent minerals (Fig. 58), and it has a strong schistosity defined by biotite and sillimanite, which is commonly parallel or nearly parallel to the compositional layering. The layering is commonly tightly folded on a small scale. Folded and disrupted quartz veins are abundant, making up to about 10% of the rock volume, and, together with the compositional layering, give the rock a gneissic appearance (Fig. 59). Locally the rock has a more massive appearance, as a result of the presence of layers or patches of poorly oriented aggregates of 0.5–1 mm biotite, plagioclase, and andalusite. The high-grade schist contains numerous interlayers of marble (Lithotype 4) and calc-silicate rock (Lithotype 5), and small bodies (presumably dikes) of granite (Lithotype 6).

Mica Mineralogy of High-Grade Schist

The type of mica in the high-grade schist has been determined by XRD analyses (see "Explanatory Notes" chapter, this volume, for the method). The type of biotite in all the samples analyzed is annite (the iron-rich end-member of the biotite series), with two characteristic

Table 8. Magnetic measurements in hard rock samples.

				AMS Data							Foliation								
											Structural		Magnetic						
Core, section	Top (cm)	Depth (mbsf)	K_m	D_K_1	I_K_1	D_K_3	I_K_3	L	F	P	Dip	Az	Dip	Az	NRM (A/m)	D/I	K_{arm} (10^{-6} SI)	IRM (A/m)	$S_{-0.3T}$
161-976B-																			
74X-1	42	675	245	300	29	78	53	1.009	1.140	1.151	40	270	258	37	1.66E–04	64/–6	22.1	1.77E–02	0.72
75R-2	88	679	419	240	41	64	49	1.017	1.048	1.066	20	270	244	41	6.99E–04	349/–74	57.6	1.63E–01	0.93
76R-1	12	681	1047	296	20	136	69	1.078	1.369	1.476	25	90	316	21	1.73E–01	270/–60	4470.1	1.76E+01	1.00
76R-2	72	683	680	240	41	64	49	1.191	1.311	1.562	32	265	244	41	8.00E–03	109/–37	5619.6	2.51E+01	0.99
77R-2	78	686	270	277	25	91	64	1.010	1.222	1.235	37	270	271	26	6.64E–04	65/36	26.5	4.01E–02	0.99
77R-3	81	688	340	95	32	271	58	1.052	1.289	1.356	35	90	91	32	4.29E–02	40/–36	892.4	4.43E+00	0.98
78R-2	64	690	268	313	3	90	86	1.040	1.143	1.188	20	270	270	4	1.97E–04	87/–32	18.1	3.90E–02	0.99
79R-1	94	699	299	355	4	91	61	1.026	1.131	1.161	27	270	271	29	7.05E–04	346/–48	26.5	8.51E–02	0.98
80R-1	27	703	284	201	4	300	64	1.037	1.154	1.197	20	260	120	26	3.73E–04	158/–22	29.7	1.14E–01	0.55
81R-1	89	708	343	246	26	75	63	1.046	1.181	1.235	30	270	255	27	1.17E–03	333/–69	31.0	1.94E–01	0.97
82R-2	68	719	295	174	9	274	50	1.027	1.148	1.179	56	90	94	40	4.84E–04	38/30	71.4	3.12E–01	0.98
83R-2	70	729	278	155	55	258	9	1.009	1.148	1.158	88	90	78	81	2.71E–02	264/1	27.9	9.75E–02	0.87
84R-1	15	737	438	152	13	244	5	1.015	1.086	1.102	81	90	64	85	2.18E–02	16/89	21.4	3.90E–02	0.96
91R-1	60	775	287	261	35	73	55	1.029	1.111	1.142	25	270	253	35	2.13E–02	267/1	22.1	3.58E–02	0.98
95R-2	50	815	504	22	25	248	56	1.020	1.121	1.144	35	40	68	34	2.76E–02	90/8	730.3	5.73E–01	0.85
96R-2	8	824	20010	111	21	262	66	1.036	1.288	1.334	26	90	82	24	1.75E+00	81/10	559.5	4.87E+01	0.83
97R-1	85	833	16710	177	2	80	72	1.139	1.366	1.556	22	270	260	18	6.42E–01	168/41	547.7	3.10E+01	0.85
101R-2	35	873	3084	200	6	98	63	1.067	1.450	1.547	20	120	278	27	5.71E–01	317/16	1320.3	1.18E+01	0.75
102R-1	77	881	290	291	7	169	77	1.017	1.136	1.156	20	310	349	13	1.30E–01	48/–27	39.2	9.55E–01	1.0

Notes: Km = mean susceptibility (10^{-6} SI); D_K_1 (I_K_1) = declination (inclination) of the maximum axis of susceptibility; D_K_3 (I_K_3) = declination (inclination) of the minimum axis of susceptibility; $L = K_1/K_2$; $F = K_2/K_3$; $P = K_1/K_3$; Dip and Az = dip and azimuth of the structural and magnetic foliation; NRM D/I = intensity and declination/inclination of NRM; K_{arm} = anhysteretic remanence susceptibility. IRM = isothermal remanent magnetization acquired at 1 T.

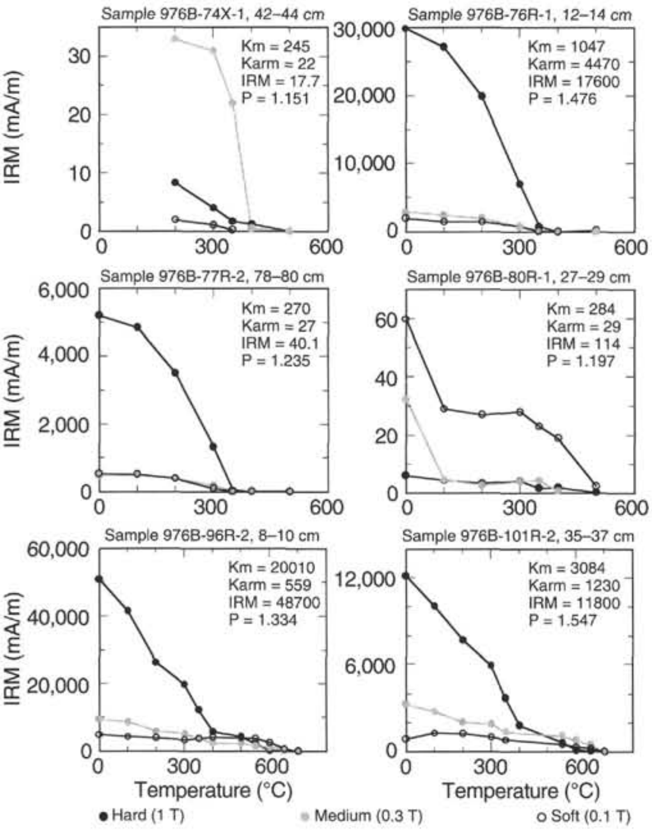

Figure 44. Thermal demagnetization of IRM imparted along X (1 T), Y (0.3 T), and Z (0.1 T) axes. Also indicated are K_m (10^{-6} SI), K_{arm} (10^{-6} SI), IRM (mA/m), and $P = K_1/K_3$.

diffractions at 8.79° and 26.5° (Fig. 60). Some quartz veins have scattered concentrations of a pale-green sheet silicate that is a mixture (possibly interlayered) between chlorite (clinochlore-ripidolite) and muscovite (illite 1M) (Fig. 61). We interpret these phases to be retrogressive.

Lithotype 2: Gneiss

Lithotype 2 has only been identified in the lower half of Hole 976B, below 794 mbsf. It consists of medium-gray felsic gneiss, commonly with visible biotite, feldspar, sillimanite, andalusite porphyroblasts up to 1 cm crowded with inclusions, inky blue or blue-green cordierite porphyroblasts up to 1 cm, and locally some muscovite. The foliation is defined by lenticles a few millimeters long of felsic material, as well as by mineral orientation, compositional layering, and abundant quartz-tourmaline veins. Irregular patches a few millimeters in size of granular felsic material are present in places. Locally the gneiss grades with increasing biotite content into high-grade schist (Lithotype 1), and with increasing felsic component into migmatitic gneiss (Lithotype 3). The transition between the schist and the gneiss in Sections 976B-92R-1 to 93R-1 is obscured by several faults, by granite dikes, and by poor recovery.

Lithotype 3: Migmatitic Gneiss

Lithotype 3 has only been identified in Hole 976B, as interlayers in Lithotype 2 below 794 mbsf. It consists of medium-gray felsic biotite-cordierite-sillimanite-andalusite-gneiss with irregular veins and segregations a few centimeters in size of light-gray, weakly foliated or unfoliated granite with biotite and tourmaline. The granitic material (leucosome) occurs as irregular veins or segregations parallel to the foliation (e.g., intervals 976B-95R-2, 0–41 cm and 89–94 cm), cutting across the foliation (Fig. 62), in extensional fractures, in the necks of boudins (e.g., interval 976B-95R-2, 45–83 cm), or it may form a network of veins giving the rock a brecciated appearance (e.g., interval 976B-95R-3, 53–63 cm). Quartz-tourmaline veins are commonly associated with the leucosome (e.g., interval 976B-97R-2, 78–83 cm). In places the leucosome contains cordierite.

Lithotype 4: Marble

Lithotype 4 consists of very pale green, gray, white, or yellow crystalline dolomite marble (predominantly in Hole 976B) and calcite marble (predominantly in Hole 976E), with minor amounts of phlogopite, chlorite, and ankerite (ankerite was determined by XRD analysis). Marble occurs as layers within the high-grade schist, and the dolomitic marble in particular is commonly associated with zones of brecciation and faulting. The calcite marble near the top of the basement in Hole 976E is interlayered on a small scale with calc-silicate rock (Lithotype 5, see below) and high-grade schist (Lithotype 1). It has a disrupted appearance due to the mechanical contrast between the marble and the schist during deformation (Fig. 63).

Lithotype 5: Calc-Silicate Rock

Lithotype 5 consists of banded but non-schistose white to green rocks with thin layers of calcite or dolomite, garnet, diopside, calcic amphibole, plagioclase, scapolite, and sphene. It commonly occurs as finely banded reaction zones between marble and schist (Fig. 64). It is particularly abundant in Hole 976E (Fig. 52).

Mineralogy of Calc-Silicate Rocks

The calc-silicate rocks present particular difficulties for the optical identification of the minerals, and they have commonly been affected by relatively low-temperature alteration of the primary minerals to a mixture of fine-grained alteration products. Several XRD determinations have therefore been made. Minerals identified by this method include calcite and minor amounts of other carbonate minerals (ankerite and Ca- and Mg-kutnohorites, a carbonate mineral with Ca, Mn, and Mg), clinopyroxene (belonging to the diopside-hedenbergite compositional series), plagioclase, orthoclase, Mn-rich garnet (e.g., interval 976B-75R-1, 105–107 cm), quartz, and amphibole. Different types of amphiboles have been determined by XRD, such as actinolite (interval 976B-75R-1, 105–107 cm) and Fe-gedrite (interval 976E-20R-2, 75 cm). Along the contacts between calc-silicate rock and high-grade schist or marble bands (e.g., interval 976E-15R-1, 53–57 cm), thin dark-green bands (2 mm or less in thickness) contain montmorillonite (with a basal spacing of 14Å) and gismondine (a Ca-rich zeolite of the phillipsite series). These are retrogressive minerals produced by the breakdown of pyroxene, plagioclase, and amphibole. Other minerals present in minor amounts are epidote (clinozoisite), sphene, and apatite.

Lithotype 6: Granite

Small bodies of light gray to almost white, fine-grained hypidiomorphic granular leucogranite occur scattered throughout the sequence, probably in the form of dikes (textural terms for igneous rocks are explained in the "Explanatory Notes" chapter, this volume). We have not seen any contact preserved between the granite and other rock-types. The granite has a grain size of 1–1.5 mm, and small amounts of biotite, tourmaline (Fig. 65), and scarce cordierite and andalusite.

Bulk Chemistry of Granitic Rocks

Whole-rock chemistry of several pieces of granite obtained from XRF analyses (Table 11) reveals a fairly constant composition in the

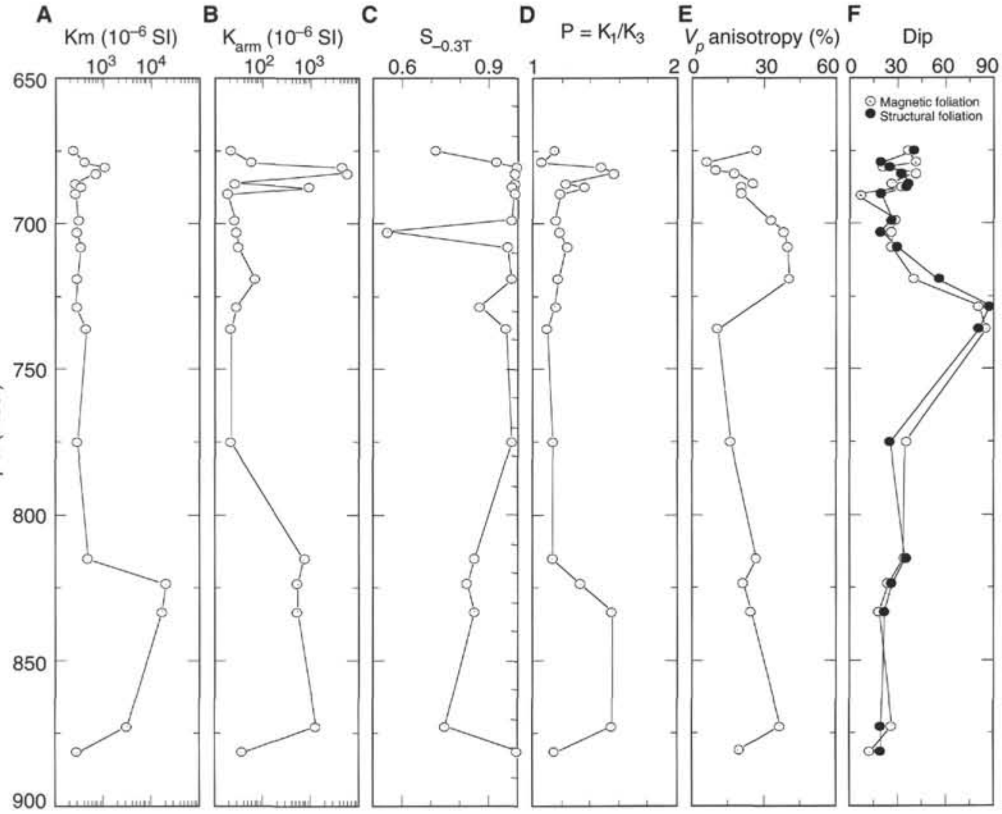

Figure 45. Magnetic mineralogy and magnetic fabric of hard-rock samples in Hole 976B. **A.** Mean susceptibility ($K_1 + K_2 + K_3$)/3. **B.** Anhysteretic remanence susceptibility. **C.** $S_{-0.3T}$ parameter. **D.** Degree of anisotropy. **E.** % velocity anisotropy (see "Physical Properties" section, this chapter) **F.** Comparison between magnetic foliation (open circles) and structural magnetic foliation (solid circles).

field of granite and alkali-granite (Fig. 66), with high silica values (Si_2O_3 between 73.5–76.5 wt%), and moderate alumina (Al_2O_3 near 14–15 wt%). Alkali content in the granite samples is always high, with $Na_2O + K_2O$ values higher than 6 wt% (6.5–7.8 wt%), and, in a sample from the Hole 976E (976E-13R-3, Piece 3), higher than 9 wt% (9.1–9.3 wt%). A moderate content of CaO (0.8–1.4 wt%) with respect to K_2O (4.9–7.6 wt%) is compatible with the observed high modal content in potassium feldspar with respect to plagioclase. Total iron content (expressed as Fe_2O_3) is variable but is always higher than magnesium, with values of 0.7–1.7 wt% and 0.1–0.4 wt%, respectively.

In the specimens analyzed the amount of LOI (loss on ignition) increases in those rocks with a large amount of tourmaline as an accessory phase. The minor elements Ba, Rb, and Sr are present in amounts higher than 100 ppm, with values of 180–790 ppm, 200–280 ppm, and 70–220 ppm, respectively. Other minor elements detected are Zr (40–110 ppm), Y (19–58 ppm), and Zn (up to 14 ppm).

Lithotype 7: Breccia

Lithotype 7 consists of breccias made of angular fragments ranging in size from <0.1–20 mm of high-grade schist, gneiss, marble, granite, or vein quartz in a fine-grained matrix. The clasts and matrix in individual breccia zones commonly show little variation (Fig. 67) and closely resemble adjacent basement lithotypes (Fig. 68).

Three sub-types of breccia can be distinguished by the nature of the clasts and matrix, although they grade into one another: (1) dark-gray brown breccia in which most of the clasts consist of high-grade schist with abundant biotite, and the matrix appears to be composed largely of biotite and sub-millimeter schist fragments; (2) white, pale yellow, or yellowish brown or red indurated breccia composed largely or wholly of dolomite or calcite marble clasts in a carbonate matrix; and (3) breccia in which, independently of clast type, the matrix is composed of carbonate minerals, and there is evidence for the involvement of sedimentary material and processes. This last type is discussed in more detail later in this section.

Lithotype 8: Fault Gouge

Fault gouge, like breccia, consists of angular fragments of basement lithotypes, but is distinguished by having a soft clay-rich matrix. Some zones of fault gouge are associated with breccia, and there is a gradation between the two types of fault rock, with higher clast/matrix ratio and induration in the breccia. The overall color of the fault gouge depends to some extent on the clast type, but is commonly pale gray. The clasts and matrix in individual gouge zones vary little in type, and resemble adjacent coherent rocks closely, except that they are usually partly altered to clay. Zones of fault gouge are commonly flanked by alteration zones up to 10 cm wide (recovered thickness), in which the country rock is heavily altered to pale gray clay. Most gouge zones contain discrete slip surfaces that are striated or have thin films of fiber-lineated calcite. Some of the more coherent gouge contains a cataclastic foliation (e.g., intervals 976B-86R-2, 79–86 cm; 976B-83R-2, 42–49 cm). The faulting is described in more detail in the next section.

Clay Mineralogy of Fault Gouge and Breccia

Using XRD determinations of selected samples, we have determined the bulk mineralogical composition of breccias with and with-

Table 9. Composite depth table for Holes 976A, 976B, 976C, and 976D.

Core	Depth (mbsf)	Offset (m)	Depth (mcd)	Comment
161-976A-				
1H	0.00	0.00	0.00	
161-976B-				
1H	0.00	0.00	0.00	
2H	3.50	0.35	3.85	
3H	13.00	0.35	13.35	No recovery
4H	22.50	0.18	22.68	
5H	32.00	0.00	32.00	
6H	41.50	0.10	41.60	
7H	51.00	0.18	51.18	
8H	60.50	0.78	61.28	
9H	70.00	1.01	71.01	
10H	79.50	1.32	80.82	
11H	89.00	1.68	90.68	
12H	98.50	3.10	101.60	
13H	108.00	4.00	112.00	
14H	117.50	4.14	121.64	
15X	127.00	4.20	131.20	
16X	136.50	3.66	140.16	
17X	146.20	3.66	149.86	
18X	155.80	3.66	159.46	
19X	165.40	3.81	169.21	
20X	175.10	2.97	178.07	
21X	184.70	2.97	187.67	1
22X	194.40	2.97	197.37	1
23X	203.90	6.25	210.15	Poor recovery
24X	213.50	2.97	216.47	1
25X	223.10	2.72	225.82	
26X	232.70	2.72	235.42	1
27X	242.40	2.72	245.12	No recovery
28X	252.10	2.72	254.82	1
29X	261.80	2.72	264.52	1
30X	271.30	3.25	274.55	
31X	280.90	3.25	284.15	No recovery
32X	290.60	−0.75	289.85	
33X	300.10	2.11	302.21	
34X	309.70	2.69	312.39	
35X	319.30	1.87	321.17	
36X	328.90	1.58	330.48	
37X	338.50	1.76	340.26	
38X	348.10	0.00	348.10	
39X	357.70	5.47	363.17	
40X	367.40	5.47	372.87	1
161-976C-				
1H	0.00	0.00	0.00	
2H	6.00	0.23	6.23	
3H	15.50	0.00	15.50	
4H	25.00	0.00	25.00	
5H	34.50	−0.10	34.40	
6H	44.00	0.63	44.63	
7H	53.50	0.36	53.86	
8H	63.00	0.86	63.86	
9H	72.50	1.32	73.82	
10H	82.00	1.19	83.19	
11H	91.50	2.00	93.50	
12H	101.00	3.78	104.78	
13H	110.50	4.09	114.59	
14H	120.00	3.95	123.95	
15X	129.50	5.15	134.65	
16X	139.20	3.57	142.77	
17X	148.80	4.51	153.31	
18X	158.50	3.84	162.34	
19X	168.10	5.41	173.51	
20X	177.80	4.61	182.41	
21X	187.40	4.61	192.01	No recovery
22X	197.10	5.95	203.05	
23X	206.60	6.09	212.69	
24X	216.20	6.14	222.34	
25X	225.80	6.41	232.21	
26X	235.40	3.83	239.23	
27X	245.10	3.83	248.93	1
28X	254.80	3.83	258.63	1
29X	264.40	3.83	268.23	1
30X	274.00	3.83	277.83	No recovery
31X	283.60	3.83	287.43	1
32X	293.20	3.60	296.80	
33X	302.70	3.77	306.47	
34X	312.30	3.77	316.07	1
35X	321.90	3.77	325.67	1
36X	331.60	3.12	334.72	
37X	341.10	4.99	346.09	
38X	350.80	4.99	355.79	1
39X	360.40	3.74	364.14	
40X	370.10	3.74	373.84	1
161-976D-				
1H	0.00	0.00	0.00	
2H	1.50	0.00	1.50	
3H	11.00	0.19	11.19	
4H	20.50	0.00	20.50	

Notes: 1 = offset carried from core above due to poor overlap. Adding offset to meters below seafloor (mbsf) within each core will produce meters composite depth (mcd). This table is also on the CD-ROM, back pocket, this volume.

out a sedimentary matrix, fault gouges, and altered schist fragments within the breccias. Basement samples near the basement-sediment contact in Hole 976E (e.g., Sample 976E-13R-3, 58–60 cm) were selected to study the alteration products in the basement rocks during faulting.

The composition of the matrix in the breccias is influenced by the type of fragments. Where the breccia has numerous fragments of high-grade schist and gneiss, annite and quartz are major components in the matrix (Fig. 69). Minor phases include illite, kaolinite, montmorillonite, and unspecified clay minerals. Using the three types of breccia described macroscopically, the mineralogy of the matrix is as follows. In the first group, represented by dark-gray breccias with schist clasts, the matrix includes dolomite and/or ankerite, annite and quartz, and calcite and siderite are absent (Fig. 70). In the second group, consisting of yellowish brown and pale yellow breccias with marble clasts, the matrix is composed of calcite, ankerite, and siderite, with variable amounts of clay minerals and quartz (Fig. 71).

The fault gouges are composed of kaolinite, interlayered clay minerals, quartz, ankerite, chlorite, smectite, and variable amounts of annite (only when high-grade schist or gneiss are in the fault zone; Fig. 72), minor siderite and kutnohorite (a carbonate mineral with Ca, Mn, and Mg), and, exceptionally, dolomite in subordinate amounts (Fig. 73). Calcite is absent.

The alteration products of high-grade schist close to the basement-sediment contact and to breccia zones are illite, kaolinite, minor siderite, ankerite, and dolomite (e.g., interval 976B-80R-1, 111–116 cm). In one calcite marble there is clear evidence of alteration to a groundmass of smectite and minor chlorite next to the basement-sediment contact (Fig. 74).

Structure

The basement cores show evidence of penetrative ductile deformation that produced a suite of fabrics and small-scale structures, followed by extensive brittle fracturing. The evidence from the cores is insufficient to establish the existence or geometry of large-scale structures, but the type of ductile deformation displayed by these rocks is normally associated with large-scale isoclinal folding and/or ductile shear that may duplicate or excise parts of the original stratigraphic sequence. The brittle faulting is also sufficiently intense that it is unlikely that the sequence of rock types observed in the two holes bears much resemblance to the structural sequence established by the folding and ductile deformation, and the original metamorphic zonation is also likely to have been modified or disrupted.

Ductile Deformational Structures

With the exception of the leucogranite dikes and the granitic leucosomes, all the basement rock types show a well-developed foliation. The variation in attitude of this foliation in Holes 976B and 976E is illustrated in Figure 75. In detail, the most prominent foliation visible in the core changes character according to rock type and is not necessarily always of the same age. Open to tight folds are also commonly visible in both the core and in thin-section; these fold a

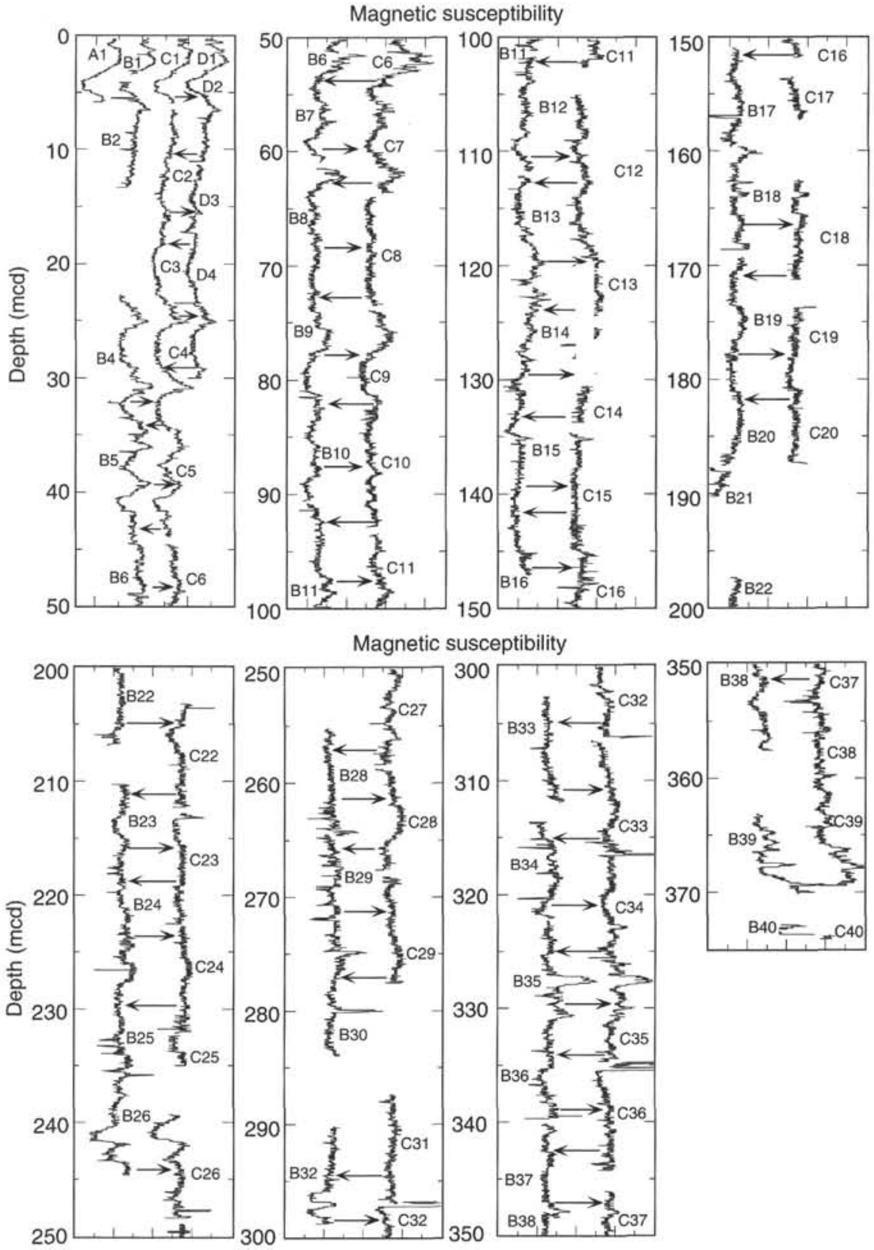

Figure 46. Magnetic susceptibility data for Holes 976A, 976B, 976C, and 976D plotted vs. meters composite depth with tie lines used to construct composite depth section. Some of the poor agreement is due to gas disturbance in the core (see Fig. 48).

pre-existing foliation, but in places appear to be intrafolial with respect to the overall attitude of the foliation seen in the core. Based on both the core descriptions and thin-section petrography, we have distinguished three discrete sets of fabrics and structures. For the purposes of structural analysis, we treat these three sets as representing three deformational events, referred to as D1, D2, and D3, in order of decreasing age. (D3 structures are only recognized in the gneiss.) The foliations formed during these deformations are referred to as S1, S2, and S3; and the lineations as L1, L2, and L3. Because many of the metamorphic minerals have grown between these deformational events, we also distinguish additional time periods: inter-D1/D2 and post-D2 in the high-grade schist, and retro (referring to the growth of late-stage retrogressive minerals) in both the high-grade schist and the gneiss. These time periods, and the minerals that we infer grew during them, are shown separately for the high-grade schist and the gneiss in Figure 75.

First Deformation and Fabric Set

The first set of fabrics described here is the earliest set that can be systematically recognized in core or in thin section from the high-grade schist. There is evidence that there may have been one or more earlier fabrics in the rocks, however, and may have been earlier phases of deformation than the one we call D1.

The earliest fabric (S1) clearly distinguishable in the high-grade schists is defined by five parallel planar fabric elements. (1) Diffuse compositional banding on a scale of approximately 10 mm is defined by varying proportions of quartz, biotite, sillimanite, and plagioclase (Fig. 58). This layering may correspond to original bedding, which has been transposed and strongly modified by subsequent deformation. (2) Quartz-rich and biotite-rich laminae 0.5–2-mm-thick are developed in the more quartz-rich schists (Figs. 76–78). This is likely to be a differentiated layering developed by deformation and is prob-

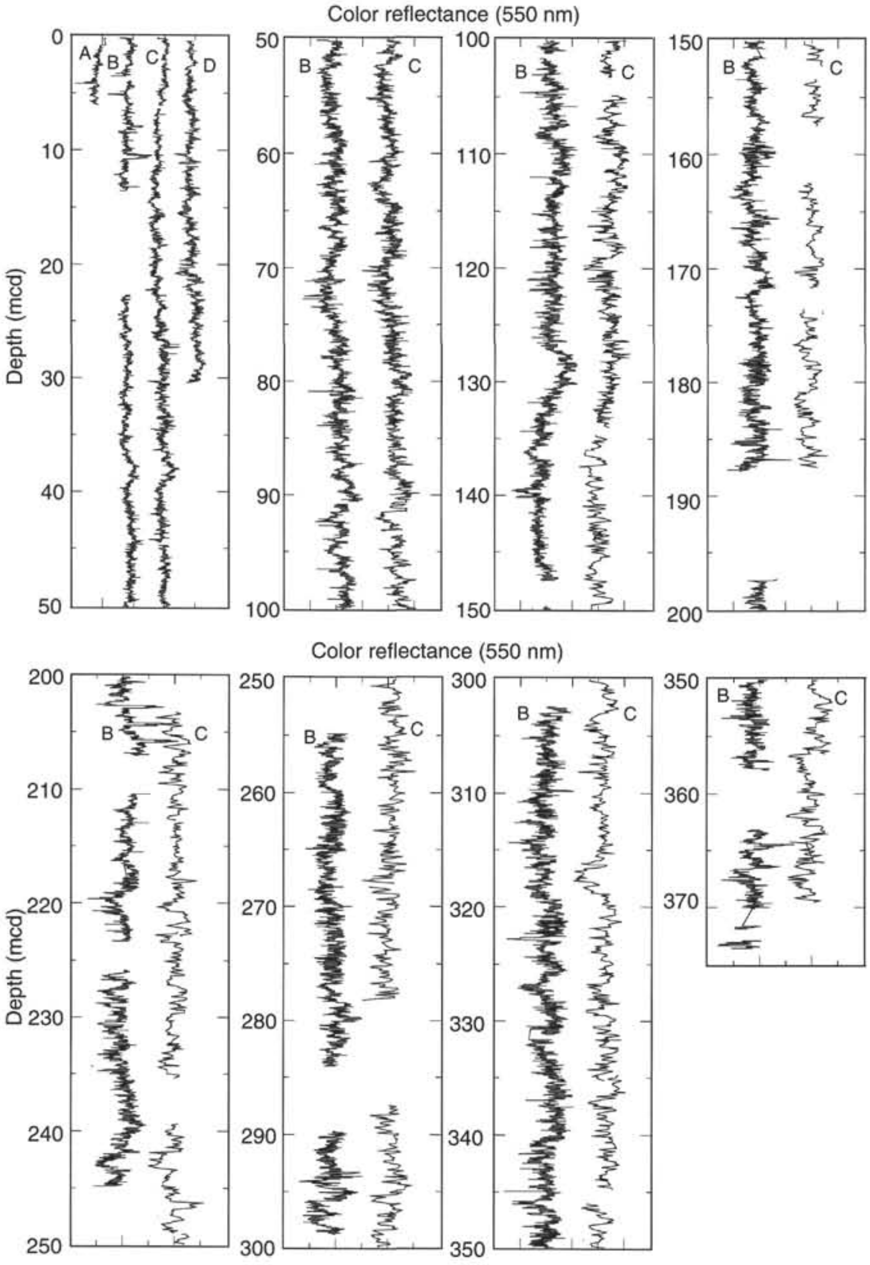

Figure 47. 550 nm-color reflectance for Holes 976A, 976B, 976C, and 976D plotted vs. mcd.

ably an original crenulation cleavage, now transposed beyond recognition. Crenulations defined by inclusion trails in early plagioclase porphyroblasts lend support to this interpretation. (3) There is a preferred orientation of early formed biotite. (4) Elongate porphyroblasts, particularly of plagioclase, have grown mimetically parallel to the mica fabric (Fig. 77). (5) Most of the quartz veins in the high-grade schist appear to have formed parallel to S1 or to have been transposed into S1 (Fig. 79).

Isoclinal folds in the compositional layering are visible in places. These may be D1 or earlier structures.

Second Deformation and Fabric Set

S1 in the high-grade schists has been affected by 1–50 mm scale D2 folds. These are commonly tight and asymmetrical (Fig. 76), but may also be symmetrical (Fig. 80). These folds are abundant throughout the core, and are particularly visible where they affect the quartz veins (Fig. 81). The compositional layering and quartz-biotite laminae that define S1 are considerably thickened in the hinges of these folds relative to the limbs, in some cases by a factor of 10 or more. Biotite is recrystallized in the hinges of these folds and tends to lie parallel to the axial surface, as do the elongate mats of fibrolite that form from the biotite, defining a weak planar fabric (S2) (Fig. 81). In places, microfolding of S1 has proceeded to the point that a crenulation cleavage (S2) is developed, particularly in the hinges of D2 folds (Fig. 82). In much of the high-grade schist the second deformation has been so strong that the main foliation is in fact a composite S1/S2 fabric: the early fabric has been transposed and strongly modified by D2 and is nearly parallel to the axial surfaces of the minor folds. It is for this reason that the small-scale D2 folds locally appear to be intrafolial.

Composite S1/S2 foliation surfaces commonly show a mineral lineation L2, defined by oriented biotite and sillimanite. In areas of high D2 strain, asymmetric tails of retrogressive minerals around garnet porphyroblasts, asymmetric boudinage of early quartz veins, and discrete 1–2 cm shear bands (Fig. 59) provide a sense of shear indi-

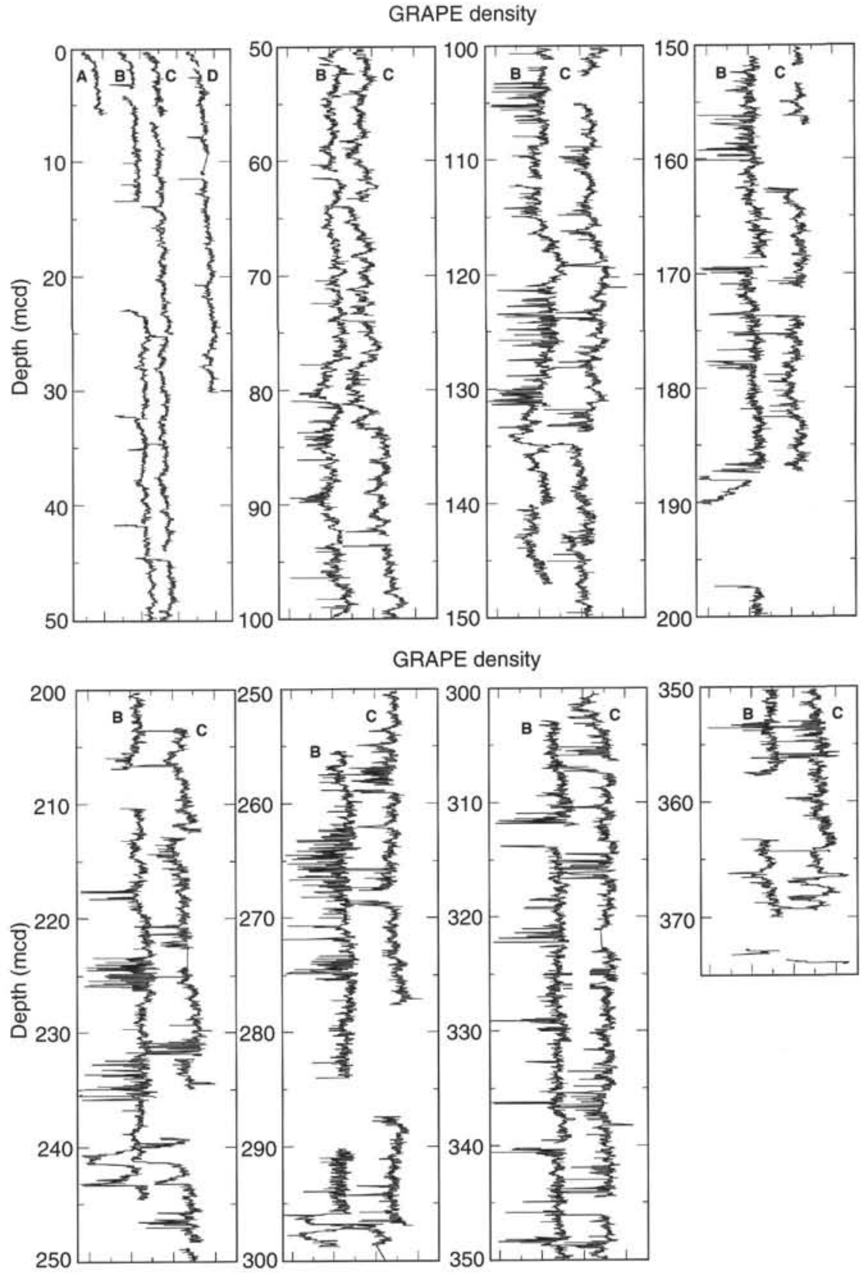

Figure 48. GRAPE density for Holes 976A, 976B, 976C, and 976D plotted vs. mcd. Data over many intervals are adversely affected by the presence of gas in the sediments, lowering bulk density.

cators. Some of the shear bands are delineated by intensely lineated sillimanite fibers that lie parallel to the penetrative mineral lineation L2.

Third Deformation and Fabric Set

There is some evidence for local post-D2 deformation in the high-grade schist, but no systematic set of fabrics and structures is developed. In the gneiss and migmatitic gneiss, however, there is a planar gneissic foliation that we refer to as S3, defined primarily by compositional layering on scales from 1–20 mm. We have not observed a clear transition between the fabrics observed in the high-grade schists and those in the gneisses, and there are significant faults in the boundary zone between these two lithotypes, so that the age of the gneissic foliation is not immediately clear. The relationships between mineral growth and the main foliation in the gneisses are also confusing and in places appear contradictory. In some thin-sections tight to isoclinal microfolds have transposed an earlier fabric, defined by remnant biotite and elongate oxide grains, into the plane of the main foliation. In these cases the foliation appears to be a crenulation cleavage defined by newly crystallized biotite and fibrolitic sillimanite, similar to S2 in the high-grade schist. Andalusite porphyroblasts contain inclusion trails of oxide that define both the earlier fabric and the microfolds, and they include biotite and sillimanite parallel to the crenulation cleavage. These observations suggest that the andalusite crystals postdate the crenulation cleavage (as in the high-grade schist). The andalusites, however, are fragmented, deformed, and partly replaced by plagioclase and muscovite, and the texture has been strongly modified by the growth of feldspar and cordierite. In other rocks, there is a single strong planar foliation: andalusite and plagioclase carry inclusion trails that are parallel to the external fabric; but, together with sillimanite, K-feldspar, and cordierite, they form augen and are fractured and recrystallized to form trails of fragments lying along the foliation. This foliation is locally mylonitic, defined by intensely foliated sillimanite.

We interpret these relations as indicating that the main foliation in the gneisses is a composite fabric, resulting from the superposition of a strong deformation on a crenulation cleavage. In view of the fact

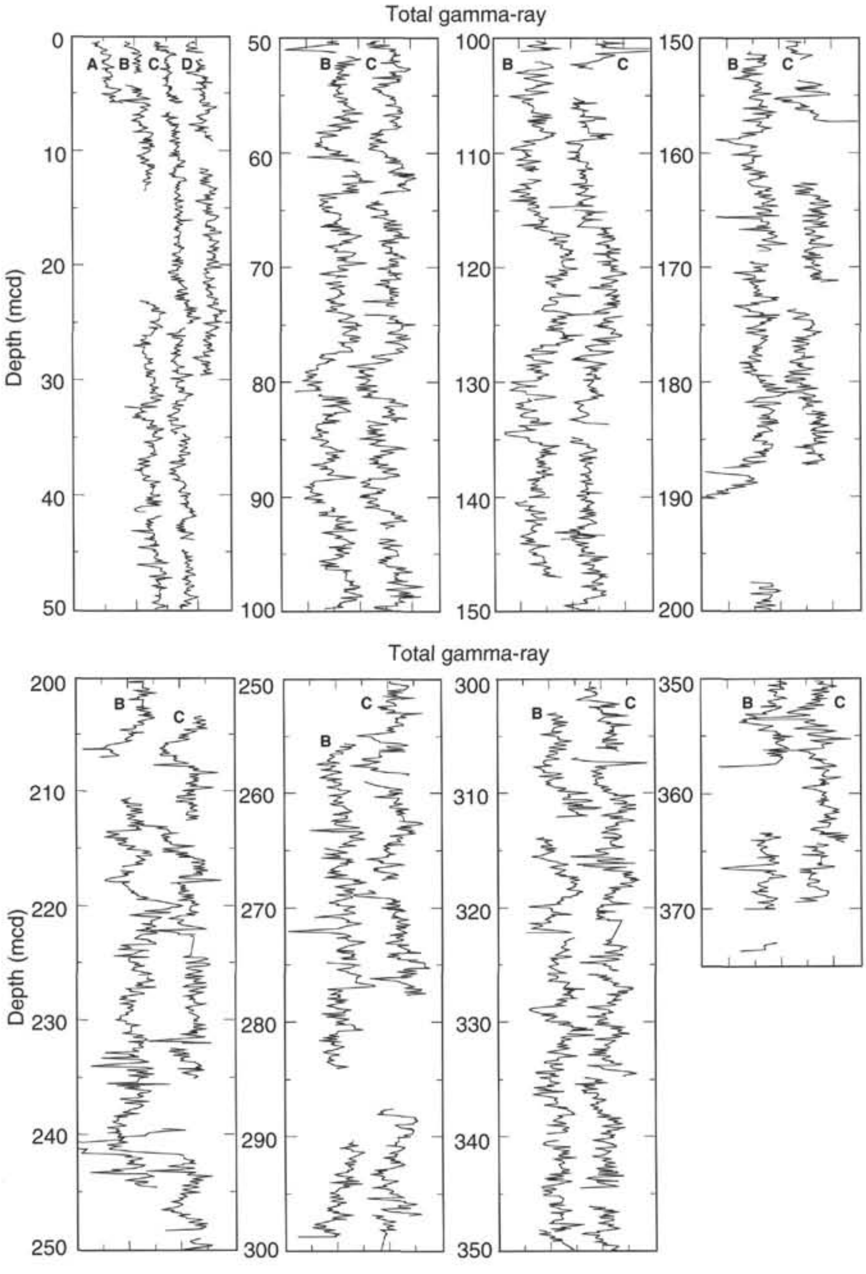

Figure 49. Natural gamma-ray records for Holes 976A, 976B, 976C, and 976D plotted vs. mcd.

that andalusite and sillimanite are late or post-deformational with respect to S2 in the high-grade schist, we suggest that the main foliation in the gneisses should be treated as a separate fabric, S3, and the relict crenulation cleavage correlated with S2 in the high-grade schists.

The foliation planes in the gneisses commonly carry a stretching lineation (L3) defined by elongate aggregates of quartz, feldspar, and (locally) sillimanite. The formation of the granitic leucosome in the migmatitic gneiss, which is largely unfoliated, probably postdates most of the deformational history.

Late Ductile Structures

In both the high-grade schists and the gneisses there are some open folds that appear to fold the main foliation, without being associated with a new axial-planar fabric. These folds probably postdate D3, but are not necessarily all of the same age.

The large changes in the dip of the main foliation shown in Figures 55 and 56 have several causes. Some are probably caused by D2 and D3 folding on a scale of 10 cm and above, but this is difficult to demonstrate in the absence of absolute orientation data. Most of them are probably a result of folding after the high-grade metamorphic peak, and some appear to be associated with zones of brittle faulting. Reconstruction of larger scale structures may be possible when Formation MicroScanner (FMS) or Borehole Televiewer (BHTV) data become available.

Brittle Deformational Structures

Five classes of brittle deformational structures can be distinguished in the basement cores.

1. Quartz veins represent extensional fractures formed under conditions of high fluid pressure; they commonly form when metamorphic reactions release water and silica either by metamorphic reactions or by pressure solution (diffusional mass transfer) during deformation. Early quartz veins in the high-

Table 10. Splice table for Site 976.

Hole, core, section, interval (cm)	Depth (mbsf)	Depth (mcd)		Hole, core, section, interval (cm)	Depth (mbsf)	Depth (mcd)
161-976				161-976		
C-1H-4, 73	5.23	5.23	tie to	D-2H-3, 73	5.23	5.23
D-2H-6, 137	10.37	10.37	tie to	C-2H-3, 115	10.15	10.38
C-2H-7, 7	15.07	15.30	tie to	D-3H-3, 111	15.11	15.30
D-3H-5, 93	17.93	18.12	tie to	C-3H-2, 112	18.12	18.12
C-3H-7, 10	24.60	24.60	tie to	D-4H-3, 109	24.59	24.59
D-4H-6, 117	29.17	29.17	tie to	B-4H-5, 49	28.99	29.17
B-4H-7, 37	31.87	32.05	tie to	C-4H-5, 106	32.06	32.06
C-4H-7, 25	34.25	34.25	tie to	B-5H-2, 76	34.26	34.26
B-5H-5, 133	39.33	39.33	tie to	C-5H-4, 43	39.43	39.33
C-5H-6, 142	43.42	43.32	tie to	B-6H-2, 22	43.22	43.32
B-6H-5, 82	48.32	48.42	tie to	C-6H-3, 80	47.80	48.43
C-6H-6, 148	52.98	53.61	tie to	B-7H-2, 94	53.44	53.62
B-7H-6, 97	59.47	59.65	tie to	C-7H-4, 128	59.28	59.64
C-7H-6, 124	62.24	62.60	tie to	B-8H-1, 130	61.80	62.58
B-8H-5, 106	67.56	68.34	tie to	C-8H-3, 146	67.46	68.32
C-8H-6, 134	71.84	72.70	tie to	B-9H-2, 19	71.69	72.70
B-9H-5, 70	76.75	77.76	tie to	C-9H-3, 94	76.44	77.76
C-9H-6, 70	80.70	82.02	tie to	B-10H-1, 121	80.71	82.03
B-10H-4, 76	84.81	86.13	tie to	C-10H-2, 144	86.44	87.63
C-10H-7, 30	91.99	93.18	tie to	B-11H-3, 19	90.81	92.49
B-11H-7, 61	95.90	97.58	tie to	C-11H-3, 114	95.64	97.64
C-11H-6, 98	99.98	101.98	tie to	B-12H-1, 37	98.87	101.97
B-12H-6, 121	107.21	110.31	tie to	C-12H-4, 108	106.58	110.36
C-12H-6, 30	108.80	112.58	tie to	B-13H-1, 58	108.58	112.58
B-13H-6, 10	115.60	119.60	tie to	C-13H-4, 52	115.52	119.61
C-13H-7, 24	119.74	123.83	tie to	B-14H-3, 46	119.70	123.84
B-14H-7, 19	125.43	129.57	tie to	C-14H-4, 112	125.62	129.57
C-14H-7, 26	129.26	133.21	tie to	B-15X-2, 52	129.02	133.22
B-15X-6, 67	135.17	139.37	tie to	C-15X-4, 20	134.20	139.35
C-15X-5, 118	136.68	141.83	tie to	B-16X-2, 16	138.16	141.82
B-16X-5, 37	142.87	146.53	tie to	C-16X-3, 76	142.96	146.53
C-16X-6, 100	147.70	151.27	tie to	B-17X-2, 49	148.19	151.85
Poor Core 17C recovery; tie Core 17B to Core 18B.						
B-18X-5, 79	162.59	166.25	tie to	C-18X-3, 92	162.42	166.26
C-18X-6, 84	166.84	170.68	tie to	B-19X-2, 25	167.15	170.96
B-19X-6, 118	174.08	177.89	tie to	C-19X-3, 116	172.19	177.60
C-19X-6, 106	176.40	181.81	tie to	B-20X-3, 73	178.83	181.80
No overlap; gap in recovery.						
B-22X-5, 136	201.76	204.73	tie to	C-22X-2, 18	198.78	204.73
C-22X-6, 86	205.28	211.23	tie to	B-23X-1, 109	204.99	211.24
B-23X-4, 97	209.37	215.62	tie to	C-23X-3, 96	209.54	215.63
C-23X-5, 110	212.68	218.77	tie to	B-24X-2, 79	215.79	218.76
B-24X-6, 31	220.62	223.59	tie to	C-24X-2, 96	217.45	223.59
C-24X-6, 114	223.63	229.77	tie to	B-25X-4, 64	227.05	229.77
No overlap; tie Core 25B to Core 26B.						
B-26X-8, 34	241.39	244.11	tie to	C-26X-4, 98	240.29	244.12
No overlap; tie Core 26C to Core 27C.						
C-27X-6, 76	253.26	257.09	tie to	B-28X-3, 37	254.37	257.09
B-28X-6, 13	258.63	261.35	tie to	C-28X-3, 94	257.52	261.35
C-28X-6, 84	261.92	265.75	tie to	B-29X-2, 94	263.04	265.76
B-29X-6, 82	268.56	271.28	tie to	C-29X-3, 90	267.46	271.29
C-29X-7, 86	273.24	277.07	tie to	B-30X-3, 16	273.82	277.07
No overlap; gap in recovery.						
C-31X-6, 44	290.72	294.55	tie to	B-32X-4, 130	295.29	294.54
B-32X-7, 103	299.37	298.62	tie to	C-32X-2, 136	295.04	298.64
C-32X-7, 26	301.40	305.00	tie to	B-33X-3, 88	302.91	305.02
B-33X-7, 73	308.60	310.71	tie to	C-33X-4, 50	306.95	310.72
C-33X-7, 31	311.26	315.03	tie to	B-34X-2, 139	312.33	315.02
B-34X-7, 22	318.49	321.18	tie to	C-34X-5, 5	317.40	321.17
C-34X-7, 91	321.26	325.03	tie to	B-35X-3, 118	323.16	325.03
B-35X-7, 25	328.02	329.89	tie to	C-35X-3, 121	326.11	329.88
C-35X-6, 125	330.53	334.30	tie to	B-36X-4, 46	332.74	334.32
B-36X-7, 79	337.57	339.15	tie to	C-36X-4, 67	336.04	339.16
C-36X-6, 95	339.32	342.44	tie to	B-37X-2, 133	340.69	342.45
B-37X-5, 145	345.31	347.07	tie to	C-37X-2, 21	342.08	347.07
C-37X-6, 21	347.73	352.72	tie to	B-38X-4, 16	352.76	352.71

Notes: Portions of cores from Holes 976B, 976C, and 976D were used to construct a complete section, avoiding gaps, overlaps, and disturbed intervals. Below Cores 976B-16X and 976C-16X several breaks occur in recovery or core overlap. In some cases the spliced record was continued using successive cores from the same hole where there was no recovery in other holes in the same interval. This table is also on the CD-ROM, back pocket, this volume.

grade schists formed during or before D1, and were probably associated with early stages in the prograde metamorphic history.

2. A few quartz veins formed at a late stage in the deformation history, in any event after D2 (Fig. 83). In the example illustrated, the quartz grains have crystal terminations suggesting that they grew into a fluid-filled space towards the center of the vein.
3. Cataclastic breccia (Fig. 68) and clay-rich fault gouge occur at intervals throughout the basement section, marking zones of brittle faulting. Some of these are associated with moderately to gently dipping fault planes. We were not able to determine the sense of displacement on these faults.
4. Several discrete brittle fault planes dipping 60°–90° were encountered in the core. These show stepped calcite fiber lineations pitching between 0°–60° (Figs. 84, 85). The sense of

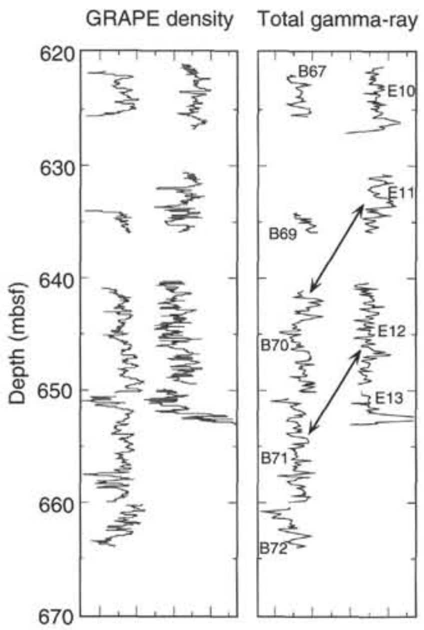

Figure 50. Natural gamma-ray and GRAPE density data from Holes 976B and 976E. Double-ended arrows indicate possible correlations between the cores, although no supporting data in the form of marker beds were available to substantiate the fits, and sediments were deposited on irregular basement topography.

shear determined from these lineations was left-lateral transtension.

5. Some of the breccia zones have a light-colored, carbonate-rich matrix that appears to be sedimentary in origin (Fig. 86). The evidence is, first, the presence of nannofossils of Miocene age in the matrix at depths of up to 40 m below the basement/sediment interface. Occurrences and ages of the nannofossils are as follows (see "Biostratigraphy" section, this chapter): Serravallian-age intervals 976B-75R-1, 1–5 cm, and 16 cm, 976B-75R-2, 22–24 cm, 41–43 cm, and 67–69 cm; Miocene-age intervals 976B-80R-1, 22 cm and 124 cm, and 81R-1, 22 cm (younger than late Aquitanian); and 976E-17R-1, 124 cm, and 20R-2, 48 cm (younger than late Aquitanian). The other line of evidence is the occurrence in one piece of core of roughly horizontal lamination (Fig. 87). The laminated material, and many other occurrences of this type of matrix, appears to be filling in spaces formed by the cracking and fissuring of the rock along fractures or foliation planes. This type of breccia appears to be the result of fissuring that reached the contemporary surface during active faulting in a marine environment.

Textural Relationships

A detailed history of metamorphism and deformation can be inferred from the textural relationships seen in thin section, particularly in the metapelitic rocks. The high-grade schist and the gneiss have somewhat different histories, so they are discussed separately. Figure 75 summarizes our conclusions for the two lithotypes. The observations on which these histories are based are described below.

High-Grade Schist

Biotite and biotite/quartz differentiation bands consistently define the first clearly distinguished foliation (for example in the hinges of D2 folds, Fig. 88), suggesting that biotite was stable during D1. Biotite is also recrystallized and reoriented parallel to the axial planes of D2 folds (Fig. 88), and randomly oriented biotite associated with inclusion-free intermediate plagioclase porphyroblasts have grown statically over the D2 fabric (Fig. 89).

Staurolite forms elongate porphyroblasts that have grown statically over S1 (Fig. 90), and are rotated by D2. There is no evidence for growth of staurolite during or after D2. It is commonly only preserved as corroded crystals enclosed in andalusite or late-stage plagioclase (Fig. 91).

Garnet commonly has inclusion trails suggesting that it grew over S1. The included fabric may be parallel or slightly rotated with respect to the external fabric, and some are slightly rotational (curved inclusion trails suggesting rotation during growth). Many of these grains show corroded outlines, suggesting that garnet became unstable at some point in the metamorphic history. On the other hand, some have an inclusion-poor outer zone suggesting a second stage of growth (Fig. 78). Locally, garnet includes staurolite; we have observed one grain that has grown over D2 crenulations (Fig. 92), and one idiomorphic grain that has inclusions of prismatic sillimanite (Fig. 93). These occurrences are presumably all second-stage garnet.

Plagioclase forms elongate porphyroblasts that have grown statically over S1 and are densely crowded with fine graphite inclusions (Fig. 77). These porphyroblasts are rotated by D2 (Figs. 82, 94). They have rims (commonly polycrystalline) of a more anorthite-rich composition (up to An_{67}), which may be relatively free of inclusions, and are free of graphite in particular (Fig. 77). The boundary between the more sodic core and the more calcic rims is commonly sharp, so that the difference in refractive index is visible. The rims, and new granoblastic grains of intermediate to calcic plagioclase, appear to postdate the D2 crenulations, and where they are abundant they obscure the fabric in the rocks (Fig. 89). Some graphite-rich porphyroblasts appear to have grown over the D2 crenulations (Fig. 95), but these are commonly composed of several individual crystals that have been rotated relative to each other during D2.

K-feldspar occurs interstitially in granoblastic quartz-rich laminae in some thin sections of high-grade schist. It becomes more abundant deeper in Hole 976B, and forms poikiloblasts up to one mm in diameter in some thin sections from close to the boundary with the gneiss. The texture suggests that it probably crystallized after D2.

Fibrolite forms elongate mats replacing biotite (Fig. 77). (This does not mean biotite was unstable, only that it was involved in the reaction that formed the fibrolite). The fibrolite aggregates are to some extent mimetic, so that they may be elongate parallel to S1 (Fig. 77). Very commonly, however, they are oblique to S1, particularly in the hinges of D2 folds, where they define the axial planar schistosity S2 (Fig. 76) and the associated mineral lineation. It is also strongly lineated along D2 shear bands. Prismatic sillimanite has commonly grown post-kinematically with respect to S2.

Andalusite forms porphyroblasts that have grown post-kinematically with respect to S2 (Fig. 96). It commonly contains abundant inclusions of biotite, plagioclase, staurolite, hercynite, graphite, and opaque oxide. Andalusite is commonly partly altered to large randomly oriented crystals of muscovite.

Corundum is present in three thin sections. In one thin section, small (100 µm) spongy porphyroblasts appear to be replacing biotite (Fig. 97) in a quartz-free plagioclase-biotite schist adjacent to a calc-silicate layer. In another, corundum forms millimeter-sized twinned porphyroblasts in a quartz-biotite-sillimanite-andalusite schist; the crystals appear to be syn- or pre-D2. In a third, millimeter-sized twinned porphyroblasts have formed at the expense of a muscovite layer in a calc-schist: this assemblage is also quartz-free.

Hercynite (green spinel) is widespread as small grains in poikiloblastic plagioclase (in places in contact with relict staurolite), and is inside andalusite with inclusions of ilmenite, staurolite, and biotite. It also occurs locally as aggregates in the biotite-rich matrix (Fig. 98).

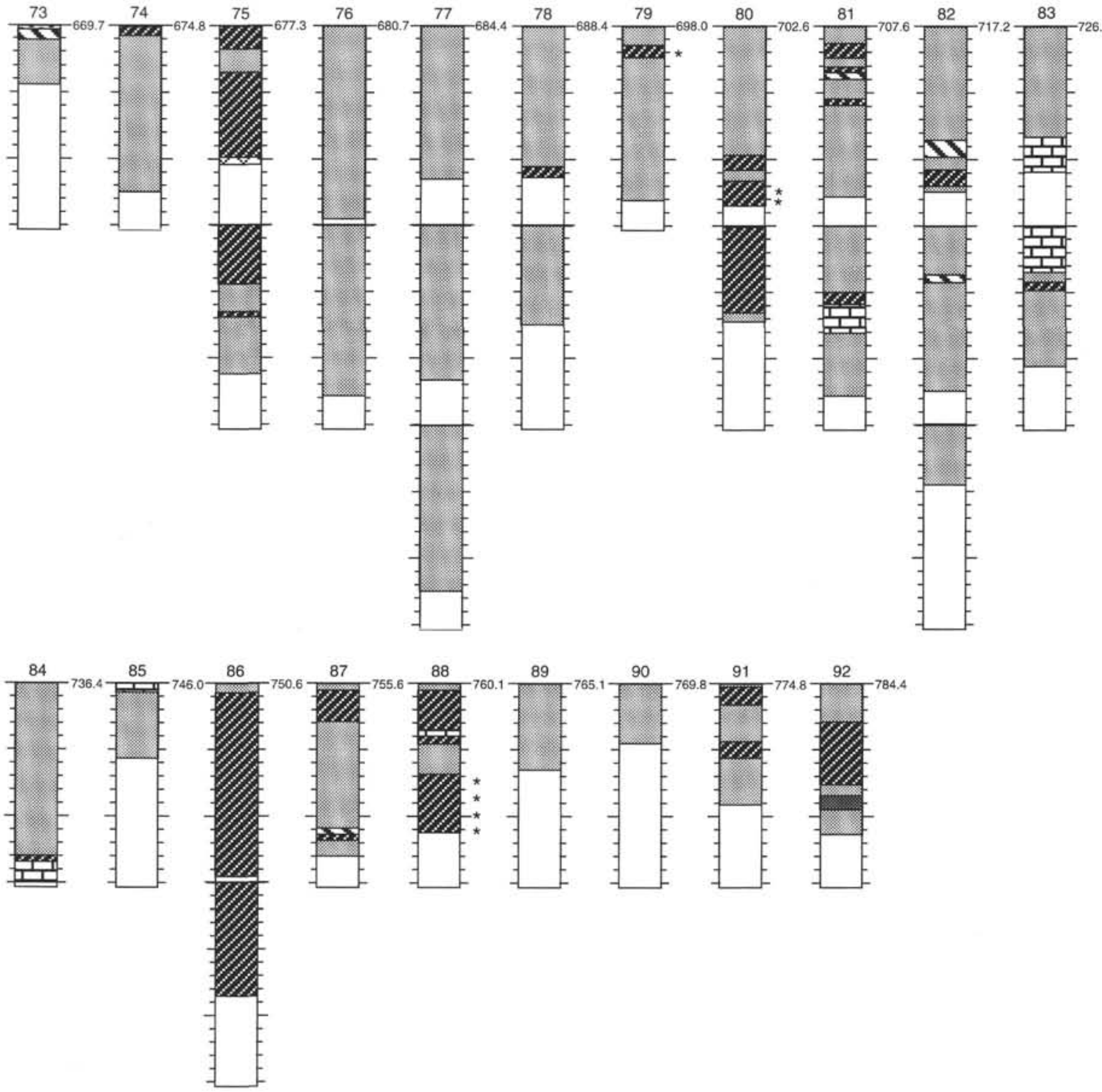

Figure 51. Lithological column for the basement rocks cored in Hole 976B. The core number is shown above each column, and the depth in meters below the sediment surface is to the right.

Rutile is present as armored inclusions in staurolite, surrounded in turn by plagioclase. Total or partial transformation of rutile to ilmenite is seen within the plagioclase grains.

Gneiss

As discussed in the section on structure, textural relations in the gneiss are difficult to interpret. The critical observations are summarized below.

Biotite locally lies parallel to an early foliation (S1), and is folded around D2 crenulations; it has recrystallized parallel to the S2 crenulation cleavage; and it appears to have recrystallized during D3. It has been partly transformed at a late stage to a mixture of muscovite and chlorite.

Andalusite forms elongate idiomorphic porphyroblasts that have inclusion trails of elongate opaque oxide crystals that define an early foliation (S1), as well as crenulations in this fabric (Fig. 99). It also includes biotite and fibrolite that define S2. The crystals are fragmented and deformed, occurring as augen within the main foliation, and are partly replaced by plagioclase (Fig. 100). Andalusite was also replaced by coarse-grained muscovite at a late stage.

Sillimanite occurs as fibrolite that has grown parallel to the crenulation cleavage (S2), but was deformed and possibly recrystallized during D3, forming a mylonitic fabric (Fig. 101). There are also widespread randomly oriented fibrolite crystals that have grown across S3.

Cordierite forms elongate porphyroblasts that have grown over the crenulation cleavage S2, but form augen within S3 (Fig. 102). In the quartz-feldspar–rich domain it is commonly corroded and altered to a mixture of fine-grained sheet-silicates (pinnite and probably muscovite; Fig. 103).

Plagioclase occurs as porphyroblasts with inclusions parallel to the main foliation, but which form augen within the foliation. It also forms granular aggregates with quartz that appear to have recrystal-

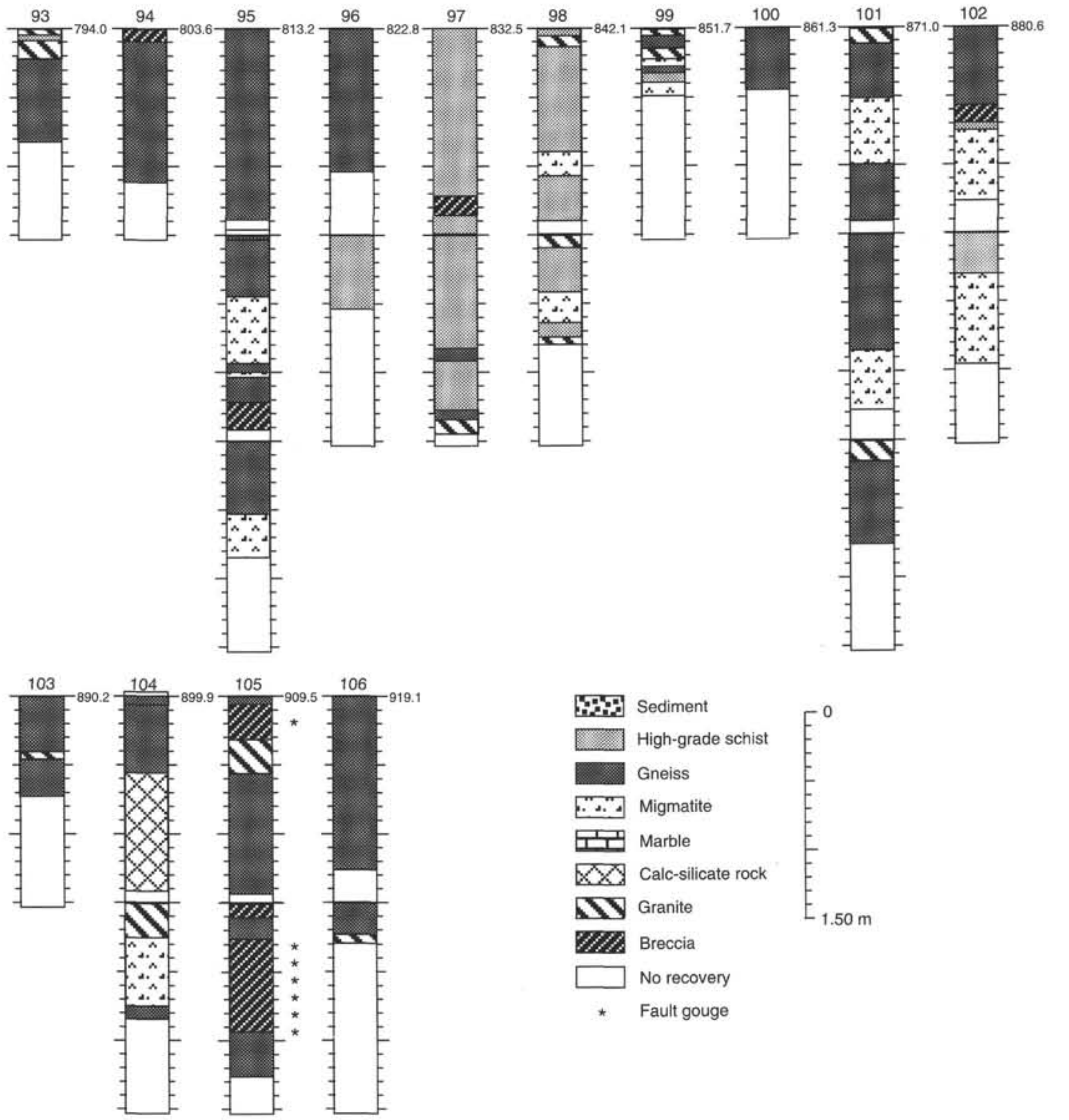

Figure 51 (continued).

lized during or after D3. It includes relict andalusite. Myrmekitic texture is present in granitic leucosome in migmatitic gneiss rocks (Fig. 104).

K-feldspar occurs as porphyroblasts full of inclusions of quartz and plagioclase (Fig. 105), which form elongate augen parallel to S3. In granite and migmatitic gneiss it also occurs as large subhedral crystals.

Garnet occurs as elongate or idiomorphic porphyroblasts growing over sillimanite crystals that lie parallel to S2 (Fig. 106). Idiomorphic small garnet without inclusions has also grown over the composite S2-S3 planar fabric of the rock.

Muscovite has grown mimetically after sillimanite and biotite and in randomly oriented aggregates after andalusite and cordierite; it appears to postdate S3.

Quartz is a widespread major constituent of the gneisses and occurs as rounded grains inside elongate K-feldspar poikiloblasts. In leucosome domains in migmatite, quartz is common as euhedral hexagonal inclusions in large porphyroblasts of K-feldspar.

The *granitic leucosome* in the migmatitic gneiss is largely undeformed, and it appears to have permeated both along and across the foliation. There is some textural evidence that granitic leucosome has locally been affected by D3, however, and it seems likely that the period of melting overlapped D3.

Metamorphism

The occurrence of metamorphic minerals in thin sections examined from Holes 976B and 976E is summarized in Tables 12, 13. Temporal sequences of partial mineral assemblages can be established for the principal rock types encountered in the core, based on the textural relationships described in the previous section. The clearest evidence that a particular set of minerals was associated is the relationship between mineral growth and deformation: for this reason many of the assemblages are linked to deformation phases. This does not mean that the onset of significant metamorphic reactions necessarily coincided with deformation. The assemblages are listed below, in order of development from older to younger. Phases shown in brackets are interpreted as having been stable but did not necessarily grow. Question marks indicate that the textural evidence for the mineral is uncertain. The earlier assemblages are incomplete, as some of

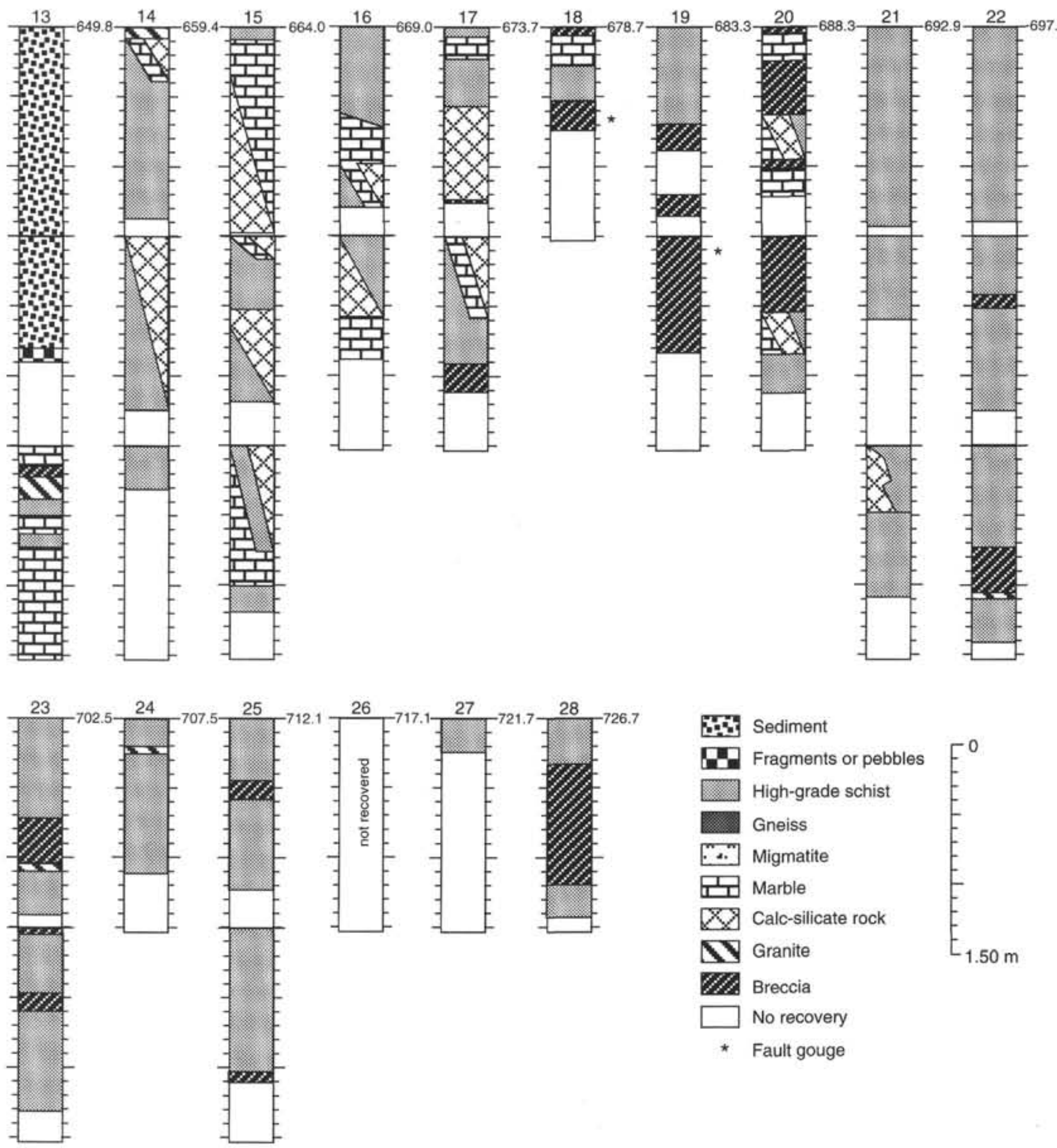

Figure 52. Lithological column for the basement rocks cored in Hole 976E. The core number is shown above each column, and the depth in meters below the sediment surface to the right.

the minerals have been totally consumed by reactions producing later assemblages. Quartz is present in the assemblages unless noted otherwise.

High-Grade Schist

1. Syn-D1: Biotite + rutile?
2. Between D1 and D2: (Biotite) + staurolite + first garnet + sodic plagioclase + rutile?
3. Syn-D2: Biotite + fibrolitic sillimanite ± K-feldspar? + ilmenite ± hercynite ± corundum. Relict garnet and staurolite still present.
4. Early post-D2: Biotite + prismatic sillimanite + intermediate plagioclase ± second garnet ± K-feldspar. Relict staurolite still present.
5. Late post-D2: Biotite + andalusite. Relict garnet still present, relict staurolite only present armored inside plagioclase or andalusite porphyroblasts (Fig. 91).

Accessory minerals include rutile, sphene, ilmenite, magnetite, tourmaline, zircon, apatite, epidote, and calcite.

Gneiss and Migmatitic Gneiss

1. Syn-D1: Biotite + opaque oxide.
2. Syn-D2: Biotite + plagioclase + sillimanite.
3. Between D2 and D3: Andalusite + plagioclase + K-feldspar + cordierite.
4. Syn-D3: Sillimanite? + plagioclase + K-feldspar + garnet
5. Post-D3: Muscovite.

Accessory minerals in these rocks include zoned tourmaline, apatite, and zircon.

Calc-Silicate Rocks

Calc-silicate rocks are made up of varying proportions of calcite + diopside + plagioclase ± garnet ± Ca-amphibole ± scapolite ± sphene. This assemblage, now heavily retrogressed in places, probably corresponds in time to assemblage 3 in the high-grade schists and gneisses. Diopside and amphibole are commonly retrogressed to mixtures of chlorite, sericite, and clay minerals. Minor constituents in these rocks include apatite, yellow epidote, and tourmaline.

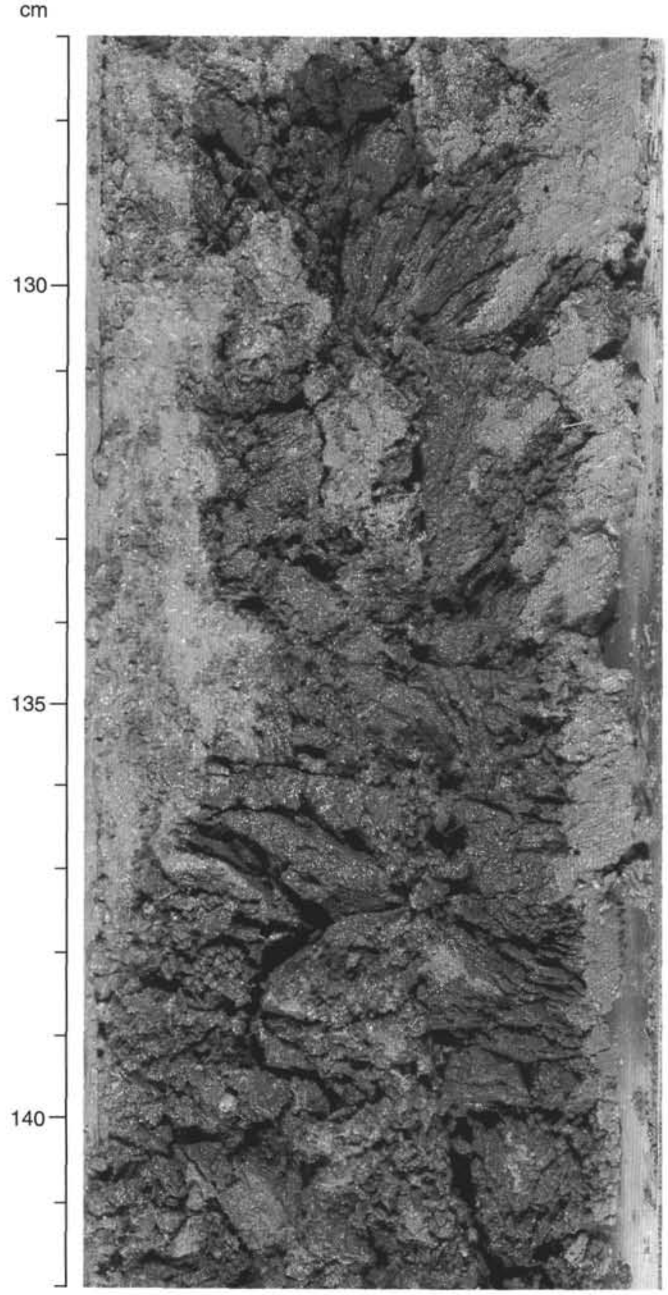

Figure 53. Disjunctive cleavage with variable orientation in the sediments lying on top of the metamorphic basement at Hole 976E (interval 976E-13R-1, 127–142 cm). This cleavage is visible for about 20 m above the basement/sediment contact.

Granite

The granitic rocks contain quartz + K-feldspar (orthoclase or microcline) + plagioclase + biotite + opaque minerals. Andalusite, sillimanite, and cordierite are present in some samples. Accessory minerals include epidote, tourmaline, apatite, and zircon. Chlorite and muscovite are present as retrogressive phases from plagioclase and cordierite.

Pressure-Temperature Conditions of Metamorphism

We have attempted to estimate approximate pressure-temperature (P-T) conditions for the assemblages listed above, based on generally

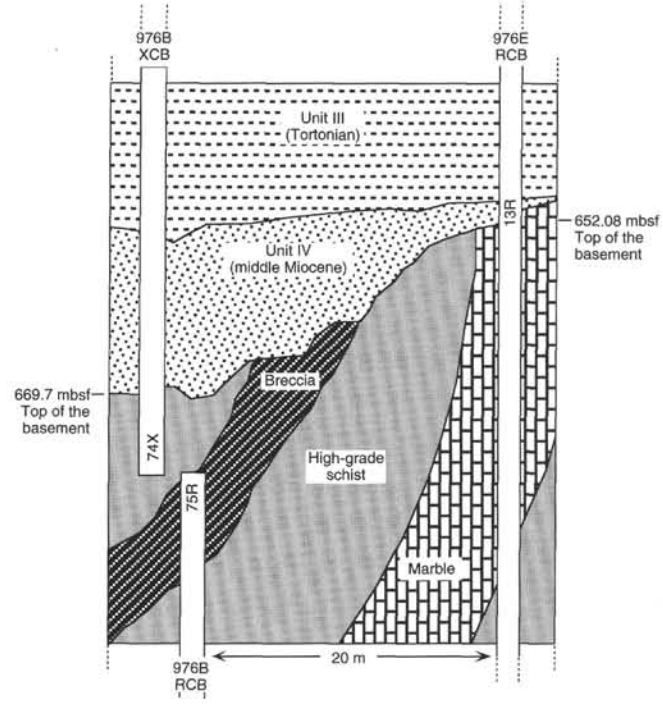

Figure 54. Diagram illustrating the relationships between Holes 976B and 976E. The scale is approximate only, and relationships among the different rock units are conjectural. Cores 976B-74X and 976B-75R were probably offset by 0.5–1 m.

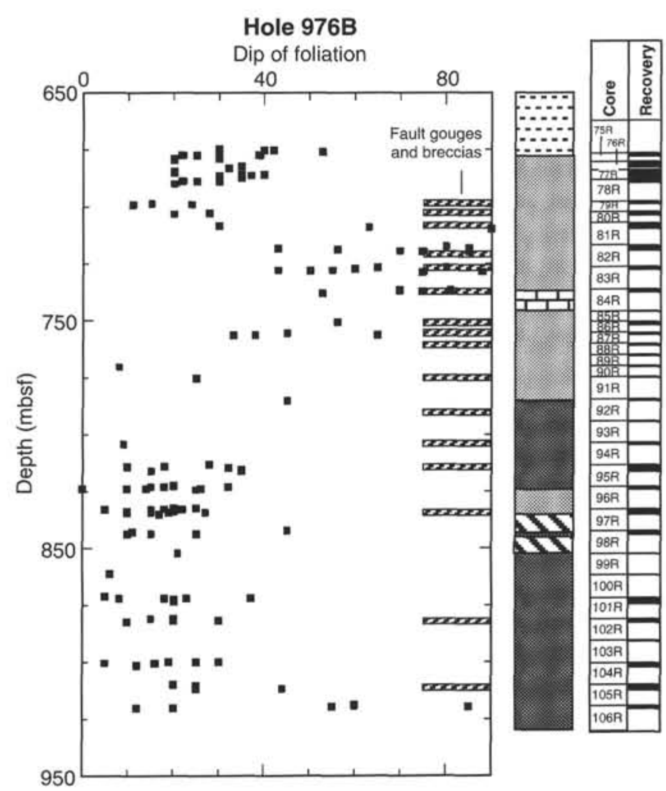

Figure 55. Variation in the dip of the main foliation in the basement from Hole 976B (note that the dip direction is unknown, but analysis of FMS and BHTV data may provide absolute orientation data post-cruise). The patterns used for the lithotypes are the same as in Figure 51.

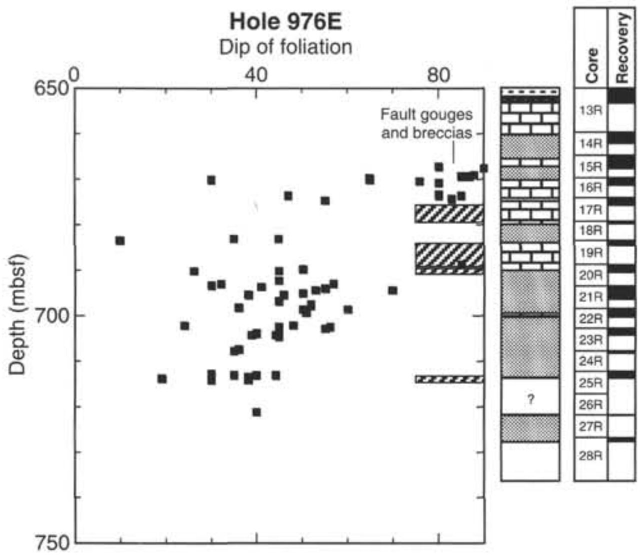

Figure 56. Variation in the dip of the main foliation in the basement from Hole 976E (note that the dip direction is unknown). The patterns used for the lithotypes are the same as in Figure 51.

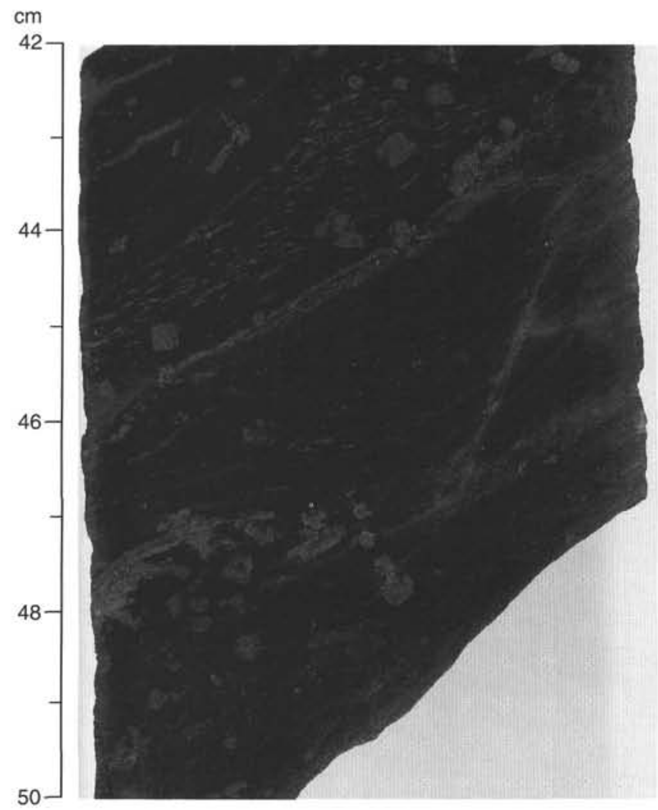

Figure 57. Banded quartz-biotite-sillimanite schist showing sillimanite (millimeter-long white lenticles), defining S2 at a low angle to the compositional banding, and post-kinematic andalusite porphyroblasts (2–3-mm square and rectangular sections). Section 976B-76R-1, Piece 7A.

accepted experimental data for simple metamorphic reactions. We note that many of these experimental P-T curves have been determined for end-member compositions of the minerals, and in the absence of data on the mineral chemistry we have not made any correction for either the major element composition or the possible effects of minor components. The experimental curves are also subject to revision: we have used a P-T grid for pelitic assemblages (KFMASH system) based on data published by Spear (1993) and references therein (Fig. 107). The data are also based on the assumption that the assemblage in question is in equilibrium. What we have observed were clearly not equilibrium assemblages: if they had been we would not be able to reconstruct the temporal sequences listed in the previous section. It is unlikely that full equilibrium was achieved at any time: relict minerals from earlier stages in the metamorphic evolution would always have been present. Conclusions based on the inferred assemblages we have listed should therefore be treated with caution. Nevertheless we believe that the broad outlines of the P-T path experienced by the rocks can be deduced with a reasonable degree of confidence.

The critical reactions we have used to constrain the various stages in the metamorphic evolution are discussed below.

Syn- to Post-D1 Assemblage in High-Grade Schist

This is the most difficult to constrain accurately. We have used what we infer to have been the immediate post-D1 assemblage: biotite + staurolite + garnet + sodic plagioclase + rutile. The assemblage almost certainly also included muscovite and an aluminosilicate phase, neither of which are preserved. The presence of rutile in place of ilmenite suggests that D1 took place at pressures higher than the reaction curve plagioclase + ilmenite = garnet + rutile at 5–7 kbar (using the end-member GRIPS equilibrium, Bohlen and Liotta, 1986). This places the pressure conditions within the stability field of kyanite.

The main constraints on temperature arise from the assemblage staurolite + biotite, which places D1 above about 560°C at 5 kbar, and the lack of evidence for melting, which suggests that the temperature did not significantly exceed the wet solidus for granite at about 630°C (using the muscovite-granite wet solidus, Le Breton and Thompson, 1988; Fig. 107). Taking the pressure and temperature constraints together, D1 is likely to have occurred in the range 580°–630°C at more than 6–7 kbar.

Syn-D2 Assemblage in High-Grade Schist

We have used the assemblage biotite + fibrolitic sillimanite + plagioclase + ilmenite ± hercynite ± corundum. The main constraints on P-T conditions for this assemblage are the stability of sillimanite, the lack of stability of staurolite or rutile, and the lack of evidence for melting (which suggest that conditions probably lay below the wet solidus for granite). These constraints suggest that D2 occurred at temperatures in the range 590°–680°C, and pressures in the range 1.5–4 kbar (Fig. 107). The lack of muscovite suggests also that conditions may have exceeded the breakdown curve muscovite + quartz = aluminosilicate + K-feldspar at 600°–650°C, 2–3 kbar (reaction taken from Helgeson et al., 1978).

Post-D2 Assemblage in High-Grade Schist

Late post-D2 metamorphism took place in the andalusite stability field, and below the wet solidus for granite. The growth of corundum during and probably after D2 metamorphism indicates that temperatures were in excess of the breakdown curve muscovite = corundum + K-feldspar + quartz (i.e., over 600°C; reaction from Helgeson et al., 1978), and this is also consistent with the growth of calcic plagioclase. These preliminary constraints suggest that post-D2 metamorphism occurred in the range 600°–700°C, at 2 kbar or less (Fig. 107).

Melting Conditions in the Migmatitic Gneisses

Conditions leading to the onset of melting in the migmatitic gneiss are approximately constrained by the stability of cordierite + K-feldspar (after D2), the stability of sillimanite during D3, and the association of K-feldspar + garnet during or after D3. Since andalusite was stable after D2, conditions must have been close to the

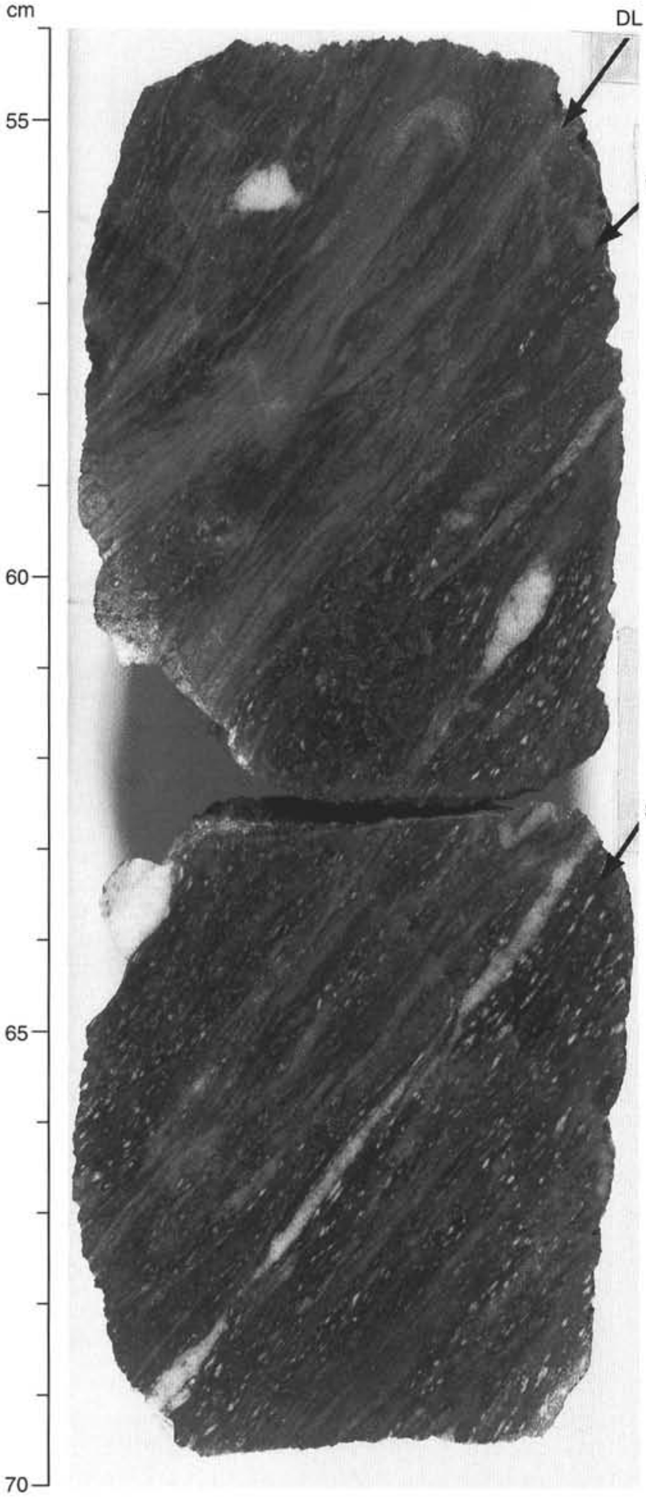

Figure 58. Quartz-biotite-sillimanite schist showing centimeter-scale compositional banding (e.g., note boundary marked C between quartz-biotite schist in top part of the piece and dark biotite-sillimanite schist below); millimeter-scale quartz-biotite differentiated layering (DL), preferred orientation of sillimanite (millimeter-long white lenticles, marked S); and quartz veins transposed, stretched, and disrupted in the plane of the foliation. Section 976B-82R-2, Pieces 7A and 7B.

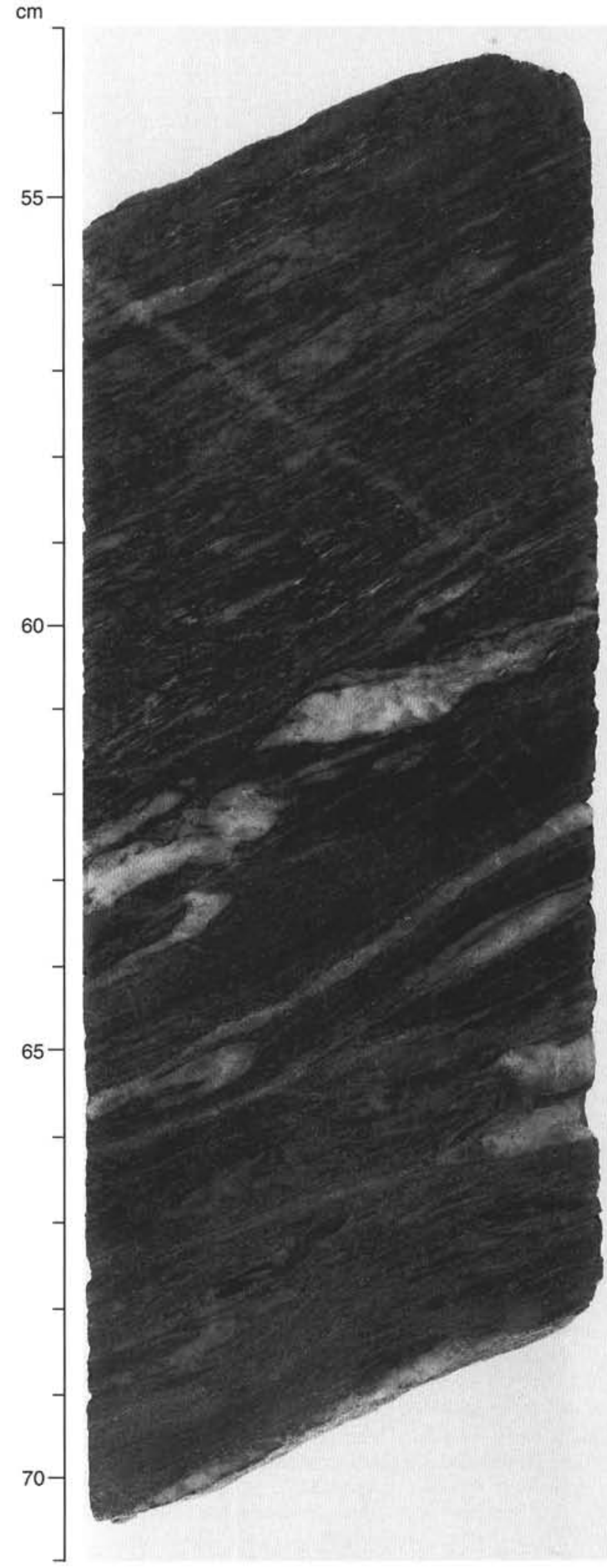

Figure 59. Quartz-biotite-sillimanite schist showing gneissic appearance produced by compositional banding, differentiated layering, and disrupted quartz veins transposed parallel to the main foliation. Note shear band cutting the quartz vein in the center of the piece with top to the left shear sense. Section 976B-78R-1, Piece 9C.

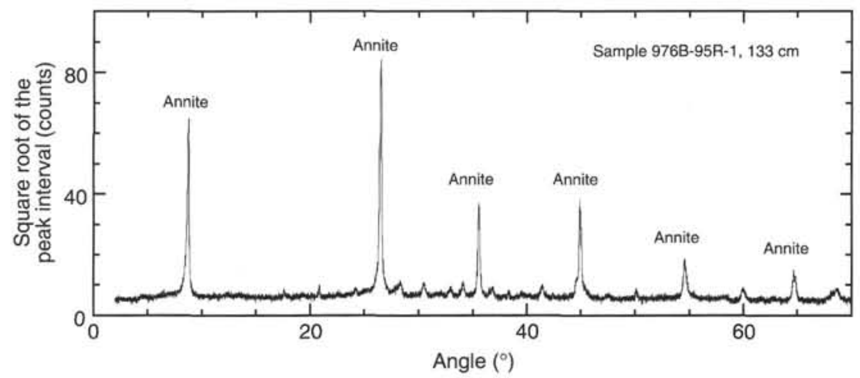

Figure 60. XRD diagram of biotite crystals lying on foliation planes.

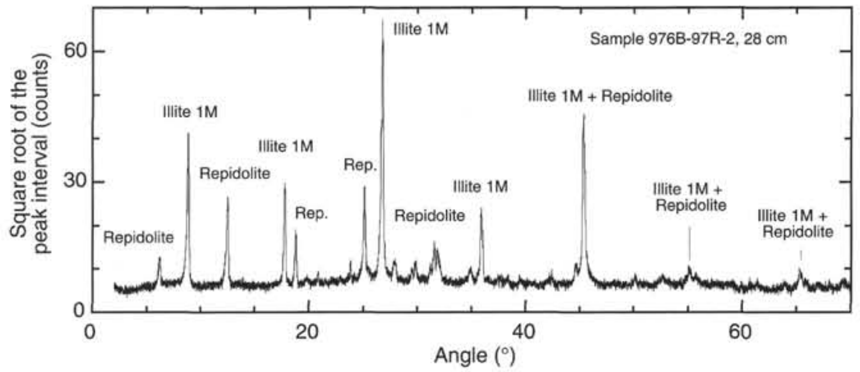

Figure 61. XRD diagram of chlorite (repidolite) and illite (type 1M) crystals in a quartz vein parallel to the main foliation in a high-grade schist.

andalusite-sillimanite curve. This suggests that melting occurred at around 700°–750°C and at 1 kbar or less.

Discussion and Conclusions

Significance of the P-T Path

Although the P-T conditions outlined above are not very tightly constrained, they clearly indicate that the high-grade schist underwent a significant decrease in pressure accompanied by constant or possibly increasing temperature. The earlier part of the metamorphic evolution in the gneiss and migmatitic gneiss is unconstrained, and may have been somewhat different from that in the high-grade schist, but it is evident that the later stages of its evolution involved decreasing pressure and significantly increasing temperature. Taken together, the metamorphic history is most easily explained in terms of the tectonic exhumation of middle crustal rocks accompanied by heating.

Regional Context for the Basement Rocks at Site 976

The protoliths of the basement rocks at Site 976 were organic-rich sediments that resemble Paleozoic sequences in any of the three main nappe complexes of the Betic Cordillera (or indeed in the Iberian meseta), but the high-temperature low-pressure metamorphism is characteristic of the latest stages of the Alpine metamorphic evolution in the Betic Cordillera. This type of metamorphism is particularly well displayed in the regions surrounding the peridotite massifs in the Serranía de Ronda (west of Málaga, Spain), attributed to the Alpujarride Complex (see "Background and Objectives" section, this chapter). In that region the high-temperature low-pressure metamorphism is fairly precisely dated at 18–22 m.y. (Zeck et al., 1992; Monié et al., 1994), that is, early Miocene. This certainly postdates the original stacking of the nappes in the Betic Cordillera, and is roughly coeval with the main period of extensional tectonics.

The rocks overlying the Ronda peridotite massif (called the Jubrique Unit by Balanyá et al., 1993), show a remarkable downward increase in metamorphic grade in a metapelitic sequence with a maximum thickness of about 5.5 km. The metamorphism changes from low-grade (with relict high-pressure assemblages, Azañón et al., 1995) at the very top of the sequence, to upper amphibolite facies and granulite-facies at the base, close to the contact with the peridotite. This metamorphism occurred under progressively decreasing pressure (Balanyá et al., 1993; Loomis, 1972; Torres-Roldán, 1981). The rocks underlying the peridotite massif also show evidence for early high-pressure metamorphism, reaching eclogite facies (Tubía and Gil-Ibarguchi, 1991), evolving to upper amphibolite facies and locally granulite facies metamorphism at low pressures (Westerhof, 1977). These rocks are characterized by the widespread appearance of marble, calc-silicate rock, augengneiss, cordierite-rich metapelites and leucogranite (Lundeen, 1978; Muñoz, 1991; Torres-Roldán, 1983; Tubía, 1988).

In terms of the metamorphic evolution, and the progressive downward increase in metamorphic grade, the basement at Site 976 shows considerable similarities to the rocks overlying the peridotite massifs. The lithological assemblage is rather different, however, evidenced particularly by the presence of marble, calc-silicate rocks, and the abundance of granitic rocks.

STRUCTURAL GEOLOGY

Structural features found in the sedimentary rocks are included in the lithostratigraphy report (see "Lithostratigraphy" section, this chapter).

Structural features found in the basement rocks are included in the basement structural geology and petrology report (see "The Structural Geology and Petrology of the Basement" section, this chapter).

ORGANIC GEOCHEMISTRY

Calcium carbonate and organic carbon concentrations were measured on samples obtained regularly from Holes 976B, 976C, 976D, and 976E. Organic matter atomic C/N ratios and Rock-Eval analyses were employed to determine the type of organic matter contained within the sediments. Analyses of extractable methyl alkenones were

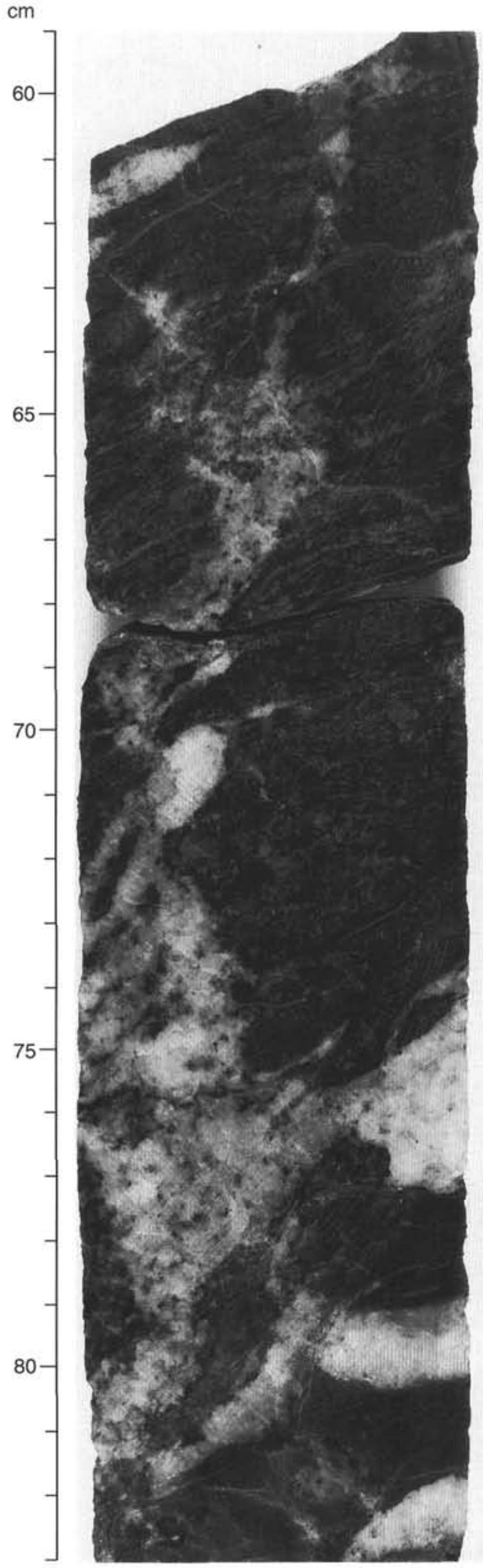

Figure 62. Migmatitic gneiss showing irregular veins of unfoliated granitic leucosome cutting the gneissic foliation. Section 976B-95R-2, Pieces 3B and 3C.

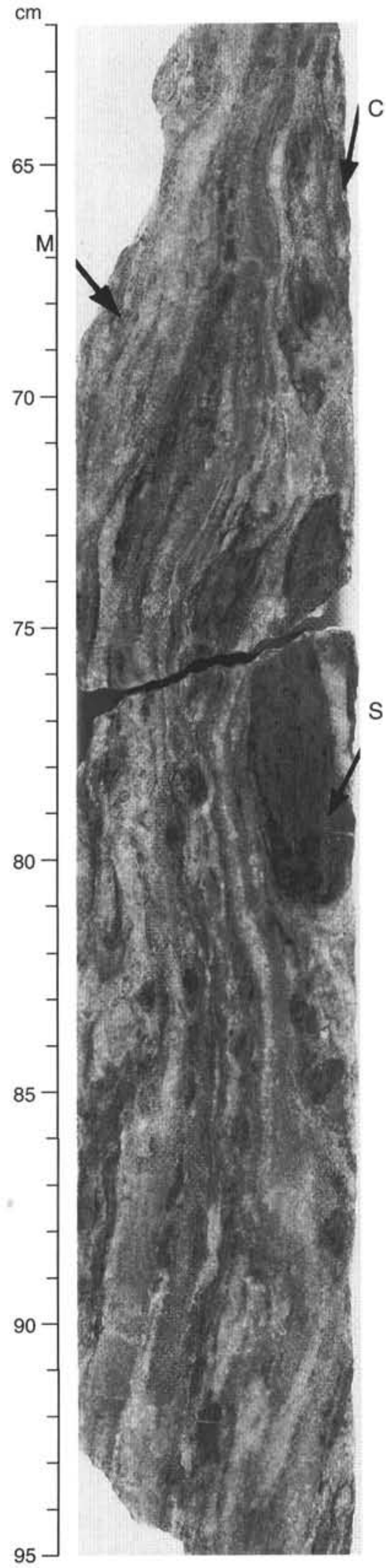

Figure 63. Interlayered biotite-sillimanite schist (S, dark gray), calc-silicate rock (C, mottled), and calcite marble (M, white). The schist has been disrupted as a result of the mechanical contrast with the more ductile marble. Section 976E-20R-1, Pieces 11A and 11B.

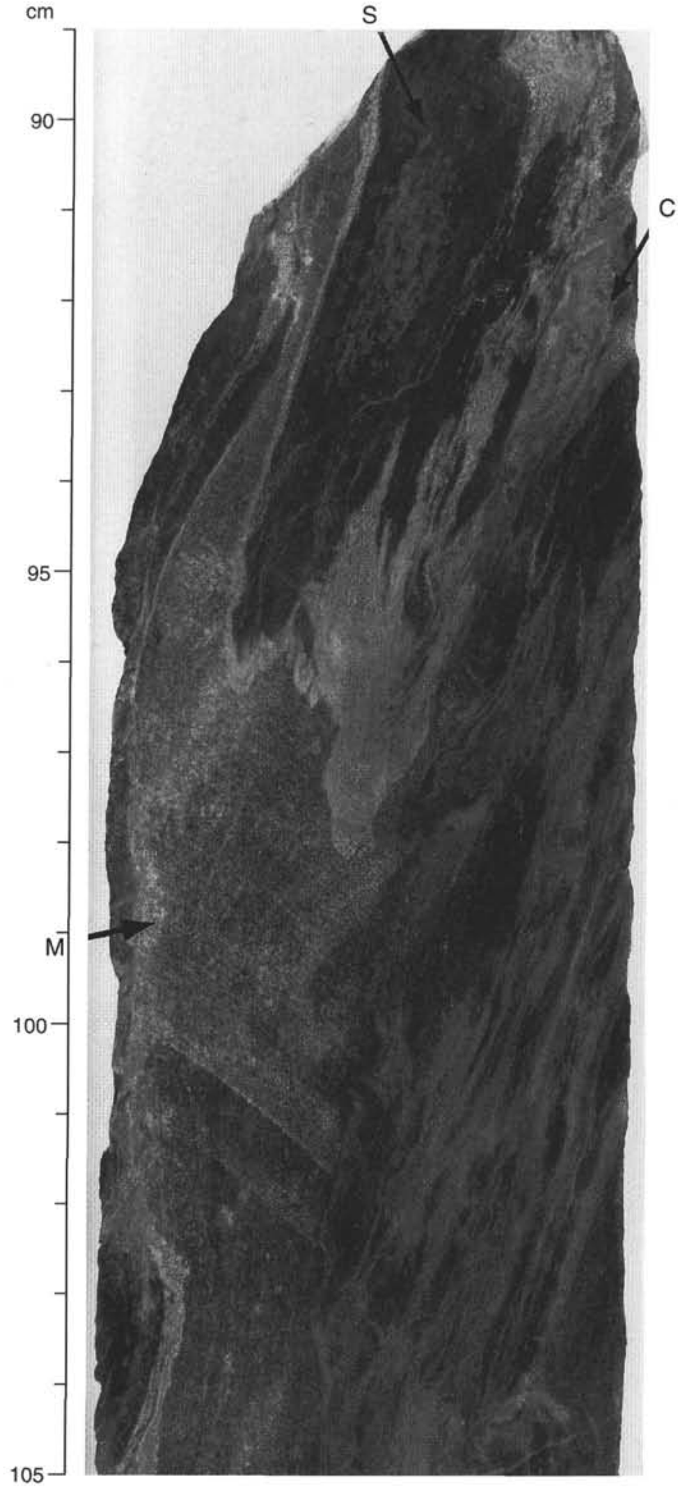

Figure 64. Reaction zone of calc-silicate rock (C) around a disrupted layer of schist (S) in marble (M). Section 976E-15R-1, Piece 6A.

attempted to obtain estimates of sea-surface paleotemperatures. Elevated amounts of headspace and core void gas contents were encountered, and routine monitoring of these gases was done for drilling safety.

Inorganic and Organic Carbon Concentrations

Concentrations of carbonate carbon vary between 0.6% and 9.4% in sediments from Site 976 (Table 14; Fig. 108). These carbonate carbon concentrations are equivalent to 5% to 78% sedimentary $CaCO_3$, assuming that all of the carbonate is present as pure calcite. The range in carbonate content reflects a varying combination of fluctuating biological productivity, dilution by non-carbonate hemipelagic sedimentary components, and post-depositional carbonate dissolution driven by oxidation of organic carbon.

Sediments at Site 976 average 0.6% TOC, which is twice the average of 0.3% compiled by McIver (1975) from DSDP Legs 1 through 33. Sediments in the upper 320 m of Hole 976B have higher

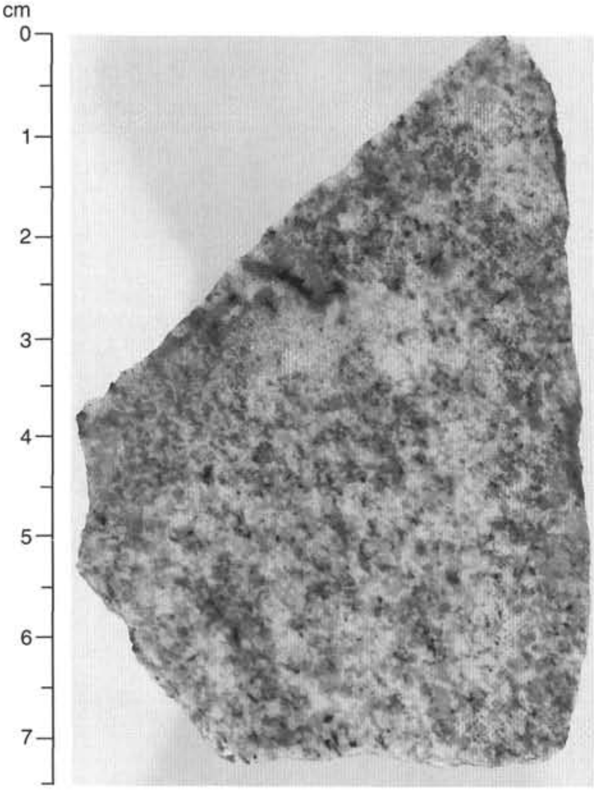

Figure 65. Leucogranite with biotite and tourmaline. Section 976E-14R-1, Piece 1.

TOC concentrations than those deeper in the sediment column (Table 14). The maximum TOC value at Site 976 is 1.85% (Sample 976B-5H-5, 25–26 cm). The generally elevated TOC concentrations are probably a consequence of the high accumulation rate of sediments at this site (see "Lithostratigraphy" section, this chapter), which would improve post-depositional organic matter preservation.

Organic Matter Source Characterization

Organic C/N ratios were calculated for Site 976 samples using TOC and total nitrogen concentrations to help identify the origin of their organic matter. Site 976 C/N ratios vary from <5 to 21 (Table 14). The low C/N ratios occur in samples especially low in organic carbon and are not accurate indicators of organic matter source. These values are probably an artifact of the low carbon content, combined with the tendency of clay minerals to absorb ammonium ions generated during the degradation of organic matter (Müller, 1977).

The C/N ratios of samples containing a minimum of 1% TOC average 12.1, which is a value that is intermediate between unaltered algal organic matter and fresh land-plant material (e.g., Emerson and Hedges, 1988; Meyers, 1994). It is likely that these organic-carbon–rich sediments contain a mixture of partially degraded algal material and continental organic matter. Preferential loss of nitrogen-rich, proteinaceous matter can elevate the C/N ratios of algal organic matter during settling to the seafloor.

A van Krevelen-type plot of the hydrogen index (HI) and oxygen index (OI) values suggests that the sediments contain Type III (land-derived) organic matter (Fig. 109). This source assignment for the organic matter conflicts, however, with the intermediate C/N ratios for these samples, which suggest that the organic matter is a mixture of marine and continental material. The contradiction between the Rock-Eval source characterization and the elemental source characterization indicates that the marine organic matter has been heavily oxidized, probably by microbial reworking. Well-preserved Type II organic matter has high HI values (Espitalié et al., 1977). In general, Hole 976B sediments having higher Rock-Eval TOC values also have higher HI values (Fig. 110). This relationship indicates that the algal organic matter has been variably oxidized. Rock-Eval TOC values agree poorly with TOC values determined by carbon analyses for sediments in the upper 150 m of Hole 976B (Tables 14, 15). Because Rock-Eval pyrolysis under-represents the carbon content of Type III organic matter, this discrepancy indicates the presence of a major fraction of continental material in these upper sediments and its lack in the deeper part of this hole. T_{max} values are relatively low (Table 15), showing that organic matter is thermally immature with respect to petroleum generation (Espitalié et al., 1977) and therefore contains little detrital material derived from erosion of ancient sediments. The land-derived organic matter in Site 976 sediments probably is from plants extant during the Pleistocene.

Alkenone Paleotemperature Estimates

Samples containing at least 1% TOC were selected from Hole 976B for extraction and analysis of their C_{37} alkenone biomarkers and calculation of sea-surface paleotemperatures. Organic matter in these samples contained too little extractable material to provide useful alkenone data. The absence of measurable alkenones contrasts with sapropel layers present elsewhere in the Mediterranean and indicates that the organic matter present at Site 976 is not as well preserved.

Headspace Gases

Concentrations of headspace methane are high in sediments from Holes 976B, 976C, and 976D (Fig. 111). Two sources of the gas are possible. First, gas from some deeper origin may have migrated into the unit, which consists of turbiditic hemipelagic sediments. Evidence for migration of methane into porous sediments from deeper sources has been found at Sites 762 and 763 on the Exmouth Plateau of northwest Australia, where a known thermogenic source exists in underlying Jurassic rocks (Meyers and Snowdon, 1993). No comparable source of gas is known on the southern margin of Iberia. A second possibility is in situ formation by methanogenic bacteria. High C_1/C_2 ratios and the absence of major contributions of higher molecular weight hydrocarbon gases (Tables 16, 17) indicate that the gas is biogenic, as opposed to thermogenic, in origin. The source of the methane is probably from in situ microbial fermentation of the marine organic matter present in this turbiditic unit. Similar microbial production of methane from marine organic matter has been inferred from high biogenic gas concentrations in Pliocene–Pleistocene sediments from Site 532 on the Walvis Ridge (Meyers and Brassell, 1985), Sites 897 and 898 on the Iberian Abyssal Plain (Meyers and Shaw, in press), and also in middle Miocene sediments from Site 767 in the Celebes Sea (Shipboard Scientific Party, 1990). A biogenic origin of the methane is supported by the disappearance of interstitial sulfate at approximately the same sub-bottom depth where methane concentrations begin to rise (see "Inorganic Geochemistry" section, this chapter). As noted by Claypool and Kvenvolden (1983), the presence of interstitial sulfate inhibits methanogenesis in marine sediments.

INORGANIC GEOCHEMISTRY

Two distinct interstitial waters sampling strategies were used at this site. At Hole 976B, 19 interstitial water samples were obtained from 1.45 mbsf to 646.6 mbsf to identify general geochemical trends. One sample every three cores was collected at the top and the deeper section was sampled only when recovery exceeded 30%. Hole 976D was sampled at 1.5-m intervals from 1.5 mbsf to 29.45 mbsf to gain

Table 11. XRF analyses of granite, gneiss, and high-grade schist rocks, Holes 976B and 976E.

Core, section, interval (cm)	Piece	Major element composition (wt%) of schist, gneiss, and granite rocks												Lithological description
		SiO_2	TiO_2	Al_2O_3	Fe_2O_3	MnO	MgO	CaO	Na_2O	K_2O	P_2O_5	Total	LOI	
161-976B-														
* 73R-1, 4–11	2	75.31	0.04	14.49	0.81	0.01	0.18	1.17	1.50	4.92	0.12	98.55	0.90	Light granite with tourmaline, biotite, and retrogressive chlorite.
* 73R-1, 4–11	2	76.41	0.05	14.69	0.85	0.02	0.20	1.16	1.54	5.06	0.12	100.10	0.90	
77R-3, 64–68	6	70.87	0.74	13.70	4.75	0.06	1.84	3.27	1.27	1.98	0.09	98.57	1.24	Banded quartz-rich schist with sillimanite.
77R-3, 64–68	6	70.15	0.75	13.54	4.67	0.06	1.81	3.23	1.23	1.98	0.09	97.51	1.24	
79R-1, 98–102	17	61.16	0.96	21.30	7.51	0.07	1.86	1.73	0.69	3.07	0.15	98.50	4.85	Graphite biotite-rich schist with sillimanite and minor andalusite.
79R-1, 98–102	17	61.14	0.97	21.26	7.63	0.07	1.89	1.74	0.89	3.12	0.16	98.87	4.85	
* 81R-1, 36–40	7	74.52	0.06	15.43	0.99	0.02	0.11	0.83	1.30	4.88	0.20	98.34	1.15	Granite with tourmaline.
* 87R-1, 112–113	15A	71.66	0.08	14.72	0.73	0.01	0.11	1.06	1.46	6.26	0.16	96.25	0.57	Leucogranite with biotite and tourmaline.
* 87R-1, 112–113	15A	73.54	0.09	15.03	0.77	0.01	0.13	1.09	1.55	6.44	0.16	98.81	0.57	
95R-2, 16–18	1C	60.34	0.89	18.73	6.98	0.07	2.38	3.89	2.38	2.15	0.07	97.88	1.90	Banded gneiss with biotite, sillimanite, and cordierite, with equigranular leucogranite bands.
95R-2, 16–18	1C	60.52	0.89	18.81	7.19	0.06	2.39	3.86	2.31	2.24	0.07	98.34	1.90	
* 97R-2, 143–144	22	72.19	0.27	14.26	1.67	0.03	0.37	1.29	0.97	6.05	0.15	97.25	0.83	Leucogranite with feldspar, quartz, tourmaline, and biotite. Abundant concentrations of biotite + quartz + cordierite?
* 97R-2, 143–144	22	73.69	0.28	14.59	1.75	0.03	0.36	1.32	1.04	6.20	0.15	99.41	0.83	
* 98R-2, 0–2	1	73.04	0.18	13.94	1.22	0.02	0.28	1.44	1.28	5.75	0.15	97.30	0.73	Leucogranite with tourmaline and biotite, scarce retrogressive chlorite. Selvage of biotite gneiss.
* 98R-2, 0–2	1	73.78	0.18	14.05	1.32	0.01	0.26	1.46	1.37	5.97	0.15	98.55	0.73	
101R-2, 25–29	3A	57.12	1.18	22.96	8.04	0.06	2.21	2.02	1.38	3.17	0.11	98.25	3.33	Banded gneiss with biotite, sillimanite, andalusite, cordierite, and plagioclase.
101R-2, 25–29	3A	56.96	1.18	22.94	7.98	0.06	2.25	2.03	1.46	3.16	0.11	98.13	3.33	
* 105R-1, 43–47	5	72.97	0.12	14.51	0.72	0.01	0.27	0.95	1.04	6.87	0.12	97.58	1.00	Leucogranite with randomly oriented biotite and tourmaline.
* 105R-1, 43–47	5	74.23	0.13	14.69	0.76	0.02	0.27	0.96	1.06	7.10	0.11	99.33	1.00	
* 106R-2, 24–29	4	74.02	0.03	13.53	0.60	0.01	0.15	0.93	1.07	6.96	0.10	97.40	0.76	Leucogranite with plagioclase, biotite, and minor tourmaline.
* 106R-2, 24–29	4	75.13	0.04	13.73	0.60	0.01	0.17	0.93	1.08	7.09	0.11	98.89	0.76	
161-976E-														
* 13R-3, 29–34	3	72.60	0.08	14.26	0.95	0.02	0.18	0.82	1.54	7.61	0.10	98.16	0.01	Biotite-rich granite with tourmaline and a diffuse felsic band.
* 13R-3, 29–34	3	73.38	0.09	14.41	0.96	0.02	0.18	0.82	1.58	7.81	0.10	99.35	0.01	

Core, section, interval (cm)	Piece	Analyses of minor elements (ppm) of schist, gneiss, and granite rocks											
		Nb	Zr	Y	Sr	Rb	Zn	Cu	Ni	Cr	V	Ce	Ba
161-976B-													
* 73R-1, 4–11	2	5	46	36	191	204	12	4	8	2	0	37	360
77R-3, 64–68	6	14	280	33	187	128	76	8	27	67	34	61	742
79R-1, 98–102	17	17	172	32	279	157	108	20	44	115	117	80	331
* 81R-1, 36–40	7	12	46	31	73	280	7	4	3	1	0	29	431
* 87R-1, 112–113	15A	7	47	19	146	280	10	6	4	1	0	21	184
95R-2, 16–18	1C	17	215	35	254	162	130	13	45	101	141	68	257
* 97R-2, 143–144	22	9	110	43	210	201	14	6	5	17	5	38	587
* 98R-2, 0–2	1	5	66	25	223	208	8	7	4	10	13	47	648
101R-2, 25–29	3A	21	223	34	210	165	142	9	48	118	161	82	683
* 105R-1, 43–47	5	6	88	58	241	228	0	5	4	5	20	62	712
* 106R-2, 24–29	4	2	44	30	243	241	0	7	5	3	0	9	793
161-976E-													
* 13R-3, 29–34	3	8	28	13	241	286	12	6	4	3	1	26	536

Note: * = granitic rock analyses.

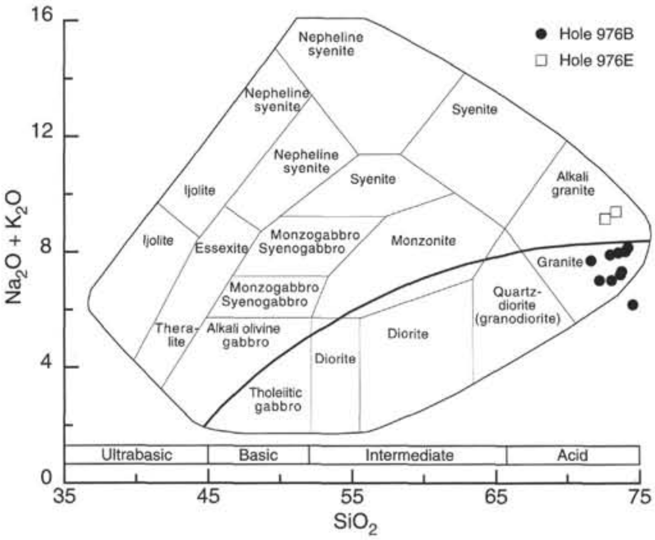

Figure 66. Chemical classification of the granitic rocks in Holes 976B and 976E using the total alkalies vs. silica (TAS) diagram (see "Explanatory Notes" chapter, this volume). The curved solid line divides the alkalic from the subalkalic rocks.

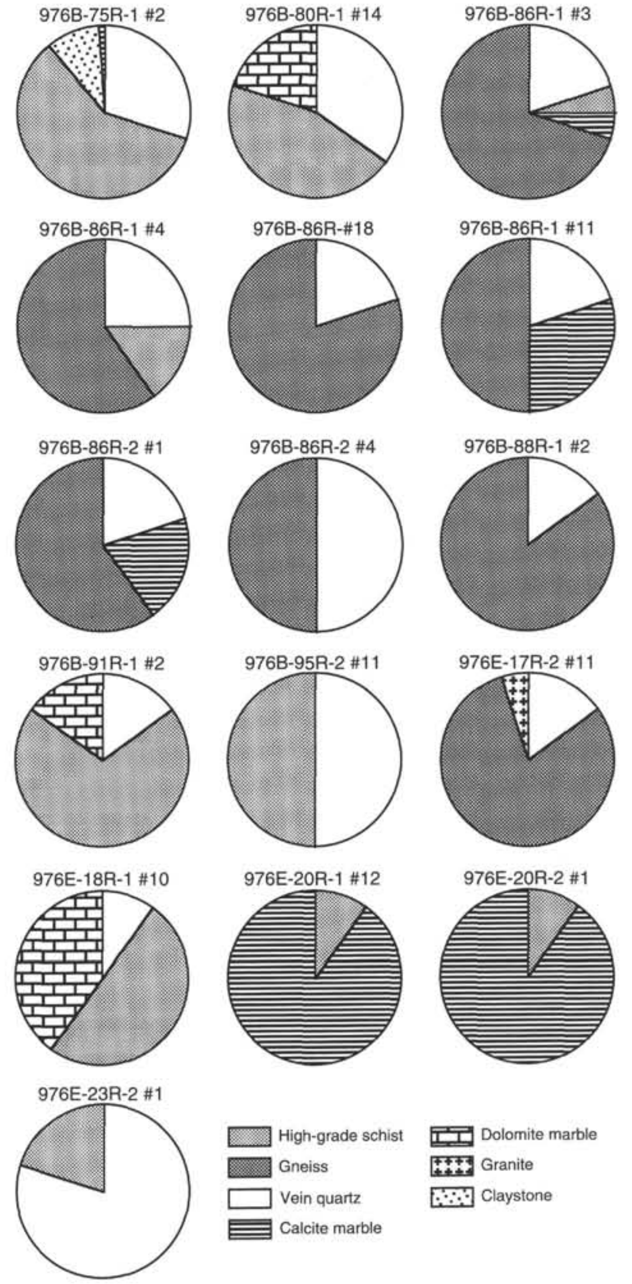

Figure 67. Distribution of clast types in breccias within the basement from Holes 976B and 976E.

a better insight into bacterially mediated redox processes. These data were supplemented with one sample per core from 30.95 to 68.95 mbsf in Hole 976C.

General Trends from Hole 976B

The dominant pattern observed is a downcore increase in salinity and in the concentrations of most of the measured elements, indicating the presence of a brine at depth (Table 18; Figs. 112–115). Chloride, sodium, and bromide are not extensively involved in diagenetic reactions within the sediment column. Their concentration profiles, therefore, can be used as a tracer for fluid migration and/or mixing. Chloride and sodium increase linearly up to 2.2 times the average seawater concentration, and bromide increases to approximately 3.3 times seawater. The shipboard bromide determination actually measures bromide + iodide, and iodide could not be measured; therefore, the bromide data should be considered as qualitative trends rather than as absolute values. However, as iodide is a minor seawater component, this correction should be relatively slight. Calcium, magnesium, strontium, and lithium, being involved in various diagenetic reactions, do not show the same linear diffusion profiles with depth as the conservative elements, but their linear increases toward the bottom of the hole suggest a common source (Figs. 112–115). Sulfate is completely depleted by organic matter degradation and, except for the topmost sample, has values close to 0 throughout the core (Fig. 116A: also see Hole 976D description below).

A single, comprehensive model cannot account for all of the features observed. Possible scenarios for the observed depth concentration trends are:

1. The interstitial water profiles reflect the presence of a paleofluid, approximately two to three times more concentrated than seawater, of possible Messinian age that was trapped by the rapidly accumulating Pliocene–Pleistocene sediments (see "Biostratigraphy" section, this chapter). This would account for the salinity, chloride, bromide, and sodium profiles, as well as for the depletion of sulfate, which can be completely consumed by bacterial sulfate reduction. However, this explanation does not account for the high lithium concentrations, which require an additional source.
2. The profiles reflect the flow of brines originating from halite dissolution in a deeper part of the basin, that migrated laterally (possibly along the basement-sediment contact). The brine chemistry and the lack of sulfate at depth suggest that halite, rather than gypsum dissolution, is the source of the brine. Sulfate would probably not be completely depleted at the basement-sediment contact if the brines were derived from dissolving gypsum. The dissolution of late-stage evaporites would also provide the high concentrations of lithium. The origin of these brines is problematic as there are no reported Messinian salts in the area, and the presence of older evaporite deposits is neither known nor likely.
3. The concentrations of some of the elements and the circulation of the fluids at Hole 976B may also be partially influenced by hydrothermal activity, possibly involving the basement. High

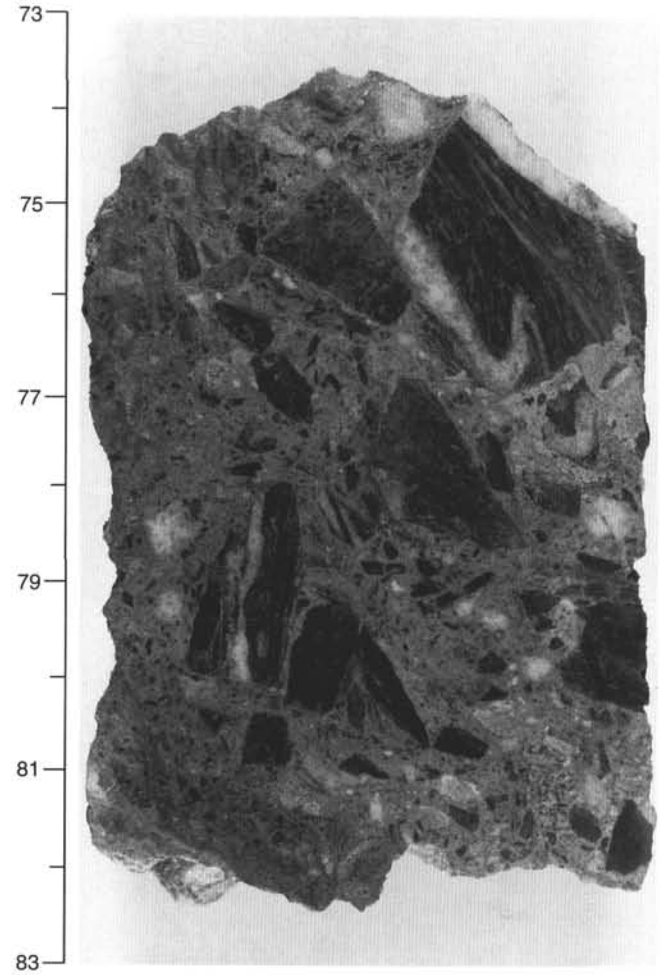

Figure 68. Breccia, showing characteristic lack of sorting, widely varying grain size, and angular shape of the clasts. The clasts mainly consist of biotite schist (one with a folded quartz vein showing an axial planar cleavage) and vein quartz. Several fragments in the breccia may originally have been joined together. Section 976B-75R-1, Piece 9.

heat flow is observed at this site and in general around the Site 976 basement high (see "In Situ Temperature Measurements" section, this chapter). Moreover, retrograde alteration zones can be observed along the faults in the basement (see "Structural Geology and Petrology" section, this chapter).

Carbonate Diagenesis

The alkalinity profile peaks at 15.13 mM at 23.95 mbsf and decreases asymptotically downcore to concentrations slightly below average seawater values (Fig. 116B). This profile indicates that the rate of organic matter decomposition is highest at shallow depths and that alkalinity is consumed at greater depths by carbonate precipitation and/or clay or zeolite formation. The coupled decrease in calcium and magnesium in the upper 100 m of the section (Figs. 112C, D) may indicate minor dolomite precipitation from solution. The strontium and, to a smaller degree, the calcium concentrations increase with depth indicating carbonate recrystallization. Although biogenic carbonate is not very strontium rich, its dissolution and inorganic reprecipitation releases strontium to interstitial waters (Manheim and Sayles, 1974).

Potassium and Silica

Interstitial potassium concentrations decrease downcore to values that are half that of seawater (Fig. 114). This profile is typical for marine sediments and indicates potassium uptake by clays. The interstitial silica profile shows a general decreasing trend with depth, with two outliers at 112.4 and 295.4 mbsf that correspond to a higher diatom abundance (see "Biostratigraphy" section, this chapter). The general trend may indicate a downcore decrease in abundance of siliceous microfossils, although this cannot be confirmed from the available sedimentological data.

Organic Matter Degradation

Ammonium concentrations of up to 5.7 mM reflect the decomposition of organic matter in these relatively organic carbon-rich sediments (average organic carbon content is 0.7%; see "Organic Geochemistry" section, this chapter). Sulfate is completely depleted at 23.95 mbsf through organic matter degradation by sulfate-reducing bacteria. At greater sub-bottom depths, organic matter degradation is mediated by methanogenic bacteria, as evidenced by high headspace methane concentrations and high C_1/C_2 ratios (see "Organic Geochemistry" section, this chapter).

The slight downcore ammonium concentration decrease can be ascribed to ion exchange reactions with clay minerals with a concomitant lithium release. The high concentrations of lithium could be explained by this process if a 1:1 exchange of lithium for ammonia would take place. Phosphate concentrations are below the lower limit of detection except in the upper 140 mbsf, where the highest rates of organic matter degradation occur. Precipitation of an inorganic phosphate phase would provide a sink for this element at depth.

Redox Profiles in Holes 976C and 976D

The major focus of Hole 976D was to study geochemical processes affected by organic matter degradation; therefore, only elements involved in redox processes are discussed here in detail. The interstitial water profiles are a classical sequence of diagenetic reactions (Figs. 116, 117). These illustrate organic carbon degradation through a series of reactions mediated by progressively lower free energy yield per mole of organic carbon metabolized. The Fe^{2+} and Mn^{2+} profiles peak at 1.5 mbsf and decrease rapidly downcore, indicating that the Mn- and Fe-reduction zones are located within the upper 1.5 m of the core. Samples at shallower depths were not collected because of drilling disturbance and subsequent seawater contamination in the uppermost part of the core. Nitrate was not determined as the NO_3^- reduction zone is located above the iron and manganese reduction zones (Froelich et al., 1979).

Sulfate decreases linearly and is completely depleted at 19.95 mbsf. This decrease is accompanied by increases in alkalinity, phosphate, and ammonia, indicating that sulfate reduction is the most important apparent process controlling organic matter degradation in the upper sediments (Table 19). The alkalinity and phosphate maxima at about 15 mbsf indicate the site of maximum organic carbon degradation. Below about 20 m, the headspace methane concentration increases rapidly (see "Organic Geochemistry" section, this chapter), marking the onset of bacterially mediated methanogenesis, which is responsible for organic matter degradation in the absence of interstitial water sulfate (Claypool and Kvenvolden, 1983). The magnesium and calcium decreases may indicate minor dolomite or high magnesium calcite precipitation.

In conclusion, the interstitial water profiles at Site 976 are strongly influenced by the presence of a deep-seated brine, which is either a paleo-fluid trapped below the Pliocene–Pleistocene sediments or a brine derived from salt dissolution with a possible hydrothermal influence. The circulation of this brine may be driven by compaction or by the thermal gradient produced by the high heat flux and channeled

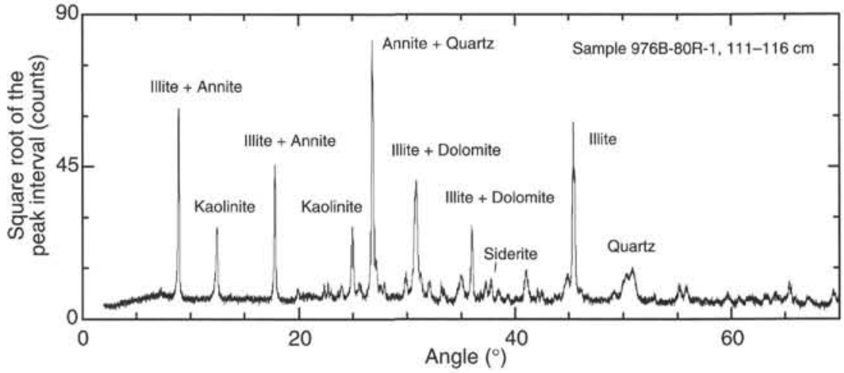

Figure 69. XRD diagram of the matrix of a cemented breccia with fragments of high-grade schist. In the matrix there are relict fragments of annite and quartz. Illite, dolomite, ankerite and minor siderite make up the cement.

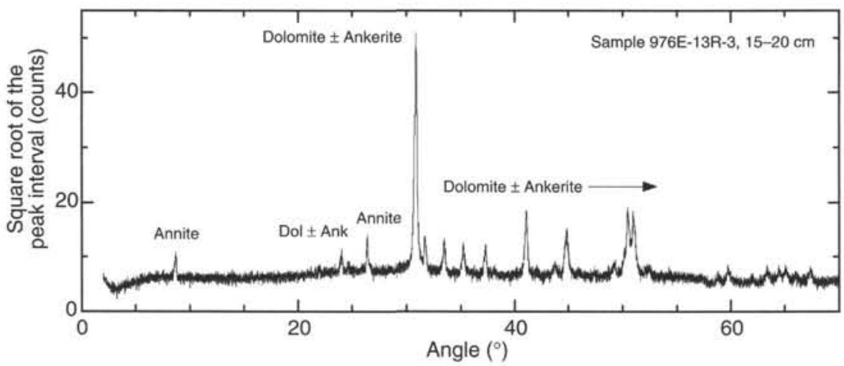

Figure 70. XRD diagram of the matrix of a dark-gray breccia with high-grade schist fragments, cemented by dolomite and ankerite. Relict annite crystals are still present.

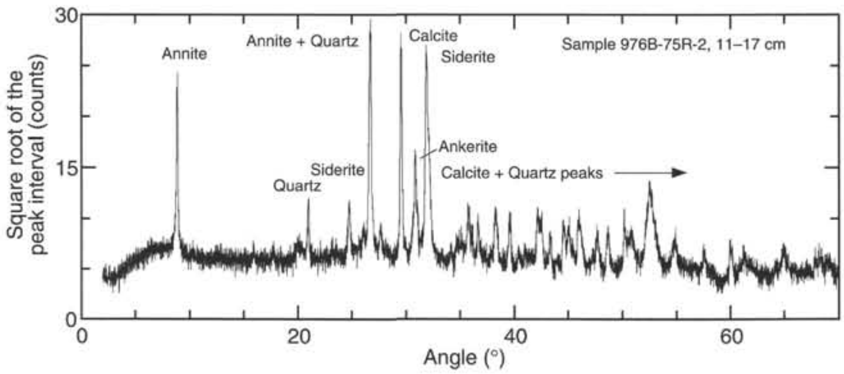

Figure 71. XRD diagram of the matrix of a yellowish brown breccia with marble fragments, cemented by calcite, siderite, and ankerite. Relict annite crystals are still present.

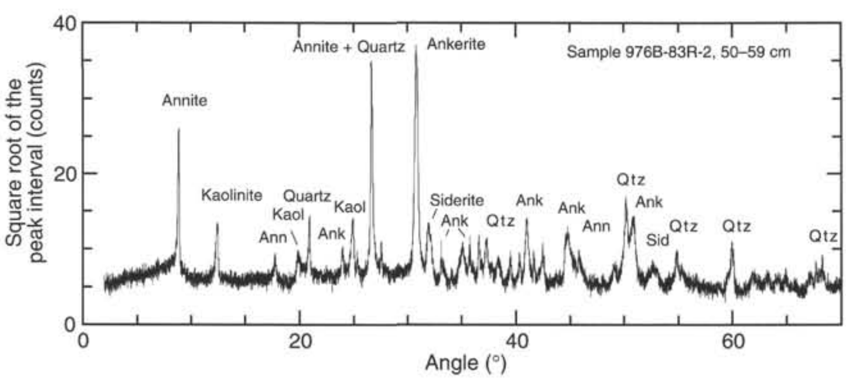

Figure 72. XRD diagram of the matrix of a grayish brown clayey breccia, with kaolinite, siderite, ankerite, quartz, and relict annite crystals.

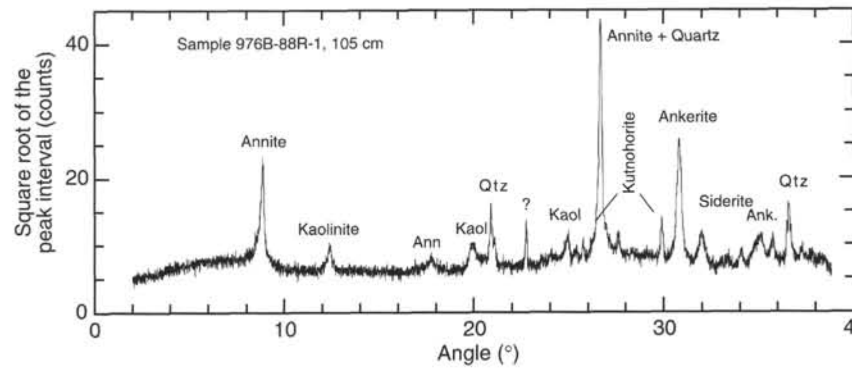

Figure 73. XRD diagram of the matrix of a fault gouge, with annite, kaolinite, and quartz. Ankerite, siderite, and kutnohorite are present in minor amounts.

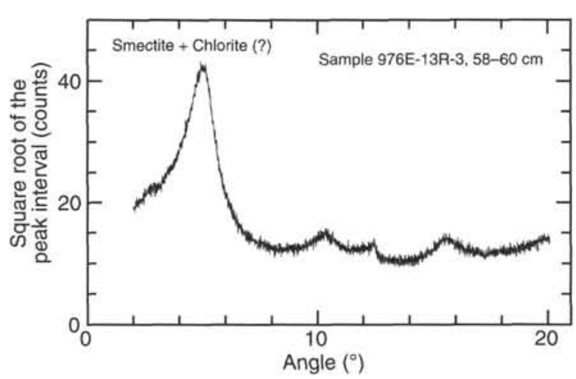

Figure 74. XRD diagram (glycolated) of a smectite and probable chlorite aggregate in a high-grade schist close to the basement-sediment contact.

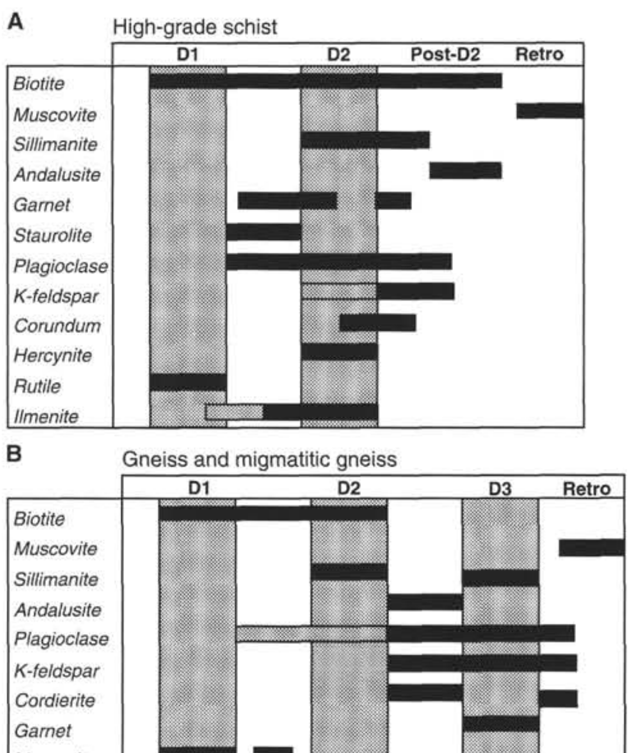

Figure 75. Relationships between metamorphic mineral growth and deformation in (**A**) high-grade schist and (**B**) gneiss. Gray boxes indicate that growth of the mineral has not been demonstrated, but it is likely to have been stable.

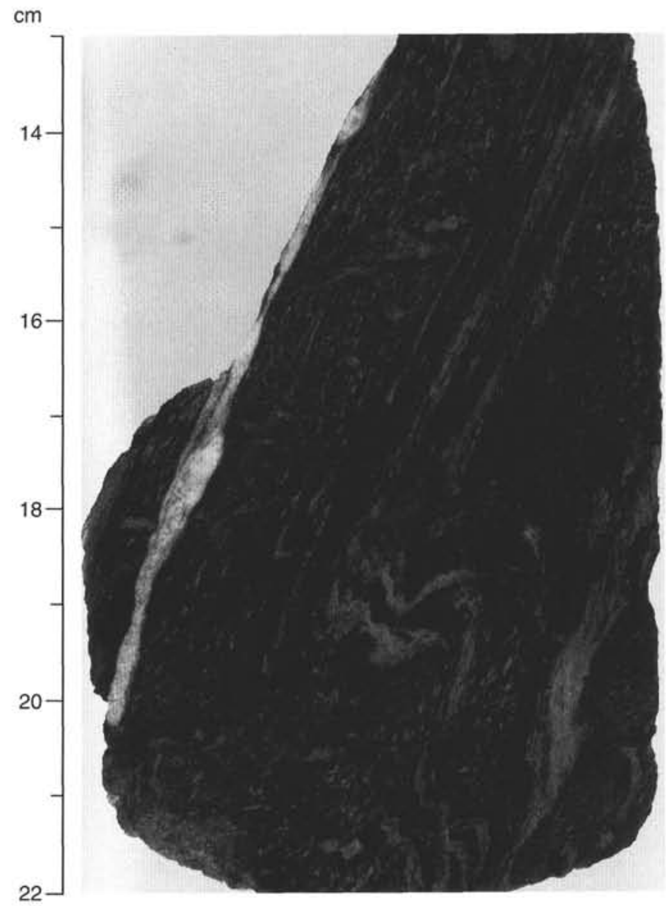

Figure 76. Quartz-biotite-sillimanite schist showing millimeter-scale quartz-biotite, with differentiated layering defining S1, folded by asymmetric D2 folds. Preferred orientation of sillimanite (millimeter-long white lenticles) in the axial plane of the folds. Section 976B-83R-1, Piece 3.

along the sediment-basement contact. Degradation of organic matter is principally mediated by sulfate-reducing bacteria in the top 20 meters and by methanogenic bacteria below that depth.

PHYSICAL PROPERTIES

Introduction

Physical property measurements were made on whole-core sections (MST and thermal conductivity), split cores (sonic velocity), and discrete samples (index properties) for all holes at Site 976. Natural gamma ray (NGR) was measured at 10-cm intervals on all cores

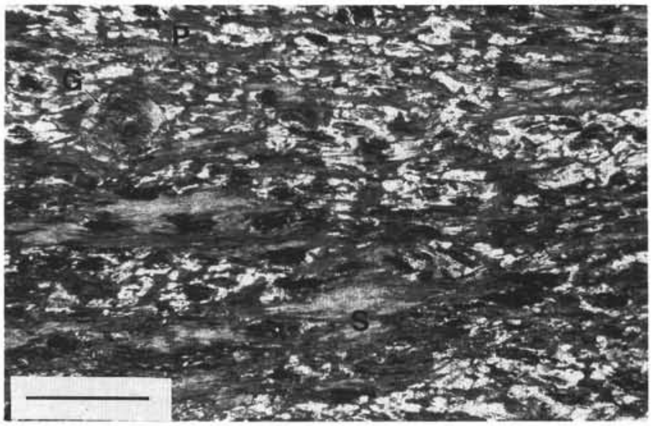

Figure 77. High-grade schist showing the character of the main foliation (composite S1 and S2). The dark background is predominantly well-oriented biotite, partly replaced by fibrolitic sillimanite (S). Abundant plagioclase porphyroblasts (P) have elongate cores colored black by trails of dense graphite dust defining an included fabric (S1) and clear rims. Garnet (G) has inclusion trails defining an internal fabric (S1) that is rotated with respect to the external foliation. The garnet also has late clear rims. Section 976B-74X-1, Piece 4C. TSB #21. Plane light, 2.5× objective. Scale bar is 1 mm.

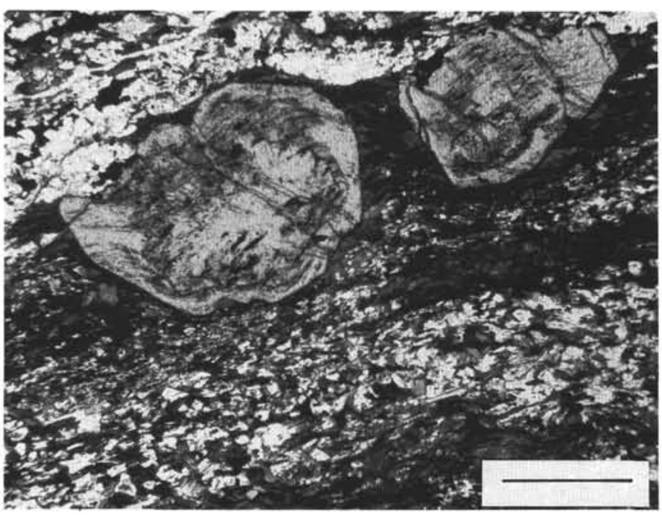

Figure 78. High-grade schist with garnet porphyroblasts. The porphyroblasts have graphitic inclusion trails indicating that they grew statically over the foliation (S1) and rims that indicate growth during or after rotation relative to the foliation. Note mm-scale quartz-biotite differentiated layering defining S1. Section 976B-76R-1, Piece 7A. TSB #28. Plane light, 2.5× objective. Scale bar is 1 mm.

as a part of the MST. Index properties and thermal conductivity were measured once per section on cores from Holes 976A and 976B. Index properties were measured on one or two samples per core for Hole 976C. Thermal conductivity was measured three times per core for Holes 976C and 976D. *P*-wave velocity was measured once per section for Holes 976A and 976B and once per core for Holes 976C, 976D and 976E.

Multisensor Track

The MST data for Holes 976A, 976B, 976C, 976D, and 976E are presented in Figures 118–122. The presentation is done in a format

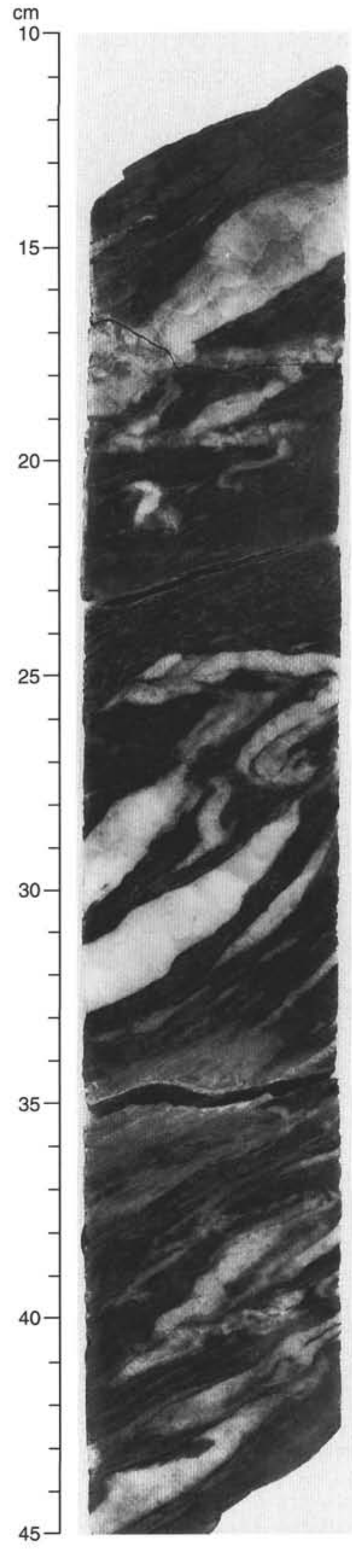

Figure 79. Quartz-biotite-sillimanite schist with abundant quartz veins lying parallel to S1 and folded by D2 folds. Section 976B-77R-1, Piece 1B, C, D.

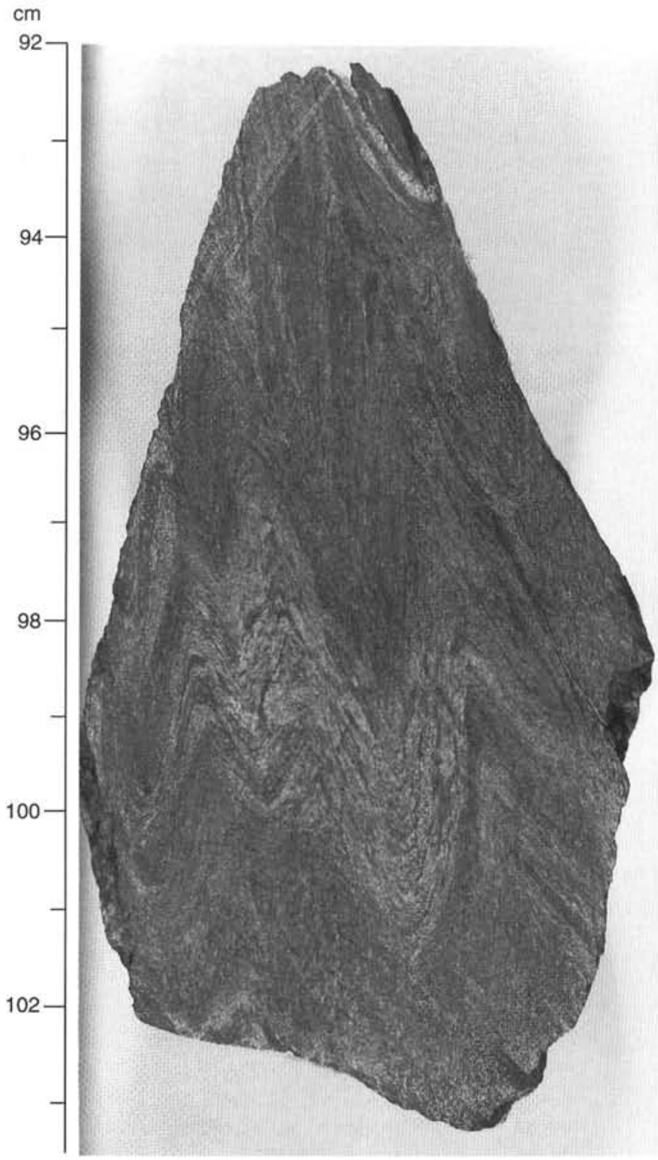

Figure 80. Quartz-biotite schist with symmetrical D2 folds affecting S1 defined by compositional banding and millimeter-scale differentiated layering. Section 976E-15R-2, Piece 11B.

similar to that used for the downhole logging data (see "Downhole Logging," this chapter) to facilitate comparison. The data for Hole 976B are presented in two scales (0–80 and 0–1000 mbsf). A strong increase in magnetic susceptibility and NGR is observed in the metamorphic basement, and will be discussed in detail later.

Thermal Conductivity

Thermal conductivity results for Holes 976A, 976B, 976C, and 976D are shown in Figure 123 and listed in Table 20 (on CD-ROM, back pocket, this volume). There is a slight downhole increase in conductivity. Thermal conductivity values are scattered between 1.0 and 1.5 W/(m·K) with a slight increase in the first 50 mbsf. There is an increase in thermal conductivity in lithostratigraphic Unit II from 375 to 500 mbsf, and a strong increase in conductivity with values reaching 3.5 W/(m·K) in the metamorphic basement (below 700 mbsf).

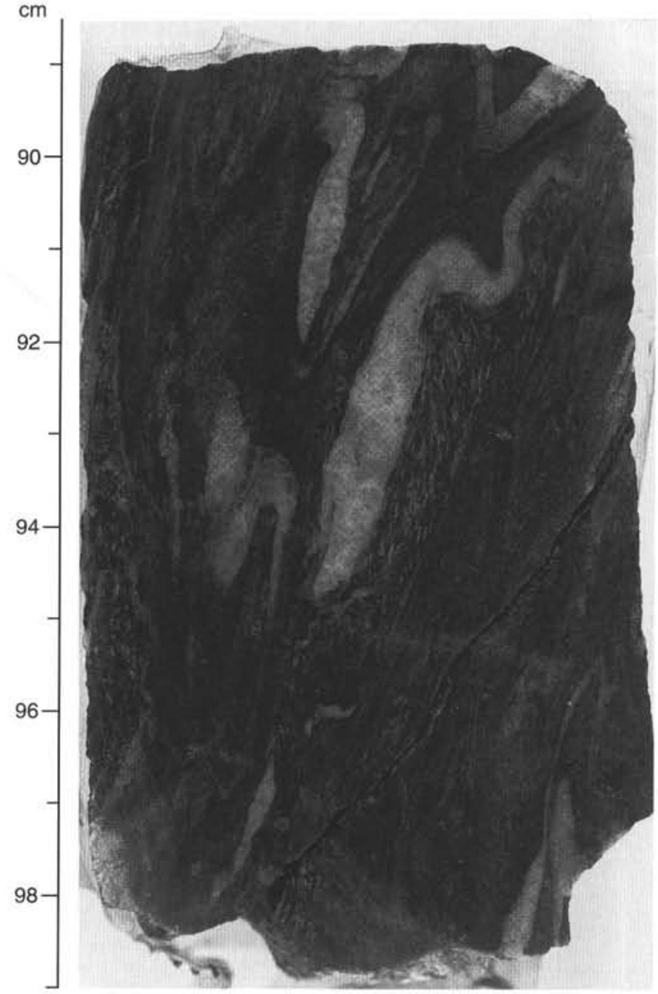

Figure 81. Quartz-biotite-sillimanite schist with D2 folds affecting abundant quartz veins lying parallel to S1. Sillimanite (millimeter-long white lenticles) defines S2 parallel to the axial surface of the fold in the center left of the photograph. Section 976B-82R-2, Piece 9B.

Index Properties

We suspect that changes in bulk density, porosity and void ratio values are strongly affected by the core disturbances because of extensive biscuiting and gas expansion.

Grain densities (Fig. 124; Table 21 on the CD-ROM, back pocket, this volume) show little change with depth, with values ranging between 2.7 and 2.8 g/cm^3.

Bulk density (Fig. 124) increases from 1.1 g/cm^3 at the seafloor to 1.5 g/cm^3 at 360 mbsf. At 360 mbsf, bulk density increases 1.7 g/cm^3 in a semi-lithified sand layer (lithostratigraphic Unit II). Because of poor recovery in lithostratigraphic Unit II, the boundary between lithostratigraphic Units II and III is not prominent. However, there is a slight decrease in bulk density to 1.5 g/cm^3 at 520 mbsf, which continues down to 650 mbsf. At 670 mbsf, there is a sharp increase in bulk density from 1.5 to 2.5 g/cm^3, which corresponds to the transition between lithostratigraphic Units III/IV and the metamorphic basement.

The changes in bulk density correlate with changes in porosity and void-ratio (Fig. 124). Porosity decreases from about 70% at the

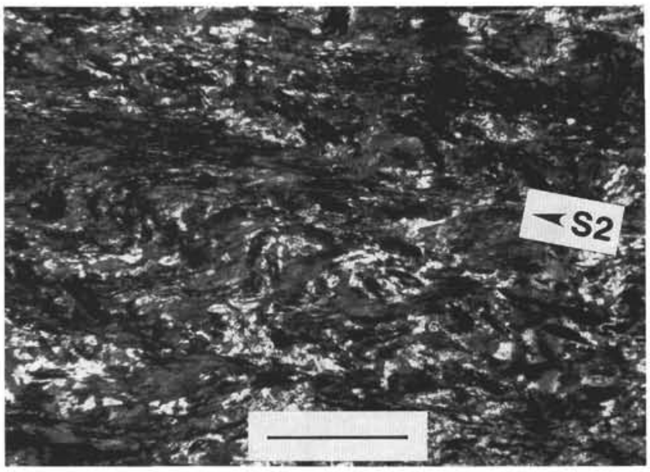

Figure 82. Quartz-biotite-sillimanite schist with a crenulation cleavage (S2). Note the early plagioclase porphyroblasts with very dark graphitic inclusion trails defining S1, which are rotated around the crenulations. The clear inclusion-poor rims on the plagioclase postdate S2. Section 976B-74X-1, Piece 4C. TSB #21. Plane light, 2.5× objective. Scale bar is 1 mm.

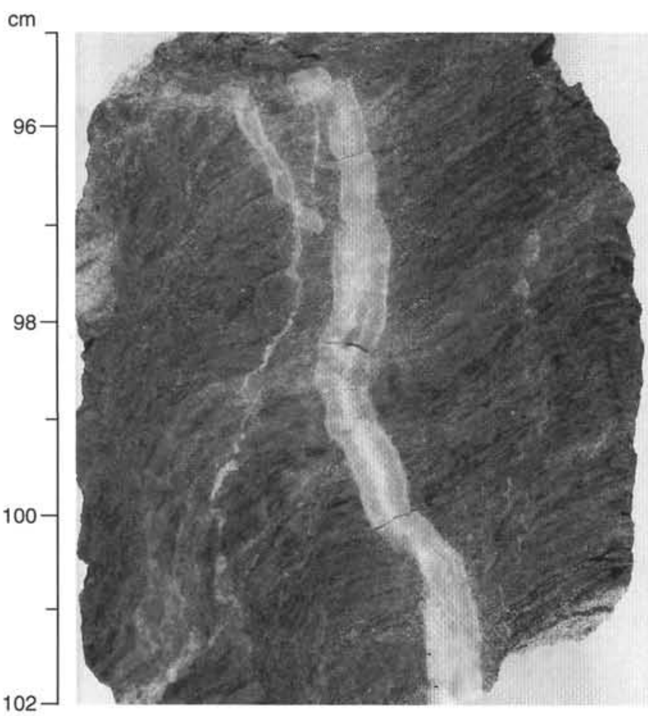

Figure 83. Quartz veins cutting gray gneiss at a high angle to the foliation, indicating that it formed at a late stage in the deformation history. The quartz grains have crystal terminations suggesting that they grew into a fluid-filled space towards the center of the vein. Section 976B-105R-2, Piece 14.

seafloor to 50% at 360 mbsf, and void-ratio decreases from about 3 to 1 at similar depths.

The basement is marked by a strong change in index properties. Bulk density increases to values about 2.5 g/cm^3 and porosity drops to values below 5%.

P-wave Velocity

Due to high gas content in the cores, *P*-wave velocity measurements (Fig. 125; Table 22 on CD-ROM, back pocket, this volume) could be measured only from 0 to 70 mbsf. Velocities of the unconsolidated sediments in this section increase from 1.5 to 1.9 km/s. Below 70 mbsf, the signal was attenuated because of partial water saturation as a result of gas expansion. Some discrete measurements made in the semi-lithified sands of lithostratigraphic Unit II gave a velocity of about 5 km/s. The metamorphic basement rocks have velocities between 5.5 and 6.4 km/s and are highly anisotropic (up to 40%).

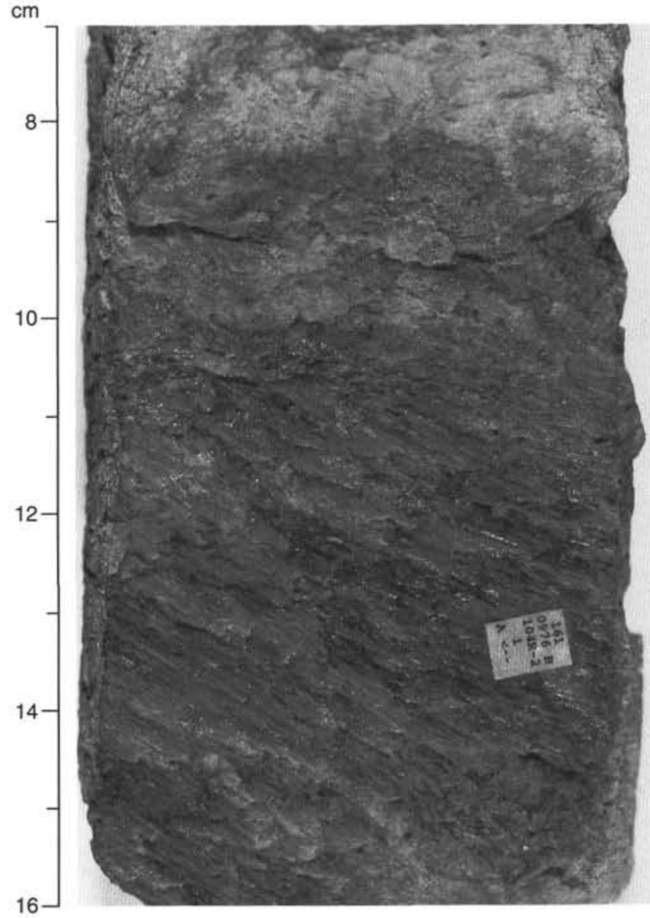

Figure 84. Stepped calcite fiber lineations on a steeply dipping fault plane cutting a zone of coherent fault gouge and breccia. The stepped terminations on the fibers indicate oblique left-lateral slip. Section 976B-104R-2, Piece 1.

Basement

The metamorphic basement cored in Holes 976B and 976E is marked by strong changes in physical properties. Measurements taken in the basement are shown in Figures 126 (velocity, anisotropy), 127 (thermal conductivity), and 128 (natural gamma radiation).

Changes in velocity, velocity anisotropy, and natural gamma radiation data allows us to sub-divide the basement into three different units. The first unit, physical property (PP) basement unit I, between 680 and 725 mbsf, shows variable velocities (3.5 to 6.5 km/s), high velocity anisotropy (40%), high thermal conductivity (3.2 W/[m·K]), and high natural radiation. The second, PP basement unit II, between 725 and 825 mbsf, shows less variability of velocity values, the velocity anisotropy drops to about 10%, and thermal conductivity and natural radiation also drop significantly. PP basement unit III (825 to 920 mbsf, total depth cored) is similar in characteristics to the top PP basement unit I. Division of the basement in three units on the basis of physical property changes is similar to those identified in the logging data and correspond to Log Units 1, 2, and 3.

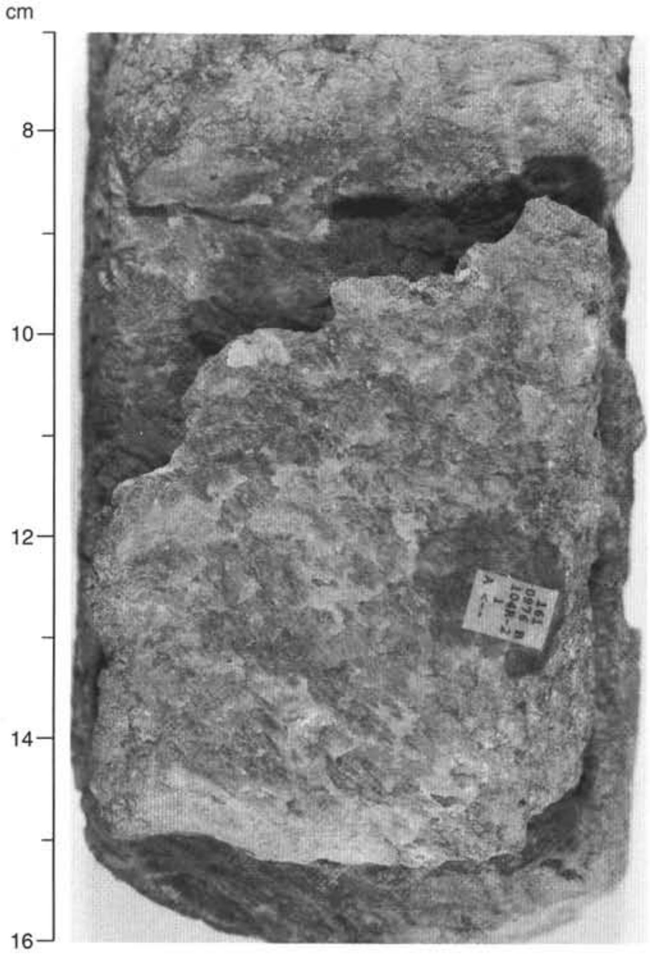

Figure 85. The hanging wall and footwall of the fault shown in Figure 84 have been separated by 1 cm to show the jagged shape of the branch line where two oblique-slip faults join in the central part of the photo (Section 976B-104R-2, Piece 1, 7–16 cm, opposite side). The branch line makes an average angle of 70° in the plane of the fault with respect to the striations.

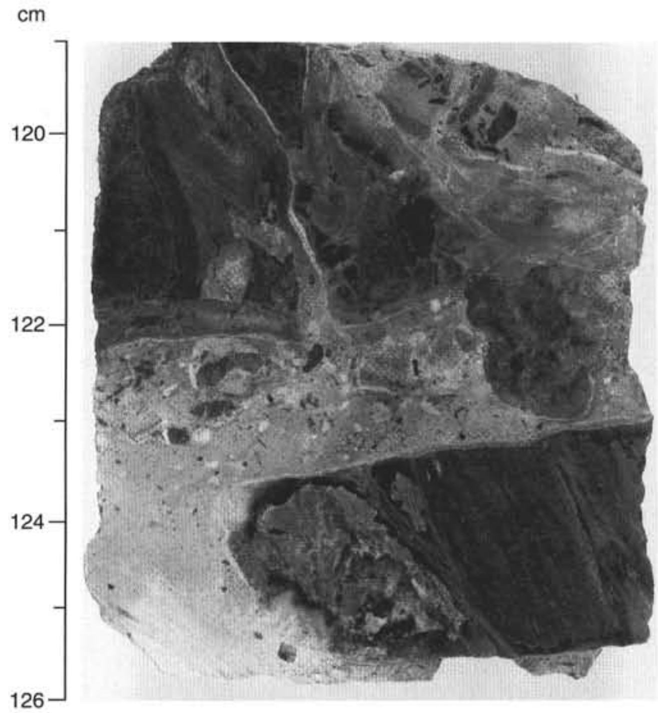

Figure 86. Breccia filling a fissure in basement rock. The carbonate-rich matrix from this breccia has yielded nannofossils of Miocene age. Section 976E-17R-1, Piece 7B.

DOWNHOLE LOGGING

Operations

A full suite of logging tools was run at Site 976 (Holes 976B and 976E; Fig. 129; Table 23). This included: quad combination (quad combo), Formation MicroScanner (FMS), geochemical tool (GLT), and BoreHole TeleViewer (BHTV). The Lamont-Doherty temperature logging tool (TLT) was attached at the base of the quad combo and the GLT.

The first set of log data were acquired in the upper part of the sedimentary sequence in Hole 976B. Only the quad combo was used, and it showed that the borehole was too large for the calipers over most of the interval, a result of serious washout (see "Operations" Section, this volume). Hence, data corrections for borehole effects are incomplete in the out-of-gauge parts of the hole.

A complete suite of log data was collected in the basement part of Hole 976B. The drill pipe was set below the sediment-basement interface (at 696.0 mbsf), to maximize the chances of success in basement logging. Hole conditions were better in the lower part of the basement. Quad combo, FMS, BHTV, and GLT tool strings were run and obtained excellent results. Repeat sections were achieved with all the tool strings. The TLT showed a borehole fluid temperature of 47°C at total depth (903 mbsf; 2022 mbrf) on the first run (Fig. 130). This temperature is significantly lower than the expected in situ temperature because of seawater circulation in the borehole during drilling and prior to logging. The data were collected only a few hours after the wiper trip. The TLT log data from the GLT run shows a maximum temperature 4°C warmer, a result of an additional 5 hr of thermal rebound (Fig. 130).

For the third logging operation, the drill pipe was pulled up above the sediment-basement interface to allow logging of the sediment/basement contact. However, bridging and hole collapse prevented the logging tools from reaching the top of basement. The quad combo data indicated major variations in hole diameter and the data were thus fair to poor in quality. Log data that are less dependent on borehole conditions, such as resistivity and velocity, may be of relatively good quality.

Logging operations in Hole 976E covered the transition between basement and sediments, a zone that was not possible to log in Hole 976B. A single run of the quad combo from the basement into the sediments and a short repeat run within the sediments were obtained. The TLT was also used while logging this hole, but the tool returned to the surface filled with clays, and the resulting temperature measurements are probably significantly lower than the real hole temperature. Twenty meters of sediment fill was found in the bottom of the hole, and the quad combo had to penetrate a bridge at the sediment/basement contact. During the upward logging run out of the hole, the sediments had closed in upon the logging cable above the tool, and the tool was extracted from basement with difficulty. The repeat run was only in the sedimentary sequence, as it proved impossible to penetrate down to the basement because the bridge was several meters thicker than during the first run.

Scientific Results

After preliminary analysis of the logging data, three main log units can be differentiated in the basement of Hole 976B (Fig. 129):

1. Log unit I (675–752 mbsf). This unit has a mean density of 2.3 g/cm^3 and a neutron porosity of ~30%–35%. The resistivity of

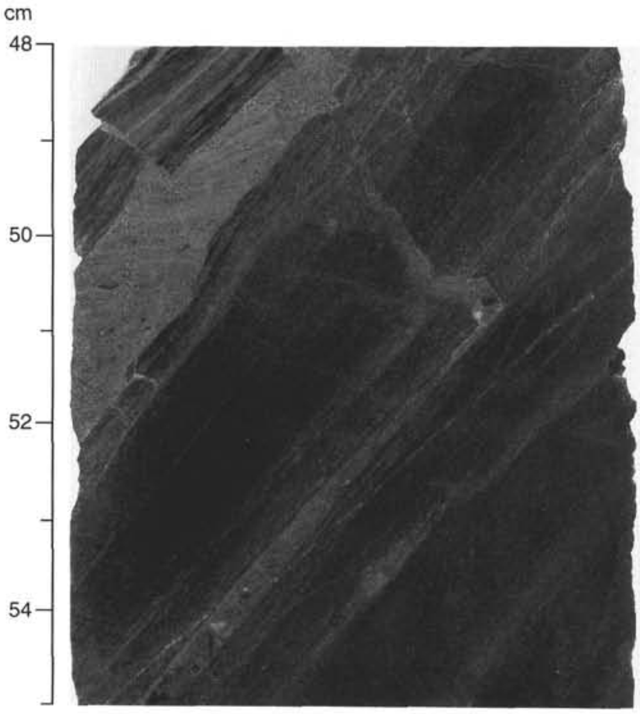

Figure 87. Horizontally laminated carbonate-rich microbreccia filling a fissure in high-grade schist. The fissure is parallel to the foliation, and has opened roughly normal to the foliation. Section 976E-21R-2, Piece 7.

this lithologic unit is uniform and rather low, averaging 3.5 Ωm.

2. Log unit II (752–788 mbsf). This unit is characterized by an increase in the borehole diameter and elongation. These are probably tectonic in origin and may reflect the presence of a brecciated fault zone. The GLT-computed chemical element ratios also distinguish this unit from the previous one (Fig. 131), with, for example, higher iron content. This indicates probable alteration of the primary rock and redistribution of different chemical elements to clays and carbonates along the fault planes. There was poor core recovery in this interval and the recovered cores present numerous indices of tectonic deformation (see "Structural Geology and Petrology of the Basement" section, this volume).
3. Log unit III (788–925 mbsf). The main logs (bulk density, neutron porosity) for the third unit are rather uniform in character. Density averages 2.4 g/cm^3, neutron porosity decreases to 20%, and resistivity is higher than in log unit I (9 to 10 Ωm). This is also suggested by the different electrical response in the two log units. The photoelectric effect is also higher, with high values correlated with light-colored rock intervals (i.e., granitic rocks, migmatites, carbonates). This unit may be subdivided into three subunits (788–825, 830–865, and 870–925 mbsf, respectively), characterized by changes in the hole diameter. The boundaries of these subunits (~5 m thick) are also characterized by an ellipticity of the borehole section, as shown by the increasing difference between the measurement of the two orthogonal FMS calipers (Fig. 129B). This elongation probably reflects a tectonic deformation in the vicinity of fault zones, perhaps a result of a local reorganization of the stress field. In the dark-colored brecciated samples recovered and described on cores, the photoelectric factor is lower.

These units fit well with the structural and petrological descriptions of cores and allow the nature of the unrecovered intervals to be partially defined. Log unit II corresponds to a highly brecciated and faulted zone that marks the transition between metasediments (above, log unit I) and gneissic material (below, log unit III). Log unit III is also characterized by higher natural radioactivity, partly because of the presence of K-feldspars in these rocks or in the granitic veins encountered in this unit. The hole diameter variations shown by caliper

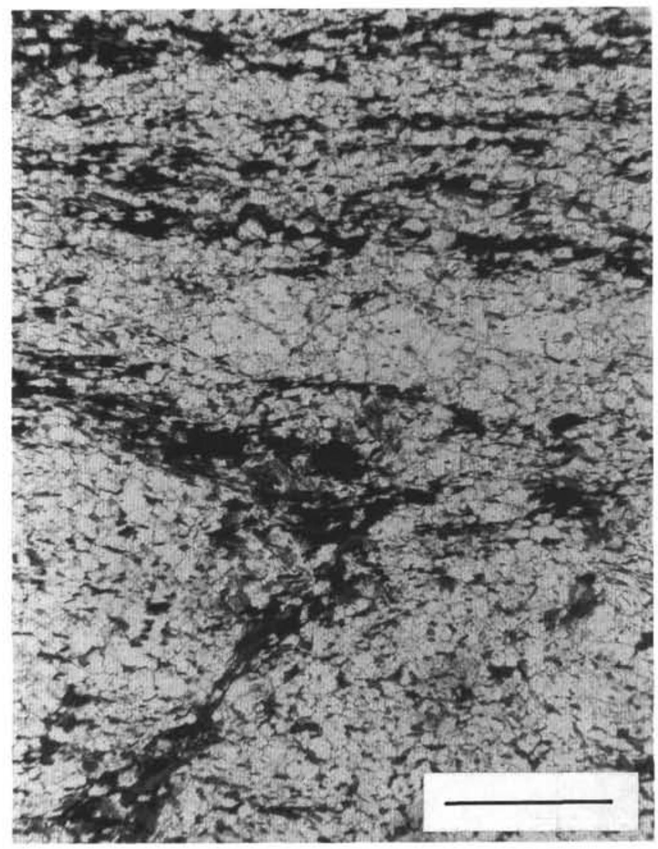

Figure 88. D2 fold deforming S1. S1 is defined by oriented biotite and by quartz-rich and biotite-rich laminae. S2 (horizontal) is defined by oriented biotite recrystallized in the fold hinge. High-grade schist, Section 976B-77R-3, Piece 6. TSB #34. Crossed polars, 2.5× objective. Scale bar is 1 mm.

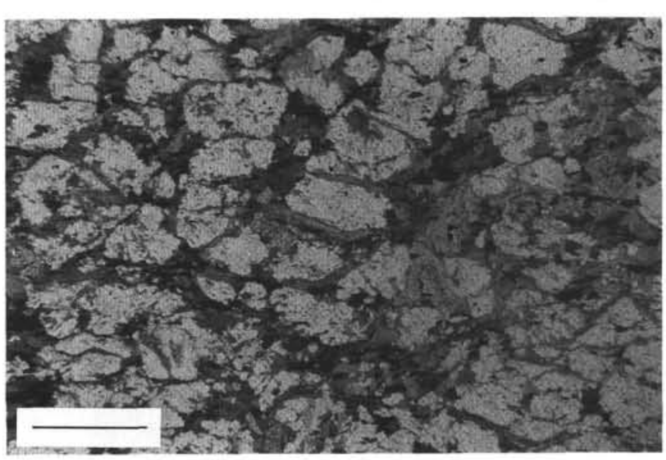

Figure 89. High-grade schist with a massive texture produced by the growth of late inclusion-poor plagioclase (light-colored) and poorly oriented biotite (dark) after D2. Section 976B-74X-1, Piece 6A. TSB #22. Plane light, 2.5× objective. Scale bar is 1 mm.

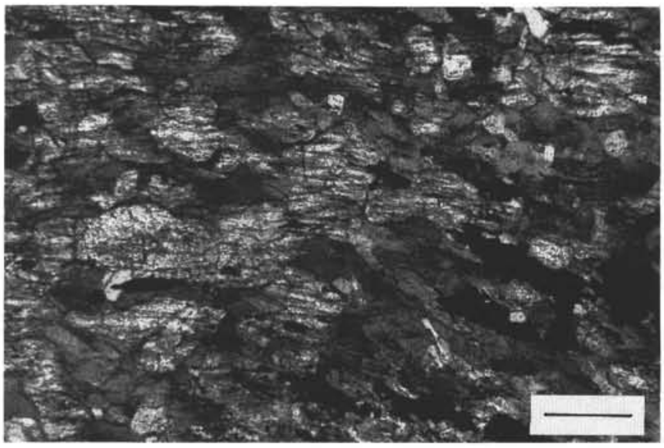

Figure 90. Elongate staurolite porphyroblasts (light-colored) with straight inclusion trails defining S1. These are parallel to the external fabric, defined by oriented biotite (dark). High-grade schist, Section 976B-76R-1, Piece 7A. TSB #28. Plane light, 10× objective. Scale bar is 200 µm.

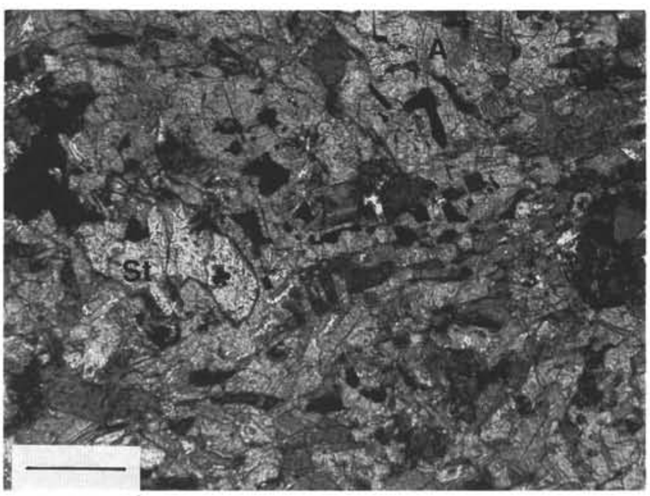

Figure 91. Relict staurolite grain (St) included in andalusite (A). Andalusite occupies most of the field of view and also includes biotite (dark) and opaque oxide (black). High-grade schist, Section 976B-74X-1, Piece 6A. TSB #22. Plane light, 10× objective. Scale bar is 200 µm.

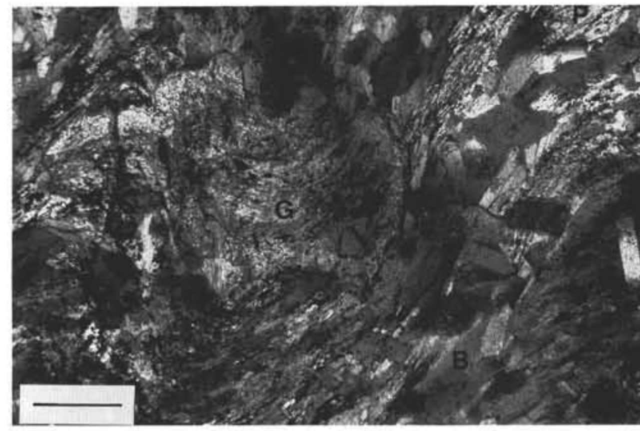

Figure 92. Garnet porphyroblast (G) with inclusion trails showing that it has grown statically over D2 crenulations in S1. The garnet crystal extends to the left-hand edge of the photograph. Note plagioclase porphyroblast (P) with straight inclusion trails, and late poorly oriented biotite (B). High-grade schist, Section 976B-76R-1, Piece 7A. TSB #28. Plane light, 10× objective. Scale bar is 200 µm.

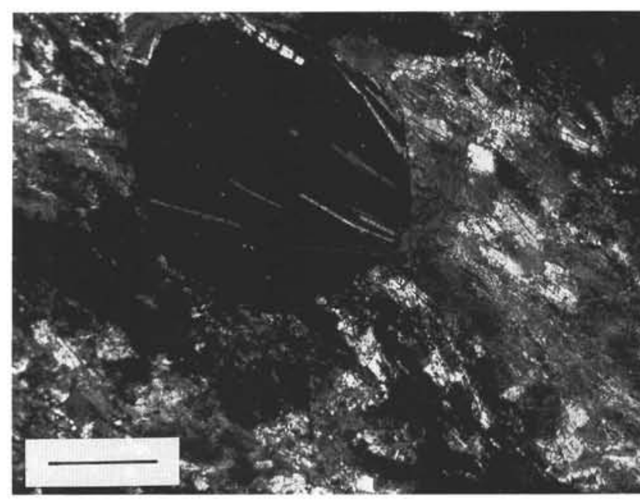

Figure 93. Idiomorphic garnet (black) with inclusions of prismatic sillimanite (white). High-grade schist, Section 976B-74X-1, Piece 4C. TSB #21. Crossed polars, 10× objective. Scale bar is 200 µm.

measurements in Log unit III appear to correspond to breccias and fault intervals. Granitic or migmatitic rocks (for example, at 844, 870, and 900 mbsf) and carbonates (for example, 723 mbsf) are also clearly identified, being correlated with higher values in the photoelectric factor and, for the granitic or migmatitic rocks, increases in the radiogenic potassium concentration due to crystallization of K-feldspar.

The large variations of hole diameter in the upper and middle (sedimentary) logged intervals in Hole 976B require post-cruise reprocessing of the data. Resistivity and velocity (from reprocessed sonic travel times) for these intervals are presented in Figure 132.

Unprocessed electrical (FMS) and acoustic (BHTV) images suggest that they are of high quality. The different log units (defined using "standard" logs) are recognized in the FMS images and show electrically distinct patterns. The more conductive intervals appear to fit well with brecciated clay-rich fault zones identified in other logs and in cores (for example, 703–707, 805–806 mbsf). Correlations can be made between changes in FMS microresistivity records, BHTV transit time and amplitude variations, as well as caliper, natural radioactivity, and photoelectric factor.

In Hole 976E, the resistivity and reprocessed velocity data are shown in Figure 133. The quad combo data from the basement in this borehole show a considerably different character from that of Hole 976B (Fig. 134), as was also detected in the recovered cores (see "Structural Geology and Petrology of the Basement" section, this chapter). In the electrical response there is a smooth transition over ~7 m from the sediments to the basement. In other logs (caliper, bulk density, potassium content, neutron porosity, photoelectric factor), the change is more abrupt and places the basement top at 652–653 mbsf (Fig. 135). Velocity and resistivity are high in the uppermost 20 m of the basement and there is then an abrupt and significant decrease in these values at 670 mbsf. This is also reflected in the other log measurements and may be correlated with the occurrence of calcareous- or dolomitic-matrix breccias containing Miocene microfossils (see "Lithostratigraphy" section, this chapter). As in Hole 976B, we found a good correlation between logs and recovered core description.

IN SITU TEMPERATURE MEASUREMENTS

Downhole temperature measurements were made with the ADARA temperature tool once in Hole 976B and four times in Hole 976C. The one run in Hole 976B was not used in the data analysis be-

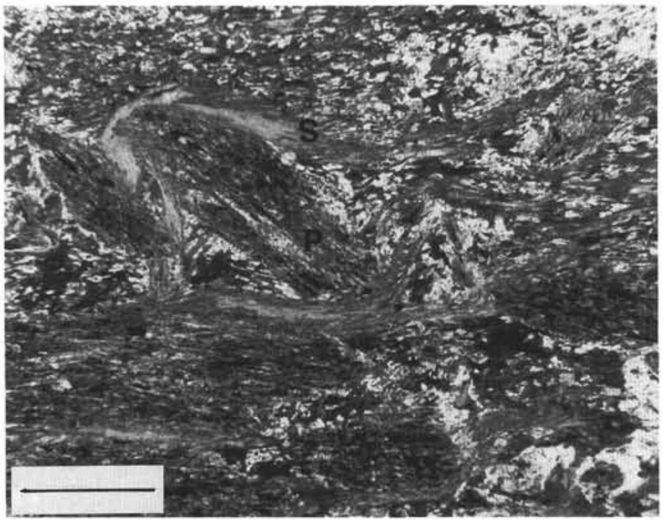

Figure 94. Large plagioclase (P) porphyroblasts in high-grade schist with graphitic inclusion trails indicating that they grew statically over an early foliation (S1), and were subsequently rotated during D2. The central porphyroblast is wrapped around by sheaves of fibrolitic sillimanite (S) that define S2. The groundmass is made up of late biotite (dark) and clear plagioclase. Section 976B-76R-1, Piece 7A. TSB #28. Plane light, 2.5× objective. Scale bar is 1 mm.

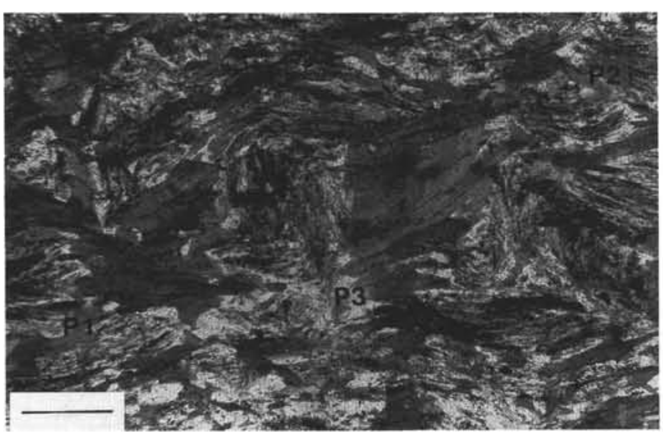

Figure 95. Plagioclase porphyroblasts with graphitic inclusion trails in a crenulated quartz-biotite-sillimanite schist. Most grains (e.g., P1) have straight inclusion trails, suggesting growth between D1 and D2. Some grains have slightly curved trails (e.g., P2) indicating that growth continued during D2. The grain at the center (P3) is made up of several individual porphyroblasts with straight or slightly curved trails. These were apparently rotated about the D2 crenulations. The microstructure in the groundmass has been strongly modified by late growth of biotite (dark). Section 976B-74X-1, Piece 6A. TSB #22. Plane light 10× objective. Scale bar is 200 µm.

cause the core barrel moved while the tool was in the formation. All of the Hole 976C measurements were good. The WSTP temperature tool was used at three depths in Hole 976B. The shallowest measurement failed because of operational problems, but the two deeper measurements were successful.

The ADARA and WSTP temperature data were reduced to in situ values (Table 24). The individual temperature measurement runs are shown in Figure 136. Temperature and thermal conductivity measurement data were combined to determine the heat flow (see "Physical Properties" section, this chapter). The thermal conductivity does

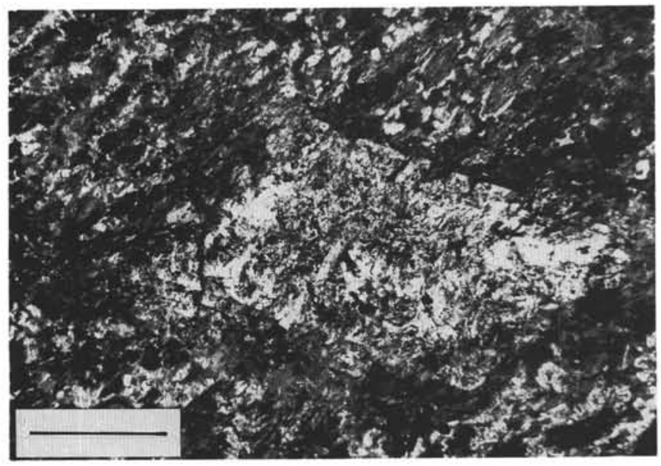

Figure 96. Andalusite porphyroblast in quartz-biotite-sillimanite schist showing a post-kinematic relationship to S2. Section 976B-84R-1, Piece 8B. TSB #48. Plane light, 2.5× objective. Scale bar is 1 mm.

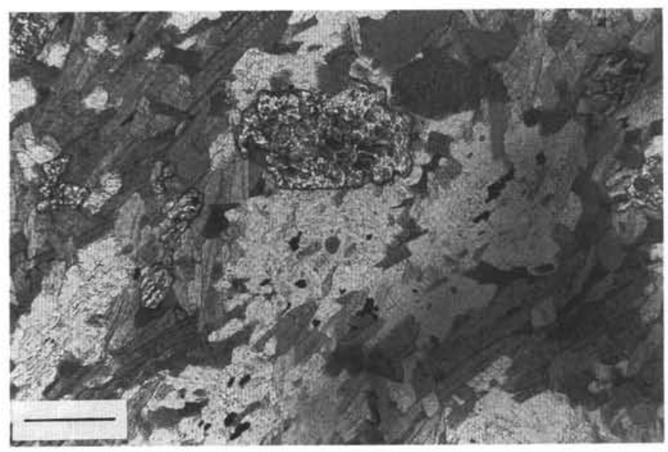

Figure 97. Corundum (very high relief) in schist with biotite (dark) and plagioclase (light). Section 976B-75R-2, Piece 7. TSB #26. Plane light, 10× objective. Scale bar is 200 µm.

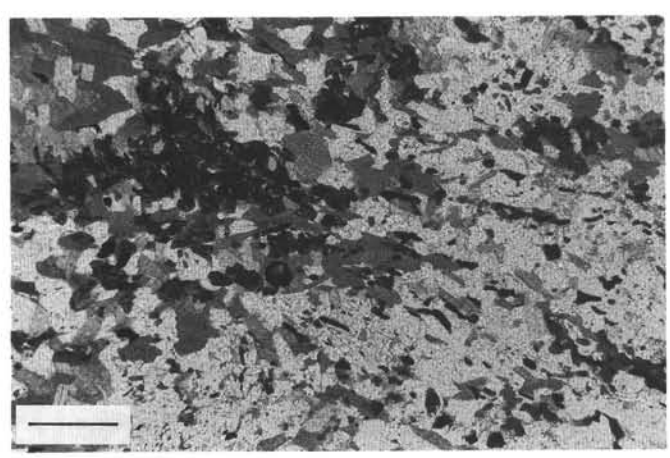

Figure 98. Aggregates of dark green spinel (hercynite) in biotite-plagioclase schist. Section 976B-76R-1, Piece 9A. TSB #29. Plane light, 10× objective. Scale bar is 200 µm.

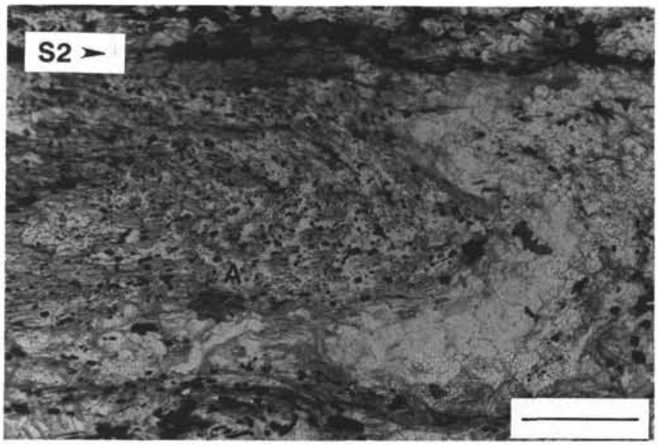

Figure 99. Andalusite porphyroblast (A) with inclusion trails of opaque oxide that define a D2 microfold. The porphyroblast occupies most of the center and left of the photograph. It also includes biotite and fibrolite lying parallel to the weak crenulation cleavage S2. The andalusite grain was subsequently broken up into a large number of small rounded grains and partly replaced by plagioclase (see Fig. 100). Gneiss. Section 976B-94R-1, Piece 3. TSB #50. Plane light, 2.5× objective. Scale bar is 1 mm.

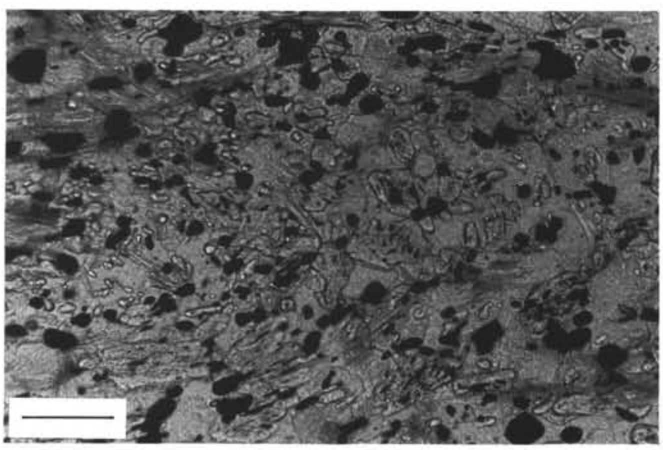

Figure 100. Close-up of the andalusite porphyroblast illustrated in Figure 99 showing how the grain has become fragmented by deformation and partial replacement by plagioclase. Note inclusions of fibrolite. Section 976B-94R-1, Piece 3. TSB #50. Plane light, 10× objective. Scale bar is 200 µm.

Figure 101. Gneiss with mylonitic fabric defined by intensely oriented sillimanite (S) and augen of opaque oxide (black) and aggregates of quartz and feldspar (white). 976B-95R-2, Piece 1C. TSB #51. Plane light, 2.5× objective. Scale bar is 1 mm.

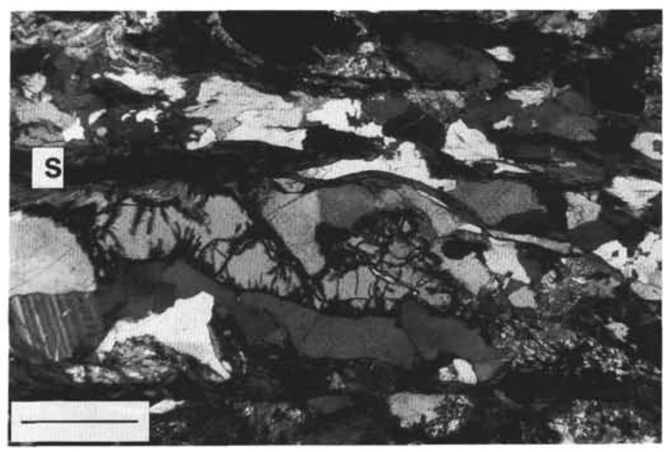

Figure 102. Gneiss with mylonitic fabric defined by intensely oriented sillimanite (S). Cordierite (elongate porphyroblast at center, showing alteration to fine-grained sheet silicates), quartz, and feldspar form augen in the foliation. Section 976B-95R-2, Piece 1C. TSB #51. Crossed polars, 2.5× objective. Scale bar is 1 mm.

not show a significant trend with depth above the sands at 375 mbsf. The temperature data were plotted vs. the integrated thermal resistivity in Figure 137. The slope of linear regression is the heat flow, 102 mW/m^2.

This value is in excellent agreement with other values measured nearby (Polyak et al., in press). The closest heat flow measurement to Site 976 is almost identical, 103 mW/m^2 (Fig. 138). There is a local maximum in surface heat flow over the basement DSDP Ridge. The magnitude of the anomaly is more than can be accounted for simply by thermal refraction and is probably caused by hydrothermal circulation within basement (Polyak et al., in press). Hydrothermal circulation associated with basement highs in areas of thick sediment cover has been encountered elsewhere (Embley et al., 1983). The thick sediment cover acting as a thermal blanket over the basement forces a concentration of circulation within the basement highs, where the thermal resistance to conductive heat flow through the overlying sediment is least. This enhanced circulation within basement has implications for sediment pore-water profiles and for alteration within the basement.

SITE GEOPHYSICS

Two intersecting seismic reflection profiles were collected over Site 976 (Figures 139–141). We used a 200-in^3 water gun for the first seismic line (Fig. 140) to better image the deep basins on either side of the basement ridge. The second seismic line (Fig. 141) was oriented along the top of the basement high and passed over Site 976 and DSDP Site 121. The sedimentary cover over the basement was much thinner along the second seismic profile, so we used an 80-in^3 water gun to better image the sedimentary sequence to be drilled. We saw almost no difference between the data collected with the two different seismic sources.

At Site 976, the sedimentary cover overlying acoustic basement exhibits three seismic units, which correspond to Western Alboran Basin seismic units I, III, and IV as defined by Comas et al. (1992) and Jurado and Comas (1992). Surrounding the basement high where Site 976 is located, the good penetration of the *JOIDES Resolution* single-channel seismic profiles reveals the distinctive seismic character of Messinian seismic unit II and the middle Miocene seismic unit V (Comas et al., 1992). The correlation of seismic and Lithostrati-

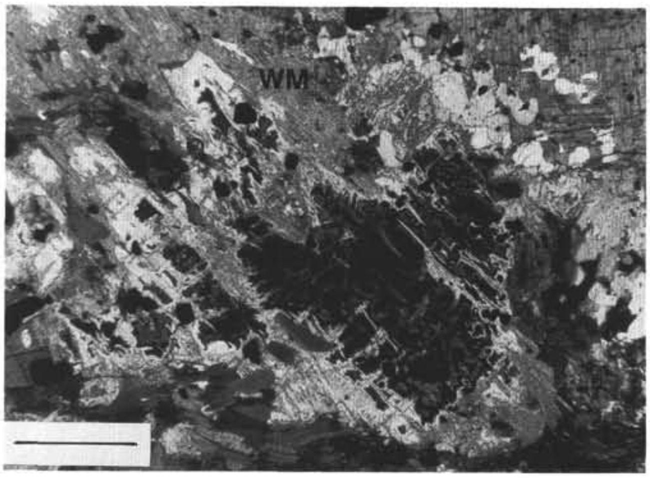

Figure 103. Cordierite porphyroblast in granitic leucosome in migmatitic gneiss, showing the characteristic alteration to fine-grained white mica (WM) and chlorite (dark). The porphyroblast occupies most of the center and left of the field of view and includes grains of opaque oxide. Large twinned plagioclase is present at top right. Section 976B-97R-1, Piece 2. TSB #52. Crossed polars, 2.5× objective. Scale bar is 1 mm.

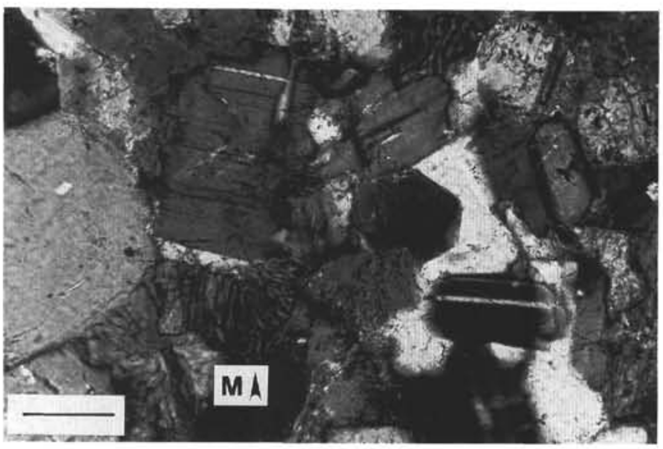

Figure 104. Myrmekitic texture (M) around plagioclase in granitic leucosome in migmatitic gneiss. Section 976B-98R-1, Piece 14. TSB #54. Crossed polars, 10× objective. Scale bar is 200 μm.

graphic Units at Site 976 (see "Lithostratigraphy" section, this chapter) is shown in Table 25.

Seismic Unit I (Pliocene–Pleistocene)

Subunit Ia: The Pleistocene sequence is characterized by parallel, high-amplitude, and continuous reflectors that roughly mimic the bottom topography and represent hemipelagic basin fill deposits. At Site 976, subunit Ia is 0.43 s (two-way traveltime [TWT]) thick (Figs. 140, 141). Subunit Ia conformably overlies subunit Ib, except where subunit Ib has been incised by channeling.

Subunit Ib: On regional scale, this seismic unit has an overall transparent character that passes upward into sub-parallel, discontinuous, and parallel reflectors that are transitional to subunit Ia. Laterally, subunit Ib seismic facies changes to medium amplitude wavy and discontinuous divergent reflections that appear as mounds or lenses and may represent channel-fill deposits. At Site 976, subunit Ib exhibits this channel facies, is 0.15 s TWT thick, and unconformably overlies seismic unit III (Fig. 139).

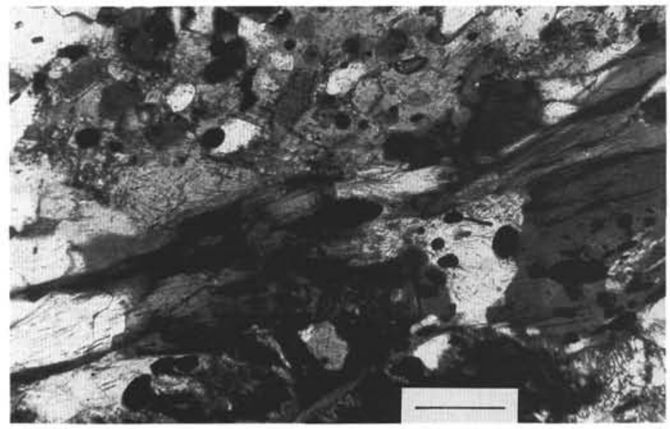

Figure 105. Elongate spongy porphyroblast of K-feldspar in gneiss (top half of photograph), full of rounded inclusions of quartz and plagioclase. The porphyroblasts form augen within the main foliation in the rock (S3), defined by oriented fibrolitic sillimanite (center) and biotite. Note that the fibrolite is included within quartz grains. Section 976B-98R-1, Piece 14. TSB #54. Crossed polars, 10× objective. Scale bar is 200 μm.

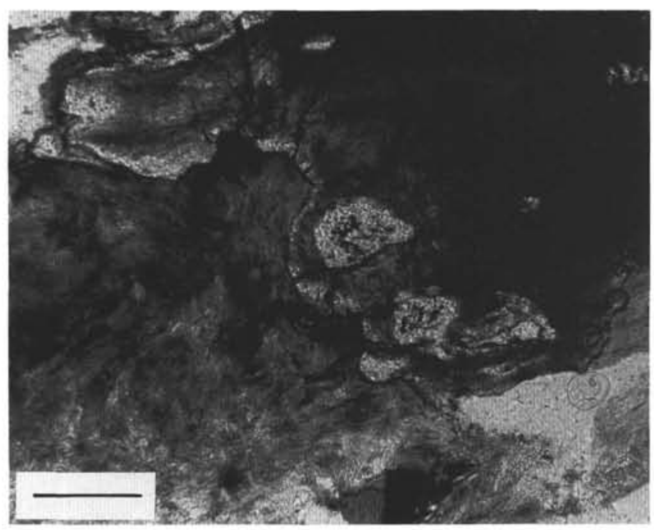

Figure 106. Late garnet growing from fibrolitic sillimanite in gneiss. The fibrolite forms a felted mat in the lower left of the photograph, and the rounded margins of the garnet are visible extending from the upper left to the lower right. The garnet extends to the right-hand side of the photograph and beyond. Most of the garnet is crowded with fibrolite needles, but small patches of clear garnet are visible in the center of the photograph. Section 976B-98R-1, Piece 5. TSB #53. Plane light, 10× objective. Scale bar is 200 μm.

The unconformable contact of seismic units I and III is marked by a high-amplitude reflector that represents an erosional unconformity that merges laterally with the top of the Messinian seismic unit II (Fig. 140).

Seismic Unit II (Messinian)

Seismic unit II was not penetrated at Site 976. About 3.5 km northwest of Site 976 (Fig. 140), unit II corresponds to a thin seismic interval (0.05 s TWT) bounded by strong high-amplitude reflectors. Regionally (see Fig. 1, back pocket, of "Underway Geophysics" chapter, this volume), this unit expands to a maximum thickness of

Table 12. Distribution of metamorphic minerals in thin sections from Hole 976B.

Thin section	Core, section	Piece	Lithotype	Mineralogy: Qtz	Bt	Ms	Chl	Sil	And	St	Grt	Crd	Fd	Pl	Crn	Px	Amp	Spl	Others
18	73X-1	5	High-grade schist	♦	♦	•		♦	♦		x		♦	♦					Cal, Trm, Ap, Opq, Grp
19	74X-1	4A	High-grade schist	♦	♦						♦			♦					Zr, Opq, Grp
20	74X-1	4A	Altered high-grade schist	♦	♦	•	•				x			♦					Cal, Ap, Zr, Opq
21	74X-1	4C	High-grade schist	♦	♦	•		♦	♦	x	x			♦					Trm, Opq, Grp
22	74X-1	6A	High-grade schist	♦	♦	•		♦	♦	x	♦			♦				x	Ap, Zr, Rt, Opq, Grp
23	74X-1	6A	High-grade schist	♦	♦						x			♦					Zr, Ap, Trm, Opq, Grp
24	74X-1	11A	High-grade schist	♦	♦			♦	♦	x	♦		♦	♦				x	Zr, Ap, Opq, Grp
26	75R-2	7	High-grade schist	♦	♦			♦						♦					Zr, Trm, Opq, Grp
27	75R-1	12	Calc-silicate rock	♦	♦	•	•				♦								Cal, Ap, Sph, Clay, Opq
28	76R-1	7A	High-grade schist	♦	♦			♦	♦	x	♦			♦					Ap, Trm, Opq, Grp
29	76R-1	9A	High-grade schist	♦	♦		•				♦			♦	♦	Di	♦	♦	Cal, Sph, Ap, Opq, Grp
30	76R-2	8B	High-grade schist											♦		Di	♦		Cal, Sph, Grp
31	77R-2	3A	High-grade schist	♦	♦	•		♦	♦					♦	♦				Trm, Opq, Grp
32	77R-2	3E	High-grade schist	♦	♦		•	♦	♦		x			♦	♦				Ap, Trm, Opq, Grp
33	77R-2	10	High-grade schist	♦	♦			♦						♦					Trm
34	77R-3	6	High-grade schist	♦	♦			♦				♦		♦					Trm
35	78R-2	1A	High-grade schist	♦	♦			♦	♦		♦			♦					Trm, Opq, Grp
36	79R-1	17	High-grade schist	♦	♦			♦	♦			x		♦					Trm, Grp
37	80R-1	3A	High-grade schist	♦	♦				♦			♦		♦					Trm, Ep, Rt, Grp
38	81R-2	3	High-grade schist	♦	♦			♦						♦					Trm, Ep, Rt, Grp
39	81R-2	6	Marble		♦	♦	♦												Cal, Sph, Rt, Opq
40	81R-1	18A	High-grade schist	♦	♦			♦	♦					♦					Trm, Grp
41	82R-1	6	High-grade schist	♦	♦			♦	♦				♦	♦					Trm, Ap, Zr, Opq, Grp
42	82R-2	8	High-grade schist	♦	♦			x						♦					Zr, Trm, Grp
43	82R-1	9	Granite	♦	♦	•		♦	♦			♦	♦	♦					
44	83R-1	3	Gneiss	♦	♦	•		♦	♦				♦	♦					Trm, Opq
45	83R-1	11A	Marble	♦	♦							x		♦		Di			Cal, Sph, Scp
46	83R-2	1	Marble	♦	♦		•							♦		Di	♦		Cal, Sph, Scp
47	84R-1	3	High-grade schist	♦	♦	•		♦	♦	♦				♦				♦	Trm, Ap, Opq, Grp
48	84R-1	8B	High-grade schist	♦	♦	•	•	♦	♦		♦			♦					Trm, Zr, Rt, Opq
49	93R-1	8	Gneiss	♦	♦	•		x	x			♦	♦	♦					Trm
50	94R-1	3	Gneiss	♦	♦	•	•	♦	♦			♦	♦	♦					Trm, Opq
51	95R-2	1C	Augen gneiss	♦	♦	•	•	♦				x	♦	♦					Trm, Rt, Opq
52	97R-1	2	Banded gneiss	♦	♦	•		♦				x	♦	♦					Trm, Ap, Opq
53	98R-1	5	Gneiss	♦	x	•		♦			x	♦	♦	♦					Trm, Opq
54	98R-1	14	Gneiss	♦	♦	•		♦			♦	♦	♦	♦					Cal, Sph, Trm, Opq
55	101R-2	3A	Gneiss	♦	♦	•		♦	♦			♦	♦	♦					Ap, Trm, Opq
56	102R-1	3	Gneiss	♦	♦	•	•	♦	♦			♦	♦	♦					Ap, Trm, Opq
57	104R-1	4	Granite	♦	♦		•					♦	♦	♦					Ep, Opq
58	104R-1	9A	Calc-silicate rock			•	•				♦			♦		Di, Aug?	♦		Cal, Ep, Ap
59	106R-1	11A	Banded gneiss	♦	♦	•		♦	x			♦	♦	♦					Trm, Opq
77	97R-2	22	Granite	♦	♦	•	•					♦	♦	♦					

Notes: mineral abbreviations: Amp = amphibole; And = andalusite; Ap = apatite; Bt = biotite; Cal = calcite; Chl = chlorite; Clay = clay minerals; Crd = cordierite; Crn = corundum; Ep = epidote; Fd = K feldspar; Grt = garnet; Grp = graphite; Ms = muscovite; Opq = opaque minerals; Pl = plagioclase; Px = pyroxene (Aug = augite; Di = diopside); Qtz = quartz; Rt = rutile; Sil = sillimanite; Scp = scapolite; Spl = spinel; St = staurolite; Sph = sphene; Trm = tourmaline; Zr = zircon. Symbols for minerals: x = relict; ♦ = primary; • = retrogressive.

about 0.25 s TWT; however, in some places, as at Site 976, it is completely eroded. We used this eroded "Messinian" window to penetrate into the basement without the safety concerns related to Messinian evaporites. The internal seismic pattern varies from transparent to high-amplitude chaotic reflectors. Commercial well data from the Spanish shelf indicate that the Messinian sequence in the western Alboran Sea is composed of carbonate and fine-grained marine sediments, and subordinate evaporite beds. The top of the Messinian seismic unit II correlates with the "M"-reflector that marks the top of the Messinian evaporite throughout most of the Mediterranean. The "M"-reflector was also identified at Sites 974 and 975 (see "Site 974" and "Site 975" chapters, this volume). The contact of unit II with seismic unit III is mostly unconformable.

Seismic Units III (Tortonian) and IV (Serravallian)

Seismic units III (Tortonian) and IV (Serravallian) were penetrated at Site 976 where they are only about 0.09 s TWT thick. Site 976 is located at the feather-edge where the seismic units pinch out and overlap onto the basement high (Fig. 140). In the depocenters that flank the basement high, seismic units III and IV thicken to >0.7 and >1 s TWT, respectively. Their seismic facies are similar in character exhibiting high-amplitude, continuous, parallel to divergent reflectors. A high-amplitude reflector that marks the lower boundary of Unit IV (at 2.8 s TWT; Fig. 140) can be traced throughout the Western Alboran Basin, and correlation to commercial well data on the Spanish Margin suggests it is related to widespread volcaniclastic and sandstone beds.

Seismic Unit V (Serravallian-Langhian)

Just above the first seafloor multiple, Line 976A (Fig. 140) shows the transparent character of the upper part of seismic unit V (Serravallian–Langhian).

Correlation of survey data with the ages of the sediments recovered at Site 978 is shown in Figures 142 and 143 (see "Lithostratigraphy" section, this chapter). The basement high at Site 976 is a horst bounded by northeast-southwest–trending normal faults (Fig. 142; see "Background and Objectives" section, this chapter). The major normal fault to the northwest terminates with smaller normal faults that branch upward from the main fault; the reflections bounded by these faults show progressive decrease in displacement with age.

The seismic data suggest that the faults bounding the horst were active since at least the middle Miocene. Seismic units IV and III (Fig. 140), Serravallian and Tortonian in age according Site 976 paleontological data, show a pinch-out and drag geometry that indicate that the major fault was active during these times (Fig. 142). Minor

Table 13. Distribution of metamorphic minerals in thin sections from Hole 976E.

Thin section	Core, section	Piece	Lithotype	Mineralogy																
				Qtz	Bt	Ms	Chl	Sil	And	St	Grt	Crd	Fd	Pl	Crn	Px	Amp	Spl	Scp	Others
61	14R-1	3B	High-grade schist	♦	♦			♦		x	♦			♦						Opq, Trm, Zr
62	15R-1	5A	Calc-silicate rock	♦	♦		●						♦	♦				♦	♦	Cal, Opq, Grp, Sph
63	15R-1	5B	Calc-silicate rock	♦	♦		●	♦						♦						Cal, Grp, Clay, Sph, Opq
64	15R-1	6B	Calc-silicate rock	♦	♦									♦		Di-Hd		♦	♦	Cal, Sph, Grp, Opq
65	17R-1	5	Calc-silicate rock		♦		●							♦		Di				Cal, Sph, Opq, Grp
66	17R-1	7A	Calc-silicate rock	♦	♦	♦	●							♦		Di-Hd, Aug				Grp, Ap, Sph, Clay, Opq
67	17R-1	7A	Calc-silicate rock	♦	♦		●							♦		Di-Hd	♦			Cal, Grp, Opq, Rt, Sph
68	17R-2	1	High-grade schist/marble	♦	♦		●						♦	♦			♦			Cal, Grp, Opq, Sph, Clay
69	20R-1	9	Breccia	♦	♦	♦	♦						♦							Cal, Ank, Clay, Opq
70	20R-1	11A	Calc-silicate rock		♦	♦	♦						♦	♦	♦	Di				Cal, Clay, Rt, Ap, Grp, Opq, Trm
71	20R-1	14	High-grade schist	♦	♦			♦	♦				♦	♦						Grp, Opq, Trm, Ap
72	20R-2	2	Breccia	♦	♦	♦						♦	♦	♦						Cal, Ank, Dol, Clay
73	21R-1	5	High-grade schist	♦	♦	●		♦	♦				♦	♦						Grp, Trm, Zr
74	21R-3	1	Calc-silicate rock	♦	♦						♦			♦		Di	♦			Cal, Sph, Ep, Rt, Opq
75	22R-2	12	Calc-silicate rock	♦	♦			♦	♦		♦			♦						Cal, Opq, Grp, Sph, Ep, Clay
76	25R-2	11	High-grade schist	♦	♦			♦	♦	x				♦						Trm, Rt, Grp

Notes: mineral abbreviations: Amp = amphibole; And = andalusite; Ank = ankerite; Ap = apatite; Bt = biotite, Cal = calcite, Chl = chlorite, Clay = clay minerals, Crd = cordierite; Crn = corundum; Dol = dolomite; Fd = K feldspar; Ep = epidote, Grt = garnet; Grp = graphite; Ms = muscovite; Pl = plagioclase; Px = pyroxene (Aug = augite; Di = diopside; Hd = hedenbergite); Opq = opaque minerals; Qtz = quartz; Rt = rutile; Scp = scapolite; Sph = sphene; Spl = spinel; St = staurolite; Trm = tourmaline; Zr = zircon. Symbols for minerals: x = relict; ♦ = primary; ● = retrogressive.

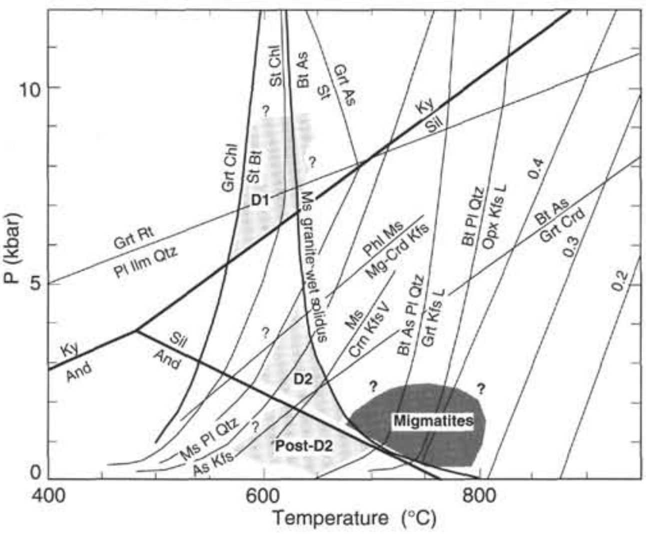

Figure 107. P-T diagram showing estimated conditions for the deformations in high-grade schist (light gray areas) and gneiss (dark gray areas). Uncertainties in boundary P-T conditions of the different deformations are shown by question marks. Approximate field of migmatite formation is also shown. P-T grid for pelites in the KFMASH system, composed from Spear (1993) and references therein. Aluminosilicate triple point after Holdaway (1971). The minimum melting conditions for pelitic rocks and the H_2O contents (as X_{H2O} in melt) necessary to saturate the granitic liquid are from Le Breton and Thompson (1988). The garnet-plagioclase-rutile-ilmenite-quartz reaction is from Bohlen and Liotta (1986). The corundum-in and muscovite-out reactions are from Helgeson et al. (1978). Mineral abbreviations: aluminosilicate (As), andalusite (And), biotite (Bt), chlorite (Chl), cordierite (Crd), corundum (Crn), garnet (Grt), ilmenite (Ilm), kyanite (Ky), muscovite (Ms), orthopyroxene (Opx), phlogopite (Phl), plagioclase (Pl), potassium feldspar (Kfs), quartz (Qtz), rutile (Rt), sillimanite (Sil), and staurolite (St). Other abbreviations: liquid (L) and vapor (V).

early Pliocene fault activity could also be inferred from the normal-fault propagation folding on either side of the horst, but this could be due to variable sedimentation over the pre-existing high.

The northeast-southwest seismic line, that passes through Site 976 and DSDP Site 121, shows significant lateral variations in thickness as well as an unconformity within the Pleistocene–middle Miocene sequence at Site 976 (Fig. 143). This unconformity corresponds to the "M"-reflector (occurring at 2.15 s at Site 976; Fig. 143), which correlates with a hiatus found in the paleontological data at 573 mbsf (Sample 976-61X-7, 71–73 cm; see "Biostratigraphy" section, this chapter). The reduced thickness of the Miocene sediments at Site 976 is likely related to the presence of erosion (or non-deposition), suggesting the possibility that the horst may have been a morphologic high throughout the entire middle to late Miocene. The irregular morphology at the top of the basement appears to be strongly controlled by faulting; erosion may also have modified the basement surface. The faulting has created several tectonic breccia intervals that were found in both Holes 976B and 976E (see "Structural Geology and Petrology of the Basement" section, this chapter).

REFERENCES

Azañón, J.M., Balanyá, J.C., and García-Dueñas, V., 1995. Registro metamorfico de alta presion-baja temperatura en la Unidad de Jubrique e Imbricaciones de Benarraba. *Geogaceta [Geol. Soc. Spain]*, 17:133–135.

Balanyá, J.C., Azañón, J.M., Sanchez-Gomez, M., and García-Dueñas, V., 1993. Pervasive ductile extension, isothermal decompression and thinning of the Jubrique Unit in the Paleogene (Alpujarride Complex, western Betics, Spain). *C. R. Acad. Sci. Ser. 2*, 316:1595–1601.

Balanyá, J.C., and García-Dueñas, V., 1987. Les directions structurales dans le Domaine d'Alboran de part et d'autre du Détroit de Gibraltar. *C. R. Acad. Sci. Ser. 2*, 304:929–932.

Bohlen, S.R., and Liotta, J.J., 1986. A barometer for garnet amphibolites and garnet granulites. *J. Petrol.*, 27:1025–1034.

Bryden, H.L., and Kinder, T.H., 1991. Recent progress in strait dynamics. *Rev. Geophys., Suppl., (U.S. Nat. Rep. Int. Union Geodesy Geophys. 1987*–1990), 617–631.

Chamberlain, C.K., 1978. Recognition of trace fossils in cores. *In* Basan, P. (Ed.), *Trace Fossil Concepts.* SEPM Short Course, 5:133–183.

Cita, M.B., and McKenzie, J.A., 1986. The terminal Miocene event. *In* Hsü, K.J. (Ed.), *Mesozoic and Cenozoic Oceans.* AGU Geodyn. Ser., 15:123–140.

Claypool, G.E., and Kvenvolden, K.A., 1983. Methane and other hydrocarbon gases in marine sediment. *Annu. Rev. Earth Planet. Sci.*, 11:299–327.

Comas, M.C., García-Dueñas, V., and Jurado, M.J., 1992. Neogene tectonic evolution of the Alboran Basin from MCS data. *Geo-Mar. Lett.*, 12:157–164.

Comas, M.C., García-Dueñas, V., Soto, J.I., and Campos, J., 1993. An extensional basin developed on a collisional orogen: the Alborán Sea. *In* Seranne, M., and Malavielle, J. (Eds.), *Late Orogenic Extension in Mountain Belts.* Doc. B.R.G.M. Fr., 219:44–46.

Embley, R.W., Hobart, M.A., Anderson, R.N., and Abbott, D.H., 1983. Anomalous heat flow in the Northwest Atlantic: a case for continued hydrothermal circulation in 80-m.y. crust. *J. Geophys. Res.*, 88:1067–1074.

Emerson, S., and Hedges, J.I., 1988. Processes controlling the organic carbon content of open ocean sediments. *Paleoceanography*, 3:621–634.

Espitalié, J., Laporte, J.L., Leplat, P., Madec, M., Marquis, F., Paulet, J., and Boutefeu, A., 1977. Méthode rapide de caractérisation des roches mères, de leur potentiel pétrolier et de leur degré d'évolution. *Rev. Inst. Fr. Pet.*, 32:23–42.

Foresi, L., Iaccarino, S., Mazzei, R., and Salvatorini, G., in press. New data on the calcareous plankton biostratigraphy of the middle to upper Miocene at the Mediterranean area. *Riv. Ital. Paleont. Stratigr.*

Froelich, P.N., Klinkhammer, G.P., Bender, M.L., Luedtke, N.A., Heath, G.R., Cullen, D., Dauphin, P., Hammond, D., Hartman, B., and Maynard, V., 1979. Early oxidation of organic matter in pelagic sediments of the eastern equatorial Atlantic: suboxic diagenesis. *Geochim. Cosmochim. Acta*, 43:1075–1090.

Galindo, J., Gonzalez Lodeiro, F., and Jabaloy, A., 1989. Progressive extensional shear structures in a detachment contact in the Western Sierra Nevada (Betic Cordilleras, Spain). *Geodin. Acta*, 3:73–85.

García-Dueñas, V., Balanyá, J.C., and Martínez-Martínez, J.M., 1992. Miocene extensional detachments in the outcropping basement of the northern Alboran basin (Betics) and their tectonic implications. *Geo-Mar. Lett.*, 12:88–95.

Haq, B.U., Hardenbol, J., and Vail, P.R., 1987. Chronology of fluctuating sea levels since the Triassic (250 million years ago to present). *Science*, 235:1156–1167.

Helgeson, H.C., Delany, J.M., Nesbitt, H.W., and Bird, D.K., 1978. Summary and critique of the thermodynamic properties of rock-forming minerals. *Am. J. Sci.*, 278A.

Holdaway, M.J., 1971. Stability of andalusite and the aluminum silicate phase diagram. *Am. J. Sci.*, 271:97–131.

Jurado, M.J., and Comas, M.C., 1992. Well log interpretation and seismic character of the Cenozoic sequence in the Northern Alboran Sea. *Geo-Mar. Lett.*, 12:129–136.

Karlin, R., 1990. Magnetic diagenesis in marine sediments from the Oregon continental margin. *J. Geophys. Res.*, 95:4405–4419.

Kornprobst, J., 1973. Petrographical studies of "acoustic basement" and associated breccia at Site 121—western Alboran Basin: a comparison with the Betico-Rifean basement. *In* Ryan, W.B.F., Hsü, K.J., et al., *Init. Repts. DSDP*, 13 (Pt. 2): Washington (U.S. Govt. Printing Office), 759–761.

Krijgsman, W., Hilgen, F.J., Langereis, C.G., Santarelli, A., and Zachariasse, W.J., in press. Late Miocene magnetostratigraphy, biostratigraphy and cyclostratigraphy in the Mediterranean. *Earth Planet. Sci. Lett.*

Le Breton, N., and Thompson, A.B., 1988. Fluid-absent (dehydration) melting of biotite in metapelites in the early stages of crustal anatexis. *Contrib. Mineral. Petrol.*, 99:226–237.

Loomis, T.P., 1972. Contact metamorphism of pelitic rocks by the Ronda ultramafic intrusion, southern Spain. *Geol. Soc. Am. Bull.*, 83:2449–2474.

Lundeen, M.T., 1978. Emplacement of the Ronda peridotite, Sierra Bermeja, Spain. *Geol. Soc. Am. Bull.,* 89:172–180.

Macdonald, A.M., Candela, J., and Bryden, H.L., 1994. An estimate of the net heat transport through the Strait of Gibraltar. *In* La Violette, P.E. (Ed.), *Seasonal and Interannual Variability of the Western Mediterranean Sea:* Washington (Am. Geophys. Union), Coastal and Estuarine Studies, 46:13–32.

Manheim, F.T., and Sayles, F.L., 1974. Composition and origin of interstitial waters of marine sediments, based on deep sea drill cores. *In* Goldberg, E.D. (Ed.), *The Sea* (Vol. 5): *Marine Chemistry: The Sedimentary Cycle:* New York (Wiley), 527–568.

McIver, R.D., 1975. Hydrocarbon occurrences from JOIDES Deep Sea Drilling Project. *Proc. Ninth Petrol. Congr.,* 269–280.

McKenzie, J.A., Sprovieri, R., and Channell, J.E.T., 1990. The terminal Messinian flood and earliest Pliocene paleoceanography in the Mediterranean: results from ODP Leg 107, Site 652, Tyrrhenian Sea. *Mem. Soc. Geol. Ital.,* 44:81–91.

Meyers, P.A., 1994. Preservation of elemental and isotopic source identification of sedimentary organic matter. *Chem. Geol.,* 144:289–302.

Meyers, P.A., and Brassell, S.C., 1985. Biogenic gases in sediments deposited since Miocene times on the Walvis Ridge, South Atlantic Ocean. *In* Caldwell, D.E., Brierley, J.A., and Brierley, C.L. (Eds.), *Planetary Ecology:* New York (Van Nostrand Reinhold), 69–80.

Meyers, P.A., and Shaw, T.J., 1996. Organic matter accumulation, sulfate reduction, and methanogenesis in Pliocene–Pleistocene turbidites on the Iberia Abyssal Plain. *In* Whitmarsh, R.B., Sawyer, D.S., Klaus, A., and Masson, D.G. (Eds.), *Proc. ODP, Sci. Results.,* 149: College Station, TX (Ocean Drilling Program), 705–712.

Meyers, P.A., and Snowdon, L.R., 1993. Sources and migration of methane-rich gas in sedimentary rocks on the Exmouth Plateau: northwest Australian continental margin. *In* Oremland, R.S. (Ed.), *Biogeochemistry of Global Change:* New York (Chapman and Hall), 434–446.

Monié, P., Torres-Roldan, R.L., and Garcia-Casco, A., 1994. Cooling and exhumation of the western Betic Cordilleras, $^{40}Ar/^{40}Ar$ thermochronological constraints on a collapsed terrane. *Tectonophysics,* 238:353–379.

Montenat, C., Bizon, G., and Bizon, G., 1975. Remarques sur le Néogène du forage Joides 121 en mer d'Alboran (Méditerranée occidentale). *Bull. Soc. Geol. Fr.,* 17:45–51.

Müller, P.J., 1977. C/N ratios in Pacific deep sea sediments: effect of inorganic ammonium and organic nitrogen compounds sorbed by clays. *Geochim. Cosmochim. Acta,* 41:765–776.

Muñoz, M., 1991. Significado de los cuerpos de leucogranitos y de los "gneises cordieriticos con litoclastos" asociados en la Unidad de Guadaiza (Alpujarrides occidentales, Beticas). *Geogaceta* [*Geol. Soc. Spain*], 9:10–13.

Pickering, K.T., Hiscott, R., and Hein, F.J., 1989. *Deep-Marine Environments: Clastic Sedimentation and Tectonics:* London (Unwin Hyman).

Platt, J.P., and Vissers, R.L.M., 1989. Extensional collapse of thickened continental lithosphere: a working hypothesis for the Alboran Sea and Gibraltar Arc. *Geology,* 17:540–543.

Polyak, B.G., Fernàndez, M., Khutorsky, M.D., Soto, J.I., Basov, I.A., Comas, M.C., Khain, V.Ye., Alonso, B., Apagova, G.V., Mazurova, I.S., Negredo, A., Tochitsky, V.O., de la Linde, J., Bogdanov, N.A., and Banda, E., in press. Heat flow in the Alboran Sea (the Western Mediterranean). *Tectonophysics.*

Rochette, P., 1987. Magnetic susceptibility of the rock matrix related to magnetic fabric studies. *J. Struct. Geol.,* 9:1015–1020.

Rochette, P., and Lamarche, G., 1986. Evolution des propriétés magnétiques lors des transformations minérales dans les roches: exemple du Jurassique Dauphinois (Alpes françaises). *Bull. Mineral.,* 109:687–696.

Ryan, W.B.F., Hsü, K.J., et al., 1973. *Init. Repts. DSDP,* 13 (Pts. 1 and 2): Washington (U.S. Govt. Printing Office).

Ryan, W.B.F., Hsü, K.J., Cita, M.B., Dumitricia, P., Lort, J.M., Maync, W., Nesteroff, W.D., Pautot, G., Stadner, H., and Wezel, F.C., 1973. Western Alboran Basin—Site 121. *In* Ryan, W.B.F., Hsü, K.J., et al., *Init. Repts. DSDP,* 13 (Pt. 1): Washington (U.S. Govt. Printing Office), 43–89.

Sarmiento, J., Herbert, T., and Toggweiler, J., 1988. Mediterranean nutrient balance and episodes of anoxia. *Global Biogeochem. Cycles,* 2:427–444.

Shipboard Scientific Party, 1990. Site 767. *In* Rangin, C., Silver, E.A., von Breymann, M.T., et al., *Proc. ODP, Init. Repts.,* 124: College Station, TX (Ocean Drilling Program), 121–193.

————, 1995. Site 926. *In* Curry, W.B., Shackleton, N.J., Richter, C., et al., *Proc. ODP, Init. Repts.,* 154: College Station, TX (Ocean Drilling Program), 153–232.

Spear, F.S., 1993. *Metamorphic Phase Equilibria and Pressure-Temperature-Time Paths:* Washington (Mineral. Soc. Am.), Monogr. 1.

Steiger, R.H., and Frick, U., 1973. Isotopic dating of Alboran "basement." *In* Ryan, W.B.F., Hsü, K.J., et al., *Init. Repts. DSDP,* 13 (Pt. 2): Washington (U.S. Govt. Printing Office), 762.

Thunell, R.C., Williams, D.F., and Howell, M., 1987. Atlantic-Mediterranean water exchange during the late Neogene. *Paleoceanography,* 2:661–678.

Torii, M., Hayashida, A., Vigliotti, L., and Wippern, J., 1992. Rock magnetic properties of sediments from Site 797, Japan Sea. *In* Tamaki, K., Suyehiro, K., Allan, J., McWilliams, M., et al., *Proc. ODP, Sci. Results,* 127/128 (Pt. 2): College Station, TX (Ocean Drilling Program), 947–957.

Torres-Roldán, R.L., 1981. Plurifacial metamorphic evolution of the Sierra Bermeja peridotite aureole (southern Spain). *Estud. Geol. (Madrid),* 37:115–133.

————, 1983. Fractioned melting of metapelite and further crystal-melt equilibria: the example of the Blanca Unit migmatite complex, North of Estepona (Southern Spain). *Tectonophysics,* 96:95–123.

Tubía, J.M., 1988. Estructura de los Alpujarrides occidentales: cinematica y condiciones de emplazamiento de las peridotitas de Ronda, Parte I. Caracteristicas litologicas. *Bol. Geol. Min.,* 99:3–50.

Tubía, J.M., and Gil-Ibarguchi, J.I., 1991. Eclogites of the Ojen nappe: a record of subduction in the Alpujárride complex (Betic Cordilleras, southern Spain). *J. Geol. Soc. London,* 148:801–804.

Watts, A.B., Platt, J.P., and Bulh, P., 1993. Tectonic evolution of the Alboran Sea Basin. *Basin Res.,* 5:153–177.

Westerhof, A.B., 1977. On the contact relations of high-temperature peridotites in the Serrania de Ronda, southern Spain. *Tectonophysics,* 39:579–591.

Wright, R., 1978. Neogene paleobathymetry of the Mediterranean based on benthic foraminifers from DSDP Leg 42. *In* Hsü, K.J., Montadert, L., et al., *Init. Repts. DSDP,* 42 (Pt. 1): Washington (U.S. Govt. Printing Office), 837–846.

Zeck, H.P., Monié, P., Villa, I.M., and Hansen, B.T., 1992. Very high rates of cooling and uplift in the Alpine belt of the Betic Cordilleras, southern Spain. *Geology,* 20:79–82.

Ms 161IR-106

NOTE: For all sites drilled, core-description forms ("barrel sheets") and core photographs can be found in Section 3, beginning on page 429. Smear-slide data can be found in Section 4, beginning on page 949. Thin-section data can be found in Section 5, beginning on page 991. See Table of Contents for material contained on CD-ROM.

Table 14. Results of inorganic and total carbon (TC) analyses of sediment samples from lithostratigraphic Units I–IV at Site 976.

Core, section, interval (cm)	Depth (mbsf)	$CaCO_3$ (wt%)	Inorg. C (wt%)	TC (wt%)	TOC (wt%)	TN (wt%)	TS (wt%)	C/N
Unit 1: Holocene to Pleistocene nannofossil-rich clay and silty clay								
161-976B-								
1H-1, 34–35	0.34	19.08	2.29	2.98	0.69	0.07	0.00	11.50
1H-3, 19–20	3.19	28.16	3.38	4.21	0.83	0.08	0.00	12.10
2H-2, 95–96	5.95	19.91	2.39	2.91	0.52	0.05	0.00	12.13
2H-5, 78–79	10.28	21.32	2.56	3.16	0.60	0.06	0.00	11.67
3H-2, 28–29	14.35	23.91	2.87	3.72	0.85	0.08	0.00	12.40
4H-2, 92–93	24.92	19.99	2.40	2.83	0.43	0.04	0.00	12.54
4H-4, 122–124	28.22	34.24	4.11	4.94	0.83	0.07	0.00	13.83
4H-CC, 28–29	32.43	22.91	2.75	3.78	1.03	0.10	0.00	12.02
5H-2, 127–128	34.77	24.66	2.96	3.63	0.67	0.06	0.00	13.03
5H-6, 125–126	40.75	31.07	3.73	4.78	1.05	0.09	0.00	13.61
5H-7, 10–11	41.10	30.49	3.66	4.43	0.77	0.07	0.00	12.83
6H-4, 84–85	46.84	22.41	2.69	3.09	0.40	0.05	0.00	9.33
7H-4, 82–83	56.32	26.91	3.23	3.99	0.76	0.07	0.00	12.67
7H-6, 10–11	58.60	35.57	4.27	5.01	0.74	0.06	0.00	14.39
7H-CC, 8–9	60.69	25.91	3.11	3.93	0.82	0.07	0.00	13.67
8H-1, 72–73	61.22	21.24	2.55	2.96	0.41	0.04	0.00	11.96
8H-3, 36–37	63.86	34.15	4.10	4.78	0.68	0.05	0.00	15.87
8H-4, 27–28	65.27	27.74	3.33	4.00	0.67	0.06	0.00	13.03
8H-4, 51–52	65.51	30.07	3.61	4.63	1.02	0.08	0.00	14.88
8H-4, 92–93	65.92	30.90	3.71	4.71	1.00	0.07	0.00	16.67
9H-3, 20–22	73.20	22.41	2.69	3.04	0.35	0.04	0.00	10.21
9H-5, 16–17	76.21	27.16	3.26	3.71	0.45	0.02	0.00	26.25
10H-3, 82–83	83.32	35.49	4.26	4.91	0.65	0.04	0.00	18.96
10H-7, 53–54	89.08	41.32	4.96	5.49	0.53	0.04	0.00	15.46
11H-2, 85–86	89.97	25.16	3.02	4.08	1.06	0.08	0.00	15.46
11H-4, 20–21	92.37	25.82	3.10	3.52	0.42	0.04	0.00	12.25
11H-5, 66–67	94.33	32.49	3.90	4.45	0.55	0.04	0.00	16.04
12H-1, 79–80	99.29	37.49	4.50	5.16	0.66	0.04	0.00	19.25
12H-7, 51–52	108.07	41.57	4.99	5.53	0.54	0.08	0.00	7.88
13H-3, 70–71	111.70	35.65	4.28	5.10	0.82	0.07	0.00	13.67
13H-6, 57–58	116.07	28.66	3.44	3.90	0.46	0.05	0.00	10.73
14H-2, 120–122	118.94	29.74	3.57	3.97	0.40	0.03	0.00	15.56
14H-7, 126–128	126.50	38.82	4.66	5.22	0.56	0.04	0.00	16.33
15X-2, 65–66	129.15	30.24	3.63	4.19	0.56	0.06	0.00	10.89
15X-4, 39–40	131.89	24.99	3.00	4.46	1.46	0.08	0.00	21.29
15X-5, 70–71	133.70	33.07	3.97	4.70	0.73	0.07	0.00	12.17
16X-1, 146–147	137.96	35.32	4.24	5.17	0.93	0.14	0.34	7.75
16X-4, 105–106	142.05	35.49	4.26	5.08	0.82	0.12	1.27	7.97
17X-2, 102–103	148.13	27.74	3.33	3.80	0.47	0.10	1.17	5.48
18X-1, 117–118	156.97	27.32	3.28	3.84	0.56	0.11	0.23	5.94
18X-3, 29–30	159.09	22.91	2.75	3.86	1.11	0.14	0.46	9.25
18X-3, 105–106	159.85	19.33	2.32	3.46	1.14	0.14	1.66	9.50
18X-3, 122–123	160.02	24.74	2.97	4.10	1.13	0.14	1.37	9.42
18X-3, 134–135	160.14	24.49	2.94	4.19	1.25	0.14	2.20	10.42
19X-1, 75–76	166.15	25.16	3.02	3.53	0.51	0.11	1.01	5.41
19X-6, 74–75	173.36	29.65	3.56	4.17	0.61	0.10	0.14	7.12
20X-3, 41–42	178.51	27.41	3.29	4.20	0.91	0.13	1.34	8.17
20X-5, 98–99	182.08	26.32	3.16	3.66	0.50	0.09	0.85	6.48
20X-7, 15–16	184.25	29.07	3.49	4.24	0.75	0.12	0.84	7.29
20X-CC, 5–6	184.57	26.91	3.23	4.08	0.85	0.12	0.69	8.26
21X-2, 50–51	186.70	18.74	2.25	3.20	0.95	0.14	1.03	7.92
22X-4, 90–91	199.80	23.32	2.80	3.29	0.49	0.10	0.22	5.72
23X-3, 75–76	207.65	36.90	4.43	5.31	0.88	0.11	0.82	9.33
23X-4, 75–76	209.15	25.16	3.02	3.32	0.30	0.08	0.50	4.38
24X-2, 41–42	215.41	31.32	3.76	4.38	0.62	0.10	5.96	7.23
24X-3, 41–42	216.91	21.99	2.64	4.22	1.58	0.12	0.21	15.36
25X-2, 50–51	223.91	22.16	2.66	2.98	0.32	0.08	0.06	4.67
25X-7, 70–71	231.61	27.32	3.28	3.81	0.53	0.10	0.29	6.18
26X-3, 89–90	235.63	34.99	4.20	4.70	0.50	0.09	0.58	6.48
26X-5, 89–90	238.63	15.66	1.88	2.26	0.38	0.10	0.98	4.43
26X-6, 58–59	239.23	27.16	3.26	4.15	0.89	0.11	1.02	9.44
26X-6, 138–139	240.03	21.91	2.63	3.42	0.79	0.11	0.56	8.38
26X-7, 35–36	240.40	19.24	2.31	3.16	0.85	0.12	1.61	8.26
29X-2, 11–12	262.21	27.07	3.25	4.20	0.95	0.09	0.00	12.31
29X-2, 22–23	262.32	32.74	3.93	4.31	0.38	0.05	0.00	8.87
29X-5, 55–56	267.02	25.49	3.06	3.91	0.85	0.05	0.00	19.83
32X-3, 90–91	293.39	26.57	3.19	3.52	0.33	0.05	0.00	7.70
32X-5, 81–82	296.30	30.82	3.70	4.02	0.32	0.04	0.00	9.33
32X-5, 131–132	296.80	21.74	2.61	3.98	1.37	0.11	0.00	14.53
32X-7, 14–15	298.48	20.16	2.42	3.49	1.07	0.09	0.00	13.87
32X-7, 38–39	298.72	20.91	2.51	3.41	0.90	0.08	0.00	13.13
33X-4, 27–28	303.80	26.07	3.13	3.79	0.66	0.06	0.00	12.83
34X-5, 81–82	316.25	23.74	2.85	2.93	0.08	0.07	0.00	1.33
35X-5, 14–15	325.01	26.74	3.21	3.98	0.77	0.09	0.00	9.98
35X-5, 32–33	325.19	25.49	3.06	3.80	0.74	0.09	0.00	9.59
35X-5, 86–87	325.73	25.07	3.01	3.23	0.22	0.08	0.89	3.21
36X-5, 85–86	334.63	39.57	4.75	5.03	0.28	0.07	0.00	4.67
36X-6, 30–31	335.58	33.57	4.03	4.44	0.41	0.08	1.60	5.98
37X-3, 85–86	341.71	30.24	3.63	4.00	0.37	0.08	0.63	5.40
38X-2, 75–76	350.35	28.16	3.38	3.79	0.41	0.09	0.20	5.31
39X-1, 80–81	358.50	29.99	3.60	3.94	0.34	0.08	1.02	4.96
39X-3, 74–75	361.44	26.41	3.17	3.71	0.54	0.09	0.10	7.00
39X-3, 146–147	362.16	28.49	3.42	3.49	0.07	0.02	0.29	4.08
161-977C-								
1H-1, 12–13	0.12	19.10	2.29	3.19	0.90	0.19	0.00	5.53
1H-1, 107–108	1.13	27.90	3.35	3.54	0.19	0.14	0.00	1.58

Table 14 (continued).

Core, section, interval (cm)	Depth (mbsf)	$CaCO_3$ (wt%)	Inorg. C (wt%)	TC (wt%)	TOC (wt%)	TN (wt%)	TS (wt%)	C/N
1H-1, 113–114	4.07	23.49	2.82	4.20	1.38	0.14	0.00	11.50
1H-3, 123–124	4.23	27.49	3.30	4.10	0.80	0.14	0.00	6.67
1H-3, 148–149	4.48	26.24	3.15	4.10	0.95	0.13	0.00	8.53
1H-4, 123–124	5.73	23.99	2.88	3.41	0.53	0.14	0.00	4.42
2H-2, 90–91	8.40	20.83	2.50	3.02	0.52	0.14	0.00	4.33
2H-4, 80–81	11.30	22.57	2.71	3.25	0.54	0.13	0.00	4.85
2H-6, 55–56	14.05	23.41	2.81	3.91	1.10	0.19	0.00	6.75
3H-1, 25–26	15.75	21.41	2.57	3.18	0.61	0.13	0.00	5.47
3H-1, 109–110	16.59	22.91	2.75	3.51	0.76	0.13	0.00	6.82
4H-1, 35–36	25.35	23.91	2.87	3.37	0.50	0.11	0.00	5.30
4H-1, 110–111	26.10	29.32	3.52	4.28	0.76	0.14	0.00	6.33
4H-5, 36–37	31.36	28.16	3.38	3.99	0.61	0.13	0.00	5.47
5H-1, 88–89	35.38	26.74	3.21	3.86	0.65	0.13	0.00	5.83
5H-3, 48–49	37.98	37.32	4.48	4.71	0.23	0.11	0.00	2.44
5H-5, 25–26	40.75	21.41	2.57	4.42	1.85	0.16	0.00	13.49
6H-1, 77–78	44.77	24.41	2.93	3.26	0.33	0.12	0.00	3.21
6H-4, 106–107	49.56	41.73	5.01	5.59	0.58	0.11	0.00	6.15
6H-5, 45–46	50.45	30.24	3.63	4.20	0.57	0.11	0.00	6.05
7H-1, 50–51	54.00	32.99	3.96	4.72	0.76	0.19	0.00	4.67
7H-2, 89–90	55.89	26.74	3.21	3.71	0.50	0.16	0.00	3.65
7H-2, 127–128	56.27	28.66	3.44	4.38	0.94	0.13	0.00	8.44
7H-3, 81–82	57.31	22.91	2.75	3.25	0.50	0.11	0.00	5.30
7H-4, 110–112	59.10	37.57	4.51	5.23	0.72	0.20	0.00	4.20
7H-5, 100–101	60.50	24.91	2.99	3.67	0.68	0.14	0.00	5.67
7H-6, 14–15	61.14	23.32	2.80	3.21	0.41	0.11	0.00	4.35
7H-6, 51–52	61.51	24.24	2.91	3.20	0.29	0.12	0.00	2.82
7H-7, 10–11	62.60	24.57	2.95	3.60	0.65	0.12	0.00	6.32
8H-1, 80–81	63.80	36.82	4.42	5.04	0.62	0.14	0.00	5.17
8H-2, 115–116	65.65	31.99	3.84	4.94	1.10	0.17	0.00	7.55
8H-2, 132–133	65.82	31.49	3.78	4.75	0.97	0.16	0.00	7.07
8H-4, 52–53	68.02	24.41	2.93	3.30	0.37	0.12	0.00	3.60
8H-4, 69–70	68.19	23.41	2.81	3.24	0.43	0.11	0.00	4.56
8H-6, 115–116	71.65	24.66	2.96	3.59	0.63	0.13	0.00	5.65
9H-2, 50–51	74.50	26.07	3.13	3.42	0.29	0.10	0.00	3.38
9H-3, 51–52	76.01	28.41	3.41	3.82	0.41	0.10	0.00	4.78
9H-4, 67–68	77.73	39.82	4.78	5.59	0.81	0.09	0.74	10.50
9H-4, 118–119	78.24	43.57	5.23	5.77	0.54	0.13	0.00	4.85
9H-6, 68–69	80.91	28.66	3.44	3.87	0.43	0.11	0.00	4.56
10H-4, 48–49	86.98	27.41	3.29	3.71	0.42	0.11	0.00	4.45
10H-5, 118–119	89.18	36.07	4.33	4.76	0.43	0.12	0.00	4.18
10H-6, 11–12	89.61	38.07	4.57	5.32	0.75	0.20	0.00	4.38
10H-6, 69–70	90.19	24.91	2.99	3.47	0.48	0.11	0.00	5.09
10H-6, 114–115	90.64	25.91	3.11	4.05	0.94	0.15	1.05	7.31
11H-1, 10–11	91.60	26.99	3.24	3.95	0.71	0.10	1.43	8.28
11H-2, 80–81	93.80	32.65	3.92	4.59	0.67	0.09	1.64	8.69
11H-4, 67–68	96.67	23.66	2.84	3.08	0.24	0.10	0.00	2.80
11H-6, 68–69	99.68	33.65	4.04	4.50	0.46	0.18	0.00	2.98
11H-6, 103–104	100.03	38.32	4.60	5.07	0.47	0.17	1.12	3.23
12H-2, 80–81	103.30	40.15	4.82	5.27	0.45	0.10	0.00	5.25
12H-4, 19–20	105.69	44.15	5.30	5.84	0.54	0.11	0.00	5.73
12H-6, 20–21	108.70	39.90	4.79	5.16	0.37	0.11	0.00	3.92
12H-CC, 46–47	111.27	36.82	4.42	5.14	0.72	0.13	0.50	6.46
13H-1, 25–26	110.75	36.99	4.44	5.11	0.67	0.12	0.71	6.51
13H-1, 136–137	111.86	36.82	4.42	5.17	0.75	0.13	0.41	6.73
13H-2, 108–109	113.08	20.33	2.44	2.76	0.32	0.10	1.31	3.73
13H-2, 139–140	113.39	35.99	4.32	5.05	0.73	0.12	0.13	7.10
13H-4, 48–49	115.48	24.07	2.89	3.26	0.37	0.10	0.56	4.32
14H-3, 39–40	123.39	28.91	3.47	3.79	0.32	0.09	0.00	4.15
14H-3, 85–86	123.85	45.32	5.44	5.86	0.42	0.10	0.00	4.90
14H-4, 80–81	125.30	39.98	4.80	5.19	0.39	0.10	0.00	4.55
14H-4, 90–91	125.40	38.57	4.63	5.19	0.56	0.11	0.00	5.94
14H-7, 60–61	129.60	37.07	4.45	4.69	0.24	0.12	0.00	2.33
15X-1, 60–61	130.10	34.39	4.14	5.12	0.98	0.14	0.37	8.17
15X-1, 92–93	130.42	29.07	3.49	4.42	0.93	0.14	0.20	7.75
15X-3, 50–51	133.00	30.65	3.68	4.43	0.75	0.12	0.86	7.29
15X-3, 131–132	133.81	32.24	3.87	4.64	0.77	0.14	0.00	6.42
15X-6, 85–86	137.85	38.90	4.67	5.46	0.79	0.13	0.00	7.09
16X-1, 50–51	139.70	34.99	4.20	4.98	0.78	0.13	0.00	7.00
16X-1, 98–99	140.18	37.32	4.48	5.44	0.96	0.15	0.00	7.47
16X-3, 108–109	143.28	30.90	3.71	4.14	0.43	0.09	1.70	5.57
16X-4, 78–79	144.48	33.15	3.98	4.73	0.75	0.12	1.39	7.29
16X-6, 70–71	147.40	34.32	4.12	4.49	0.37	0.11	0.00	3.92
17X-2, 60–61	150.90	26.99	3.24	4.03	0.79	0.11	1.44	8.38
18X-1, 10–11	158.60	21.41	2.57	3.40	0.83	0.12	3.48	8.07
18X-1, 100–101	159.50	19.33	2.32	3.15	0.83	0.13	3.00	7.45
18X-1, 137–138	159.87	24.07	2.89	4.14	1.25	0.13	1.83	11.22
18X-2, 10–11	160.10	29.90	3.59	3.89	0.30	0.12	1.22	2.92
18X-3, 61–62	162.11	23.41	2.81	3.43	0.62	0.10	0.78	7.23
18X-5, 52–53	165.02	25.74	3.09	3.48	0.39	0.09	1.12	5.06
19X-4, 90–91	173.43	31.57	3.79	4.22	0.43	0.09	1.61	5.57
19X-6, 59–60	175.93	28.16	3.38	4.15	0.77	0.12	1.89	7.49
20X-2, 10–11	179.40	24.07	2.89	3.47	0.58	0.10	1.72	6.77
20X-2, 76–77	180.06	23.32	2.80	3.47	0.67	0.11	0.72	7.11
20X-2, 116–117	180.46	22.24	2.67	3.51	0.84	0.12	1.58	8.17
20X-3, 100–101	181.80	23.82	2.86	3.41	0.55	0.07	0.68	9.17
22X-4, 104–105	202.46	25.16	3.02	3.79	0.77	0.11	1.98	8.17
22X-6, 58–59	205.00	30.99	3.72	4.25	0.53	0.08	1.44	7.73
23X-6, 96–97	214.04	24.49	2.94	3.45	0.51	0.09	1.58	6.61
24X-2, 4–5	216.53	25.57	3.07	3.57	0.50	0.10	2.00	5.83
24X-4, 120–121	220.69	23.82	2.86	3.28	0.42	0.09	1.48	5.44
25X-1, 59–60	226.39	31.57	3.79	4.33	0.54	0.09	0.62	7.00

Table 14 (continued).

Core, section, interval (cm)	Depth (mbsf)	$CaCO_3$ (wt%)	Inorg. C (wt%)	TC (wt%)	TOC (wt%)	TN (wt%)	TS (wt%)	C/N
25X-2, 121–122	228.51	24.32	2.92	3.68	0.76	0.09	0.83	9.85
26X-1, 21–22	235.61	33.65	4.04	4.66	0.62	0.08	0.13	9.04
26X-1, 87–88	236.27	24.49	2.94	3.62	0.68	0.10	1.97	7.93
26X-1, 99–100	236.39	21.91	2.63	3.12	0.49	0.10	2.05	5.72
26X-2, 14–15	236.64	19.08	2.29	2.83	0.54	0.10	1.41	6.30
26X-2, 108–109	237.58	15.41	1.85	2.33	0.48	0.10	2.99	5.60
26X-3, 4–5	238.04	26.41	3.17	4.24	1.07	0.13	1.41	9.60
26X-3, 14–15	238.14	26.16	3.14	4.16	1.02	0.12	0.88	9.92
26X-3, 128–129	239.28	19.49	2.34	3.21	0.87	0.12	0.60	8.46
26X-4, 21–22	239.52	24.24	2.91	3.52	0.61	0.10	0.75	7.12
26X-4, 77–78	240.08	23.99	2.88	3.12	0.24	0.08	1.33	3.50
26X-6, 52–53	242.83	36.57	4.39	4.83	0.44	0.08	0.38	6.42
26X-7, 22–23	243.91	41.40	4.97	5.73	0.76	0.09	0.17	9.85
26X-7, 59–60	244.28	21.57	2.59	3.00	0.41	0.09	2.18	5.31
26X-7, 81–82	244.50	32.57	3.91	4.45	0.54	0.10	0.28	6.30
27X-2, 111–112	247.71	30.07	3.61	4.15	0.54	0.08	2.16	7.88
27X-6, 30–31	252.80	29.82	3.58	4.29	0.71	0.11	2.68	7.53
27X-CC, 30–31	254.77	30.49	3.66	4.57	0.91	0.13	3.36	8.17
28X-2, 6–7	255.14	33.24	3.99	4.50	0.51	0.08	0.25	7.44
28X-4, 142–143	259.50	21.82	2.62	2.92	0.30	0.08	0.24	4.38
28X-CC, 13–14	263.85	25.74	3.09	3.97	0.88	0.12	1.94	8.56
29X-3, 13–14	266.69	22.41	2.69	3.46	0.77	0.11	2.13	8.17
29X-6, 55–56	271.61	27.49	3.30	3.65	0.35	0.08	0.00	5.10
29X-cc, 50–51	274.27	21.66	2.60	3.26	0.66	0.10	0.65	7.70
31X-3, 91–92	286.69	25.41	3.05	3.46	0.41	0.08	0.43	5.98
31X-7, 32–33	292.02	29.82	3.58	4.49	0.91	0.12	2.58	8.85
32X-1, 35–36	293.55	26.66	3.20	3.74	0.54	0.10	1.26	6.30
32X-2, 14–15	293.82	23.66	2.84	3.32	0.48	0.10	2.33	5.60
32X-2, 102–103	294.70	27.32	3.28	3.61	0.33	0.08	1.68	4.81
32X-3, 61–62	295.79	25.74	3.09	3.65	0.56	0.10	2.02	6.53
32X-4, 75–76	297.43	26.57	3.19	3.53	0.34	0.09	1.05	4.41
32X-5, 48–49	298.62	23.57	2.83	3.51	0.68	0.10	4.35	7.93
32X-6, 34–35	299.98	23.07	2.77	3.23	0.46	0.09	1.87	5.96
32X-6, 98–99	300.62	26.32	3.16	3.87	0.71	0.10	2.11	8.28
32X-7, 39–40	301.53	28.66	3.44	3.80	0.36	0.08	2.05	5.25
33X-3, 66–67	305.61	29.99	3.60	4.12	0.52	0.08	1.10	7.58
34X-1, 6–7	312.36	24.99	3.00	3.53	0.53	0.09	0.39	6.87
34X-2, 4–5	312.89	23.41	2.81	3.27	0.46	0.08	2.60	6.71
34X-4, 59–60	316.44	39.98	4.80	5.28	0.48	0.07	0.51	8.00
34X-5, 66–67	318.01	30.32	3.64	4.01	0.37	0.09	0.03	4.80
34X-5, 93–94	318.28	29.65	3.56	3.98	0.42	0.09	1.03	5.44
34X-7, 14–15	320.49	28.82	3.46	3.67	0.21	0.08	0.54	3.06
34X-7, 89–90	321.24	31.82	3.82	4.25	0.43	0.08	0.72	6.27
35X-1, 139–140	323.29	25.66	3.08	3.81	0.73	0.11	2.29	7.74
35X-2, 57–58	323.97	24.66	2.96	3.44	0.48	0.08	1.07	7.00
35X-5, 89–90	328.79	40.40	4.85	5.10	0.25	0.10	0.00	2.92
36X-3, 132–133	335.19	29.57	3.55	3.67	0.12	0.07	6.69	2.00
36X-6, 92–93	339.29	35.99	4.32	4.56	0.24	0.07	0.12	4.00
37X-2, 18–19	342.05	29.90	3.59	3.90	0.31	0.07	0.59	5.17
37X-4, 13–14	344.89	27.24	3.27	3.79	0.52	0.10	0.21	6.07
37X-4, 101–102	345.77	27.41	3.29	3.56	0.27	0.08	0.50	3.94
38X-1, 10–11	350.90	30.90	3.71	4.05	0.34	0.08	2.24	4.96
38X-2, 102–103	352.62	25.16	3.02	3.42	0.40	0.09	1.84	5.19
38X-4, 19–20	354.79	26.16	3.14	3.50	0.36	0.08	0.55	5.25
38X-5, 90–91	357.00	23.41	2.81	3.24	0.43	0.08	2.14	6.27
38X-7, 7–8	359.17	22.49	2.70	3.09	0.39	0.08	0.62	5.69
39X-1, 123–124	361.63	30.90	3.71	4.09	0.38	0.07	0.13	6.33
161-976D-								
1H-1, 90–91	0.90	25.57	3.07	3.74	0.67	0.11	0.05	7.11
1H-1, 123–128	1.26	23.99	2.88	3.61	0.73	0.11	0.77	7.74
2H-1, 140–145	2.93	28.49	3.42	4.24	0.82	0.12	1.52	7.97
2H-2, 140–145	4.40	26.49	3.18	4.11	0.93	0.12	0.33	9.04
2H-3, 140–145	5.90	22.57	2.71	3.22	0.51	0.09	1.20	6.61
2H-4, 140–145	7.40	26.07	3.13	3.68	0.55	0.09	1.06	7.13
2H-6, 140–145	10.40	21.16	2.54	3.11	0.57	0.10	0.84	6.65
3H-1, 140–145	12.43	21.24	2.55	3.26	0.71	0.11	1.74	7.53
3H-2, 42–43	12.92	22.66	2.72	3.48	0.76	0.12	1.57	7.39
3H-2, 140–145	13.90	23.24	2.79	3.76	0.97	0.13	1.86	8.71
3H-3, 140–145	15.45	21.16	2.54	3.12	0.58	0.13	2.17	5.21
3H-4, 140–145	16.90	25.16	3.02	3.92	0.90	0.12	0.81	8.75
3H-5, 140–145	18.40	22.49	2.70	3.39	0.69	0.10	0.51	8.05
3H-6, 140–145	19.90	26.07	3.13	4.21	1.08	0.14	0.98	9.00
4H-1, 145–150	21.95	25.49	3.06	3.81	0.75	0.11	1.80	7.95
4H-2, 145–150	23.45	22.99	2.76	3.32	0.56	0.10	0.03	6.53
4H-3, 145–150	24.95	23.32	2.80	3.19	0.39	0.07	1.60	6.50
4H-4, 145–150	26.45	28.85	3.46	4.38	0.92	0.11	0.96	9.76
4H-5, 145–150	27.95	28.82	3.46	4.47	1.01	0.10	0.70	11.78
4H-6, 145–150	29.45	30.24	3.63	4.30	0.67	0.10	0.66	7.82
Unit 2: upper Pliocene and Pleistocene sand and nannofossil clay								
161-976B-								
40X-1, 22–23	367.62	26.32	3.16	3.58	0.42	0.08	1.09	6.13
44X-1, 36–38	406.26	33.57	4.03	4.29	0.26	0.05	0.35	6.07
44X-1, 135–136	407.25	32.24	3.87	4.09	0.22	0.04	0.12	6.42
44X-2, 17–18	407.57	33.49	4.02	4.36	0.34	0.06	0.57	6.61
47X-2, 109–110	437.39	29.07	3.49	3.86	0.37	0.07	0.05	6.17
47X-3, 16–17	437.96	30.74	3.69	3.92	0.23	0.04	0.13	6.71
47X-3, 52–54	438.32	31.74	3.81	4.09	0.28	0.06	0.00	5.44
48X-1, 76–77	445.26	32.07	3.85	4.03	0.18	0.06	0.08	3.50
48X-2, 54–55	446.54	36.32	4.36	4.36	0.00	0.03	0.21	0.00
51X-1, 28–29	473.58	29.90	3.59	3.71	0.12	0.02	0.06	7.00

Table 14 (continued).

Core, section, interval (cm)	Depth (mbsf)	$CaCO_3$ (wt%)	Inorg. C (wt%)	TC (wt%)	TOC (wt%)	TN (wt%)	TS (wt%)	C/N
51X-1, 34–35	473.64	45.32	5.44	5.48	0.04	0.06	0.00	0.78
52X-1, 16–17	482.96	27.99	3.36	3.44	0.08	0.09	0.03	1.04
52X-1, 40–41	483.20	41.40	4.97	5.21	0.24	0.05	0.34	5.60
53X-1, 21–22	492.61	28.57	3.43	4.20	0.77	0.05	0.70	17.97
53X-1, 29–30	492.69	28.99	3.48	3.93	0.45	0.08	0.08	6.56
53X-2, 18–19	494.08	34.40	4.13	4.33	0.20	0.04	0.08	5.83
54X-1, 50–51	502.50	44.82	5.38	5.55	0.17	0.04	0.12	4.96
161-967C-								
39X-4, 55–56	365.45	32.24	3.87	3.92	0.05	0.02	0.28	2.92
40X-cc, 3–4	370.53	45.15	5.42	5.70	0.28	0.05	0.00	6.53
Unit 3: lower Pliocene to Tortonian nannofossil and nannofossil-rich clay and claystone								
161-976B-								
58X-2, 84–85	536.30	30.65	3.68	3.93	0.25	0.08	0.89	3.65
58X-4, 82–83	539.28	52.73	6.33	6.73	0.40	0.06	0.42	7.78
58X-7, 94–95	543.90	33.65	4.04	4.40	0.36	0.08	0.42	5.25
59X-3, 41–43	548.01	55.81	6.70	7.24	0.54	0.08	0.00	7.88
59X-4, 15–16	549.25	38.32	4.60	4.90	0.30	0.07	0.44	5.00
59X-6, 98–99	553.08	33.40	4.01	4.20	0.19	0.08	0.00	2.77
60X-4, 94–95	558.51	33.82	4.06	4.32	0.26	0.07	0.00	4.33
60X-6, 76–77	561.28	68.06	8.17	8.52	0.35	0.04	0.00	10.21
61X-2, 27–28	564.54	38.48	4.62	4.91	0.29	0.07	0.00	4.83
61X-5, 88–89	569.65	44.65	5.36	5.63	0.27	0.07	0.00	4.50
62X-CC, 19–20	573.69	29.99	3.60	4.01	0.41	0.08	0.00	5.98
63X-1, 17–18	583.27	29.32	3.52	3.74	0.22	0.06	0.00	4.28
63X-2, 70–72	585.30	30.32	3.64	3.92	0.28	0.07	0.00	4.67
63X-5, 92–93	590.02	34.24	4.11	4.42	0.31	0.10	0.00	3.62
63X-6, 141–142	592.01	26.49	3.18	3.65	0.47	0.08	0.00	6.85
63X-CC, 23–25	592.84	36.24	4.35	4.66	0.31	0.07	0.00	5.17
64X-1, 78–79	593.58	44.07	5.29	5.52	0.23	0.07	0.00	3.83
64X-2, 31–32	594.61	35.65	4.28	4.51	0.23	0.07	0.00	3.83
64X-2, 71–72	595.01	36.40	4.37	4.57	0.20	0.08	0.00	2.92
64X-5, 131–132	600.11	38.48	4.62	4.67	0.05	0.07	0.00	0.83
65X-1, 8–9	602.48	31.32	3.76	3.94	0.18	0.08	0.00	2.63
65X-1, 94–95	603.34	42.57	5.11	5.24	0.13	0.07	0.00	2.17
65X-5, 17–18	608.07	32.40	3.89	4.14	0.25	0.08	0.00	3.65
66X-7, 80–81	620.37	34.82	4.18	4.27	0.09	0.07	0.00	1.50
67X-1, 108–109	622.68	27.66	3.32	3.76	0.44	0.08	0.00	6.42
67X-3, 21–22	624.81	25.91	3.11	3.36	0.25	0.09	0.00	3.24
69X-1, 78–79	634.68	32.49	3.90	4.07	0.17	0.08	0.00	2.48
69X-2, 43–44	635.83	35.32	4.24	4.57	0.33	0.08	0.00	4.81
70X-2, 88–89	643.28	44.23	5.31	5.46	0.15	0.07	0.00	2.50
70X-4, 42–43	645.67	34.15	4.10	4.28	0.18	0.08	0.00	2.63
70X-5, 99–100	647.74	39.48	4.74	4.82	0.08	0.07	0.00	1.33
70X-6, 45–46	648.70	33.57	4.03	4.27	0.24	0.08	0.00	3.50
71X-2, 49–50	651.92	46.15	5.54	5.52	0.00	0.08	0.00	
71X-3, 54–55	653.47	39.90	4.79	5.03	0.24	0.08	0.00	3.50
71X-7, 85–86	659.74	34.82	4.18	4.31	0.13	0.08	0.00	1.90
161-976E-								
6R-1, 71–72	583.01	33.32	4.00	4.33	0.33	0.07	2.37	5.50
6R-2, 132–133	585.12	37.90	4.55	5.27	0.72	0.10	0.56	8.40
6R-3, 60–61	585.90	24.07	2.89	3.42	0.53	0.09	0.89	6.87
6R-5, 96–97	589.26	42.40	5.09	5.34	0.25	0.06	1.18	4.86
7R-1, 137–138	593.37	30.74	3.69	4.18	0.49	0.07	0.07	8.17
10R-2, 120–121	623.60	41.40	4.97	5.11	0.14	0.10	0.11	1.63
11R-1, 70–71	631.30	34.65	4.16	4.56	0.40	0.10	0.75	4.67
11R-3, 19–20	633.79	30.32	3.64	3.98	0.34	0.10	1.30	3.97
12R-1, 52–53	640.72	32.65	3.92	4.34	0.42	0.12	0.00	4.08
12R-1, 129–130	641.49	38.15	4.58	4.85	0.27	0.09	0.82	3.50
12R-5, 129–130	647.49	49.23	5.91	6.33	0.42	0.09	0.05	5.44
13R-1, 22–23	650.02	30.07	3.61	3.94	0.33	0.12	0.13	3.21
13R-2, 15–16	651.45	35.90	4.31	4.71	0.40	0.10	0.34	4.67
Unit 4: Serravallian calcite and zeolitic sand and pebbly sand								
161-976B-								
72X-1, 43–44	660.63	77.97	9.36	9.68	0.32	0.01	0.00	37.33
72X-2, 71–72	662.41	27.07	3.25	3.21	0.00	0.02	0.00	0.00
72X-3, 62–63	663.60	5.16	0.62	0.31	0.00	0.05	0.00	0.00
161-976E-								
13R-2, 75–76	652.05	48.56	5.83	6.21	0.38	0.08	0.00	5.54

Notes: Total organic carbon (TOC) concentrations are calculated from the difference between inorganic carbon and TC concentrations. C/N ratios are calculated from TOC and total nitrogen (TN) concentrations and are given as atom/atom ratios. TS = total sulfur concentration. This table is also on the CD-ROM, back pocket, this volume.

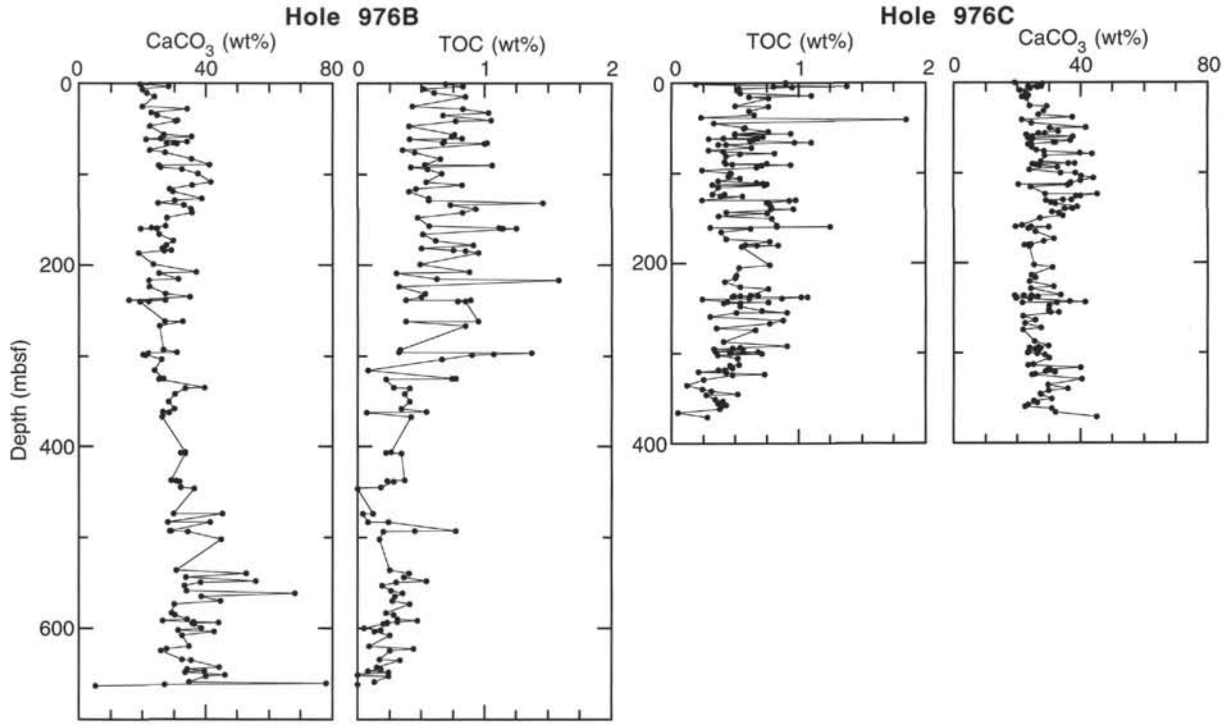

Figure 108. Organic carbon and $CaCO_3$ concentrations in sediment samples from Holes 976B and 976C.

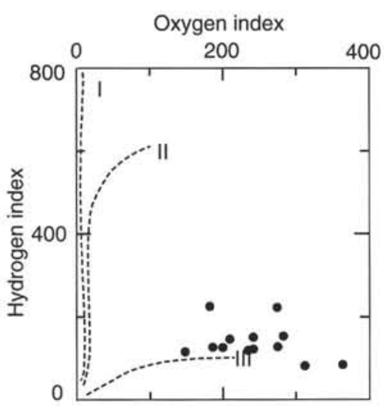

Figure 109. Rock-Eval van Krevelen-type diagram of Pleistocene sapropels from Hole 976B. Organic matter appears to be a mixture of Type II algal material that has been variably oxidized and Type III continental or detrital organic matter. Hydrogen index = mg hydrocarbons/g organic carbon; oxygen index = mg CO_2/g organic carbon.

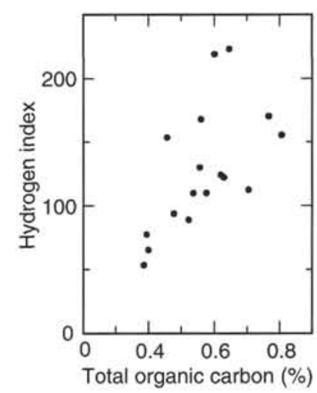

Figure 110. Comparison of Rock-Eval hydrogen index values and total organic carbon concentrations of sapropels from Hole 976B. The correspondence between increases in both parameters indicates that preservation of organic matter is important to enhancing the organic-carbon richness of sediments in the Alboran Sea.

Table 15. Results of Rock-Eval pyrolysis analyses of organic-rich layers selected from Hole 976B.

Core, section, interval (cm)	Depth (mbsf)	TOC (%)	T_{max} (°C)	S_1	S_2	S_3	PI	S_2/S_2	PC	HI	OI
161-976B-											
1H-3, 19–20	3.19	0.51	397	0.15	0.78	2.11	0.16	0.36	0.07	152.00	413.00
3H-2, 28–29	14.35	0.64	400	0.21	0.56	1.95	0.28	0.28	0.06	87.00	304.00
4H-4, 122–124	28.22	0.55	397	0.11	0.51	1.99	0.18	0.25	0.05	92.00	361.00
5H-6, 125–126	40.75	0.71	412	0.12	0.91	1.94	0.12	0.46	0.08	128.00	273.00
6H-6, 139–140	49.90	0.39	387	0.10	0.25	1.79	0.29	0.13	0.02	64.00	458.00
7H-6, 10–11	58.60	0.38	390	0.07	0.29	1.99	0.19	0.14	0.03	76.00	523.00
8H-4, 92–93	65.92	0.75	411	0.10	0.81	1.78	0.11	0.45	0.07	108.00	237.00
10H-3, 82–83	83.32	0.36	382	0.08	0.19	1.76	0.31	0.10	0.02	52.00	488.00
11H-2, 85–86	89.97	0.86	411	0.39	1.04	1.62	0.27	0.64	0.11	120.00	188.00
13H-3, 70–71	111.70	0.67	409	0.43	0.73	1.59	0.37	0.45	0.09	108.00	237.00
15X-4, 39–40	131.89	0.84	417	0.13	1.03	1.69	0.11	0.60	0.09	122.00	201.00
18X-3, 29–30	159.09	0.72	415	0.13	1.20	2.01	0.10	0.59	0.11	166.00	279.00
18X-3, 105–106	159.85	0.81	420	0.22	1.76	2.21	0.11	0.79	0.16	217.00	272.00
18X-3, 122–123	160.02	1.14	416	0.21	1.92	2.79	0.10	0.68	0.17	168.00	244.00
18X-3, 134–135	160.14	1.22	414	0.22	1.87	2.65	0.11	0.70	0.17	153.00	217.00
29X-2, 11–12	262.21	1.01	415	0.16	1.12	1.50	0.12	0.74	0.10	110.00	148.00
32X-5, 131–132	296.80	0.90	412	0.28	1.99	1.63	0.12	1.22	0.18	221.00	181.00

Notes: Total organic carbon (TOC) concentrations are derived from the Rock-Eval parameters and therefore differ somewhat from the TOC values of the same samples in Table 14. Units of the various Rock-Eval parameters are given in the "Explanatory Notes" chapter (this volume).

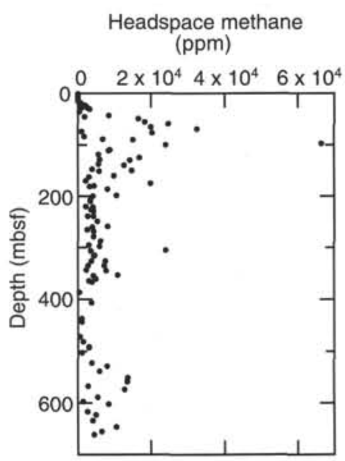

Figure 111. Headspace methane concentrations in sediments from Holes 976B, 976C, and 976D. Note that gas concentrations remain high below Unit II, a sandy interval from 368 to 502 mbsf in Hole 976B.

Table 16. Results of headspace gas analyses of sediments from Holes 976B, 976C, and 976D.

Core, section, interval (cm)	Depth (mbsf)	C_1	C_2	C_3	C_1/C_2
161-976B-					
1H-3, 0–5	3	2			0
2H-4, 0–5	8	2			0
4H-4, 0–5	27	600			0
5H-4, 0–5	36	289			0
6H-4, 0–5	46	1732			0
7H-4, 0–5	55	18170	3		6057
8H-4, 0–5	65	19835	4		4959
9H-4, 0–5	75	938			0
10H-4, 0–5	84	1762			0
11H-2, 0–5	89	6717	3		2239
12H-1, 0–5	98	66555	22	3	3025
13H-4, 0–5	112	8339	5		1668
14H-7, 0–5	125	16787	9		1865
15X-4, 0–5	131	14166	8		1771
16X-4, 0–5	141	12527	10	3	1253
17X-4, 0–5	150	14662	11	2	1333
18X-4, 0–5	160	9811	11	4	892
19X-4, 0–5	170	2089	2		1045
20X-4, 0–5	180	4293	7	2	613
21X-2, 0–5	186	8103	13	5	623
22X-4, 0–5	199	10427	14	3	745
23X-3, 0–5	207	3260	5		652
24X-6, 0–5	220	2098	5	2	420
25X-4, 0–5	226	3459	7		494
26X-6, 0–5	239	2610	6		435
28X-7, 0–5	260	3809	8		476
29X-4, 0–5	265	2501	7	2	357
30X-6, 0–5	278	4239	10	2	424
32X-5, 0–5	295	2984	6		497
33X-4, 0–5	304	23934	43	9	557
34X-4, 0–5	314	4561	10	2	456
35X-5, 0–5	325	7475	18	4	415
36X-5, 0–5	334	7140	11		649
37X-5, 0–5	344	7770	12	2	648
38X-4, 0–5	353	10877	15		725
39X-3, 0–5	361	4819	6		803
40X-1, 0–5	367	3920	4		980
42X-CC, 0–5	387	425			0
44X-2, 0–5	407	3734	3		1245
47X-3, 0–5	438	1113			0
48X-1, 0–5	444	944			0
51X-1, 0–5	473	480			0
52X-1, 0–5	483	1320	2		660
53X-1, 0–5	492	2926	2		1463
54X-1, 0–5	502	1075	2		538
56X-4, 0–5	522	3813	9		424
57X-3, 0–5	528	8026	20		401
58X-4, 0–5	538	5989	14		428
59X-5, 0–5	551	13599	51	3	267
60X-4, 0–5	558	13561	37	2	367
61X-4, 0–5	567	2817	19	3	148
62X-CC, 0–5	573	12754	67	6	190
63X-4, 0–5	588	5422	33	2	164
64X-4, 0–5	597	1378	12		115
65X-1, 0–5	602	8371	54	3	155
66X-5, 0–5	617	2590	30	2	86
67X-2, 0–5	623	4922	38	2	130
69X-2, 0–5	635	3957	50	3	79
70X-5, 0–5	647	10490	68	3	154
71X-5, 0–5	656	6450	51	2	126
72X-2, 0–5	662	4421	16		276
161-976C-					
1H-3, 0–5	3	4			
2H-4, 0–5	10	8			
3H-4, 0–5	20	612			
4H-5, 0–5	31	3107			
5H-7, 0–5	43	8373			
6H-5, 0–5	50	16456	2		8228
7H-5, 0–5	59	24631	4		6158
8H-5, 0–5	69	32543	7		4649
9H-4, 0–5	77	20318	5		4064
10H-7, 0–5	91	14963	6		2494
11H-7, 0–5	100	23893	8		2987
12H-7, 0–5	110	8734	4		2184
13H-7, 0–5	119	5614	4		1404
14H-7, 0–5	129	5907	4		1477
15X-7, 0–5	138	5511	4		1378
16X-7, 0–5	148	3912	3		1304
17X-3, 0–5	152	5783	6	2	964
18X-4, 0–5	163	2979	3		993
19X-6, 0–5	175	19717	13	2	1517
20X-3, 0–5	181	3129	7	4	447
22X-3, 0–5	200	3985	5		797
23X-4, 0–5	210	3396	6	2	566
24X-5, 0–5	221	4068	6		678
25X-3, 0–5	229	4172	7	1	596
26X-3, 0–5	238	4153	14	7	297
27X-3, 0–5	248	5219	10	3	522
28X-4, 0–5	258	8106	17	4	477
29X-4, 0–5	268	4097	8	2	512
31X-4, 0–5	287	6114	11	2	556
32X-4, 0–5	297	5938	12	3	495
33X-4, 0–5	306	3539	7		506
34X-4, 0–5	316	4323	8		540
35X-4, 0–5	326	3621	5		724
36X-3, 0–5	334	2777	4		694
37X-3, 0–5	343	2263	4		566
38X-4, 0–5	355	4109	8		514
39X-4, 0–5	365	2993	3		998
161-976D-					
1H-1, 123–128	1	5			
2H-1, 140–145	3	7			
2H-2, 140–145	4	5			
2H-3, 140–145	6	6			
2H-4, 140–145	7	2			
2H-6, 140–145	10	10			
3H-1, 140–145	12	11			
3H-2, 140–145	14	12			
3H-3, 140–145	15	30			
3H-4, 140–145	17	131			
3H-5, 140–145	18	586			
3H-6, 140–145	20	501			
4H-1, 145–150	22	798			
4H-2, 145–150	23	1915			
4H-3, 145–150	25	2078			
4H-4, 145–150	26	1318			
4H-5, 145–150	28	903			
4H-6, 145–150	29	2545			

Note: Dominance of methane indicates that the gases originate from in situ fermentation of organic matter.

Table 17. Results of vacutainer gas analyses of sediments from Holes 976B and 976C.

Core, section, interval (cm)	Depth (mbsf)	C_1	C_2	C_3	i-C_4	n-C_4	i-C_5	C_1/C_2
161-976B-								
10H-1, 145–150	81	7477						3574
11H-1, 145–150	91	7187						3264
12H-1, 145–150	100	689786	193	23				3574
13H-1, 145–150	109	802924	246	33	8			3264
14H-1, 145–150	119	715537	240	30	8			2981
15X-4, 145–150	133	508296	233	37	9			2182
16X-4, 145–150	142	703940	339	56	12		7	2077
17X-4, 145–150	152	682246	316	44	10			2159
18X-4, 145–150	162	555421	305	46	10			1821
19X-4, 145–150	171	578822	321	45	9			1803
20X-4, 145–150	181	672971	477	75	13		9	1411
21X-4, 145–150	186	647478	509	90	17		11	1272
22X-4, 145–150	200	611780	475	68	12		8	1288
24X-4, 145–150	219	537490	472	72	12		9	1139
25X-4, 145–150	228	668026	678	111	18		17	985
26X-4, 145–150	238	110760	113	13				980
28X-4, 145–150	257	614892	659	94	14		16	933
29X-4, 145–150	265	515928	589	88	12		15	876
30X-4, 145–150	275	681577	772	112	13		19	883
32X-4, 145–150	295	355825	446	63	8		14	798
33X-4, 145–150	305	729609	850	117	12	7	23	858
34X-4, 145–150	315	675715	785	107	11	9	22	861
35X-4, 145–150	323	676286	708	101	9	13	21	955
36X-4, 145–150	334	680840	739	86	7	15	17	921
37X-4, 145–150	344	698140	643	66		20	13	1086
38X-4, 145–150	354	658059	577	43		20	9	1140
39X-4, 145–150	364	314809	254	5		11		1239
56X-4, 145–150	524	717296	720	16	13			996
57X-4, 145–150	531	693776	827	24	18			839
58X-4, 145–150	540	793993	1103	37	30			720
59X-4, 145–150	551	788901	1395	50	35			566
60X-4, 145–150	559	756849	1372	50	39			552
61X-4, 145–150	598	728908	1520	54	38			480
63X-4, 145–150	589	760137	2238	75	42	7	8	340
64X-4, 145–150	599	751983	1171	38	20			642
65X-4, 145–150	607	5472						
66X-4, 145–150	615	3588						
67X-4, 145–150	625	8209	19					432
70X-4, 145–150	647	7900	16					494
71X-4, 145–150	656	1121	13					86
72X-4, 145–150	662	832						
161-976C-								
18X-6, 0–5	166	706592	365	52				1935.87
19X-6, 0–5	175	552742	327	54	11	25	7	1690.34

Note: Dominance of methane indicates that the gases originate from in situ fermentation of organic matter.

Table 18. Interstitial water data from Hole 976B.

Core, section, interval (cm)	Depth (mbsf)	pH	Alkalinity (mM)	Salinity (‰)	Cl (mM)	Ca (mM)	Mg (mM)	Mn (µM)	Sr (µM)	SO_4 (mM)	NH_4 (µM)	H_4SiO_4 (µM)	Li (µM)	Na (mM)	K (mM)	PO_4 (µM)	Br + I (µM)
Surface water:				37	582	11.35	56.43	0.71	104	31.6			25	526	11.19		
161-976B-																	
1H-2, 145–150	2.95	7.28	8.39	38	621	9.35	57.68	12.5	94.7	25.76	665	555.32	32	539	11.93	32.20	1182
4H-3, 145–150	26.95	7.45	15.135	35	606	3.41	43.78	2.84	94.5	0.25	3206	519.13	32	501	10.13	34.28	
7H-3, 145–150	55.45	7.50	13.526	34.5	616	3.31	40.41	2.34	118	0.02	3190	580.86	38	511	9.46	31.70	
10H-3, 145–150	84.00	7.34	10.771	35	628	4.84	37.54	1.16	142	0.14	4260	442.49	52	517	10.17	12.51	1541
13H-3, 145–150	112.45	7.40	8.91	36	645	6.04	38.84	2.21	175	0.00	4933	863.99	67	531	8.81	7.85	
16X-3, 145–150	140.90	7.37	9.556	37.5	674	7.48	40.54	2.03	199	1.43	5760	319.02	111	549	8.53	6.81	1824
19X-3, 145–150	169.57	7.42	7.432	38.5	694	9.75	42.29	2.23	234	1.62	5670	382.89	126	556	8.08	n.d.	2082
22X-3, 145–150	198.80	7.44	6.05	40	707	10.40	43.86	1.32	279	0.39	5346	319.02	145	575	7.42	n.d.	
25X-3, 135–140	226.31	7.34	5.011	42	747	13.63	44.97	1.65	355	1.19	5249	363.73	181	598	6.64	n.d.	2302
29X-4, 0–10	265.10	7.55	3.339	44	779	18.10	46.40	3.36	500	1.43	4544	n.d.	200	620	7.00	n.d.	
32X-4, 145–150	295.39	7.16	3.565	46	788	21.84	47.35	4.3	646	0.53	1026	714.98	187	648	5.70	n.d.	2610
35X-4, 129–139	324.77	7.49	1.761	49	850	23.63	51.14	2.82	899	0.08	4673	184.91	197	687	5.89	n.d.	2441
38X-3, 145–150	352.50	7.54	1.712	51	907	27.34	50.83	3.66	1197	1.34	4471	148.72	218	715	6.90	n.d.	
47X-2, 135–150	437.65	7.92	1.456	56.5	1020	36.13	43.63	2.45	1383	0.28	4446	93.37	231	804	6.59	n.d.	3007
56X-3, 140–150	521.94	7.07	1.727	63	1100	61.35	59.51	4.27	2312	2.18	3684	267.93	489	856	7.55	n.d.	3026
59X-4, 135–150	550.45	6.82	2.01	70	1168	70.81	62.04	3.94	3094	1.06	4341	246.64	680	877	7.21	n.d.	3498
63X-3, 135–150	587.45	n.d.	n.d.	71	1228	84.18	68.66	6.8	3692	1.21	4219	301.99	764	903	6.52	n.d.	3217
66X-4, 108–123	616.42	n.d.	n.d.	77	1276	93.53	75.58	n.d.	4040	0.98	4074	n.d.	902	932	7.13	n.d.	3754
70X-4, 135–150	646.60	n.d.	n.d.	76	1278	95.50	81.22	5.26	3880	1.55	3879	n.d.	900	913	5.95	n.d.	3233

Note: n.d. = not determined. This table is also on the CD-ROM, back pocket, this volume.

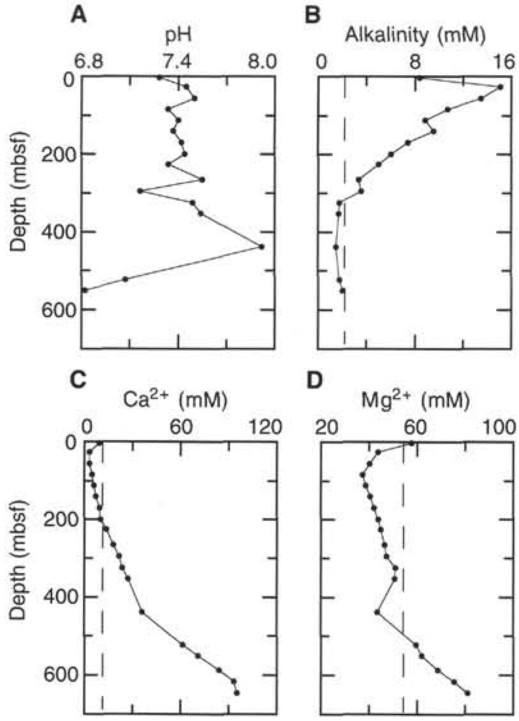

Figure 112. Concentration profiles of (**A**) pH, (**B**) alkalinity, (**C**) calcium, and (**D**) magnesium in Hole 976B. The dashed lines indicate standard seawater (International Association for the Physical Sciences of the Ocean [IAPSO]) composition.

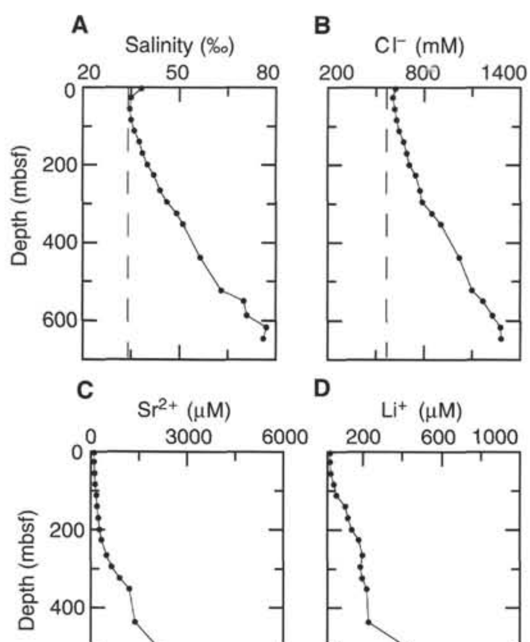

Figure 113. Concentration profiles of (**A**) salinity, (**B**) chloride, (**C**) strontium, and (**D**) lithium in Hole 976B. The dashed lines indicate standard seawater (IAPSO) composition.

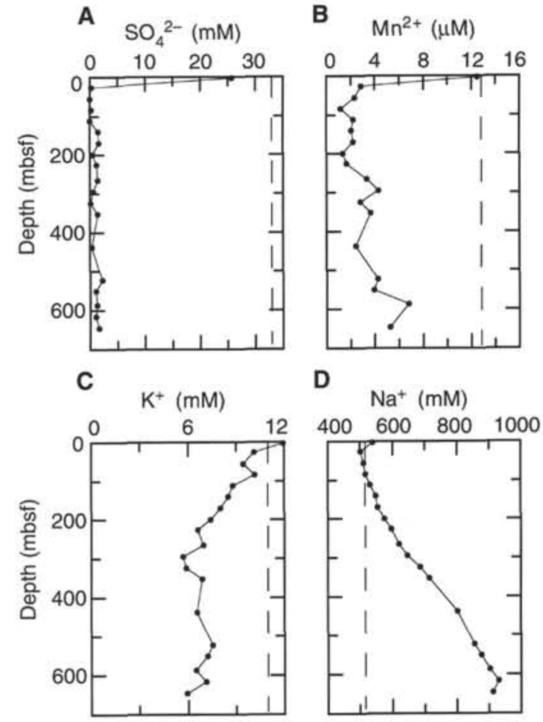

Figure 114. Concentration profiles of (**A**) sulfate, (**B**) manganese, (**C**) potassium, and (**D**) sodium in Hole 976B. The dashed lines indicate standard seawater (IAPSO) composition.

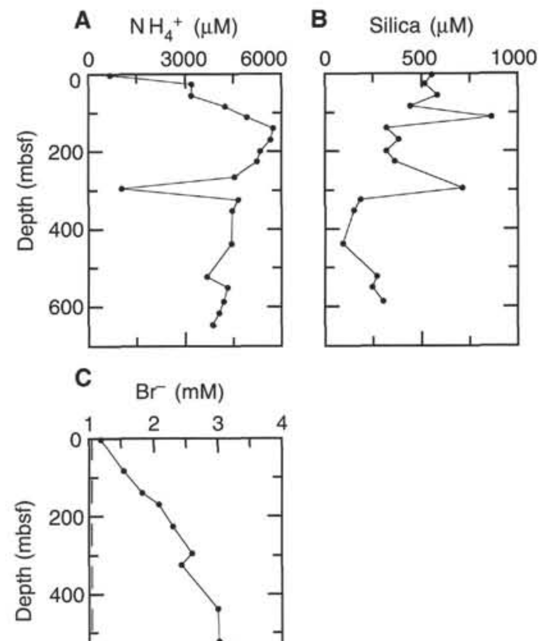

Figure 115. Concentration profiles of (**A**) ammonium, (**B**) silica, and (**C**) bromine in Hole 976B.

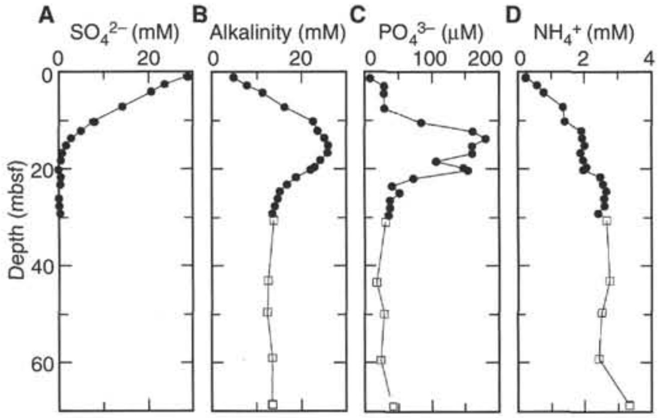

Figure 116. Concentration profiles of (**A**) sulfate, (**B**) alkalinity, (**C**) phosphate, and (**D**) ammonia in Holes 976C and 976D. Solid circles are samples from Hole 976D and open squares from Hole 976C.

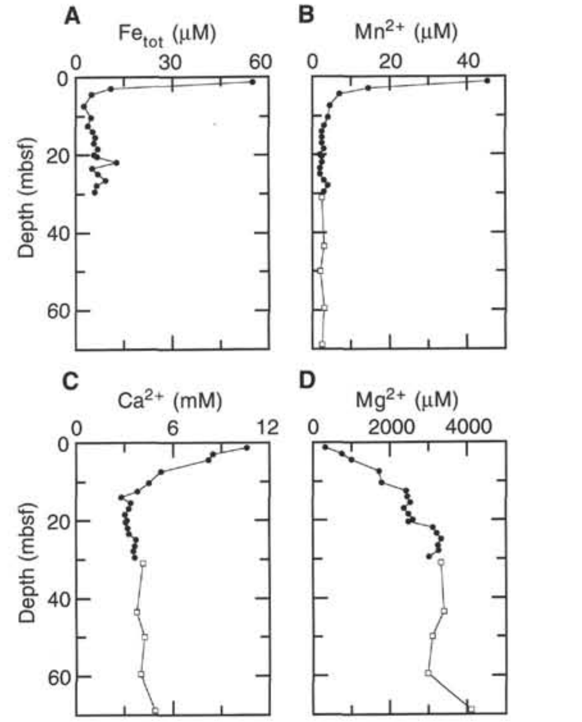

Figure 117. Concentration profiles of (**A**) iron, (**B**) manganese, (**C**) calcium, and (**D**) magnesium in Holes 976C and 976D. Solid circles are samples from Hole 976D and open squares from Hole 976C.

Table 19. Interstitial water data from Hole 976D.

Core, section, interval (cm)	Depth (mbsf)	pH	Alkalinity (mM)	Salinity (‰)	Cl (mM)	Ca (mM)	Mg (mM)	Mn (μM)	Sr (μM)	SO_4 (mM)	NH_4 (μM)	H_4SiO_4 (μM)	Li (μM)	Na (mM)	K (mM)	PO_4 (μM)	Fe (μM)
161-976D-																	
1H-1, 128–133	1.28	7.35	5.408	40	619	10.63	56.51	45.5	103	29.32	318	239.61	30	535.85	11.47	8.95	55.10
2H-1, 145–150	2.95	7.45	8.334	39	618	8.51	57.61	14.5	98	24.21	746	570.65	29	526.46	12.47	29.58	10.90
2H-2, 145–150	4.45	7.50	11.928	38	614	8.23	56.10	7	86	21.18	992	730.82	31	550.74	11.44	28.90	5.00
2H-4, 145–150	7.45	7.48	16.831	36	610	5.26	54.10	4.5	83	14.68	1716	602.68	34	541.27	10.76	29.58	2.60
2H-6, 145–150	10.45	7.56	23.157	36	610	4.49	53.31	4	75	7.91	1777	662.48	32	517.23	10.77	84.61	4.70
3H-1, 145–150	12.45	7.50	24.256	36	616	3.77	51.32	3	77	5.22	2416	764.99	30	522.25	10.89	162.99	3.80
3H-2, 145–150	13.95	7.21	25.815	36	614	2.81	42.53	2.5	77	3.01	2436	777.81	29	443.80	9.48	182.27	5.40
3H-3, 145–150	15.45	7.27	26.57	36	617	3.37	49.33	2.5	81	1.85	2527	668.89	30	525.63	10.06	161.64	6.10
3H-4, 145–150	16.95	7.57	26.455	35.5	614	3.29	48.92	2.5	82	0.85	2369	651.80	28	538.10	9.23	161.64	5.80
3H-5, 145–150	18.45	7.55	24.782	36	616	3.04	48.82	3	87	0.57	2469	698.79	26	531.83	9.72	106.63	6.90
3H-6, 145–150	19.95	7.53	23.464	35	616	3.12	47.45	2	88	–0.26	2586	811.98	26	519.45	9.46	147.89	5.70
3H-7, 45–50	20.45	7.48	22.541	35	618	3.08	46.84	2.5	90	–0.02	2469	829.07	26	530.39	9.65	154.76	6.80
4H-1, 145–150	21.95	7.58	19.216	35	622	3.17	44.71	2.5	90	0.54	3108	615.50	27	482.24	9.58	72.25	12.80
4H-2, 145–150	23.45	7.50	17.212	34.5	610	3.25	44.11	2	92	0.38	3205	577.05	27	522.79	9.48	39.90	5.20
4H-3, 145–150	24.95	7.58	15.508	34.5	611	3.70	43.58	2	91	–0.30	3326	470.27	28	529.14	9.52	50.90	6.90
4H-4, 145–150	26.45	7.58	15.043	34.5	616	3.63	42.87	3	93	0.01	3243	440.37	29	523.99	9.59	36.45	9.30
4H-5, 145–150	27.95	7.55	14.399	34.5	619	3.56	42.45	4	91	0.11	3251	532.20	27	534.29	9.74	36.45	6.60
4H-6, 145–150	29.45	7.54	13.771	34	616	3.62	43.01	3	94	0.25	3003	500.17	28	538.03	9.48	33.70	6.00
4H-4, 145–150	30.95	7.58	14.061	35	615	4.14	42.36	2.5	99	n.d.	3326	512.98	29	519.55	9.39	28.90	n.d.
5H-6, 145–150	43.45	7.61	12.639	35	620	3.76	37.91	3	122	n.d.	3401	498.03	34	501.10	9.20	14.45	n.d.
6H-4, 145–150	49.95	7.54	12.394	35	620	4.23	40.70	2	124	n.d.	3101	386.98	36	545.91	9.84	25.45	n.d.
7H-4, 145–150	59.45	7.56	13.4	35	629	3.98	39.96	3	128	n.d.	2972	568.51	38	552.65	8.10	19.95	n.d.
8H-4, 145–150	68.95	7.53	13.191	35	632	4.89	36.86	2.5	140	n.d.	4107	767.13	46	510.46	8.47	36.45	n.d.

Note: n.d. = not determined. This table is also on the CD-ROM, back pocket, this volume.

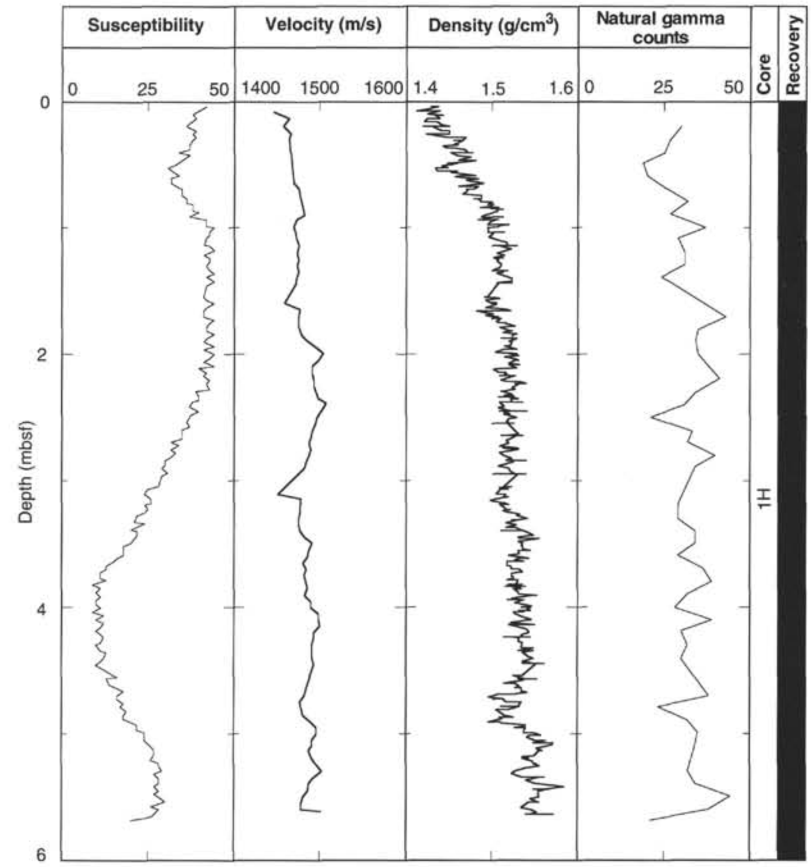

Figure 118. MST data (susceptibility, velocity, density, and natural gamma) for Hole 976A. Cored intervals and recovery amounts are shown on the right.

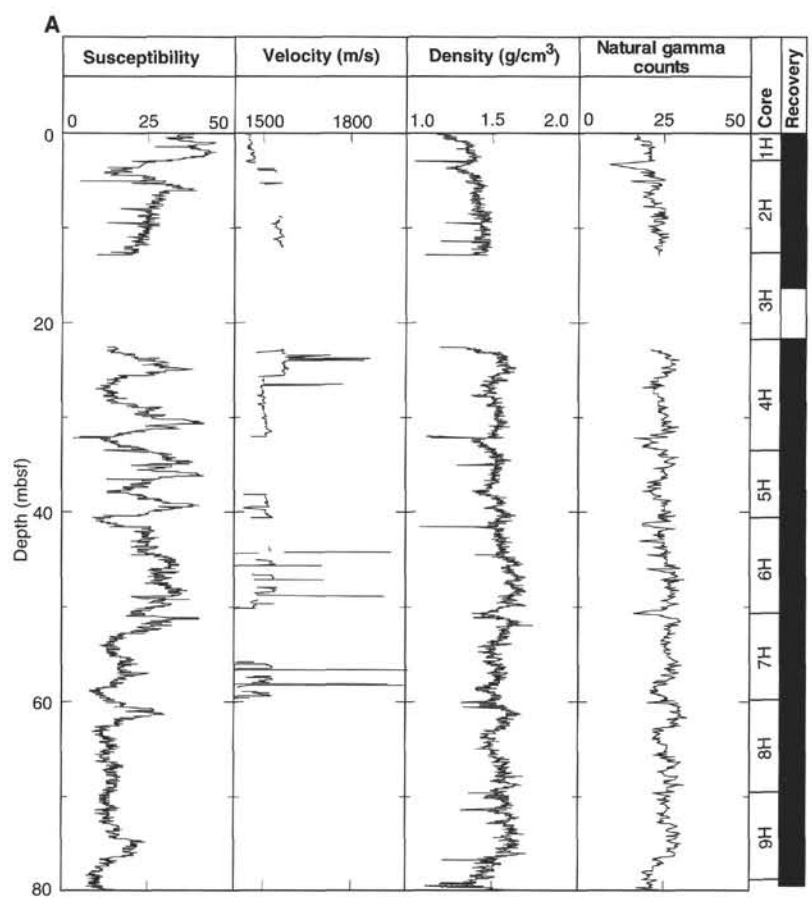

Figure 119. MST data (susceptibility, velocity, density, and natural gamma) for Hole 976B: (**A**) 0–80 mbsf, (**B**) 0–1000 mbsf. Cored intervals and recovery amounts are shown on the right.

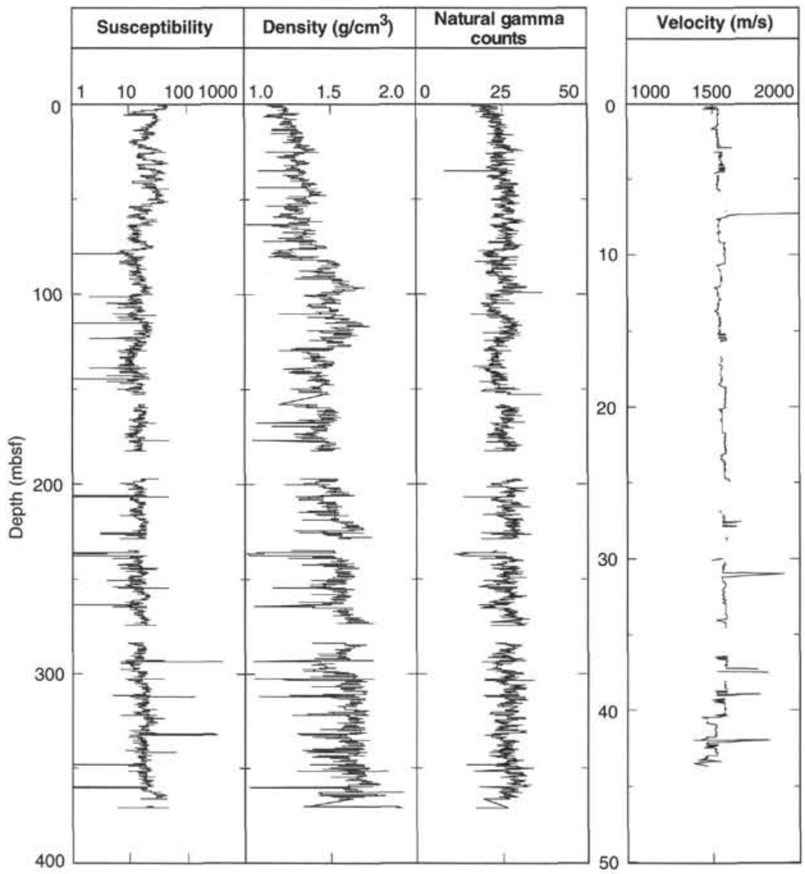

Figure 120. MST data (susceptibility, velocity, density, and natural gamma) for Hole 976C.

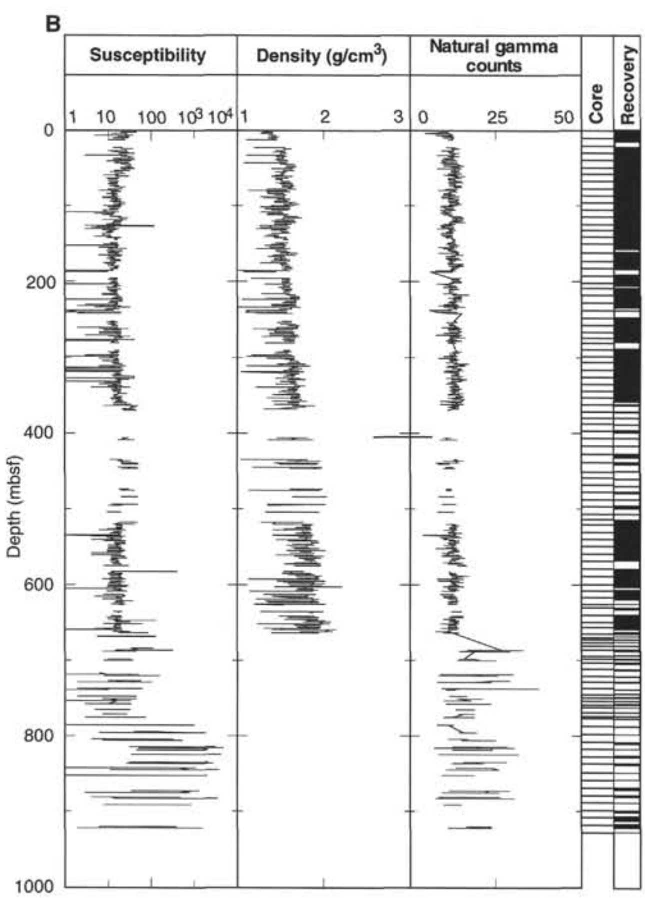

Figure 119 (continued).

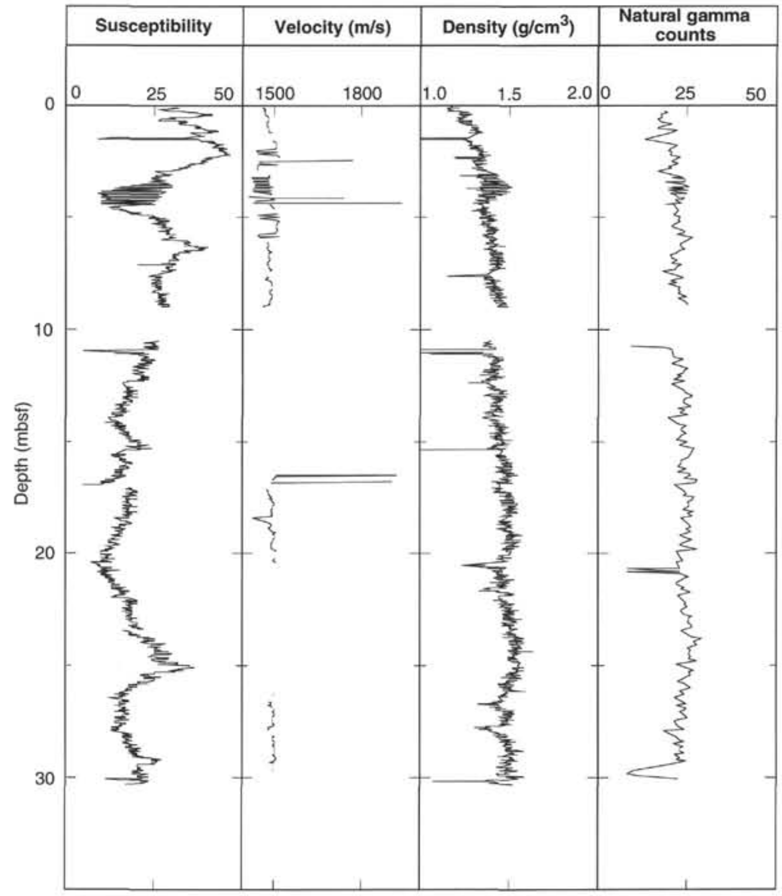

Figure 121. MST data (susceptibility, velocity, density, and natural gamma) for Hole 976D.

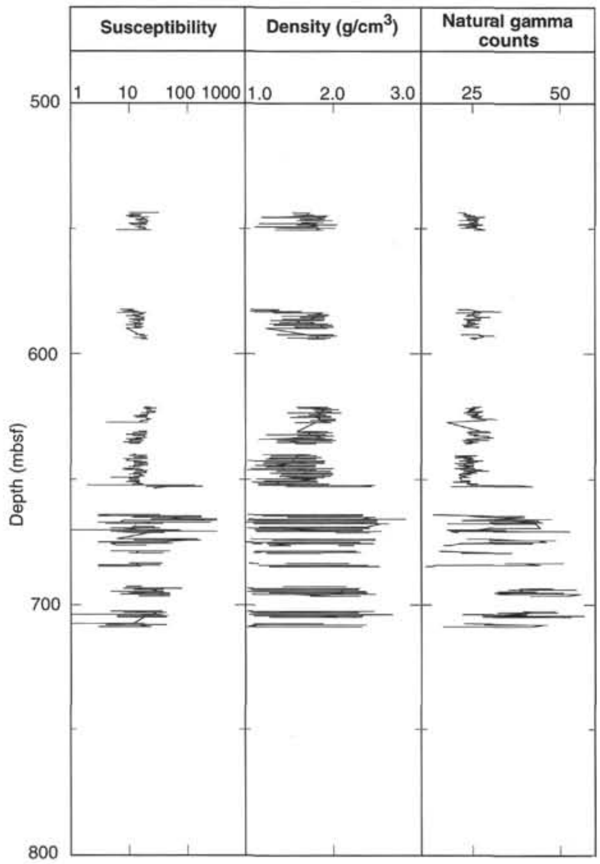

Figure 122. MST data (susceptibility, density, and natural gamma) for Hole 976E.

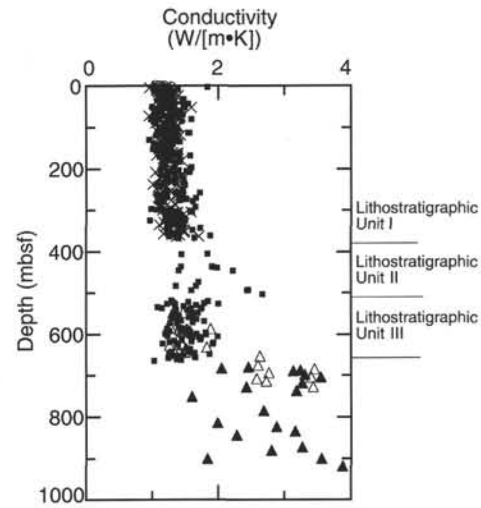

Figure 123. Thermal conductivity for Holes 976A, 976B, 976C, 976D, and 976E. Two symbols for Hole 976B denote measurements on unconsolidated (solid squares) and hard sections (solid triangles). Open circles = 976A, × = 976C, + = 976D, open triangles = 976E.

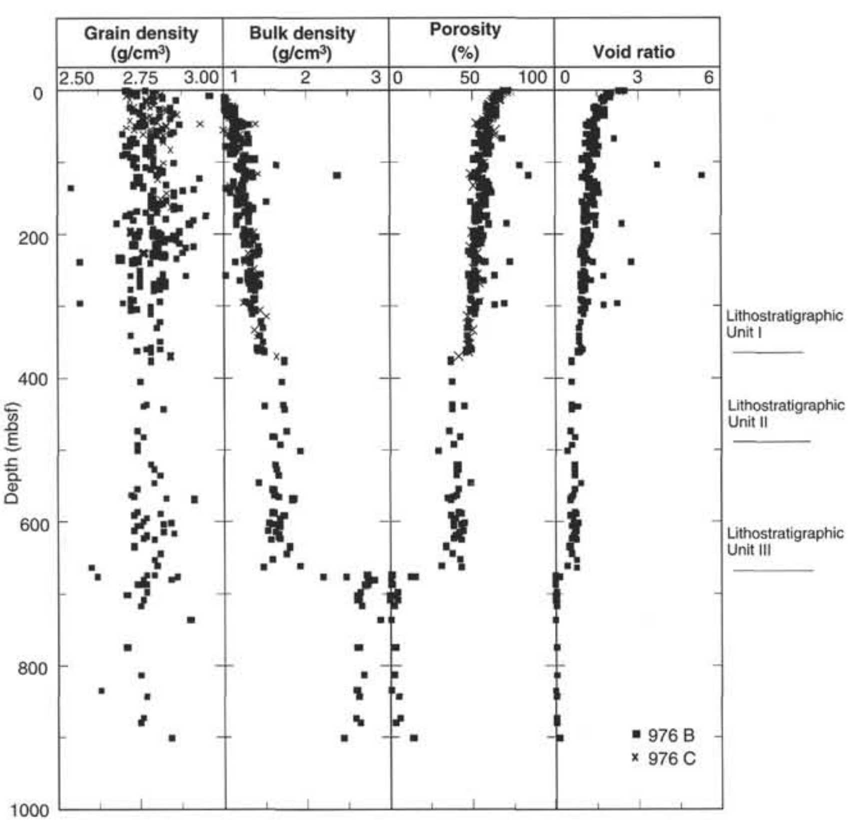

Figure 124. Index properties for Holes 976B and 976C.

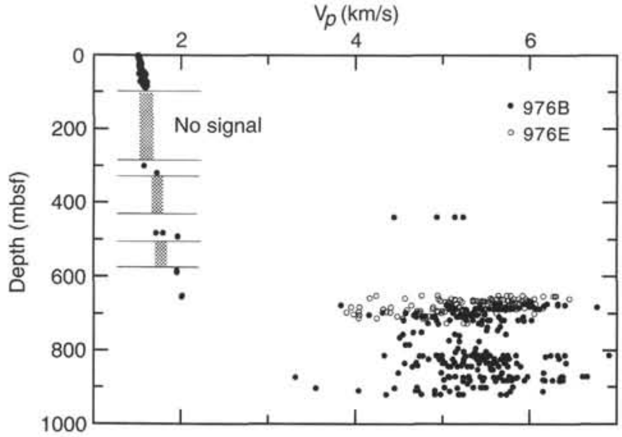

Figure 125. Seismic velocity for Holes 976A, 976B, 976C, 976D, and 976E.

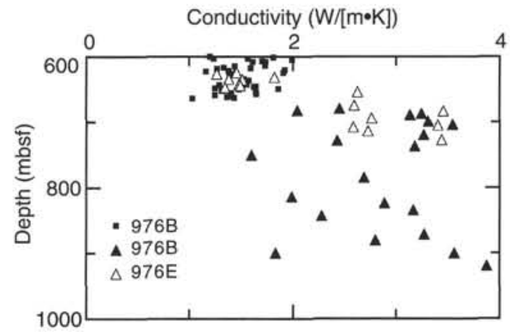

Figure 127. Thermal conductivity variations in the basement unit for Holes 976B and 976E. Two symbols for Hole 976B denote measurements on unconsolidated (solid squares) and hard sections (solid triangles).

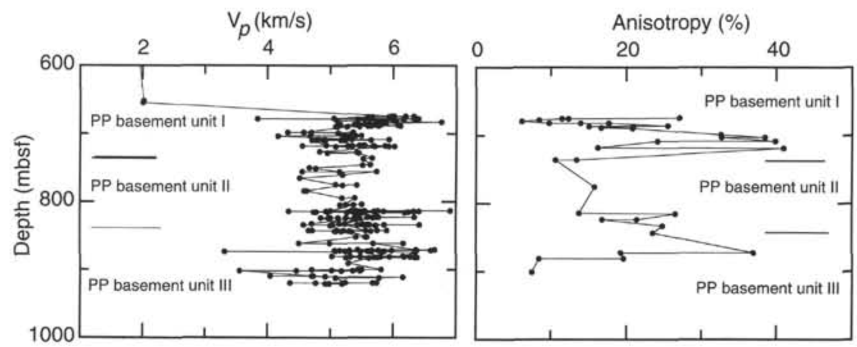

Figure 126. Seismic velocity variations and velocity anisotropy in the basement unit for Holes 976B and 976E.

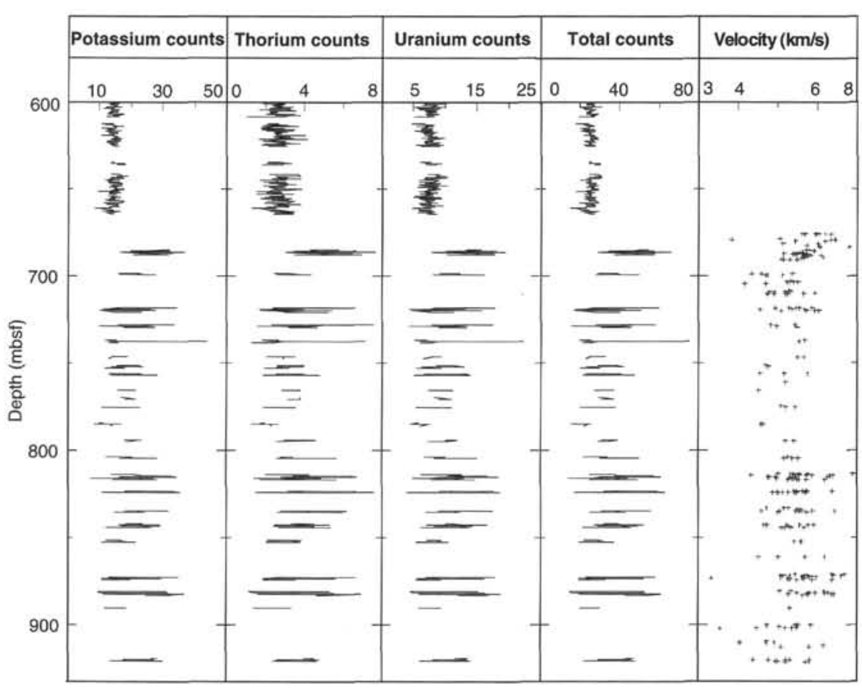

Figure 128. Natural gamma radiation in the basement unit of Hole 976B.

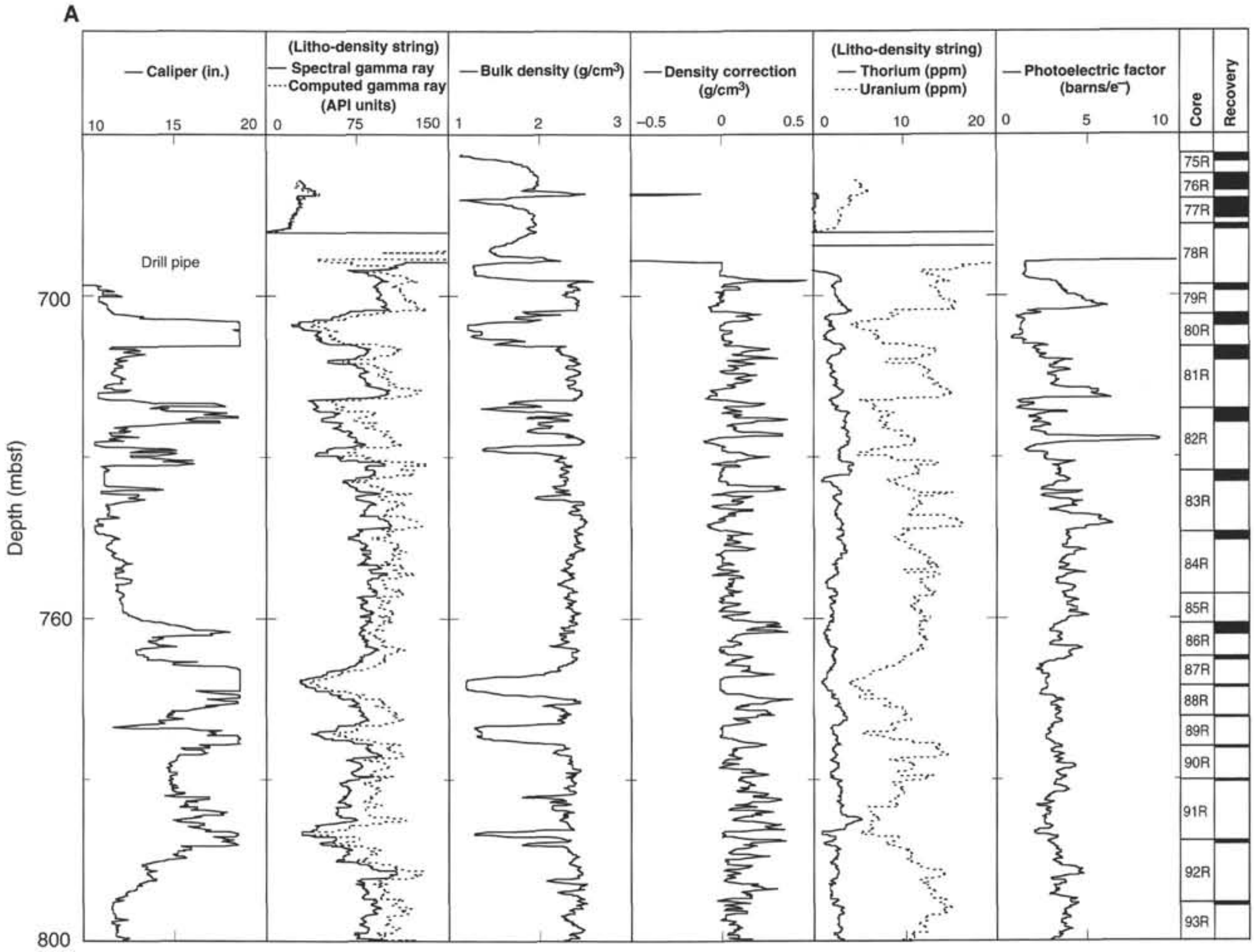

Figure 129. Quad combo tool results (**A, B**) and FMS (main logs) calipers (**C, D**) for the basement of Hole 976B. The two curves of thermal neutron porosity are thermal neutron porosity (NPHI, dashed line), and high-resolution thermal neutron porosity (HTNP).

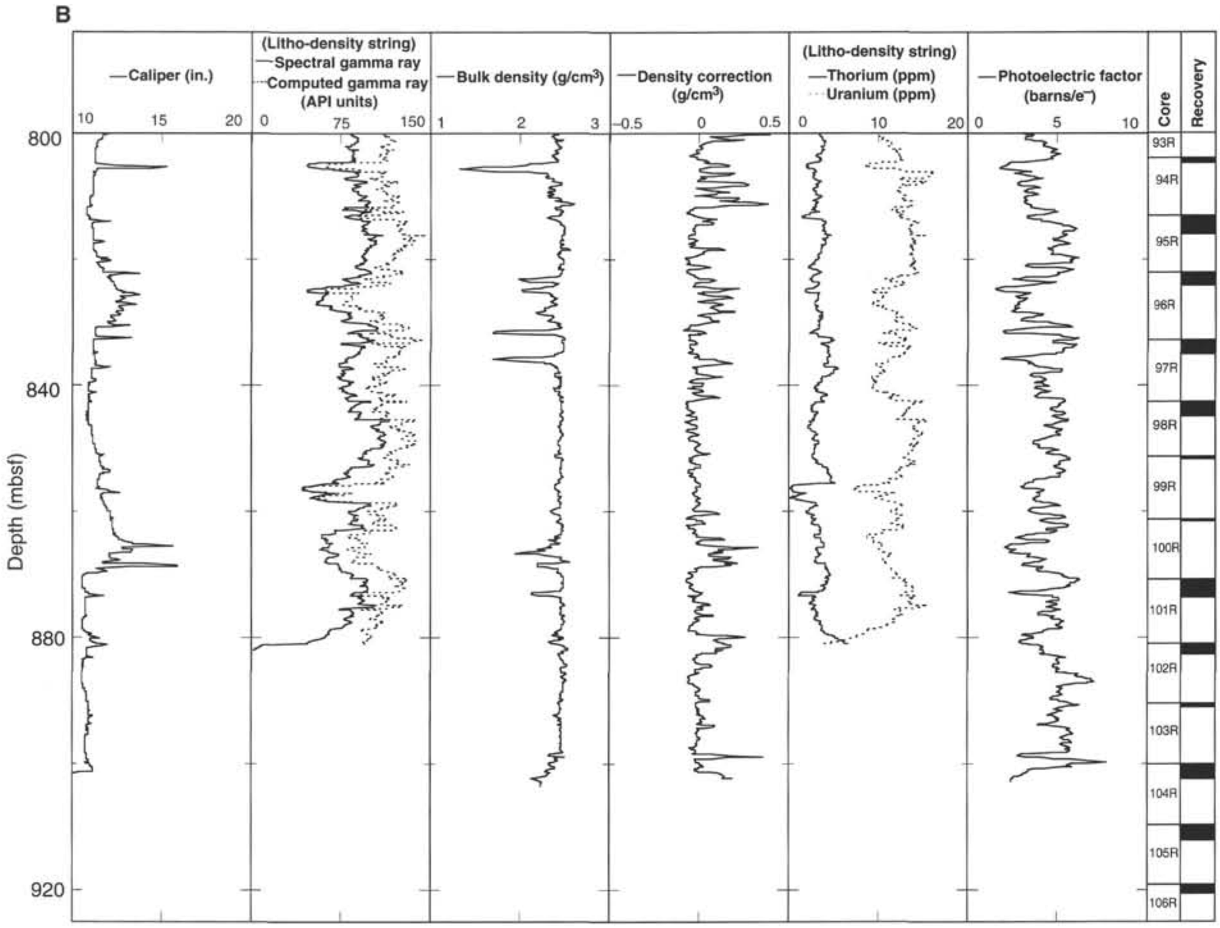

Figure 129 (continued).

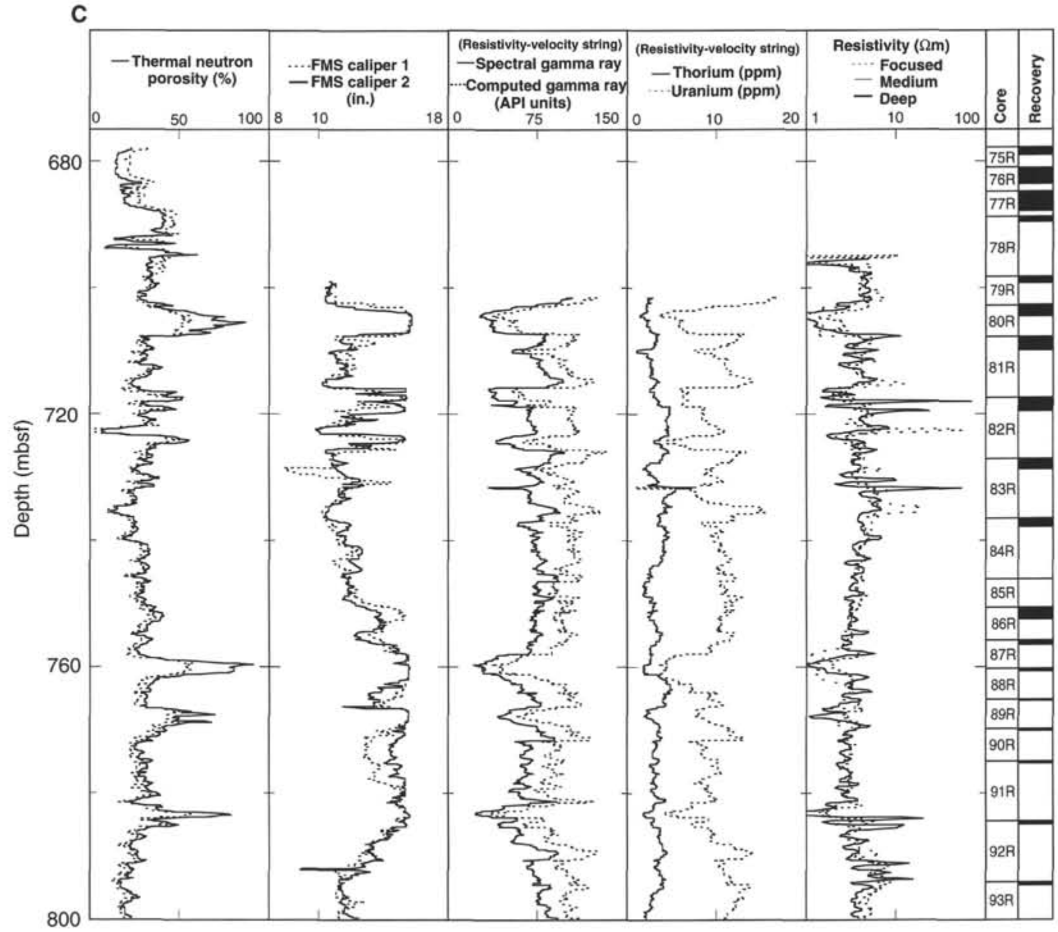

Figure 129 (continued).

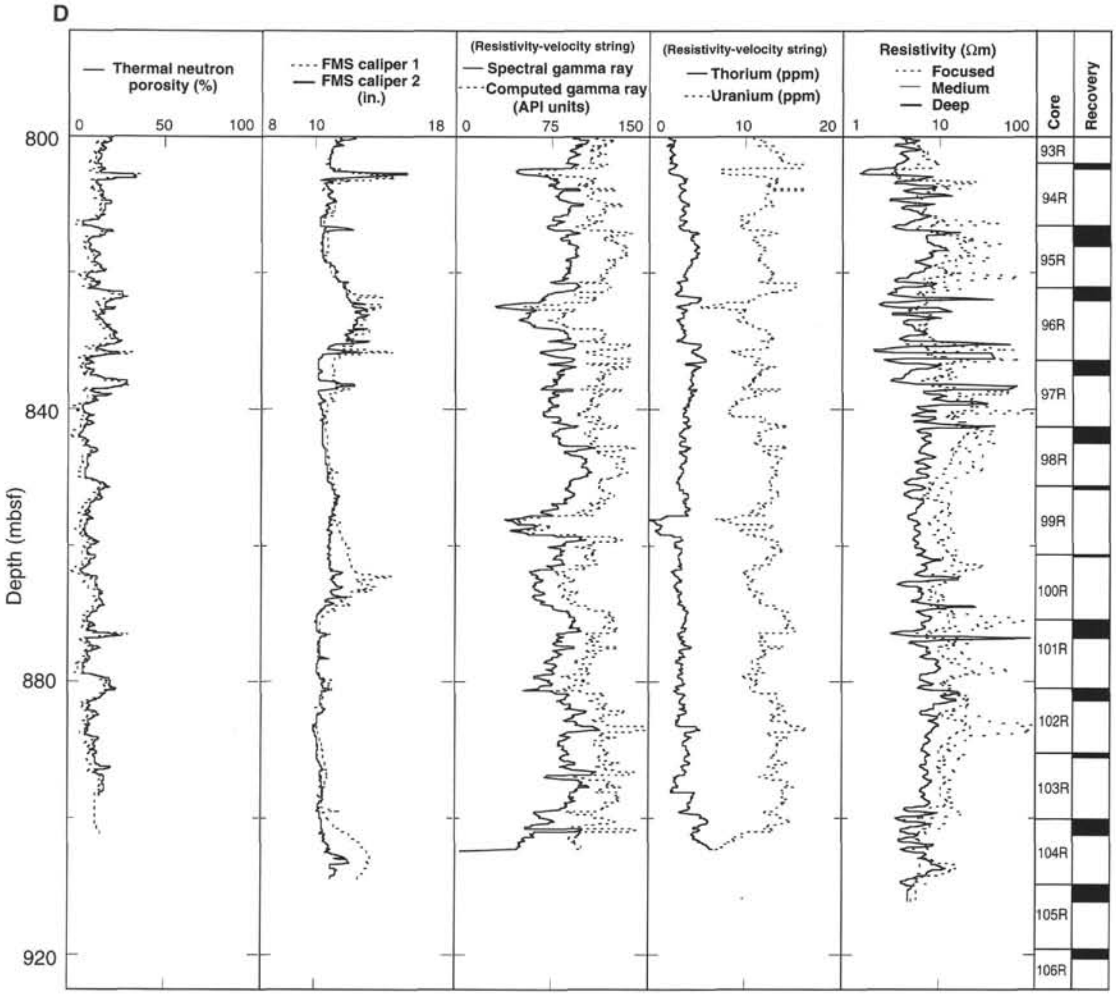

Figure 129 (continued).

Table 23. Logged depth intervals in Holes 976B and 976E.

String	Run	Depth (mbsf)	Depth (mbrf)	Tools
Hole 976B				
Quad combo	Up	343.5–56.0	1462.5–1175.0	NGT/SDT/CNT-G/HLDT/DIT-E
	Up	628.0–519.0	1741.0–1638.0	NGT/SDT/CNT-G/HLDT/DIT-E
	Up 1	903.0–683.0	2022.0–1802.0	NGT/SDT/CNT-G/HLDT/DIT-E/TLT
	Up 2*	905.5–725.5	2024.5–1844.5	NGT/SDT/CNT-G/HLDT/DIT-E/TLT
FMS	Up 1	913.0–697.2	2032.0–1816.2	NGT/FMS/GPIT
	Up 2*	911.5–698.2	2030.5–1817.2	NGT/FMS/GPIT
GLT	Up 1	907.0–737.4	2026.0–1856.4	GSTA/ACTC/CNTG/NGTC/TCCB/TLT
	Up 2*	806.0–690.0	1925.0–1809.0	GSTA/ACTC/CNTG/NGTC/TCCB/TLT
BHTV	Up 1	906.0–686.0	2025.0–1805.0	NGT/GPIT/MCDG/BTTB
	Up 2*	905.5–757.0	2024.5–1876.0	NGT/GPIT/MCDG/BTTB
Hole 976E				
Quad combo	Up 1	704.0–555.0	1823.0–1674.0	NGT/SDT/CNT-G/HLDT/DIT-E/TLT
	Up 2*	645.0–555.0	1764.0–1674.0	NGT/SDT/CNT-G/HLDT/DIT-E/TLT

Notes: * = repeat section; mbsf = meters below seafloor, mbrf = meters below rig floor.

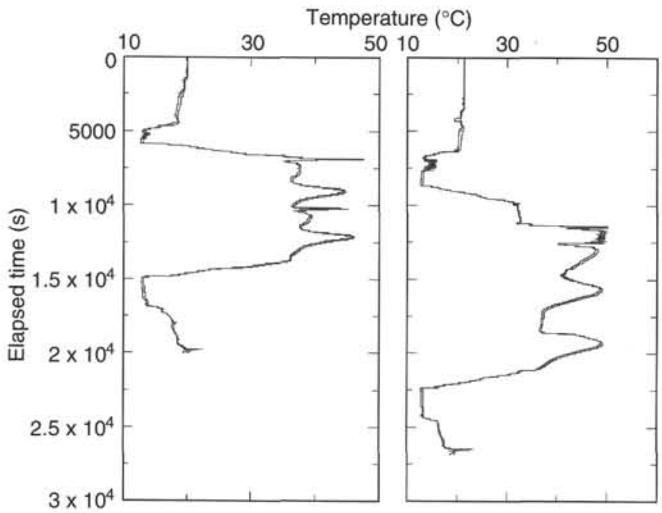

Figure 130. Hole temperature recorded by the TLT in Hole 976B, during quad combo run (left) and during GLT run (right), a few hours later.

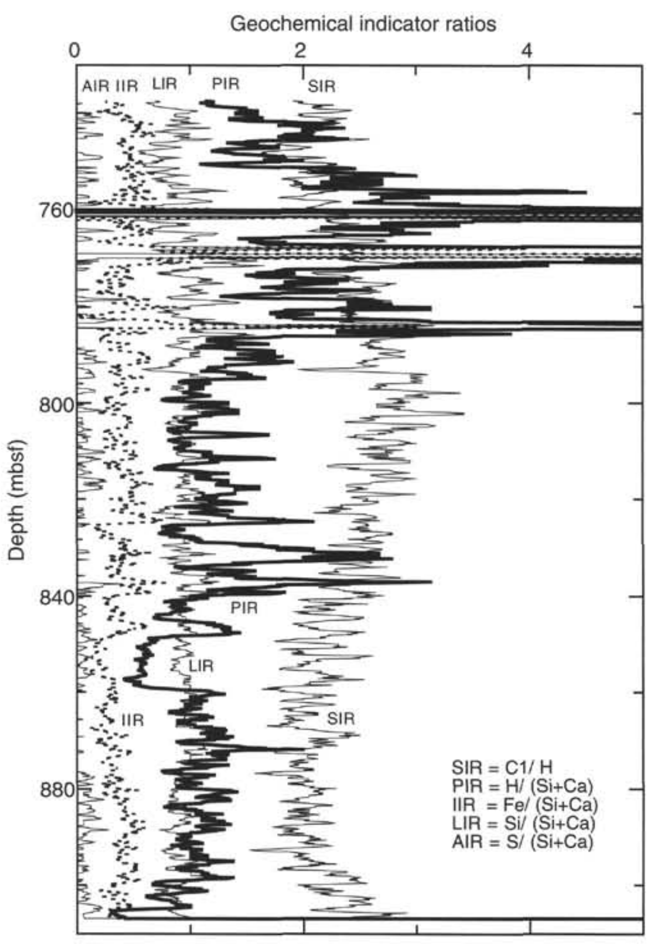

Figure 131. Geochemical indicator ratios from geochemical logging tool in the basement in Hole 976B. Note the clear signature of the brecciated and faulted log unit II, 752–788 mbsf.

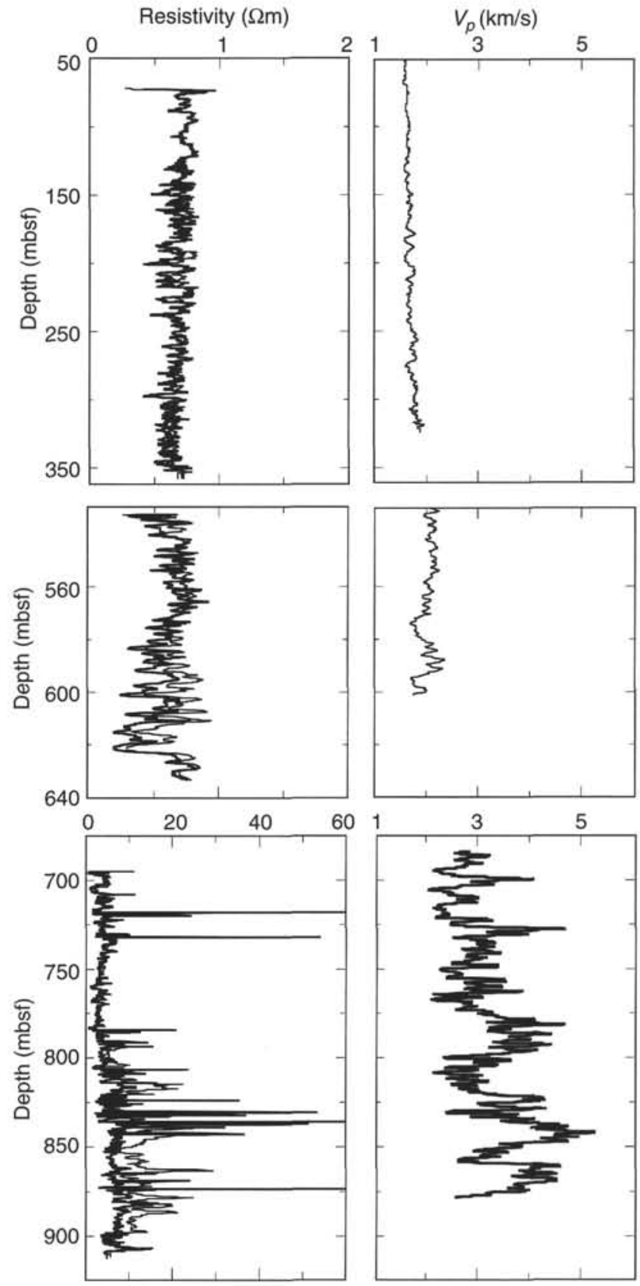

Figure 132. Resistivity and acoustic velocity in Hole 976B, in the three intervals logged. The velocity data in the basement log interval have been smoothed using a 10-point moving filter.

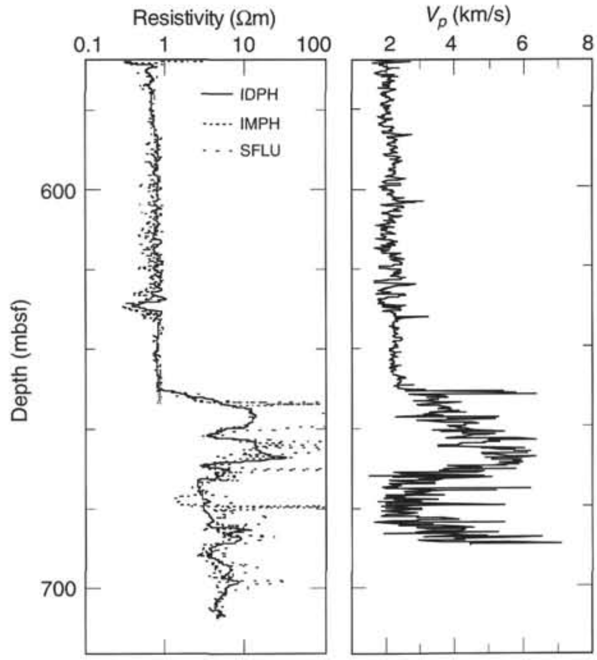

Figure 133. Resistivity and acoustic velocity in Hole 976E. The velocity data have *not* been smoothed. The top of the basement is at 653.0 mbsf. Note the contrast in character in basement compared with Hole 976B.

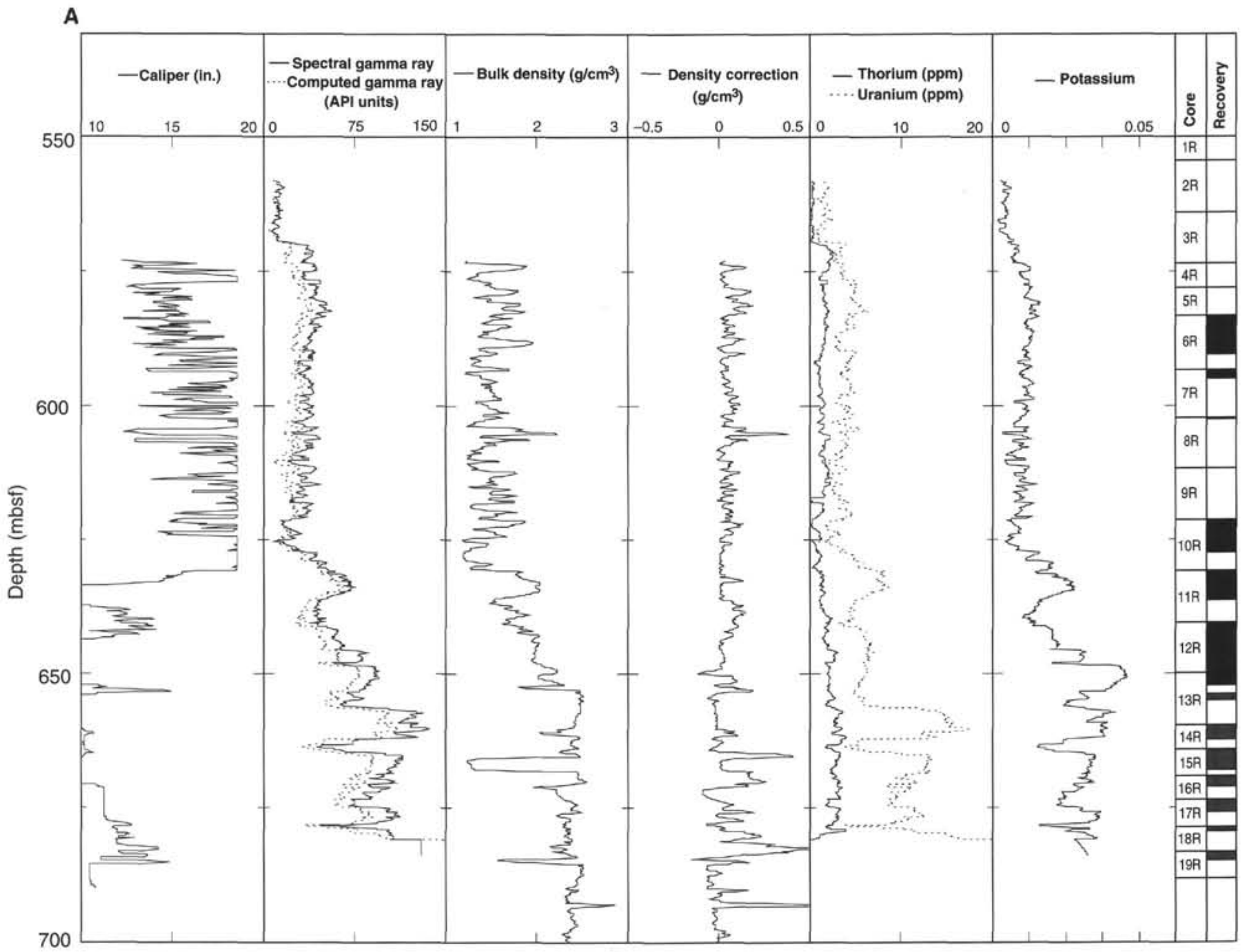

Figure 134. **A, B.** Quad combo tool selected results for the basement in Hole 976E.

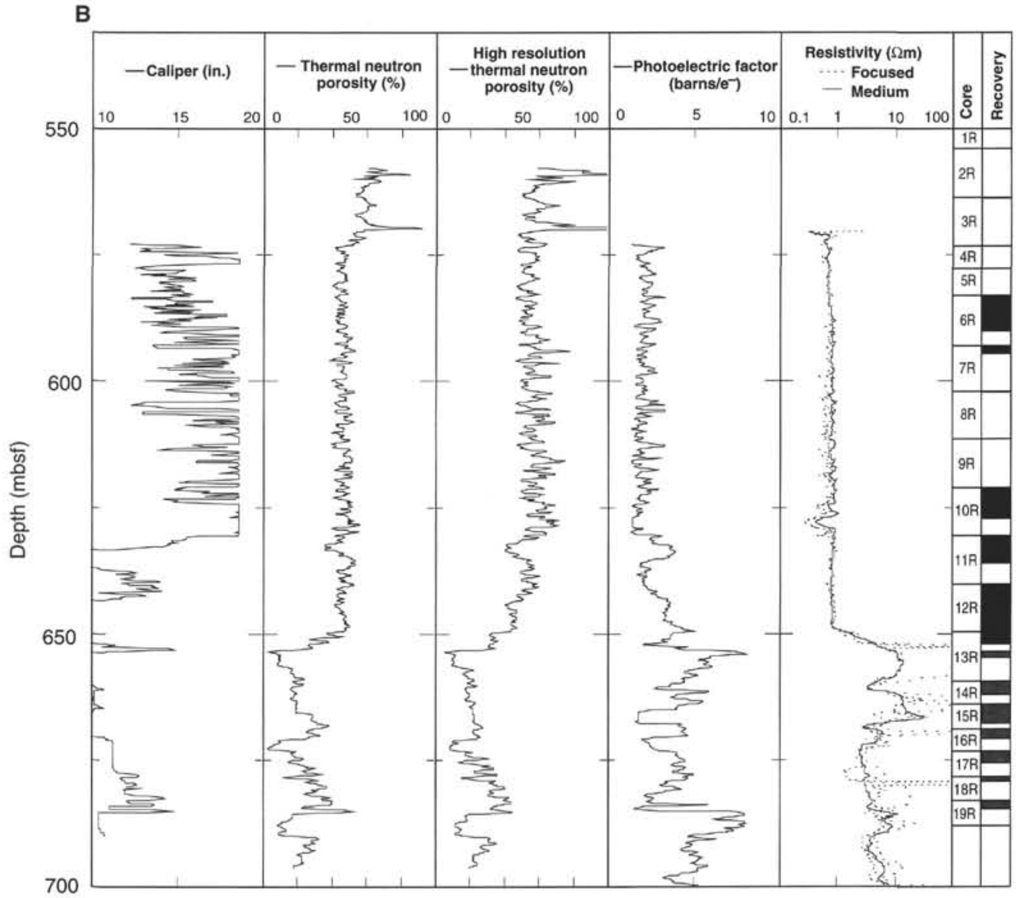

Figure 134 (continued).

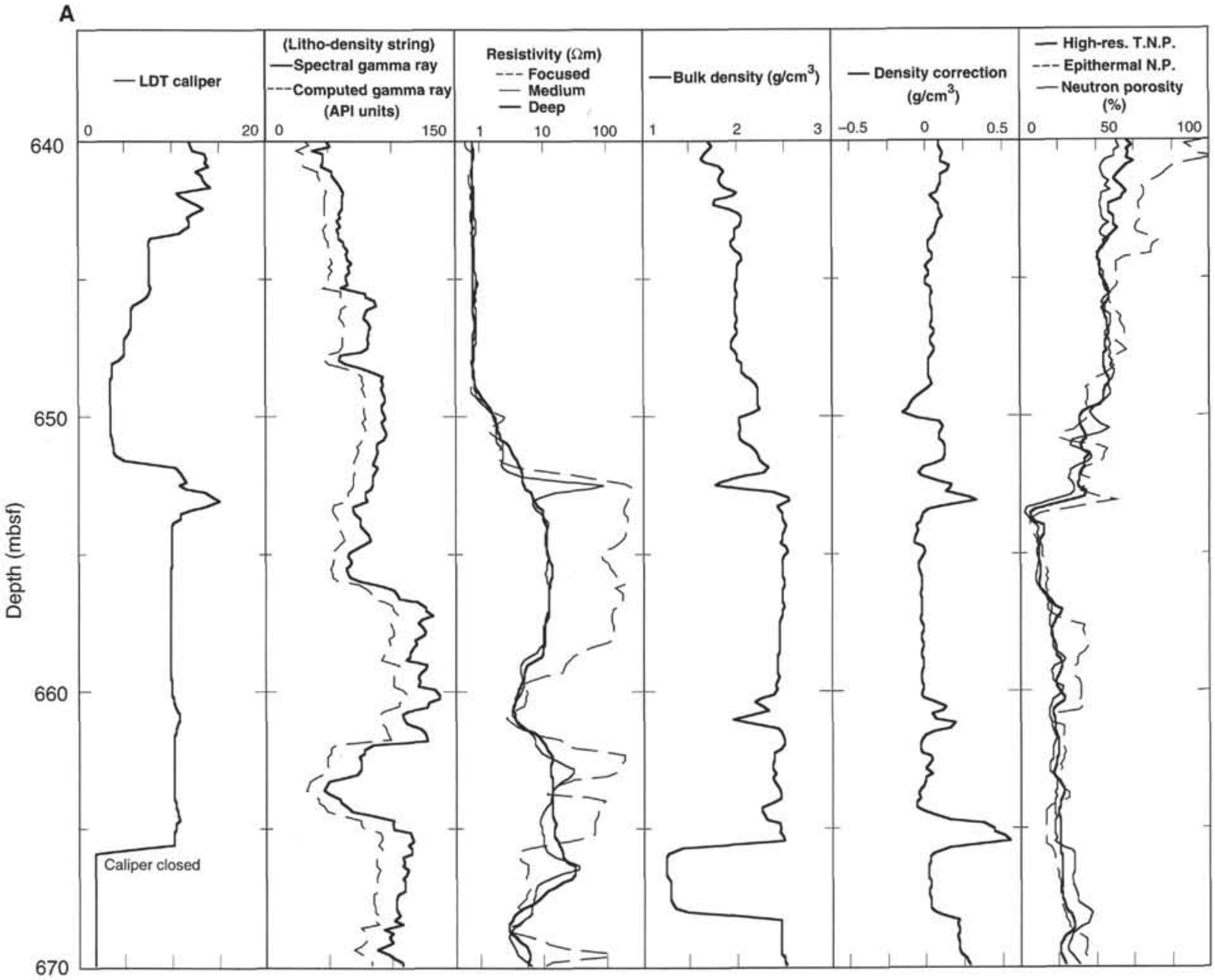

Figure 135. **A, B.** Quad combo logs showing the transition between basement and sediments in Hole 976E. The transition is smooth on deep-reaching electrical resistivity measurement, but is more clearly identified at 652.0–653.0 mbsf on other logs.

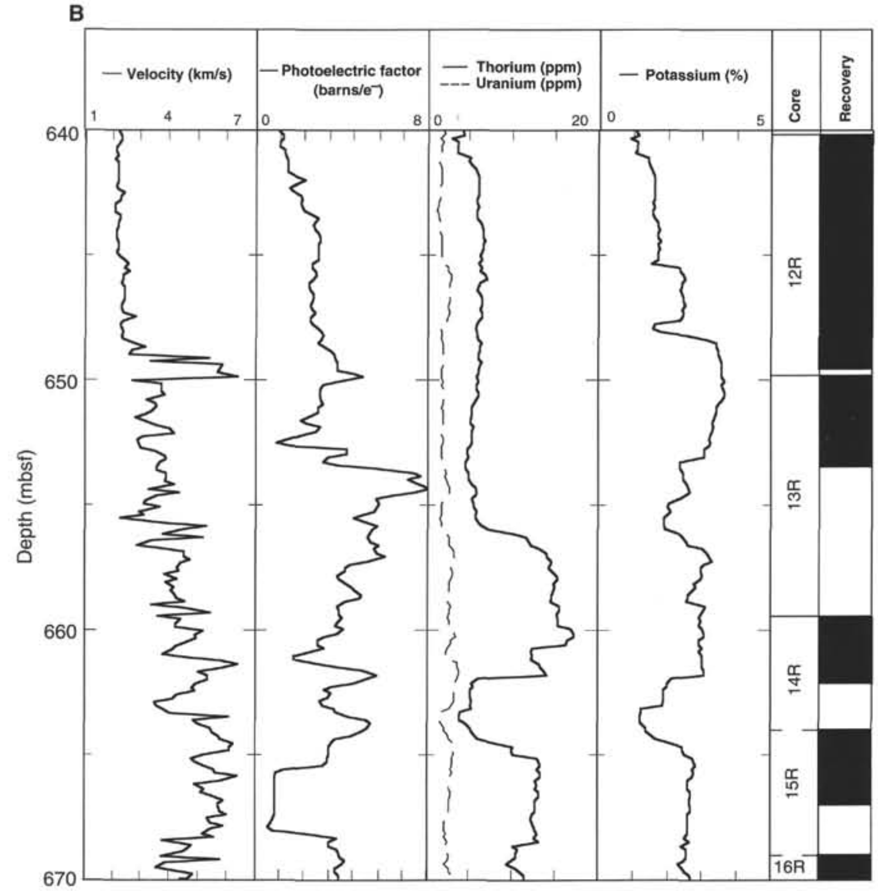

Figure 135 (continued).

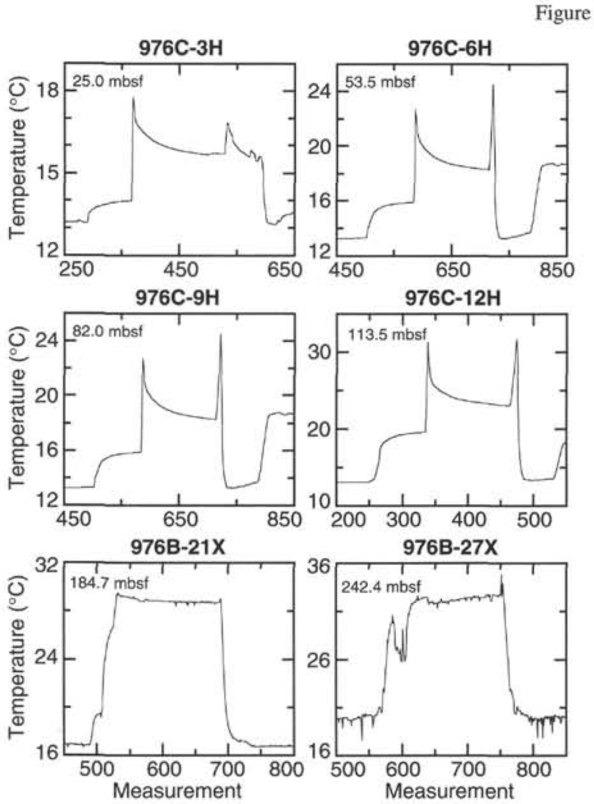

Figure 136. Temperature vs. time for the individual ADARA and WSTP temperature tool runs at Holes 976B and 976C.

Table 24. Depths and calculated equilibrium temperatures for the ADARA and WSTP temperature tool runs at Holes 976B and 976C.

Depth (mbsf)	Temperature (°C)
25.0	14.935
53.5	17.160
82.0	19.587
113.5	21.666
184.7	28.603
242.4	32.896

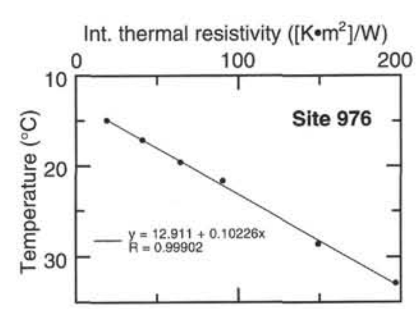

Figure 137. Temperature vs. integrated thermal resistivity for Site 976. The best-fitting linear regression to the data is shown by the straight line and shows a heat flow of 102 mW/m^2.

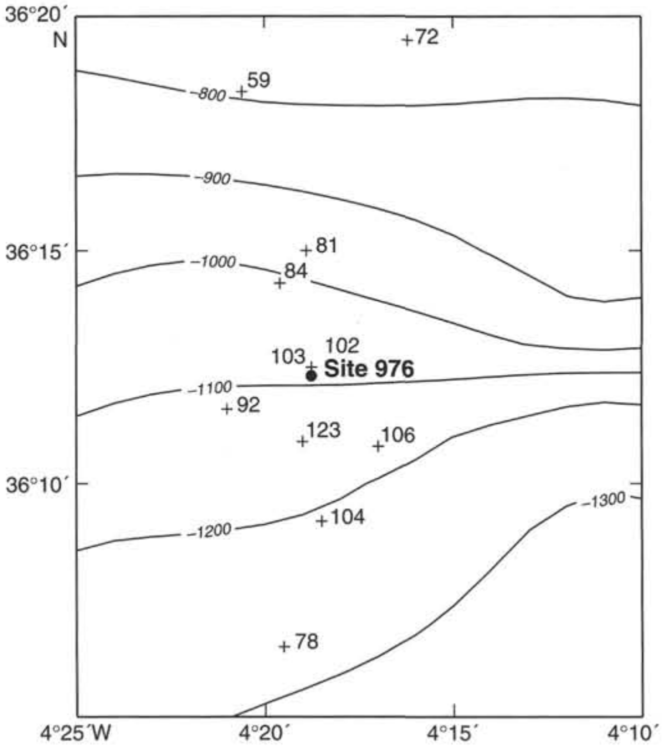

Figure 138. Heat-flow measurements with values in mW/m² in the vicinity of Site 976 (shown by the filled circle). Data shown by crosses are from Polyak et al. (in press). Bathymetric contours at 100-m intervals.

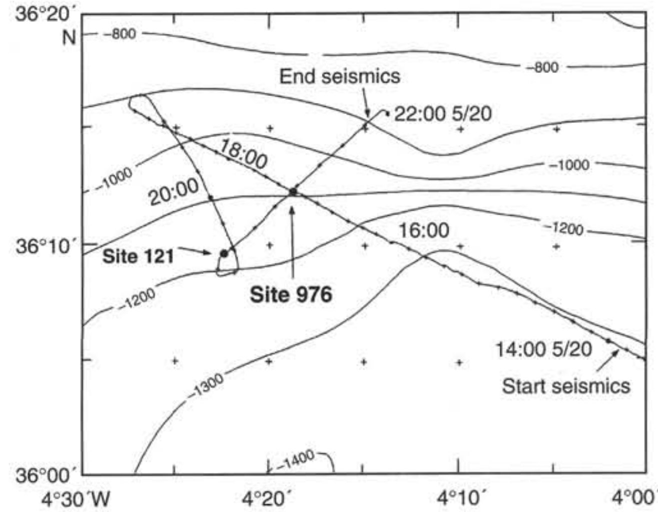

Figure 139. Ship track showing location *JOIDES Resolution* single-channel seismic data collected over Site 976. Portions of these seismic profiles are shown in Figures 140–143. The complete profiles are shown in the back-pocket foldout (Fig. 1 of "Underway Geophysics" chapter, this volume).

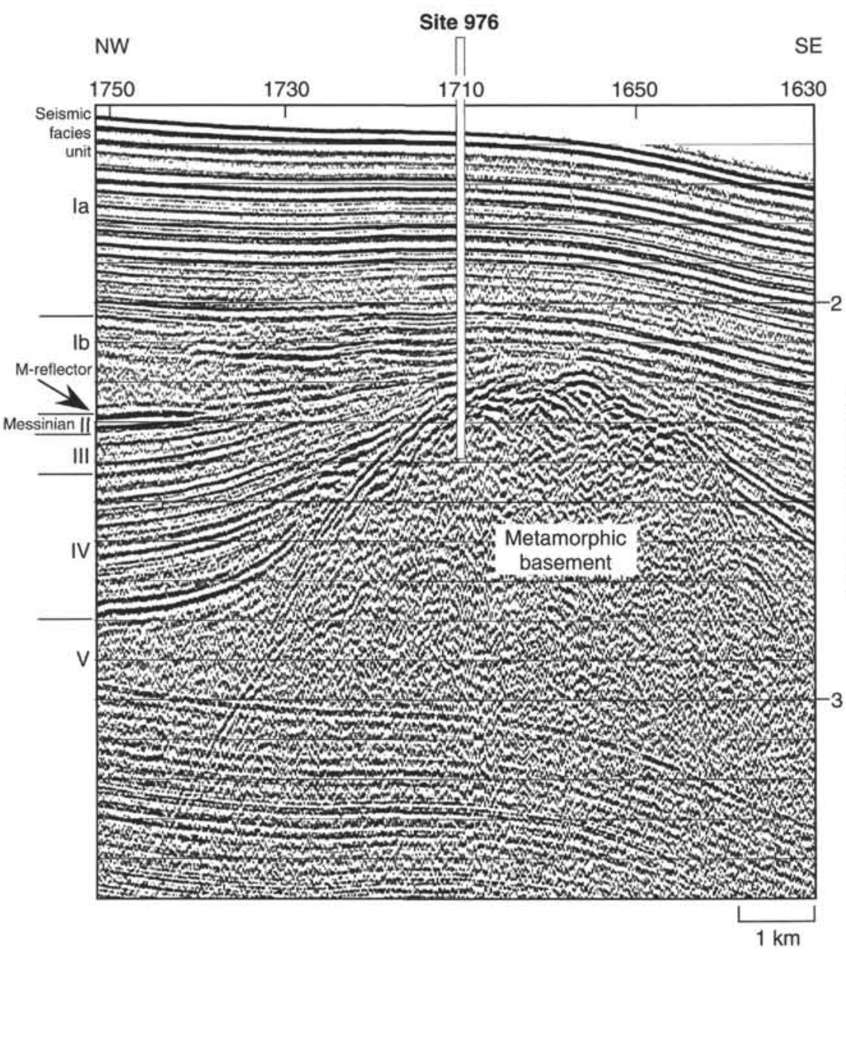

Figure 140. Portion of northwest-southeast single-channel seismic profile across Site 976. The location of this profile is shown in Figure 139. The complete profile is shown in the back-pocket foldout.

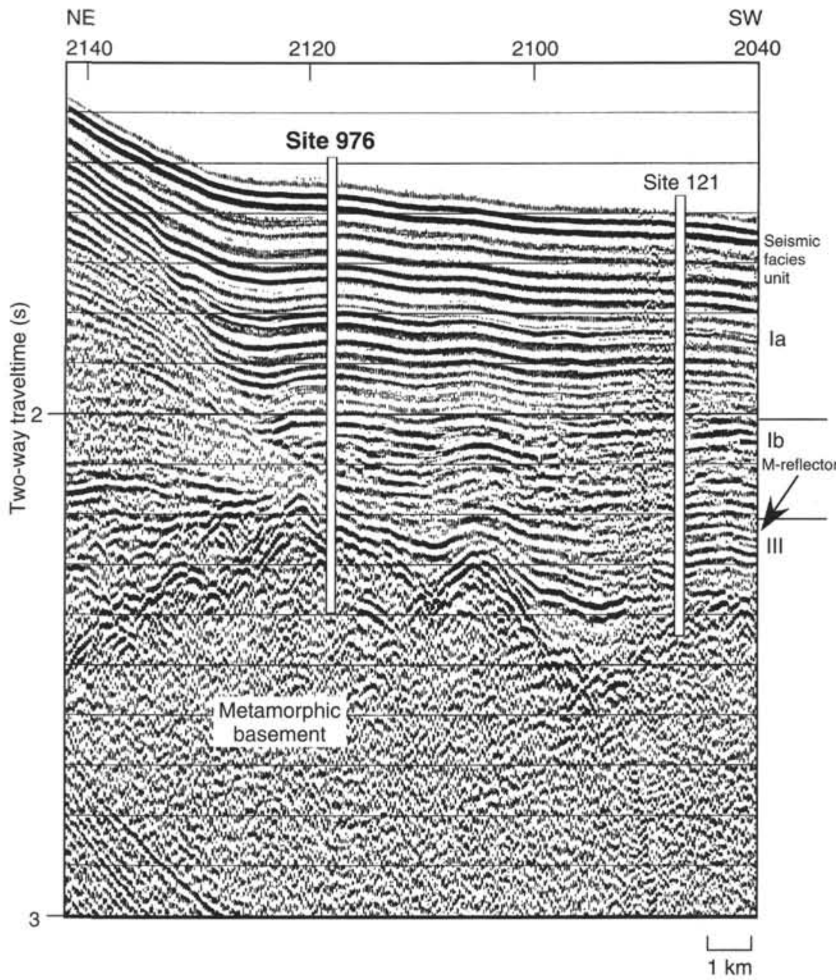

Figure 141. Portion of northeast-southwest single-channel (80-in³ water gun) seismic profile across Site 976. The location of this profile is shown in Figure 139. The entire profile is shown in the back-pocket foldout.

Table 25. Correlation of seismic and lithostratigraphic units at Site 976*.

Seismic units	Depth below seafloor (two-way traveltime [s])	Depth (mbsf)	Lithostratigraphic units
Subunit IA	0–0.43	0–375	Unit I (Pleistocene)
Subunit IB	0.43–0.58	375–520	Unit II (Pliocene)
Units III and IV	0.58–0.67	520–670	Unit III (Tortonian–Serravalian)

Note: *see "Lithostratigraphy" section, this chapter.

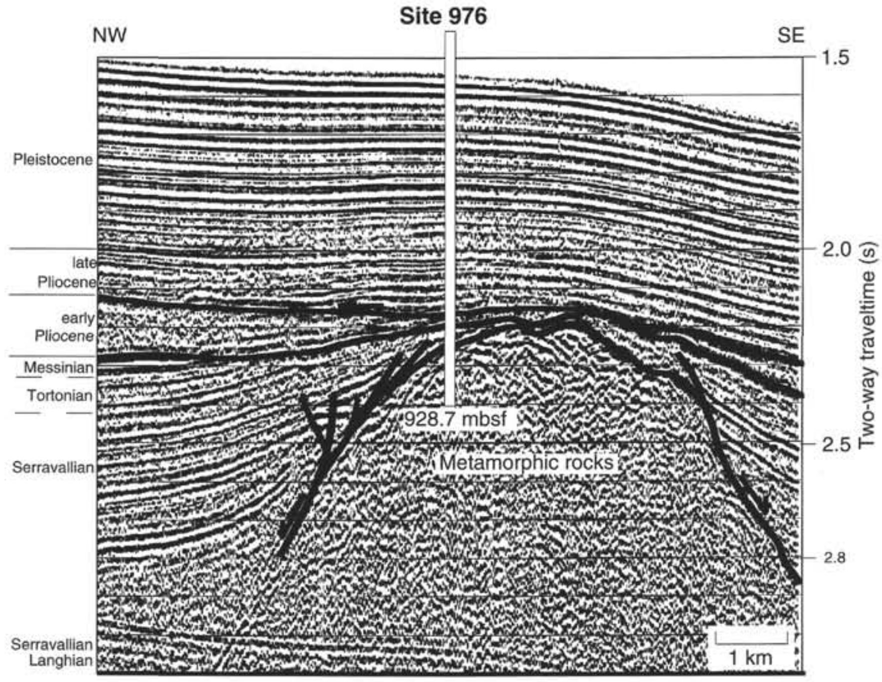

Figure 142. Interpreted northwest-southeast seismic profile shown in Figure 140. The normal faults that bound the basement high are clearly delineated. Site 976 penetrated the irregular topography of the basement horst.

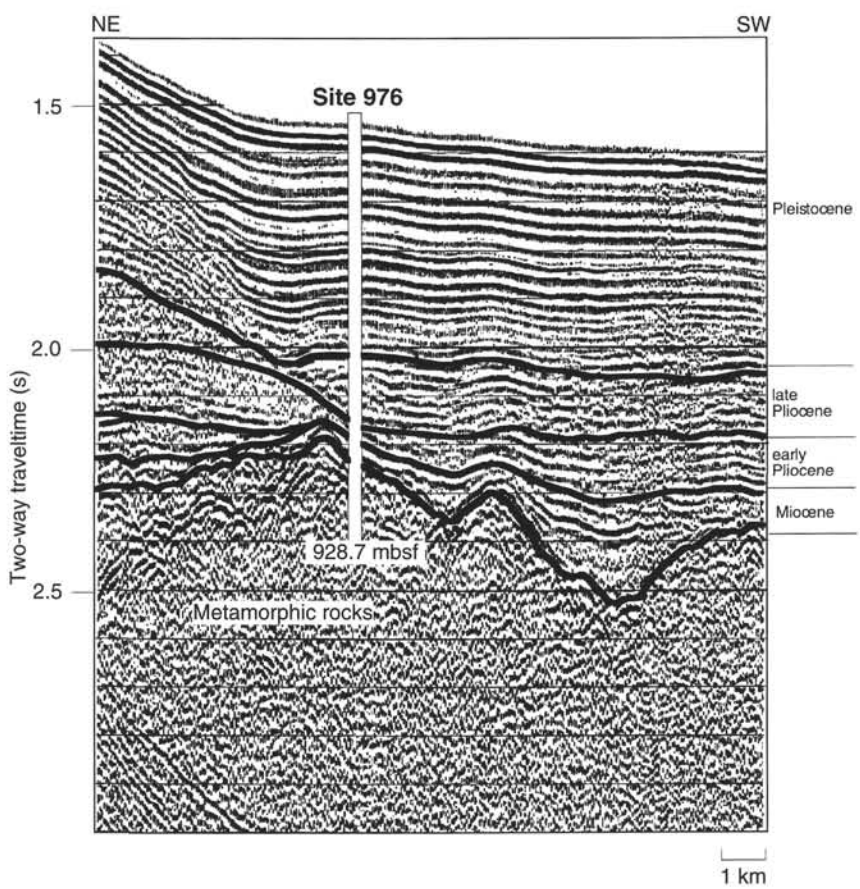

Figure 143. Interpreted northeast-southwest seismic profile shown in Figure 141. In places thicker Miocene sequences fill in the irregular morphology of the top of the metamorphic basement.

SHORE-BASED LOG PROCESSING

Hole 976B

Bottom felt: 1119.1 mbrf (used for depth shift to seafloor)
Total penetration: 928.7 mbsf
Total core recovered: 535.54 m (57.7%)

Logging Runs

Logging string 1: DIT/SDT/HLDT/CNTG/NGT (3 sections)
Logging string 2: FMS/GPIT/NGT (2 passes)
Logging string 3: BHTV/NGT
Logging string 4: ACT/GST/NGT (2 passes)
Wireline heave compensator was used to counter ship heave.

Bottom-Hole Assembly

The following bottom-hole assembly depths are as they appear on the logs after differential depth shift (see "Depth shift" section, this hole) and depth shift to the seafloor. As such, there might be a discrepancy with the original depths given by the drillers onboard. Possible reasons for depth discrepancies are ship heave, use of wireline heave compensator, and drill string and/or wireline stretch.

DIT/SDT/HLDT/CNTG/NGT: Bottom-hole assembly at ~71 mbsf (upper section).

DIT/SDT/HLDT/CNTG/NGT: Bottom-hole assembly at ~533 mbsf (middle section).

DIT/SDT/HLDT/CNTG/NGT: Bottom-hole assembly at ~690 mbsf (lower section).

FMS/GPIT/NGT: Did not reach bottom-hole assembly.

ACT/GST/NGT: Did not reach bottom-hole assembly.

Processing

Depth shift: Reference run for depth shift: DIT/SDT/HLDT/CNTG/NGT lower section. All original logs from the lower part of the hole have been interactively depth shifted with reference to NGT from DIT/SDT/HLDT/CNTG/NGT lower section and to the seafloor (−1119.1 m). The middle and upper section of the DIT/SDT/HLDT/CNTG/NGT do not overlap with any other runs and therefore have not been depth shifted. The first pass of the FMS/GPIT/NGT does not need any depth shift.

Gamma-ray processing: NGT data have been processed to correct for borehole size and type of drilling fluid.

Acoustic data processing: The array sonic tool was operated in two modes: linear array mode, with the 8-receivers providing full waveform analysis (compressional and shear) and standard depth-derived borehole compensated mode, including long-spacing (8-10-10-12 ft) and short-spacing (3-5-5-7 ft) logs. In the middle and upper section of the hole the long-spacing logs showed a slightly better quality than the short-spacing or array mode logs and have been processed in order to eliminate some of the noise and cycle skipping experienced during the recording.

Geochemical processing: (For detailed explanation of the processing please refer to the "Explanatory Notes" chapter, this volume, or to the geochem.doc file on the enclosed CD-ROM). The elemental yields recorded by the GST tool represent the relative contribution of only some of the rock-forming elements (iron, calcium, chlorine, silica, sulfur, hydrogen, gadolinium, and titanium—the last two computed during geochemical processing) to the total spectrum. Because other rock-forming elements are present in the formation (such as aluminum, potassium), caution is recommended in using the yields to infer lithologic changes. Instead, ratios (see acronyms.doc on CD-ROM) are more appropriate to determine changes in the macroscopic properties of the formation. A list of oxide factors used in geochemical processing includes the following:

$SiO_2 = 2.139$
$CaO = 1.399$
$FeO^* = 1.358$
$TiO_2 = 1.668$
$K_2O = 1.205$
$Al_2O_3 = 1.889$

FeO^* = computed using an oxide factor which assumes a 50:50 combination of Fe_2O_3 and FeO factors. The geochemical data from main and repeat sections have been spliced at about 737.b mbsf. The results of the processing are presented along with the weight percentages of the XRF measurements performed on board.

Quality Control

Data recorded through bottom-hole assembly, such as the gamma ray and neutron porosity data above 71, 533, and 690 mbsf, should be used qualitatively only because of the attenuation on the incoming signal.

Hole diameter was recorded by the hydraulic caliper on the HLDT tool (CALI) and the caliper on the FMS string (C1 and C2).

FACT = quality control curve in geochemical processing. Accuracy of the estimates is inversely proportional to the magnitude of the curve.

Note: Details of standard shore-based processing procedures are found in the "Explanatory Notes" chapter, this volume. For further information about the logs, please contact:

Cristina Broglia
Phone: 914-365-8343
Fax: 914-365-3182
E-mail: chris@ldeo.columbia.edu

Elizabeth Pratson
Phone: 914-365-8313
Fax: 914-365-3182
E-mail: beth@ldeo.columbia.edu

Hole 976B: Natural Gamma Ray-Resistivity-Sonic Logging Data

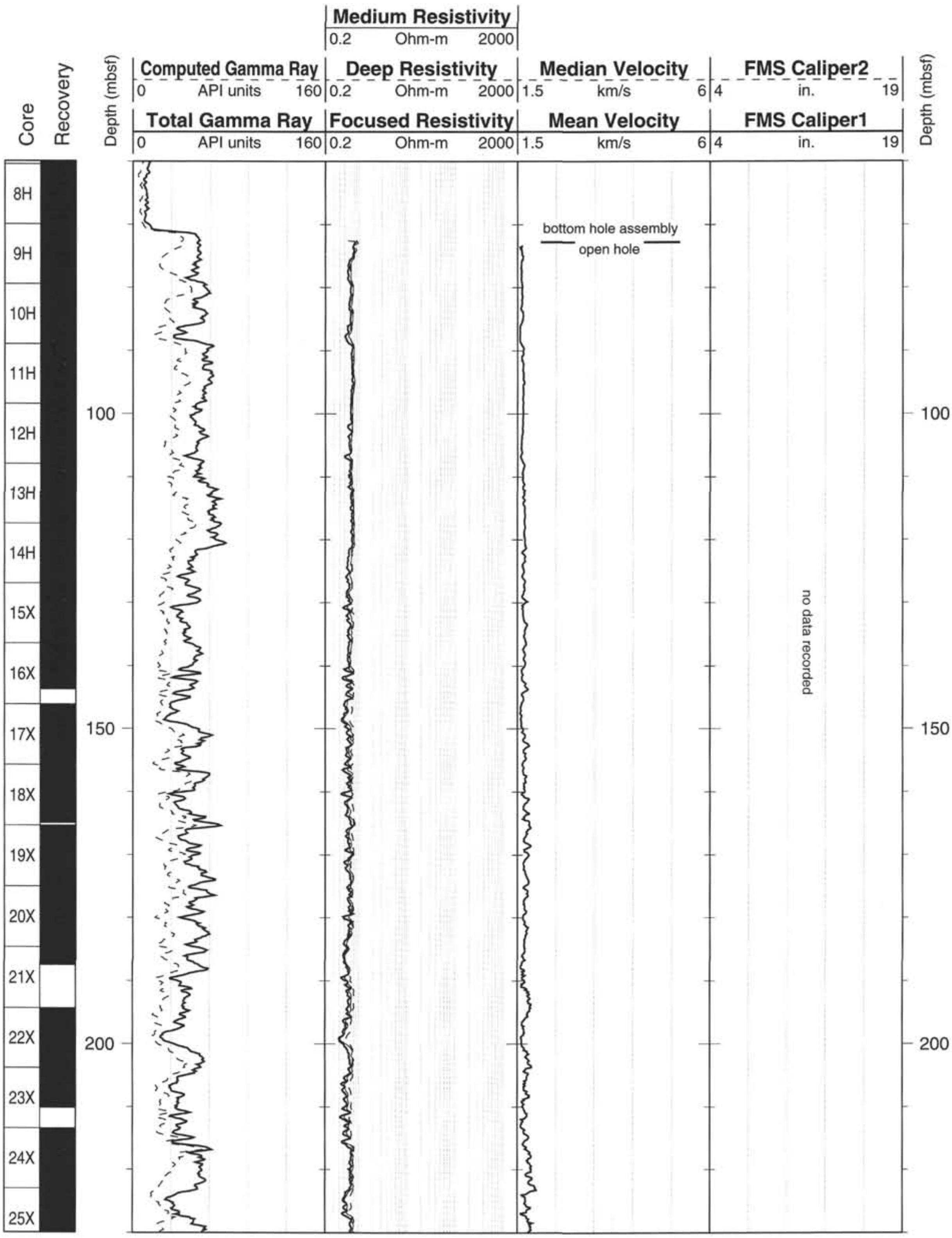

Hole 976B: Natural Gamma Ray-Resistivity-Sonic Logging Data (cont.)

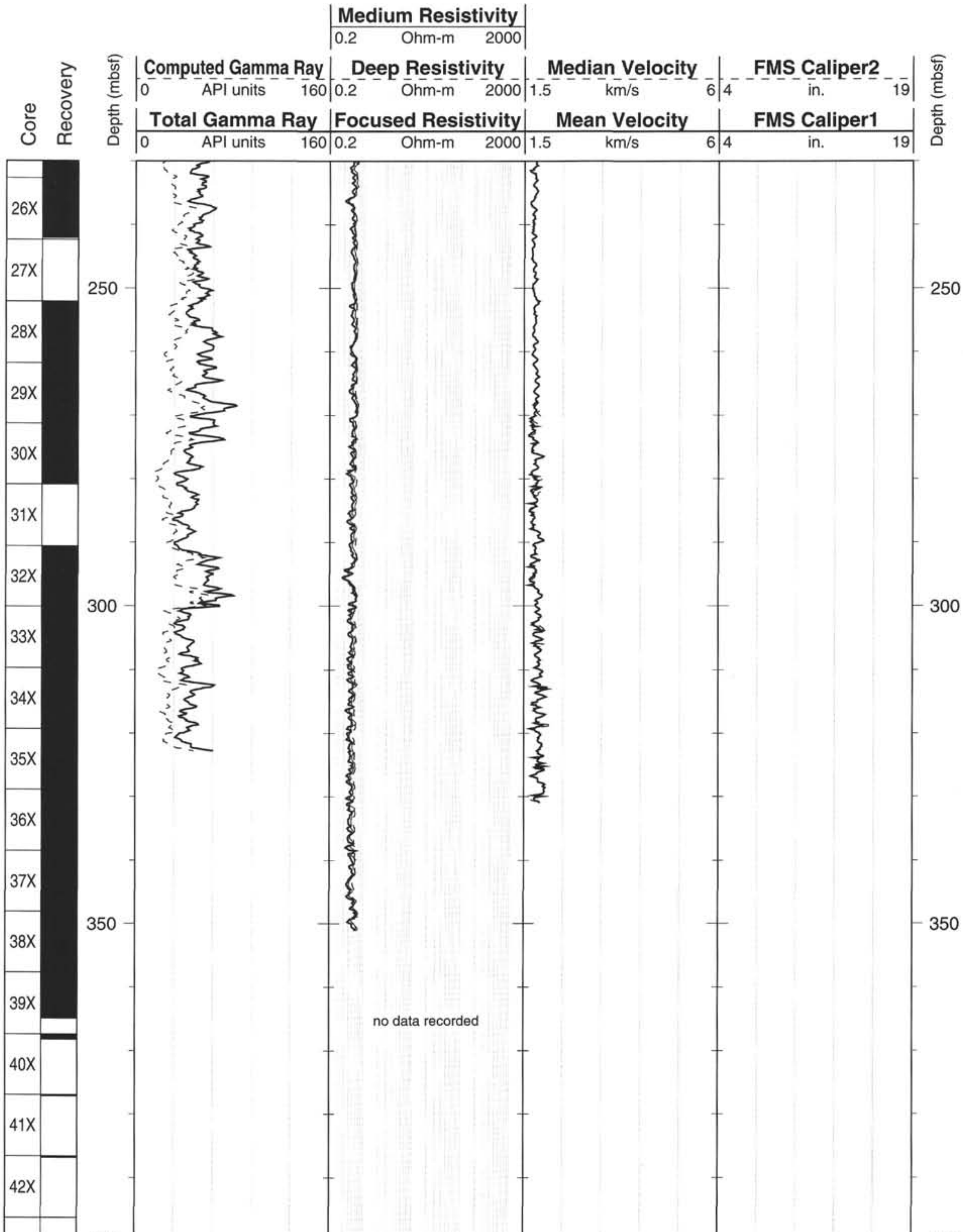

Hole 976B: Natural Gamma Ray-Resistivity-Sonic Logging Data (cont.)

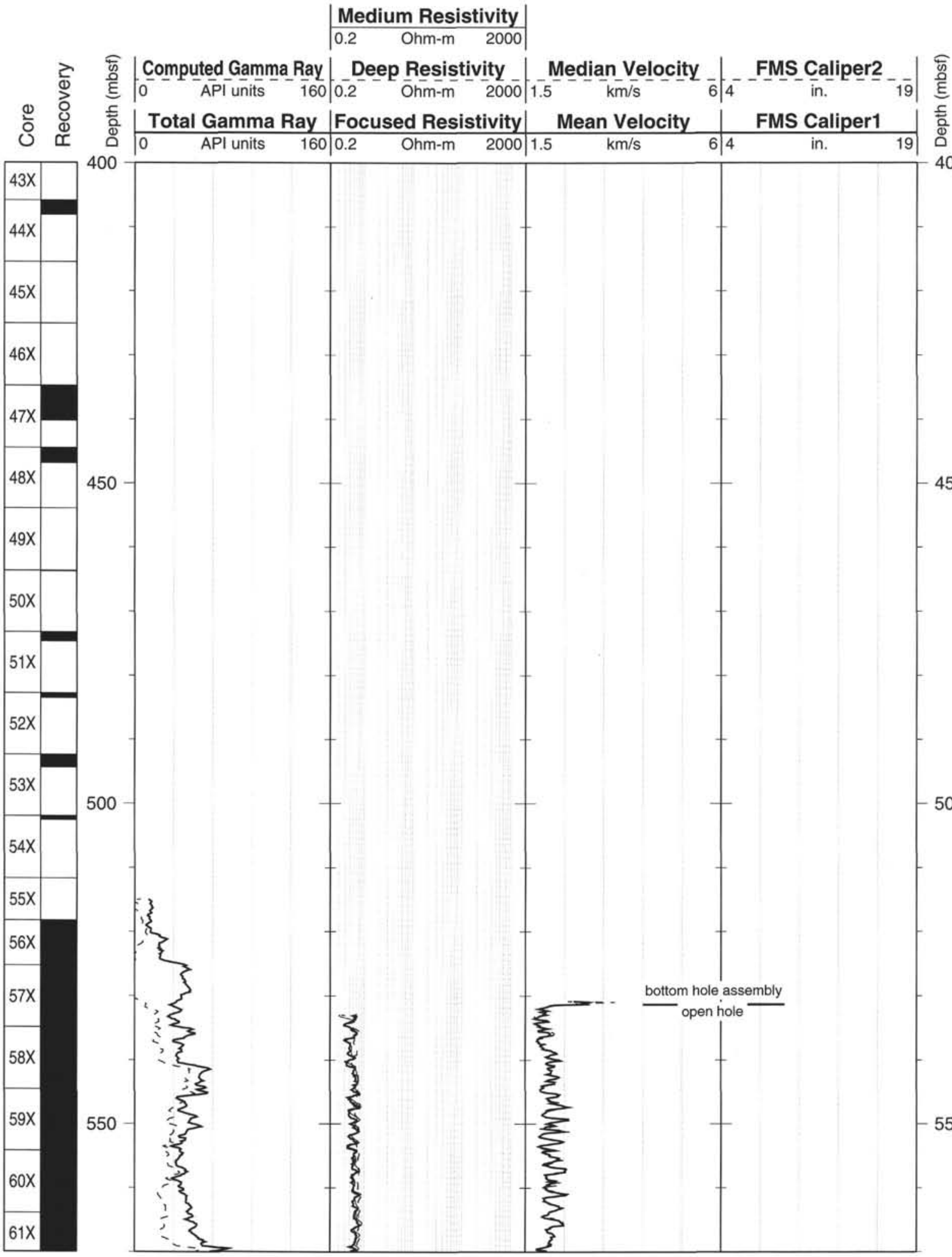

Hole 976B: Natural Gamma Ray-Resistivity-Sonic Logging Data (cont.)

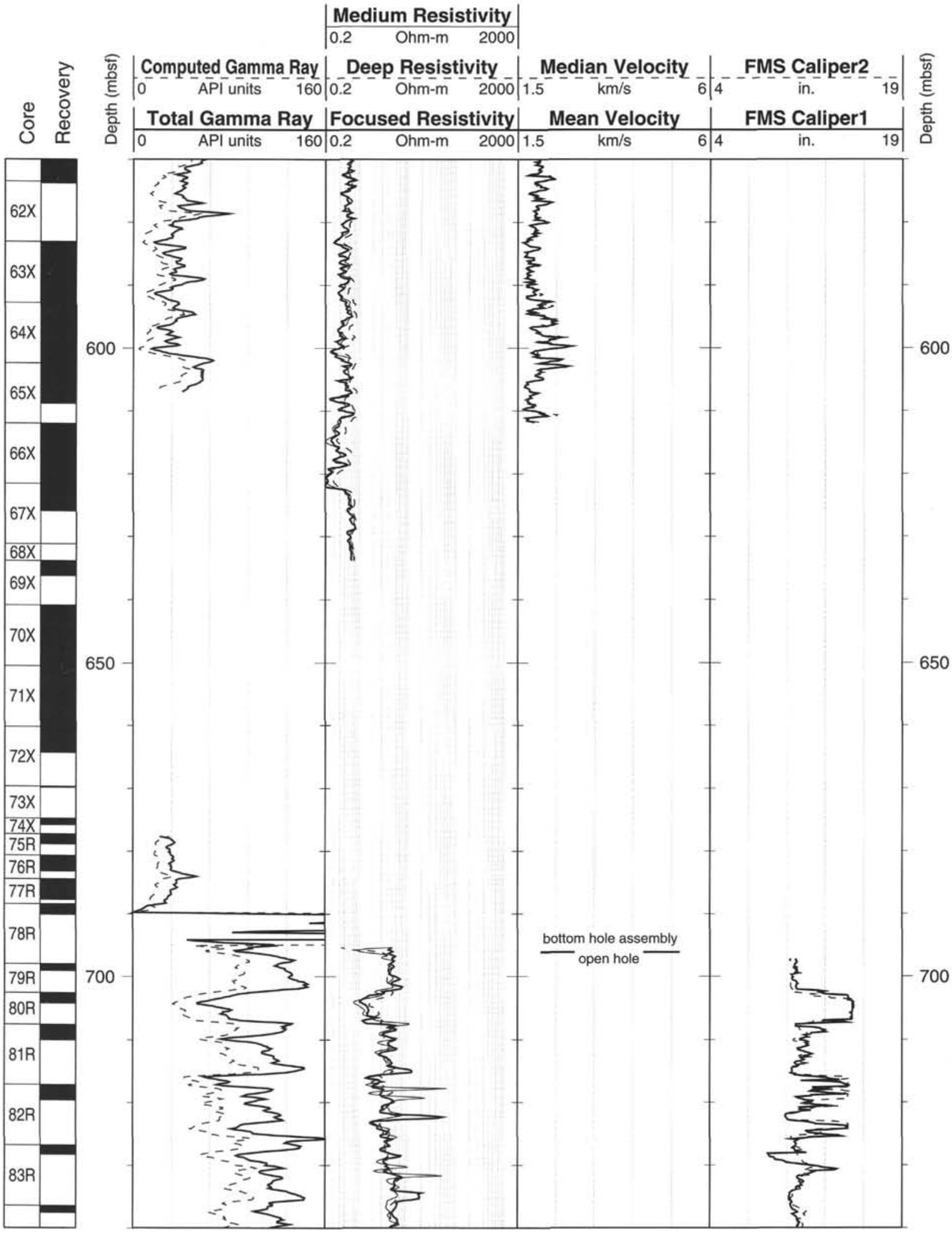

Hole 976B: Natural Gamma Ray-Resistivity-Sonic Logging Data (cont.)

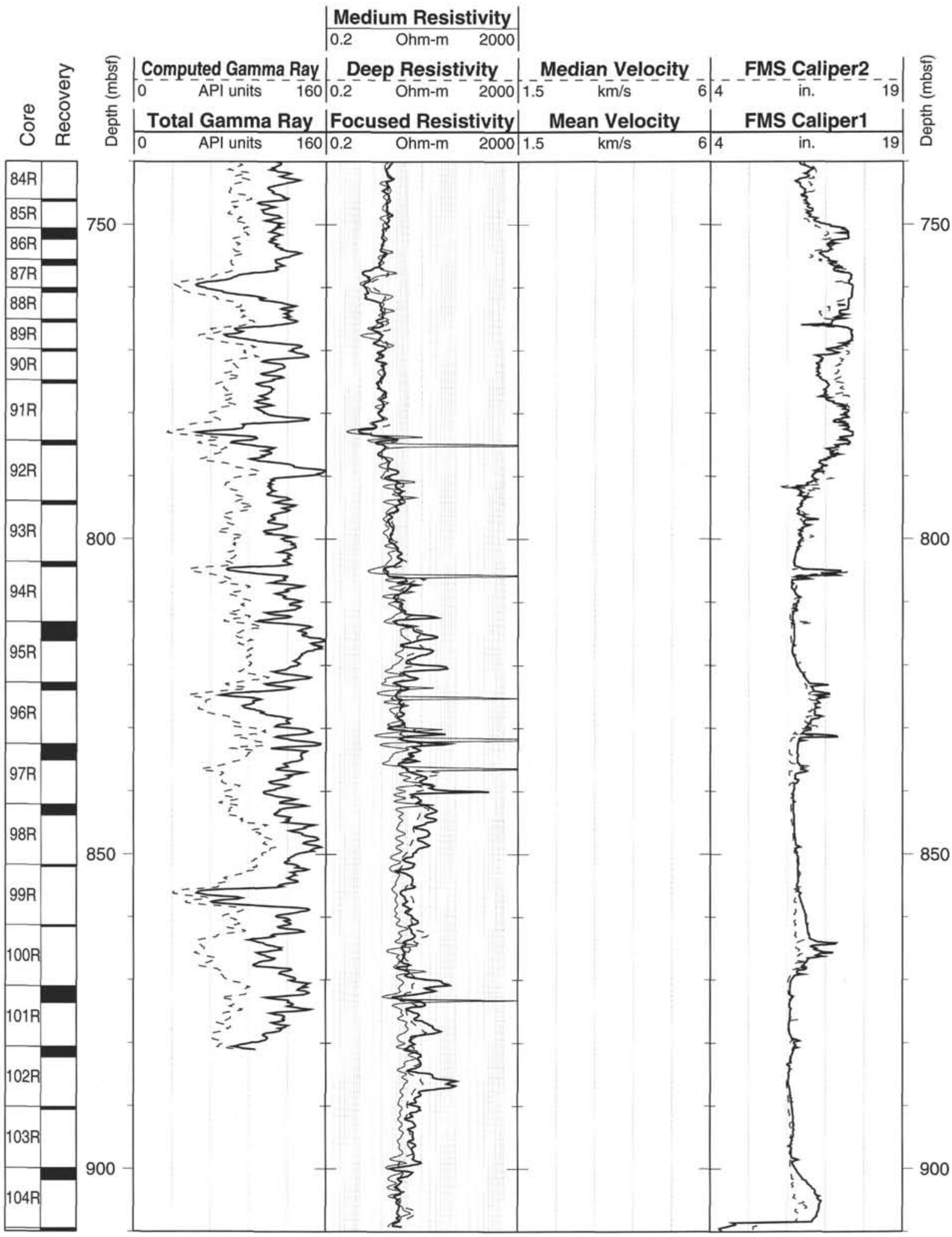

Hole 976B: Natural Gamma Ray-Density-Porosity Logging Data

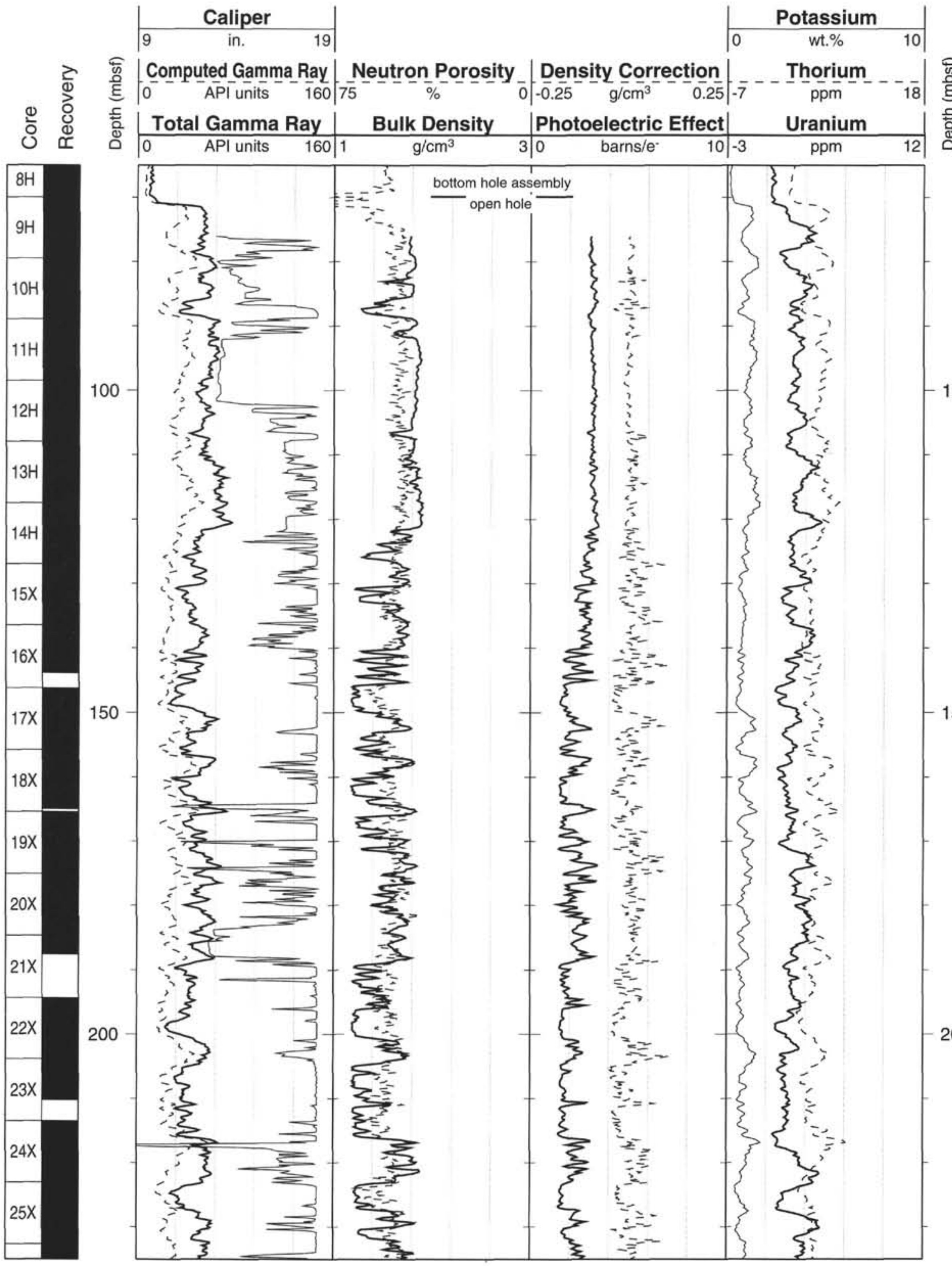

Hole 976B: Natural Gamma Ray-Density-Porosity Logging Data (cont.)

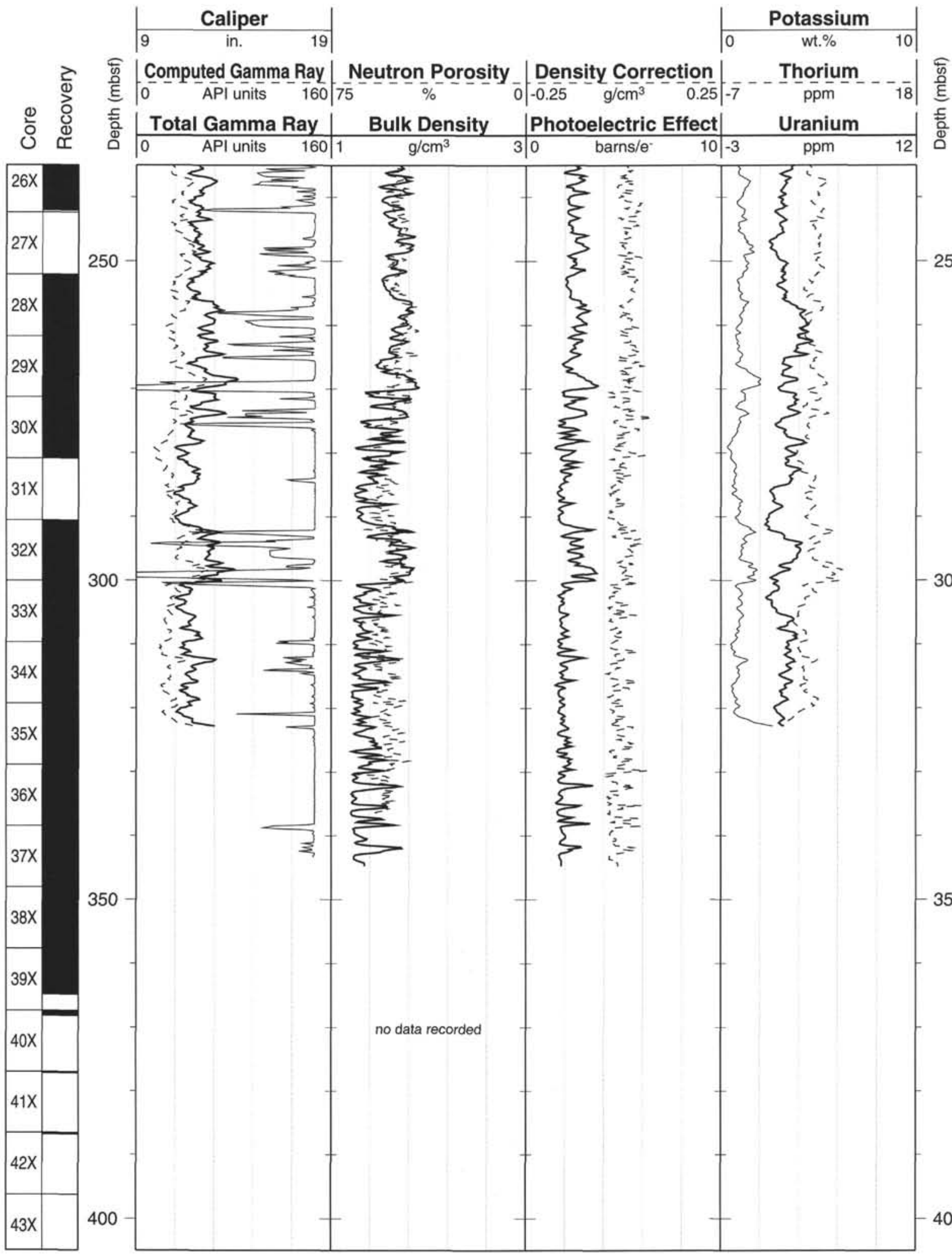

Hole 976B: Natural Gamma Ray-Density-Porosity Logging Data (cont.)

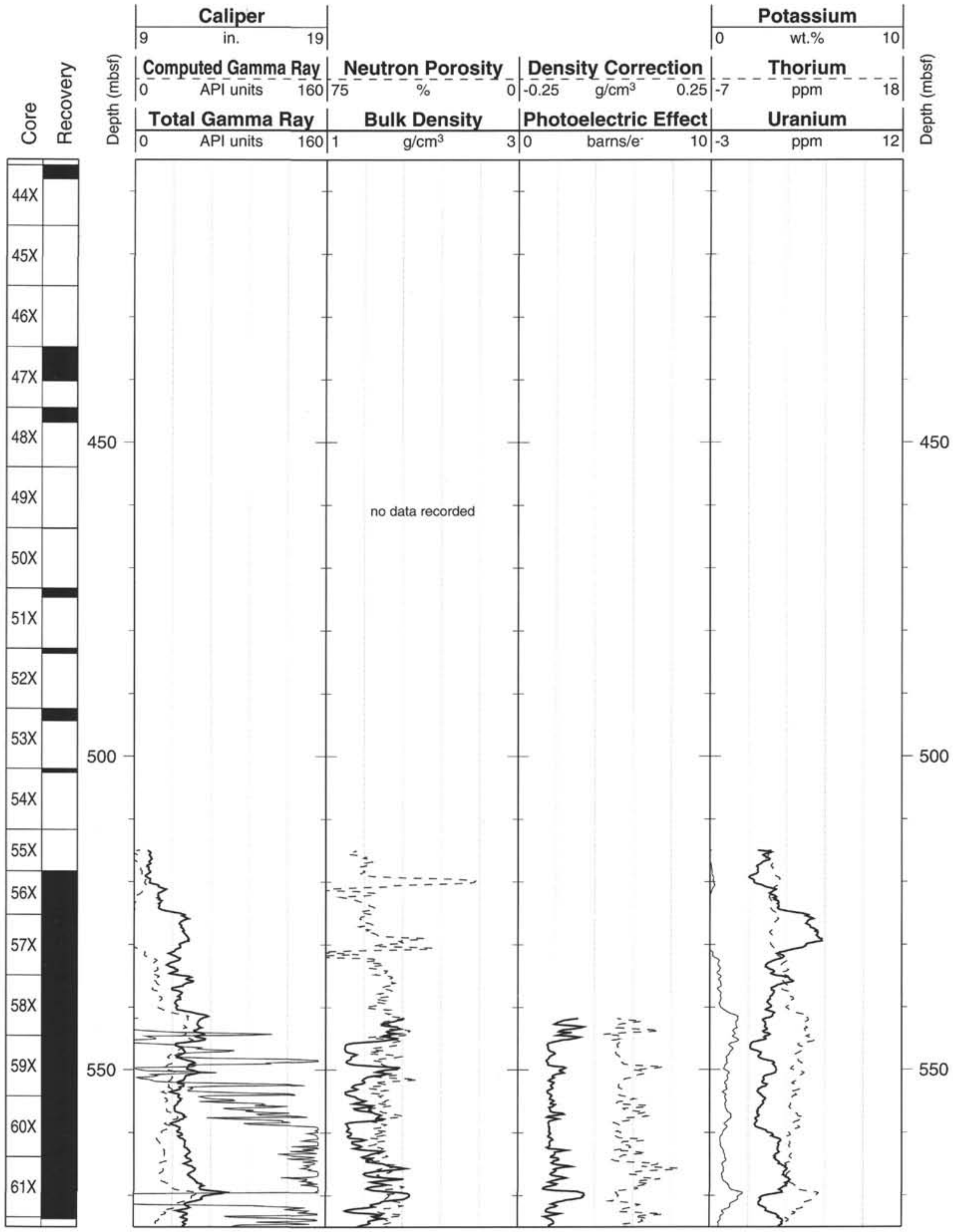

Hole 976B: Natural Gamma Ray-Density-Porosity Logging Data (cont.)

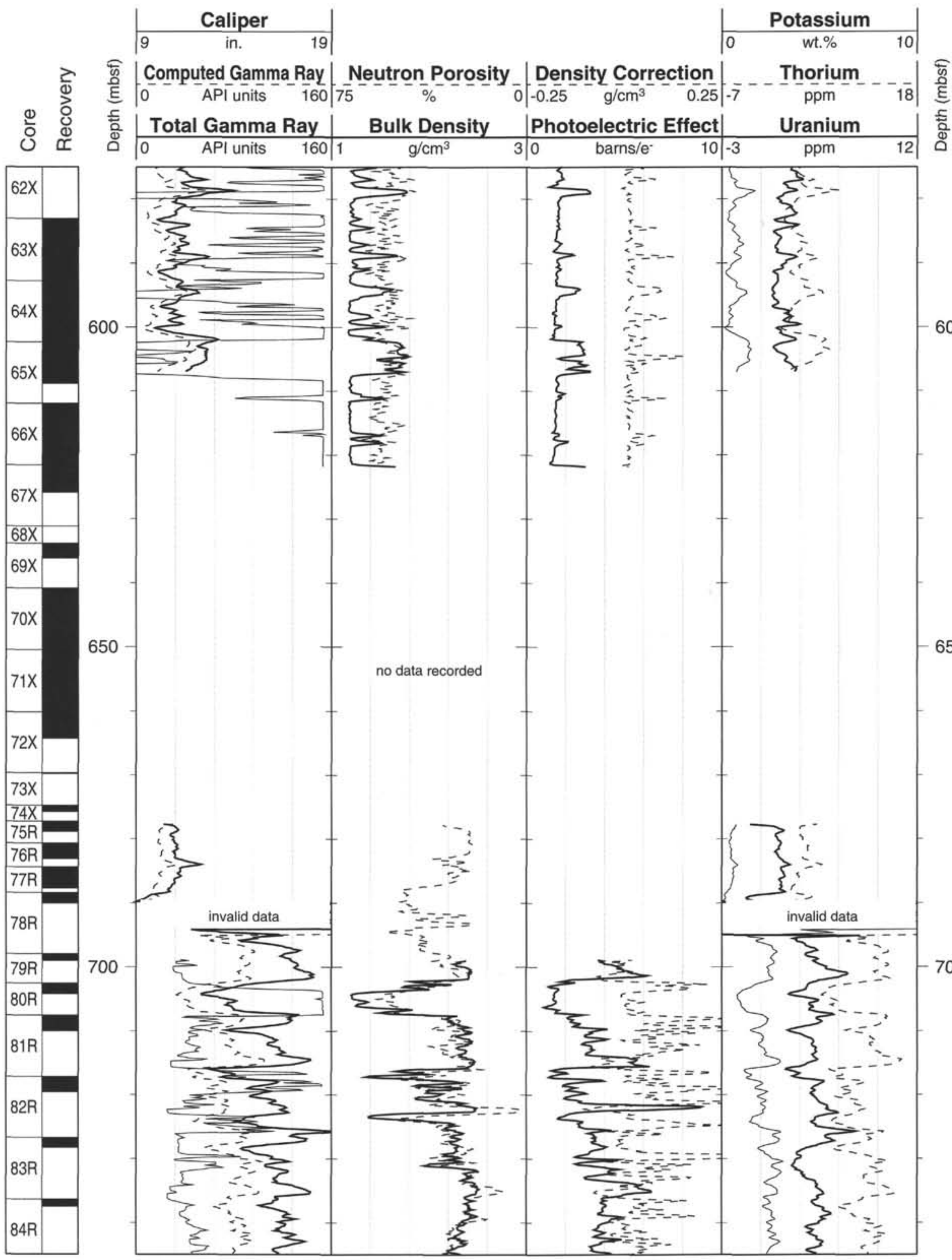

Hole 976B: Natural Gamma Ray-Density-Porosity Logging Data (cont.)

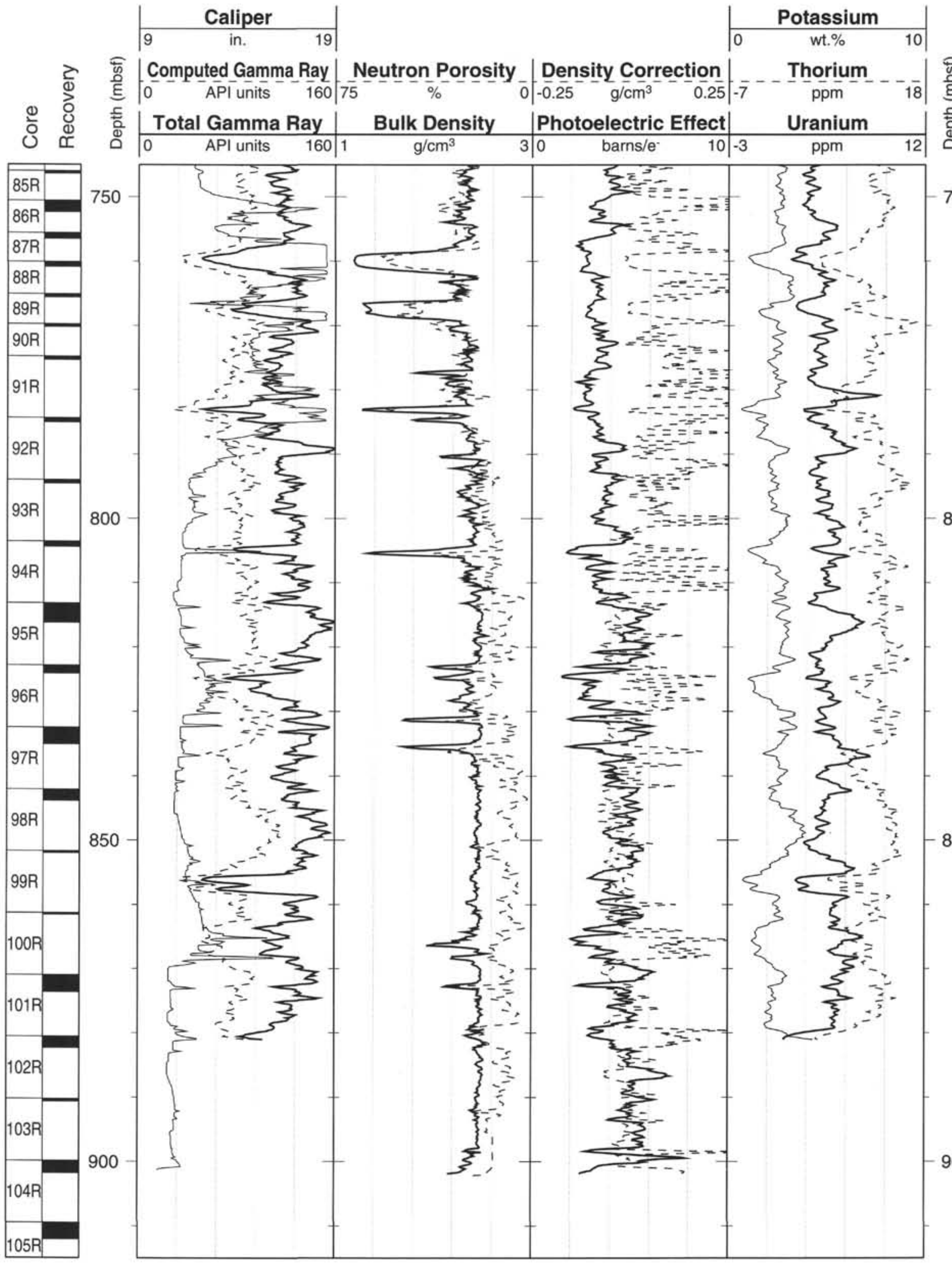

Hole 976B: Natural Gamma Ray Logging Data

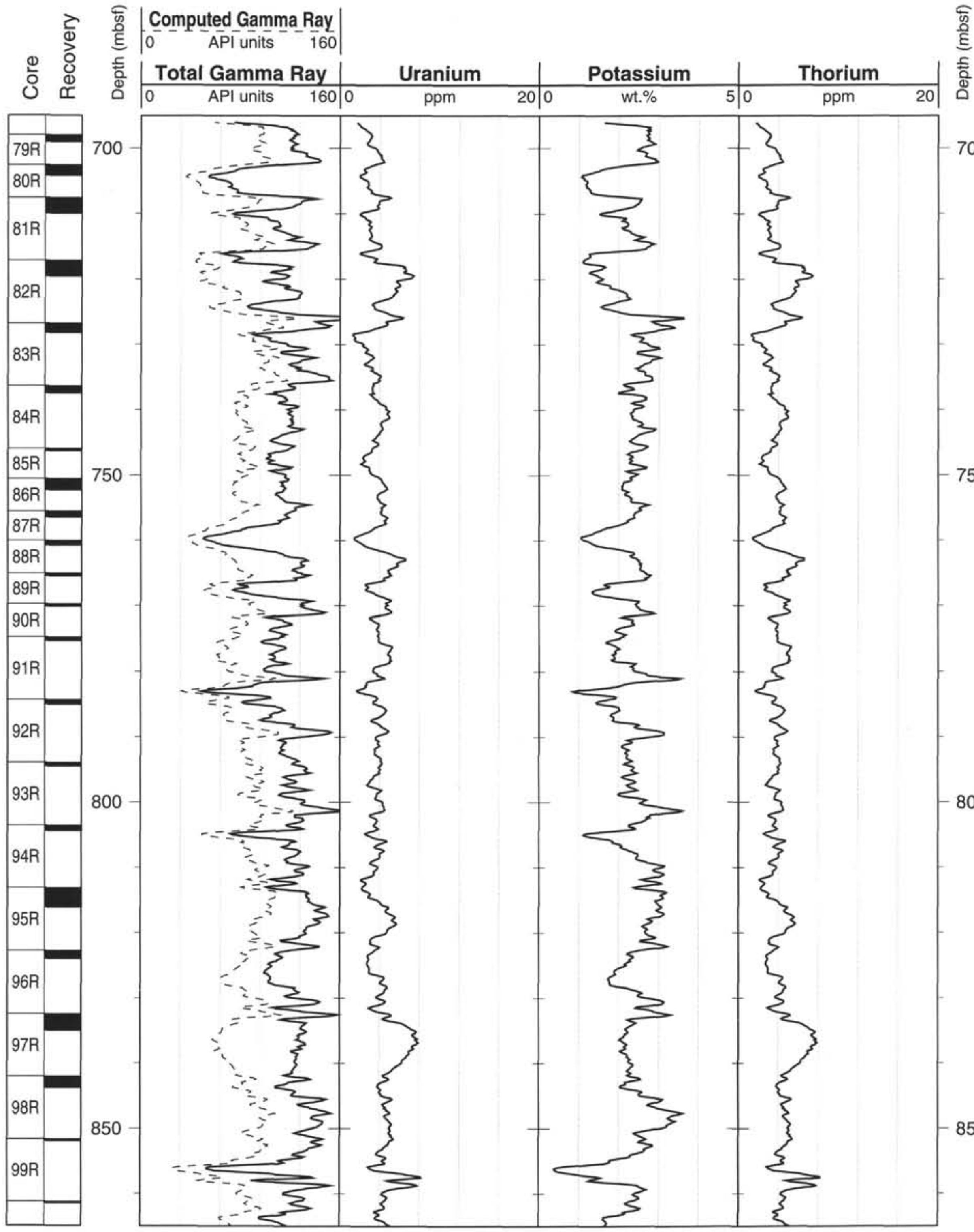

Hole 976B: Natural Gamma Ray Logging Data (cont.)

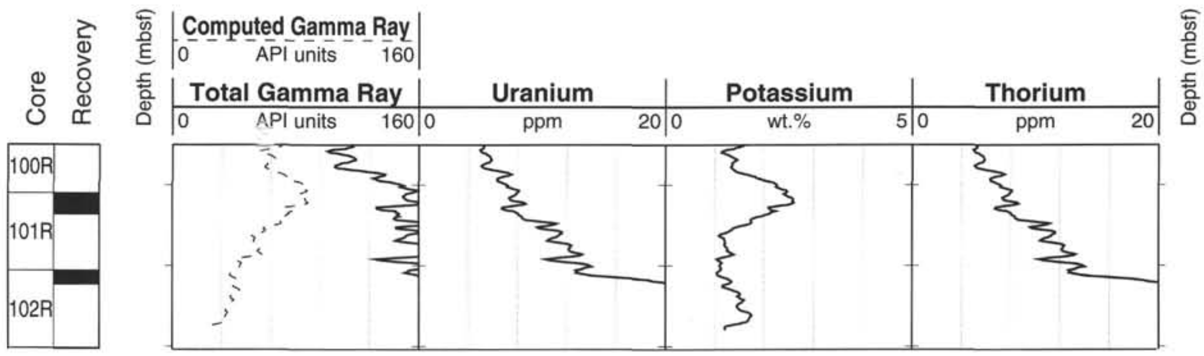

Hole 976B: Geochemical Logging Data

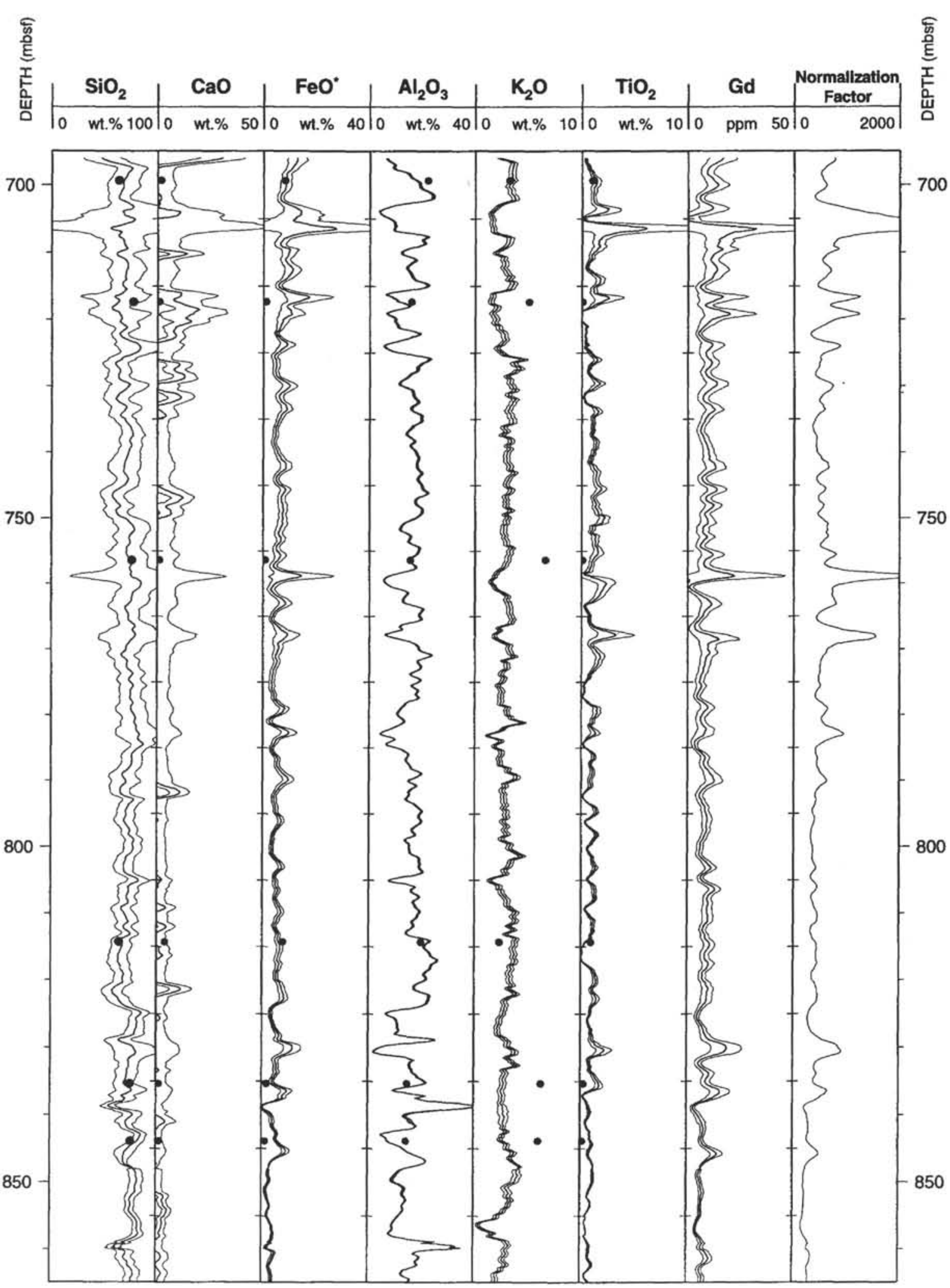

Hole 976B: Geochemical Logging Data (cont.)

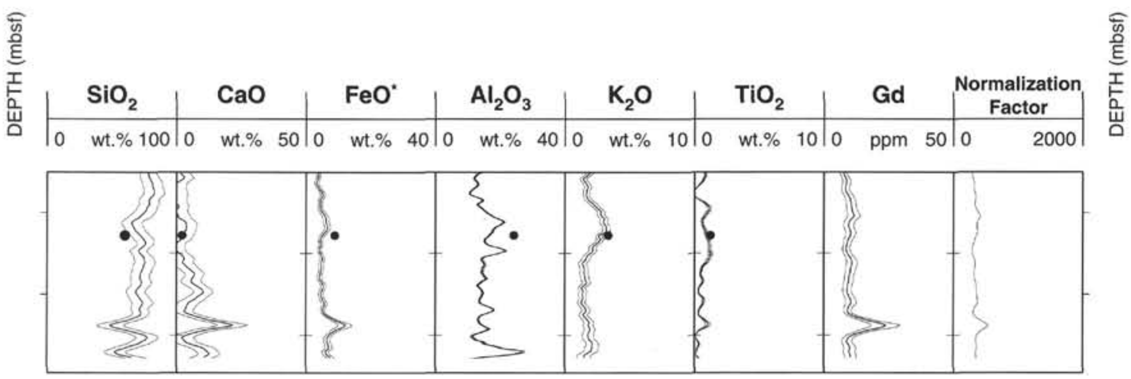

SHORE-BASED LOG PROCESSING

Hole 976E

Bottom felt: 1119 mbrf (used for depth shift to seafloor)
Total penetration: 736.3 mbsf
Total core recovered: 64.85 m (33.7%)

Logging Runs

Logging string 1: DIT/SDT/HLDT/CNTG/NGT
Wireline heave compensator was used to counter ship heave.

Bottom-Hole Assembly

The following bottom-hole assembly are as they appear on the logs after differential depth shift (see "Depth shift" section, this hole) and depth shift to the seafloor. As such, there might be a discrepancy with the original depths given by the drillers onboard. Possible reasons for depth discrepancies are ship heave, use of wireline heave compensator, and drill string and/or wireline stretch.

DIT/SDT/HLDT/CNTG/NGT: Bottom-hole assembly at ~569.5 mbsf.

Processing

Depth shift: No differential depth shift necessary as only one tool string was run. All original logs have been depth shifted to the seafloor (−1119 m).

Gamma-ray processing: NGT data have been processed to correct for borehole size and type of drilling fluid.

Acoustic data processing: The array sonic tool was operated in two modes: linear array mode, with the 8-receivers providing full waveform analysis (compressional and shear) and standard depth-derived borehole compensated mode, including long-spacing (8-10-10-12 ft) and short-spacing (3-5-5-7 ft) logs. In the sedimentary section down to 650 mbsf, the long-spacing logs showed a slightly better quality than the short-spacing ones and have been processed in order to eliminate some of the noise and cycle skipping experienced during the recording. No processing was attempted in the basement section where the logs are too affected by the very poor hole conditions.

Quality Control

A large (>12 in) and irregular borehole affects most recordings, particularly those that require eccentralization (CNTG, HLDT) and a good contact with the borehole wall. In Hole 976A the quality of both density and neutron logs was degraded by the extremely large (caliper often saturated at 18.5 in) and irregular hole. Also, due to lack of centralization and to a 5°–7° deviation which causes the tool to lean on one side of the hole, the sonic data are of poor quality. While reprocessing of the long-spacing logs yielded decent results in the sedimentary section, the logs recorded in linear array mode provided better readings in the basement section.

Data recorded through bottom-hole assembly, such as the neutron and gamma ray data above 569.5 mbsf should be used qualitatively only because of the attenuation on the incoming signal.

Hole diameter was recorded by the hydraulic caliper on the HLDT tool (CALI).

Note: Details of standard shore-based processing procedures are found in the "Explanatory Notes" chapter, this volume. For further information about the logs, please contact:

Cristina Broglia
Phone: 914-365-8343
Fax: 914-365-3182
E-mail: chris@ldeo.columbia.edu

Elizabeth Pratson
Phone: 914-365-8313
Fax: 914-365-3182
E-mail: beth@ldeo.columbia.edu

Hole 976E: Natural Gamma Ray-Resistivity-Sonic Logging Data

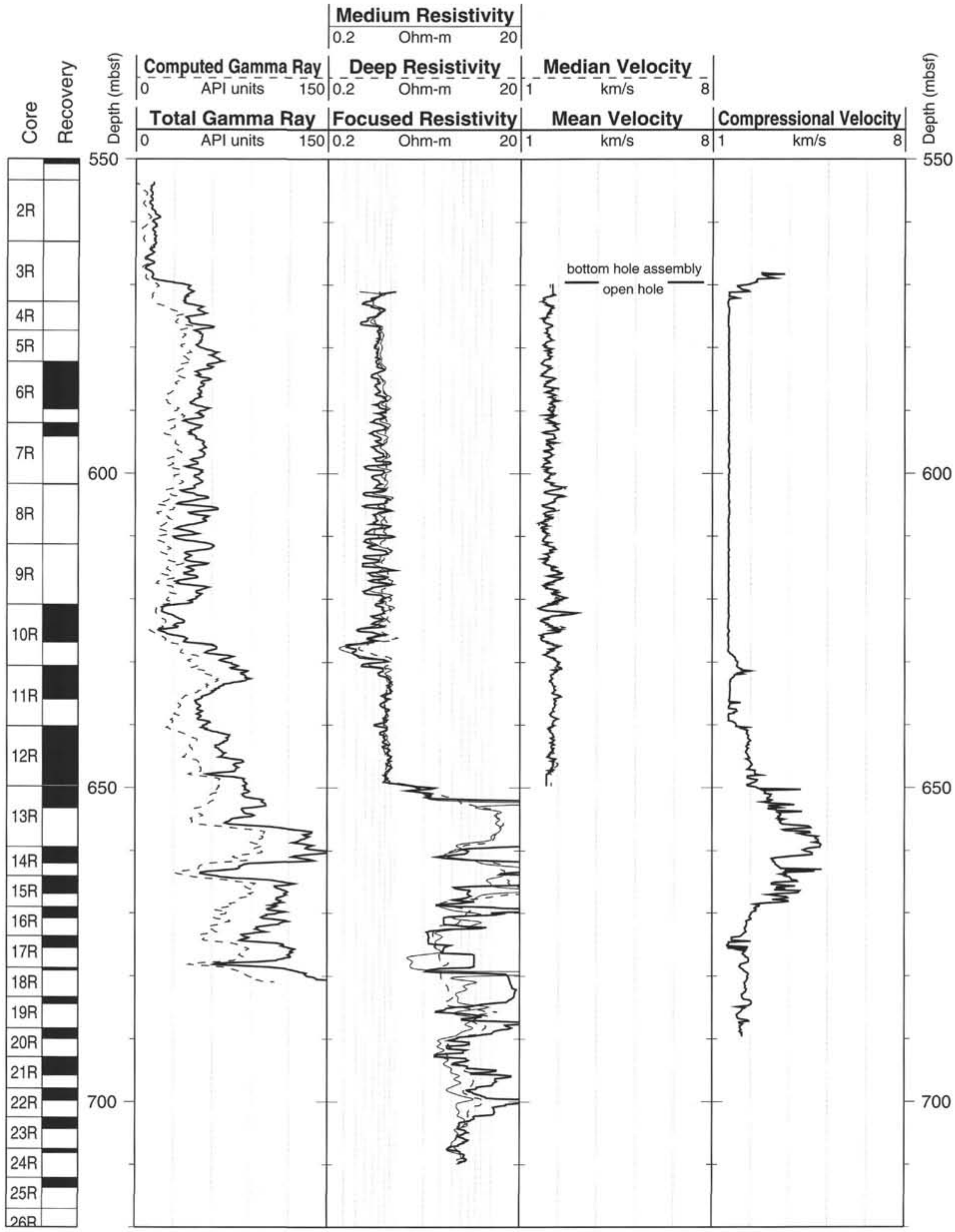

Hole 976E: Natural Gamma Ray-Density-Porosity Logging Data